UNIVERSITAT POLITÈCNICA DE VALÈNCIA

Instituto Interuniversitario de Investigación de Reconocimiento Molecular y Desarrollo Tecnológico

Augusto Juste Dolz

Biogratings: diffractive transducers for biosensing in photonic platforms

PhD. Supervisors

Miquel Avella Oliver

Ángel Maquieira Catalá

Valencia, March 2023

"Las personas, a la postre, siempre vamos a fracasar. Lo único que está en nuestra mano es fracasar mejor"

Juan Ignacio Delgado Alemany (2018)

AGRADECIMIENTOS

Las palabras de agradecimiento siempre tienen un sabor a despedida. En parte lo son. Como mínimo son la despedida de una aventura que comenzó hace ya unos cuantos años. Durante esta etapa de mi vida me han acompañado muchas personas y es en este momento, en el final del camino, cuando me doy cuenta de que no conozco a la mitad de vosotros ni la mitad de lo que querría, y que lo que yo querría es menos de la mitad de lo que la mitad de vosotros merecéis. Es imposible sintetizar en unas pocas líneas toda la gratitud que siento, pero sí me gustaría dedicar unas palabras a todas aquellas personas que han estado conmigo durante estos años de tesis. ¡No os distraeré mucho tiempo!

Empezaré por mis directores. En primer lugar, quería dar las gracias a Ángel Maquieira por abrirme las puertas del grupo SYM, por tu apoyo constante y tu trabajo de supervisión en esta tesis. También por enseñarme que durante la tesis se aprenden muchas cosas (y no solo de química) y que muchas reuniones y charlas valen más que una carrera o un máster.

A Miquel, mi hermano mellizo fenotípico. Gracias por todos los buenos momentos que hemos pasado juntos, tanto dentro como fuera del laboratorio. Nunca podré agradecerte lo suficiente todo lo que he aprendido de ti día tras día ni todo lo que has hecho por mi durante estos años. He tenido la gran suerte de poder contar contigo y con tus consejos, y has sido todo un ejemplo y referente. Ilúvatar sabe que me has acompañado y guiado en esta aventura para librarme de mi anillo único.

Además de mis directores, he tenido el placer de trabajar con excelentes personas que han sido clave en mi crecimiento científico y personal. Quería dar las gracias especialmente a David Giménez. Llegué a este laboratorio con el único objetivo de terminar mi TFG, pero confiaste en mí y me hiciste ver que podía llegar más lejos. Me has enseñado que un buen científico también ha de ser una buena persona. He podido contar contigo desde el primer día, me has prestado tu ayuda cuando ha estado en tus manos y siempre has querido lo mejor para mí. No habría llegado hasta aquí si no fuese por ti.

Por supuesto, también merece una mención especial Estrella Fernández. Gracias por compartir tu experiencia y conocimiento. Tu ayuda ha sido clave en muchos momentos y he podido aprender mucho de ti. No me puedo olvidar de Ángel López, quien desinteresadamente me ha echado una mano siempre que ha podido. Sin embargo, no todo ha sido trabajo, también hemos compartido buenas cervezas y buen rock.

Ahora llega el turno de la parte más importante de esta tesis. Parada obligatoria de cotillas y la única que la mayoría de vosotros vais a leer. Si, habéis adivinado: los agradecimientos a los compañeros de laboratorio. Espero no decepcionaros.

Empezaré por los más veteranos, que nadie se ofenda. En primer lugar, quería dar las gracias a Sergi Morais. He tenido la suerte de poder trabajar contigo y ver que en el mundo de la investigación *No hay tregua* y que *It's a long way to the top if you want rock n roll.* A Miguel Ángel González por enseñarnos todos los años lo importante que es celebrar y compartir; a María José Bañuls por demostrarme la necesidad de pasar más tiempo por el laboratorio (tú sabes por qué) y por solicitar la beca conmigo; a Luís Tortajada por tantas charlas interesantes y por encajar cinco cervezas de forma admirable; a Javi Carrascosa por hacer que todo funcione; a Nuria Pastor por tu ayuda, suministrarnos mascarillas y herramientas y por encargarte de los pedidos durante tanto tiempo; a Eva Brun por tu incansable trabajo en la sala de máquinas y a Arantxa Martínez, Enrique Guijarro y Ana Artigues por procesar tantas solicitudes de GEA y comisiones de servicios. Por último, también quería dar las gracias al resto de profesores y profesoras que forman o han formado parte de este grupo como José Luís López, Patricia Noguera, Pilar Aragón, Rosa Puchades, Julia Atienza y María Asunción Herrero.

Una de las mejores cosas que me llevo después de todos estos años es el haber podido compartir este periodo de tesis con mis compañeros. A vosotros tengo que daros especialmente las gracias por amenizar el día a día y por compartir tantos buenos momentos. Empiezo con las verdaderas leyendas de este laboratorio: la vieja guardia (tan vieja que ya hay hasta segunda generación). Gracias a María José Juárez por todo lo vivido y por compartir alegrías, penas y reflexiones que reconfortan el día a día; a Pedro Quintero por sacarme todos los días unas cuantas risas y por vivir y sufrir conmigo las partes más duras de una tesis, a Maribel Lucío por tu ayuda, consejos y citas diarias; a Gabi Sancho por alegrar el ambiente del laboratorio (siempre te hemos dicho que

empezamos a estar más tranquilos cuando te fuiste, pero la realidad es que se te echa de menos); a Salva Mas por el *thunder*, los setos y legado cadaperrista; a Dani González por sus chistes (malos) e incansable labor de *tembuilding*; a Ana Lázaro por ser la mejor compañera de sitio y el hombro recíproco en el que apoyarme cuando algo no iba bien; a Sara Martorell por transmitirme todos los días felicidad y buen rollo y a Eric Seiti Yamanaka por transmitirme tranquilidad y paciencia; a Noelle do Nascimento por guiarme cuando llegue al laboratorio; a Vicky González por compartir tantos almuerzos en mis primeros días; a Pilar Jiménez por invitarme a jugar a casi todos los deportes que se pueden practicar en la universidad; a Edurne Peña por enseñarme a poner límites cuando es necesario; a Andy Hernández por las cervezas y el pádel y a Zeneida Díaz por los días-están-buenos y las colas-de-caballo que animaban las comidas. Quería dar las gracias también a Noelia Carbó, Raquel Montón, Rafa Alonso, Ahmed Ali, José Dutch, Noemí Farinós, y a todos los estudiantes que han pasado en algún momento por el laboratorio durante esta etapa.

Continúo con la alineación titular del grupo SYM. Gracias a William Teixeira *porque talvez a parte mais bela deste trabalho seja conhecer pessoas como você. Vou levar um amigo comigo para sempre.* Gracias también a Aitor Cubells, por enseñarme lo que es ser buen colega y mejor *bro*; a Yulieth Banguera por colombianizarme cada día un poco más; a Cynthia Collantes por compartir tantas partidas de pádel y organizar eventos que hacen piña; a Amadeo Sena por echarme un cable siempre que has podido; a Yeray Pallás por compartir 'qucemeamientos' en tantos hospitales y clínicas; a Paola Zezza *grazie per il tiramisù, il limoncello e gli arrosti*; y a Laia Mira por fabricar fagos en tiempo récord y por contar conmigo para tratar de materializar algunas ideas locas. Gracias también a los fichajes de invierno, Juan Jesús González, Arturo Patrone, Ana Hernanz, Pilar Martínez, Blanca Martín y Sofía Ocampos por *blablablublublubla* y aportar aire fresco y energías renovadas a este laboratorio (no porque huela a queso).

Fuera de este grupo he podido trabajar con investigadores que me han aportado otra perspectiva de la ciencia y el mundo de la investigación. Quería dar las gracias a Miguel Andrés por abrirme las puertas de tu laboratorio y por acogerme como un miembro más de tu grupo. También a Martina Delgado por todo lo que me has enseñado, por estar siempre dispuesta a ayudarme y, básicamente, por tu contribución clave en esta tesis.

En esta misma línea, también merece mención especial José Luís Cruz, gracias por tu ayuda y colaboración en el segundo capítulo de esta tesis. Por supuesto también quería dar las gracias a Antonio Díez, Yuri Barmenkov, Christian Cuadrado, Antonio Carrascosa, Luís Sánchez, Tomás Marqueño, Abraham Loredo, Xavi Roselló, Manuel Sevillano y Carolina Rondero por sus interesantes y distendidas discusiones sobre temas científicos (y no tan científicos).

Gracias también a Daniel Pastor, Pascual Muñoz, Luís Bru y Gloria Micó de *Photonics Research Labs* por vuestras ideas y por vuestro trabajo. Habría sido muy complicado conseguir lo que hemos conseguido sin vuestra ayuda, instalaciones y dispositivos.

I would also like to thank Jakob Reck, Moritz Kleinert, and Norbert Keil for hosting me at Fraunhofer HHI. Many thanks also to Martin Kresse, Margit Frestl, Cafercan Yilmaz, Klara Mihov, Philipp Großhennig, and David Felipe. It was really interesting to see what you do, and it was a pleasure to learn from you. Herzlichen Dank! Ich hoffe, Sie bald wieder in Berlin zu sehen.

Viaje antes que destino, o eso dicen los caballeros radiantes. Si hay alguien que me ha acompañado durante todo este viaje ha sido Carlos. Nos conocemos desde más de la mitad de nuestras vidas, antes de que me plantease siquiera ser químico, y aquí seguimos como uña y mugre. Gracias por estar ahí y por darme fuerzas en los momentos de flaqueza como un *honorspren*, aunque sea a través de métodos cada vez menos convencionales. Por supuesto, gracias también a Marta por apoyarme e inspirarme con tu creatividad.

Turno para el team Alacuás: Alba, Luisfer, Belén y Arantxa. Aunque ahora sea team Alacuás – Barcelona – Tárrega. La distancia, los trabajos y las obligaciones de personas adultas han hecho que cada vez podamos pasar menos tiempo juntos, pero aun así sabemos que estamos ahí. Gracias por celebrar los éxitos, apoyar en los fracasaos y ayudar en los momentos de incertidumbre. Parte de esta tesis también es vuestra. Gracias también a Víctor Ramos, por compartir durante todo este tiempo el amor por el metal y los videojuegos que tanto me han ayudado a evadirme de la tesis cuando lo he necesitado.

Gracias a mis gatos Félix, Luke, Leia, Kairi, Trisha, Nata y Oreo. *Miau miau mia miau miau miau mia miau miau miau mia miau miau miau mia miau miau miau mia miau miau miau mia miau miau miau miau*. Y a mi perro Trasto. *Guau guau guau guau guau guau guau guau guau*.

A mi familia. Gracias a mis padres Augusto y María Ángeles, por ser mi primera entidad financiadora, por darme las oportunidades, educación y valores que me han convertido en lo que soy hoy en día (para bien o para mal) y por haberme permitido siempre perseguir mis sueños; a Miriam por demostrarme que una hermana es lo mejor que te puede pasar en la vida; a Fernando por elegirnos (aunque como daño colateral) y a mi tía Cristina por preocuparte por mí, darme siempre lo que he necesitado y tratarme como a un hijo. Gracias al resto de la familia Juste-Ferrón-Aviñó-Sancho, por el apoyo durante todos estos años. Gracias también a la familia Clemente-Benita por acogerme como a uno más desde el primer día y hacerme sentir como en casa. Gracias a los que ya no están, porque lo que me habéis dado lo llevaré conmigo eternamente.

Por último, si ahora mismo estoy escribiendo estas líneas es principalmente gracias a Alba. Siempre en la trinchera para pertrecharme. Siempre tranquilizándome y serenándome para quitarme mis fantasmas. Siempre dándome el valor para enfrentarme a todos mis miedos. Siempre iluminando los días más oscuros. Siempre guiándome cuando no veía el camino. Siempre haciéndome sentir que podía con esto. Siempre celebrando mis éxitos y ayudándome a relativizar mis fracasos. Siempre ahí. Porque lo que es de verdad, es para siempre.

ABSTRACT

The scientific and technological progress in recent decades has given rise to sensor systems capable of obtaining, processing, and transmitting information on a multitude of physical and chemical aspects and using it to improve key aspects of many areas of our society. Chemical sensors are compact, miniaturized devices capable of offering alternative solutions to conventional instrumental analysis techniques. In particular, biosensors have become highly relevant due to the progress they have brought to strategic sectors such as clinical diagnostics, the food industry, and the environment.

Optical biosensors rely on interactions between light and matter to transduce biosensing events and provide important features such as stability, immunity to external stimuli, and versatility in the development of label-free approaches. This last aspect usually exploits nanoscopic phenomena and its development in closely linked to the progress in nanoscience and nanotechnology.

A key aspect of label-free biosensing is the discovery and development of new transduction strategies. In this regard, although they are at an early stage of development, diffractive biosensors offer great potential in terms of simplicity, miniaturization, and the ability to minimize unwanted signals from non-specific interactions, among other aspects.

This thesis aims to innovate diffractive biosensing and to expand its scope by conceptualizing, designing, and implementing diffractive structures composed of biomolecules, herein called biogratings. Biogratings are networks of bioreceptors fabricated on solid substrates that are designed according to a grating structure. The periodic structuration of biomolecules generates a topographic and refractive index modulation that is able to diffract an incident laser beam. The detection of specific analytes by the biomolecules that compose the biogratings results in a selective accumulation of biological matter in the biograting, which generates an increment of the variation of the refractive index and the thickness that leads to an increase in its diffraction efficiency. Therefore, the diffraction efficiency of the biogratings allows the label-free quantification of biointeractions.

This thesis comprises five scientific publications divided into three chapters. The first chapter focuses on microcontact printing as a technique for the fabrication of biogratings. This technique uses elastomeric moulds to transfer molecular structures to solid substrates and has become a powerful strategy to fabricate biogratings thanks to its simplicity and low cost. However, biomolecules structured by microcontact printing may undergo conformational changes and alter their biological activity. The first part of the chapter explores this phenomenon and introduces an alternative strategy to avoid this problem, herein called indirect microcontact printing. This alternative involves fabricating structures of backfilling agents by standard microcontact printing and then immobilizing the bioreceptors of interest by physisorption in the gaps of the patterned structure. The work develops a general strategy using bovine serum albumin as a backfilling agent to fabricate antibody biogratings and demonstrates its functionality through an immunoassay to detect specific antibodies by diffractive measurements.

In addition to conducting the transfer of bioreceptors by physisorption, microcontact printing also allows the incorporation of chemical reactions to obtain more stable immobilizations. The second part of the first chapter deals with the fabrication of protein biogratings through physisorption, thiol-ene, and imine reactions, and compares the main aspects of the resulting structures (homogeneity, thickness, functionality, etc.) by immunoassays for antibody detection. In the work, the viability of these structures as transducers for the detection of immunoglobulin G is also demonstrated in the fabrication and application of biogratings of proteins involved in allergies to cow milk.

In addition to the problems related to the activity of the patterned bioreceptors, microcontact printing presents other limitations such as the low reproducibility and homogeneity of the structures, high concentrations of biomolecules and long fabrication times. The second chapter presents a new fabrication method for biogratings that relies on the periodic and selective denaturation of proteins by ultraviolet irradiation as a powerful alternative to microcontact printing. It consists of generating an interference pattern on a continuous biolayer in which the proteins exposed to to constructive interferences are deactivated and those exposed to destructive interferences keep their activity. This methodology enables the generation of large areas of biogratings (around 18 mm2) with high homogeneity and in less than two minutes. Moreover, the resulting

biogratings are able to transduce biorecognition events in the same way as those fabricated by microcontact printing and can also be used for the direct analysis of biological samples.

Finally, the implementation of diffractive phenomena in waveguides for biosensing is a key aspect to develop miniatuirzed and compact devices that allow the integration of optical, electronic, and fluidic functionalities in a single platform. The third chapter of this thesis studies for the first time the incorporation of biogratings in waveguides, herein called bio Bragg gratings (BBGs). These structures introduce new transduction mechanisms in label-free biosensing and expand the scope of biogratings in this scenario. The first part of the chapter focuses on the implementation of BBGs in optical fibers and reports a theoretical and experimental study that demonstrates this transduction mechanism for the first time. This study proves the concept with a model immunoassay and serum samples, demonstrates the main bioanalytical and optical features, and sets the basis for transferring BBGs to other types of waveguide-based photonic platforms. Along these lines, the second part of the chapter focuses on the implementation of BBGs in integrated photonic platforms composed of rib waveguides in order to obtain more robust miniaturized devices with a higher degree of integration.

RESUMEN

El desarrollo científico y tecnológico de las últimas décadas ha dado lugar a sistemas sensores capaces de obtener, procesar y transmitir información sobre multitud de aspectos físicos y químicos, y utilizarla para mejorar aspectos clave de multitud de áreas de nuestra sociedad. Los sensores químicos son dispositivos compactos y miniaturizados capaces de ofrecer soluciones alternativas a las técnicas de análisis instrumental convencionales. En especial, los biosensores han adquirido gran relevancia por los avances que han supuesto para sectores estratégicos como el diagnóstico clínico, la industria alimentaria y el medio ambiente.

Los biosensores ópticos se basan en interacciones entre la luz y la materia para transducir eventos de bioreconocimiento y presentan prestaciones importantes como la estabilidad, inmunidad a estímulos externos y versatilidad en el desarrollo de aproximaciones sin marcaje (label-free). Este último aspecto suele aprovechar fenómenos nanoscópicos y su desarrollo se encuentra muy ligado al progreso de la nanociencia y nanotecnología.

Un aspecto clave en el biosensado sin marcaje consiste en descubrir y desarrollar nuevas estrategias de transducción. En este sentido, aunque se encuentren aun en una etapa temprana de desarrollo, los biosensores difractivos presentan un gran potencial en términos de simplicidad, miniaturización, y capacidad para minimizar señales no deseadas fruto de interacciones no específicas, entre otros aspectos.

Esta tesis persigue innovar en biosensado difractivo y ampliar su ámbito de aplicación, abordándolo a través de la conceptualización, el diseño y la implementación de estructuras difractivas compuestas por biomoléculas, que hemos denominado biogratings. Los biogratings son redes de bioreceptores fabricadas sobre un soporte sólido que están diseñadas de acuerdo con una estructura de tipo grating de difracción. De este modo, la estructuración periódica de biomoléculas genera una modulación topográfica y de índice de refracción que permite difractar un haz láser incidente. El reconocimiento de analitos específicos por parte de las biomoléculas que componen el biograting produce una acumulación de la materia que lo conforma, lo cual genera un incremento en la variación de índice de refracción y el grosor de la red, y se traduce en

un aumento de su eficiencia de difracción. De este modo, la eficiencia de difracción de los biogratings permite cuantificar biointeracciones sin marcaje.

Esta tesis comprende cinco publicaciones científicas distribuidas a lo largo de tres capítulos. El primer capítulo se centra en la impresión por microcontacto como técnica de fabricación de biogratings. Esta técnica utiliza moldes elastoméricos para transferir estructuras moleculares a los sustratos sólidos de interés y gracias principalmente a su simplicidad y bajo coste se ha convertido en una estrategia muy potente para fabricar biogratings. Sin embargo, las biomoléculas estructuradas mediante impresión por microcontacto pueden sufrir cambios conformacionales y modificar su actividad biológica. La primera parte del capítulo profundiza en el estudio de este fenómeno e introduce una estrategia alternativa para evitar este problema, la cual recibe el nombre de impresión por microcontacto indirecta. Esta alternativa consiste en fabricar estructuras de un agente de relleno mediante impresión por microcontacto estándar y después inmovilizar por fisisorción los bioreceptores de interés en los huecos de la estructura estampada. El trabajo desarrolla una estrategia general utilizando albúmina de suero bovino como agente de relleno para fabricar biogratings de anticuerpos y demuestra su funcionalidad a través de un inmunoensayo para detectar anticuerpos específicos mediante medidas difractivas.

Además de llevar a cabo la transferencia de bioreceptores por fisisorción, la impresión por microcontacto permite también incorporar reacciones químicas para obtener inmovilizaciones más estables. La segunda parte del primer capítulo aborda la fabricación de biogratings de proteínas a través de fisiorción y las reacciones tiol-eno e iminas, y compara los principales aspectos de las estructuras resultantes (homogeneidad, grosor, funcionalidad, etc.) mediante inmunoensayos para la detección de anticuerpos. En el trabajo, la viabilidad de estas estructuras como transductores para la detección de inmunoglobulinas G, se demuestra también en la fabricación y aplicación de biogratings de proteínas que participan en alergias a la leche de vaca.

Además de los problemas relacionados con la actividad de los bioreceptores, la impresión por microcontacto presenta otras limitaciones como la baja reproducibilidad y homogeneidad de las estructuras, concentraciones elevadas de biomoléculas y largos tiempos de fabricación. En el segundo capítulo se presenta un nuevo método de

fabricación de biogratings que se basa en la desnaturalización periódica y selectiva de proteínas mediante irradiación ultravioleta que supone una alternativa potente a la estampación por microcontacto. Consiste en generar un patrón de interferencia sobre una biocapa continua de modo que las proteínas expuestas a las interferencias constructivas se desactivan y las expuestas a las destructivas mantienen su actividad. Esta metodología permite fabricar grandes áreas de biogratings (alrededor de 18 mm^2) con una elevada homogeneidad y en menos de dos minutos. Además, los biogratings resultantes son capaces de llevar a cabo la transducción de eventos de bioreconocimiento de la misma manera que los fabricados mediante impresión por microcontacto pudiendo ser utilizados incluso para el análisis directo de muestras biológicas complejas.

Por último, la implementación de fenómenos difractivos en guías de onda para biosensado constituye un aspecto clave para desarrollar dispositivos miniaturizados y compactos que permita integrar todas las funcionalidades ópticas, electrónicas y fluídicas en una única plataforma. El tercer capítulo de esta tesis estudia por primera vez la incorporación de biogratings sobre guías de onda, que hemos denominado como bio Bragg gratings (BBGs). Estas estructuras introducen nuevos mecanismos de transducción en biosensado sin marcaje y expanden el ámbito de aplicación de los biogratings. La primera parte del capítulo se centra en la implementación de BBGs en fibras ópticas y reporta un estudio teórico y experimental que demuestra por primera vez este mecanismo de transducción. Este estudio prueba el concepto con un inmunoensayo modelo y muestras de suero, demuestra las principales características bioanalíticas y ópticas, y establece las bases para transferir los BBGs a otros tipos de plataformas fotónicas basadas en guías de onda. Siguiendo esta línea, la segunda parte del capítulo se centra en la implementación de los BBGs en plataformas fotónicas integradas compuestas por guías de onda de tipo rib con la finalidad de obtener dispositivos miniaturizados más robustos y con un mayor grado de integración.

RESUM

El desenvolupament científic i tecnològic de les últimes dècades ha donat lloc a sistemes sensors capaços d'obtindre, processar i transmetre informació sobre multitud d'aspectes físics i químics, i utilizar-la per a millorar aspectes clau de multitud d'arees de la nostra societat. Els sensors químics són dispositius compactes i miniaturitzats capaços d'oferir solucions alternatives a les tècniques d'analisi instrumental convencionals. Especialment, els biosensors han adquirit gran rellevància pels avanços que han suposat per als sectors estratègics com el diagnòstic clínic, la industria alimentària i el medi ambient.

Els biosensors òptics es basen en interaccions entre la llum i la matèria per a transduir esdeveniments de bioreconèixement i presenten prestacions importants com estabilitat, immunitat a estímuls externs i versatilitat en el desenvolupament d'aproximacions sense marcatge (label-free). Aquest últim aspecte sol aprofitat fenòmens nanoscòpics i el seu desenvolupament es troba molt lligat al progrés de la nanociència i nanotecnologia.

Un aspecte clau en el biosensat sense marcatge consisteix a descobrir i desenvolupar noves estratègies de transducció. En aquest sentit, encara que es troben fins i tot en una etapa primerenca de desenvolupament, els biosensors difractius presenten un gran potencial en termes de simplicitat, miniaturització, i capacitat per a minimitzar senyals no desitjats fruit d'interaccions no específiques, entre altres aspectes.

Aquesta tesi persegueix innovar en biosensat difractiu i ampliar el seu àmbit d'aplicació, abordant-lo a través de la conceptualització, el diseny i la implementació d'estructures difractives compostes per biomolècules, que hem denominat biogratings. Els biogratings són xarxes de bioreceptors fabricades sobre un suport sòlid que están disenyades d'acord amb una estructura de tipus grating de difracció. D'aquesta manera, l'estructuració periòdica de biomolècules genera una modulació topogràfica i d'índex de refracció que permet difractar un feix láser incident. El reconeixement d'analits específics per part de les biomolècules que componen el biograting produeix una acumulació de la materia que el conforma, la qual cosa genera un increment de la variació d'índex de refracció i del gruix de la xarxa, i es tradueix en un augment de la

seua eficiència de difracció. D'aquesta manera, l'eficiència de difracció dels biogratings permet quantificar biointeraccions sense marcatge.

Aquesta tesi comprén cinc publicacions científiques distribuïdes al llarg de tres capítol. El primer capítol es centra en la impressió per microcontacte com a tècnica de fabricació de biogratings. Aquesta técnica utilitza motles elastomèrics per a transferir estructures moleculars als substrats sòlids d'interés i gràcies principalment a la seua simplicitat i baix cost s'ha convertit en una estratègia molt potent per a fabricar biogratings. No obstant això, les biomolècules estructurades mitjançant impressió per microcontacte poden patir canvis conformacionals i modificar la seua activitat biològica. La primera part del capítol aprofundeix en l'estudi d'aquest fenomen i introdueix una estratègia alternativa per a evitar aquest problema, la qual rep el nom de impressió per microcontacte indirecte. Aquesta alternativa consisteix a fabricar estructures d'un agent de farciment mitjançant impressió per microcontacte estàndard i després immobilitzar per fisisorció els bioreceptors d'interés en els buits de l'estructura estampada. El treball desenvolupa una estratègia general utilitzant albúmina de sèrum boví com agent de farciment per a fabricar biogratings d'anticossos i demostra la seua funcionalitat a través d'un immunoassaig per a detectar anticossos específics mitjançant mesures difractives.

A més de dur a terme la transferència de bioreceptors de fisisorció, la impressió per microcontacte permet també incorporar reaccions químiques per a obtindre immobilitzacions més estables. La segona part del primer capítol aborda la fabricació de biogratings de proteïnes a través de fisisorció i les reaccions tiol-é i imines, i compara els principals aspectes de les estructures resultants (homogeneïtat, gruix, funcionalitat, etc.) mitjançant immunoassajos per a la detecció d'anticossos. En el treball, la viabilitat d'aquestes estructures com a transductors per a la detecció d'immunoglobulines G, es demostra també en la fabricación i aplicació de biogratings de proteïnes que participen en al·lèrgies a la llet de vaca.

A més dels problemes relacionats amb l'activitat dels bioreceptors, la impressió per microcontacte presenta altres limitacions com la baixa reproducibilitat i homogeneïtat de les estructures, concentracions elevades de biomolècules i llargs temps de fabricación. En el segon capítol es presenta un nou mètode de fabricació de biogratings que es basa en la desnaturalització periòdica i selectiva de proteïnes mitjançant

irradiació ultraviolada que suposa una alternativa potent a l'estampació per microcontacte. Consisteix a generar un patró d'interferència sobre una biocapa contínua de manera que les proteïnes exposades a les destructives mantenen la seua activitat. Aquesta metodologia permet fabricar grans àrees de biogratings (al voltant de 18 mm2) amb una elevada homogeneïtat i en menys de dos minuts. A més, els biogratings resultants són capaços de dur a terme la transducció d'esdeveniments de bioreconèixement de la mateixa manera que els fabricats mitjançant impressió per microcontacte podent ser utilitzats fins i tot per a l'anàlisi directa de mostres biològiques complexes.

Finalment, la implementació de fenòmens difractius en guies d'ona per a biosensat constitueix un aspecte clau per a desenvolupar dispositius miniaturitzats i compactes que permeta integrar totes les funcionalitats óptiques, electròniques i fluídiques en una única plataforma. El tercer capítol d'aquesta tesi estudia per primera vegada la incorporación de biogratings sobre guies d'ona, que hem denomitat com a bio Bragg gratings (BBGs). Aquestes estructures introdueixen nous mecanismes de transducció en biosensat sense marcatge i expandeixen l'àmbit d'aplicació dels biogratings. La primera part del capítol es centra en la implementació de BBGs en fibres óptiques i reporta un estudi teòric i experimental que demostra per primera vegada aquest mecanisme de transducció. Aquest estudi prova el concepte amb un immunoassaig model i mostres de sèrum, demostra les principals característiques bioanalítiques i óptiques, i estableix les bases per a transferir els BBGs a altres tipus de plataformes fotóniques basades en guies d'ona. Seguint aquesta línia, la segona part del capítol es centra en la implementació dels BBGs en plataformes fotòniques integrades compostes per guíes d'ona de tipus rib amb la finalitat d'obtindre dispositius miniaturitzats més robustos amb un major grau d'integració.

DISSEMINATION OF RESULTS

The studies performed during the thesis period have led to the scientific documents listed below.

Articles in indexed scientific journals:

1. A. Juste-Dolz, M. Avella-Oliver, R. Puchades, A. Maquieira, "*Indirect Microcontact Printing to Create Functional Patterns of Physisorbed Antibodies*"
   Sensors, 18(9) (2018), 3173
   Impact Factor (2018): 3.018 (Q1)
2. A. Juste-Dolz, E. Fernández-Sánchez, M. Avella-Oliver, A. Maquieira, "*Patterned Biolayers of Protein Antigens for Label free Biosensing in Cow Milk Allergy*".
   Biosensors, 13(2) (2023), 214
   Impact Factor (2021): 5.743 (Q1)
3. A. Juste-Dolz, M. Delgado-Pinar, M. Avella-Oliver, E. Fernández, J.L. Cruz, M.V. Andrés, A. Maquieira, "*Denaturing for nanoarchitectonics: Local and periodic UV-laser photodeactivation of protein biolayers to create functional patterns for biosensing*"
   ACS applied materials and interfaces, 14 (2022), 41640-41648
   Impact Factor (2021): 10.383 (Q1)
4. A. Juste-Dolz, M. Delgado-Pinar, M. Avella-Oliver, E. Fernández, D. Pastor, M.V. Andrés, A. Maquieira, "*Bio Bragg Gratings on microfibers for label-free biosensing*".
   Biosensors and Bioelectronics, 176 (2021), 112916
   Impact Factor (2021): 12.545 (Q1)
5. A. Juste-Dolz, E. Fernández, M. Avella-Oliver, D. Pastor, A. Maquieira, "*Transducing Biorecognition Events Using Surface Bragg Gratings of Proteins Patterned on Integrated Waveguides*"
   Sensors and Actuators B: Chemical, (submitted)
   Impact Factor (2021): 9.221 (Q1)

Patents:

1. A. Juste Dolz, M. Delgado-Pinar, J.M. Avella Oliver, E. Fernández Sánchez, D. Pastor Abellán, P. Muñoz Muñoz, M.V. Andrés Bou, "*Dispositivo Difractivo de Análisis Químico y Biológico*"
   National publication number: 2749689
   International publication number: WO 2021/009397 A1

Communications in conferences:

1. A. Juste-Dolz, M. Avella-Oliver, E. Fernández, R. Puchades, A. Maquieira, "*Assessing different immobilization chemistries to create biomolecular gratings by microcontact printing*"
   XII International Workshop on Sensors and Molecular Recognition, Valencia (Spain), 2018
2. A. Juste-Dolz, M. Avella-Oliver, E. Fernández, R. Puchades, A. Maquieira, "*Metallic nanostructures of Metallica*"
   XII International Workshop on Sensors and Molecular Recognition, Valencia (Spain), 2018
3. M. Avella-Oliver, A. Juste-Dolz, E. Fernández, M. Delgado-Pinar, M. V. Andrés, D. Pastor, A. Maquieira, "*Exploring Holography for Biosensing*"
   XXXVII Reunión Bienal de la Real Sociedad Española de Química, Donostia-San Sebastian (Spain), 2019
4. A. Juste-Dolz, M. Avella-Oliver, A. Maquieira, "*Metallic nanostructures of Metallica*"
   Jornada Jóvenes Investigadores ICMUV, Burjassot (Spain), 2019.
5. A. Juste-Dolz, M. Delgado-Pinar, M. Avella-Oliver, E. Fernandez, D. Pastor, M.V. Andrés, A. Maquieira, "*Label-free biosensors based on biogratings patterned on microfibers*"
   Jornada 25 anys de ciència dels materials del ICMUV, Burjassot (Spain), 2020
6. A. Juste-Dolz, M. Delgado-Pinar, M. Avella-Oliver, E. Fernández, D. Pastor, M.V. Andrés, A. Maquieira, "*Bio Bragg gratings: structured molecular networks for on-fiber bioanalysis*".
   European Conference on Lasers and Electro-Optics and the European Quantum Electronics Conference 2021, Munich (Germany), 2021

7. A. Juste-Dolz, M. Avella-Oliver, M. Delgado-Pinar, E. Fernández, D. Pastor, M.V. Andrés, A. Maquieira, "*Bio Bragg gratings: diffractive molecular networks for on-fiber label-free biosensing*"
   XIV International workshop on sensors and molecular recognition, Valencia (Spain), 2021
8. A. Juste-Dolz, M. Avella-Oliver, M. Delgado-Pinar, E. Fernández, J.L. Cruz, M.V. Andrés, A. Maquieira, "*Selective inactivation of proteins by UV-laser to create functional patterns for biosensing*"
   XIV International workshop on sensors and molecular recognition, Valencia, (Spain), 2021
9. M. Avella-Oliver, A. Juste-Dolz, E. Fernández, R. Puchades, A. Maquieira, "*Diffractive Bioreceptor Networks for the Optical Transduction Biorecognition Events*".
   Europt(r)ode XV, Warsaw (Poland), 2021
10. A. Juste-Dolz, M. Avella-Oliver, M. Delgado-Pinar, E. Fernández, D. Pastor, M.V. Andrés, A. Maquieira, "*Biomolecular gratings on micrometric optical fibers for label-free biosensing*".
    Europt(r)ode XV, Warsaw (Poland), 2021
11. A. Juste-Dolz, M. Avella-Oliver, M. Delgado-Pinar, E. Fernández, D. Pastor, M.V. Andrés, A. Maquieira, "*Protein assemblies on waveguides as surface diffractive gratings for biological applications*".
    XXXVIII Reunión Bienal de la Real Sociedad Española de Química, Granada (Spain), 2022
12. A. Juste-Dolz, M. Avella-Oliver, M. Delgado-Pinar, E. Fernández, D. Pastor, M.V. Andrés, A. Maquieira, "*Bio Bragg gratings on photonic integrated platforms*".
    XV workshop on sensors and molecular recognition, Valencia (Spain), 2022

ACRONYMS AND ABBREVIATIONS

1D	One-dimension
AFM	Atomic force microscopy
APTES	(3-aminopropyl)triethoxysilane
Au	Gold
BBG	Bio Bragg grating
BG	Bragg grating
BLG	β-lactoglobulin
BSA	Bovine serum albumin
CRP	C-reactive protein
DAQ	Digital acquisition card
DBS	Diffraction-based sensing
DNA	Deoxyribonucleic acid
DUT	Device under test
FBG	Fiber Bragg grating
EDC	N-(3-Dimethylaminopropyl)-N’-ethylcarbodiimide
ELISA	Enzyme-linked immunosorbent assay
FESEM	Field emission scanning electron microscopy
GERT	Gap-enhanced Raman tag
HEM	Haemoglobin
hIgG	Human immunoglobulin G
HRP	Horseradish peroxidase
HSA	Human serum albumin
IFFT	Inverse fast Fourier transform
IgE	Immunoglobulin E
IgG	Immunoglobulin G
iSPR	Imaging surface plasmon spectroscopy

LFIA	Lateral flow immunoassay
LOD	Limit of detection
LOQ	Limit of quantification
LPFBG	Long-period fiber Bragg grating
LSPR	Localized surface plasmon resonance
MIP	Molecularly imprinted polymer
n_{eff}	Effective refractive index
NHS	N-hydroxysuccinimide
NP	Nanoparticle
NSB	Non-specific bindings
OFDR	Optical frequency domain reflectivity
PBS	Sodium phosphate buffer
PBS-T	PBS with polysorbate 20
PC	Polycarbonate
PDMS	Poly(dimethylsiloxane)
PE	Polyester
PIC	Photonic integrated circuit
PMMA	Polymethyl methacrylate
PMNIA	Porous microneedles and immunochromatographic assay
PS	Polystyrene
RIgG	Rabbit immunoglobulins G
RSD	Relative standard deviation
RSV	Respiratory syncytial virus
Sap2	Secreted aspartyl proteinase 2
SERS	Surface-enhanced Raman spectroscopy
SNR	Signal to noise ratio
SPR	Surface plasmon spectroscopy

ssDNA	Single-stranded deoxyribonucleic acid
TFBG	Tilted fiber Bragg grating
TIR	Total internal reflection
TL	Tunable laser
TMB	3,3’,5,5’-tetramethylbenzidine
UDTMS	10-undecenyltrimethoxysilane
UV	Ultraviolet
μCP	Microcontact printing
η	Diffraction efficiency

CONTENTS

INTRODUCTION

1. The rise of sensors and biosensors

1.1. General overview

Today, we enjoy the outcome of scientific and technological progress in most aspects of our daily lives. Most of the appliances, devices, and gadgets that we constantly employ, such as computers, smartphones, automatic doors, routers, thermometers, refrigerators, headphones, smoke detectors, or PIN pads rely on the use of sensors.[1] A sensor can be defined as a sum of components and modules that transforms physical (heat, mass, pressure, movement, etc.) or chemical (pH, ionic strength, concentration, binding affinity, enzyme activity, etc.) magnitudes into measurable signals.[2,3] Nowadays, nanoscience and nanotechnology have become increasingly relevant in the progress of sensors to conceive miniaturized, compact, and low-cost sensing devices with potential applications in key areas of our society such as industry, environmental control, medicine, and defense.[4–16]

In chemistry, the rise of chemical sensors (or chemosensors) has contributed to developing alternative solutions to solve the limitations of standard instrumental systems in terms of sensitivity, selectivity, simplicity, robustness, price, and automation.[17] A chemosensor is a device that integrates a receptor designed to interact selectively with a target compound (analyte), and a transducer to convert this interaction into processable signals.[18,19] In addition to these main components, a chemosensor can also integrate other elements to process samples and signals, such as microfluidics or microcontrollers.

Among all the different types of chemical sensors, those designed to sense biological molecules (proteins, nucleic acids, metabolites, etc.) and microorganisms (cells, bacteria, and viruses) have attracted great interest mostly since the second half of the 20th century. This kind of chemosensor, known as biosensors, has led to a great and growing scientific activity within the last 25 years, reaching more than 6500 publications in scientific indexed journals in the year 2021. The biosensor market has also burst in the worldwide economy, valued at USD 25.5 billion in 2021, and is projected to reach UDS 36.7 billion by 2026.[20] It is expected that this market will grow at the highest rate from 2021 to 2026, led by companies such as Abbott, Roche, Bio-Rad Laboratories,

Merck, and Bayer. The main aspects that support this increment are the development of sharp solutions applied in health and the growing prevalence of infectious (malaria, typhoid fever, HIV, etc)[21–23] and chronic (cardiovascular, cancer, diabetes, and mental)[24,25] diseases. Since its worldwide outbreak in March of 2020, the COVID-19 pandemic has promoted an ongoing demand for remote monitoring, home-based point-of-care devices, and affordable diagnostics.[26–31]

1.2. Biosensors

According to the IUPAC definition, a biosensor is a self-contained integrated device that is capable of providing specific quantitative or semi-quantitative analytical information using biological (i.e protein, nucleic acid, enzymes, aptamers), or biomimetic (i.e molecularly imprinted polymers) recognition elements that are in direct contact with a physicochemical transducer, capable of producing a measurable signal in presence of an analyte (Figure 1).[32] From a broader viewpoint, the term biosensing addresses the development of biosensors and bioanalytical techniques. A crucial phenomenon involved in biosensing is molecular recognition,[33] or biorecognition, between biological receptors (probes) and analytes (targets). Biorecognition processes are based on the intrinsic capability of many macromolecules of living organisms to selectively bind to their target compounds performing a huge number of biological functions. Therefore, the use of biomolecular species as receptors allows selective analysis of the complementary species with extraordinary affinity.[34]

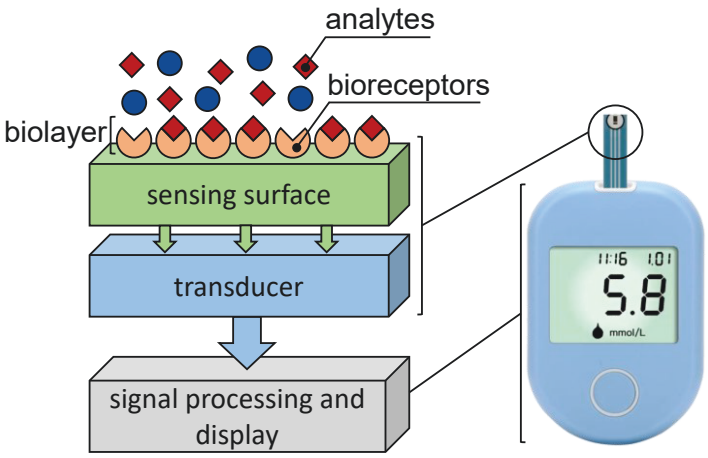

Figure 1. General scheme of a biosensor and analogy with a glucometer.

Since the first biosensor developed by Leland Charles Clark Jr in 1962 to detect glucose by an amperometric enzymatic electrode,[35] the progress in biosensors has been remarkable, especially in the field of clinical diagnosis[30,36–41] but also in other strategic sectors such as agrifood, industrial, and environmental.[42–50] Currently, the research and development of biosensors involve different disciplines that converge in three fundamental areas: discovering new elements for molecular recognition, new tools and materials for miniaturized and low-cost devices, and new strategies to detect and transduce biorecognition events. This doctoral thesis focuses on these two last areas and the next sections will state their most relevant aspects.

1.3. Sensing surface

Biosensing systems can be classified as homogeneous when probes and targets are in the same phase, typically aqueous,[51] and heterogeneous when probes and targets are in different phases typically solid and aqueous.[52] In heterogeneous assays, probes are commonly attached to solid substrates, known as sensing surfaces, to sense target compounds present in liquid samples.[53] A wide range of immobilization strategies of probes in heterogeneous biosensing formats can be employed, ranging from passive adsorption (physical adsorption) to covalent chemistries, and more sophisticated approaches such as affinity interactions and physical entrapment.

Physical adsorption relies on weak forces (Van der Waals, hydrogen bonding, and electrostatic interactions) between the biological probes and the sensing surface (Figure 2A).[54] This is a paradigmatic strategy widely employed in a multitude of materials such as glass, polymers, and carbon substrates without previous chemical modification. However, due to the reversible and random nature of this process, even though passive adsorption is a practical method to immobilize biomolecules, other immobilization methods can result to be more convenient depending on the nature of the bioreceptor, the sensing surface, and the assay.[55]

In covalent immobilization, bioreceptors become attached to the host substrate through a chemical reaction between their functional groups and the chemical groups of the sensing surface. Consequently, more controlled and stable immobilizations can be

achieved. A pre-treatment of the sensing surface is generally required to generate active chemical groups, which usually involves the use of reactants and time-consuming processes. Paradigmatic reaction pathways in the biosensing field are the activation of carboxylic acids in esters mediated by the reaction between carbodiimides and succinimides, the formation of Schiff bases between amine groups, and aldehydes (Figure 2B), and click reactions between thiols and alkene groups to form thioethers.[56,57]

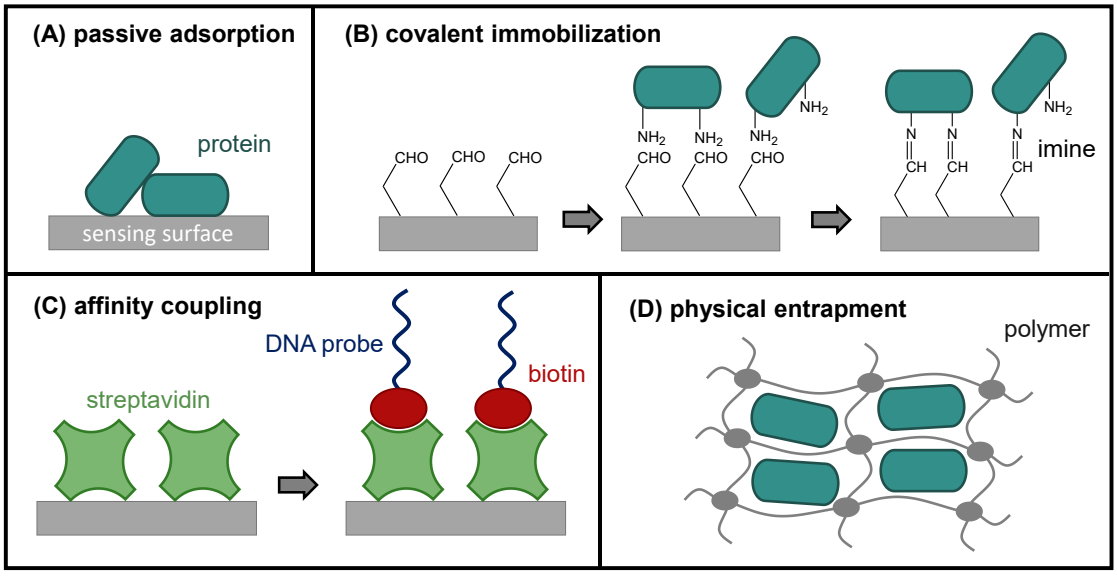

Figure 2. Examples of immobilization of bioreceptors by **(A)** passive adsorption, **(B)** covalent attachment by the formation of Schiff bases, **(C)** affinity coupling based on the avidin-biotin interaction, and **(D)** physical entrapment.

Bioreceptors can also be attached to host substrates using coupling biomolecules. This method exploits the strong specific interaction of complementary biomolecules such as biotin with avidin or streptavidin (Figure 2C), Protein A or G with antibodies, or lectins with sugars.[58] It should be noted that the previous attachment of one of the biomolecules to the host substrate is still required in this approach.[59] One of the main advantages of indirect coupling relies on the reversible and oriented immobilization of bioreceptors, being possible to break the interaction between complementary biomolecules and reuse the substrates.[60]

Finally, bioreceptors can also be retained physically in the internal cavities of porous polymeric materials such as polyacrylates, polyacrylamides, polymethacrylates, and

polystyrene (Figure 2D).[61] In general, this immobilization method is carried out by interfacial polymerization, simple evaporation of solvents, and membrane retention, being strongly limited by the diffusion of bioreceptors through the materials.

1.4. Micro and nano structuration of biolayers

In heterogeneous biosensors, the immobilized bioreceptors form a film or layer of biological material on the sensing surface, typically called biolayer. The biolayer can cover the entire surface (Figure 3A), or only coat discrete areas following millimetric, micrometric, and nanometric patterns to meet specific requirements for particular purposes. One of the most widespread techniques is microarraying, which is based on spotting arrays of small volumes of probe solutions (nanoliters or picoliters) in small areas (Figure 3B).[62] This technique has been typically employed using colorimetric and fluorometric markers to quantify simultaneously multiple analytes such as clinical biomarkers, nucleic acids with polymorphisms, allergens, pathogens, and toxins. As a worth-mentioning example, fluorometric microarrays have been developed for massive screening in genomics and proteomics.[63–67]

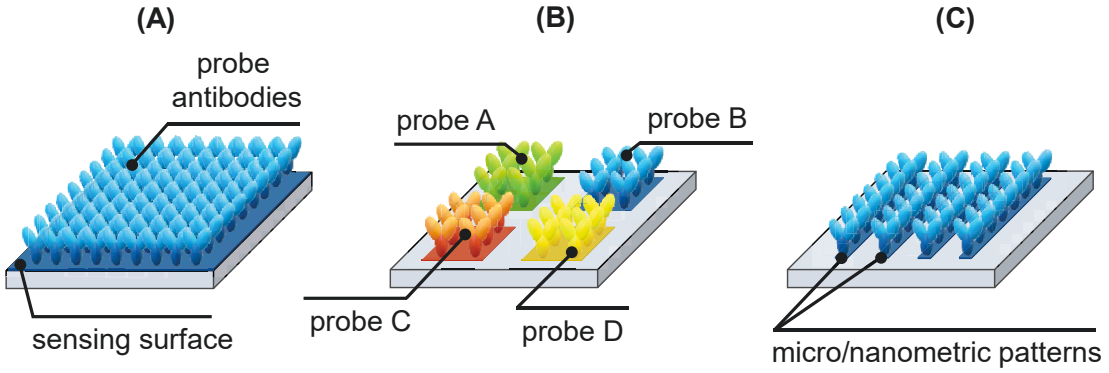

Figure 3. Visualization of a **(A)** continuous, **(B)** microarrayed, and **(C)** micro/nanostructured biolayer.

In addition to providing interesting multiplexing capabilities, some micrometric and nanoscopic patterns have the potential to contribute actively to the transduction of biointeractions, particularly enabling light-matter phenomena that can be employed to

quantify biorecognition events (Figure 3C).[68,69] Nanostructuration techniques such as photolithography, electron-beam lithography, and dip-pen lithography have been applied to produce optically-active structures in different kinds of substrates.[70] However, even though these techniques provide excellent control and homogeneity of the resulting structures, they present some limitations for biosensing due to their complexity, need for expensive facilities, time-consuming operations, and short-scale manufacturing.[71]

Soft-lithography is an alternative to standard nanofabrication techniques and relies on the use of elastomeric "soft" molds to transfer structures to final substrates.[72] Among these techniques, microcontact printing (μCP) has gained popularity due to its potential to create two-dimensional periodic distributions of molecules on different materials.[73,74] In μCP, the elastomeric mold is fabricated by pouring a solution of poly(dimethylsiloxane) (PDMS) prepolymer onto a previously patterned master structure.[75,76] Then, the resulting polymeric structures (stamps), are immersed (inking) into a solution of the molecules to be patterned (organic molecules, proteins, DNA, cells, etc), which are finally transferred (stamped) to the sensing surface and immobilized following the complementary pattern of the master structure (Figure 4).[77]

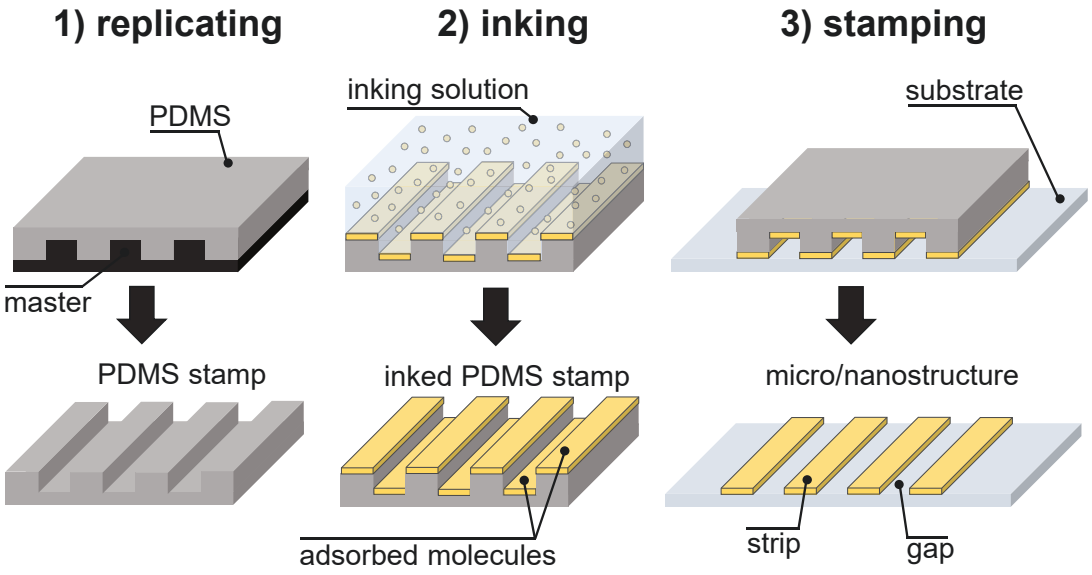

Figure 4. Representation of the μCP process to generate a structured biolayer of molecules onto a sensing surface.

The transfer of bioreceptors during the stamping stage is usually driven by physical forces, and the performance of this process ultimately depends on the relative tendency of the inked molecules to become physisorbed onto the sensing surface. Alternatively, μCP can be tailored to incorporate coupling chemical reactions between the ink molecules and the sensing surface.[78–82] In this variation of μCP more stable attachment chemistries are prone to improve the immobilization strength and the performance of the patterned bioreceptors.

The simplicity, inexpensiveness, minimal need for nanofabrication facilities, and large-scale capability are important advantages of μCP over standard nanofabrication techniques. However, μCP presents some limitations, such as the moderate reproducibility of the resulting patterns, high concentrations of inking molecules needed, long inking times, and difficult industrial scalability. Along these lines, finding alternative structuration methods that overcome the limitations of the abovementioned techniques is nowadays a scientific challenge that remains to be solved.

1.5. Transduction principles

Transduction principles are the mechanisms employed to transform physicochemical quantities into measurable signals. According to the operating principle of the transducer, biosensors are broadly categorized as electrochemical, thermal, acoustic-gravimetric, and optical.[1]

In electrochemical biosensing, a change in an electrical signal (voltage, current, impedance, capacitance, etc.) is produced after the binding reaction between the bioreceptors and the analytes.[83] Electrochemical biosystems are the most available biosensors in the market and they exhibit good bioanalytical performances due to the combination of the sensitivity of the electrochemical techniques with the intrinsic selectivity of biorecognition events. However, they are extremely sensitive to chemical interferents and temperature changes which must be considered to some point-of-care applications.[84]

Thermal biosensors exploit the thermodynamic properties of biological reactions.[85] Temperature changes measured during an exothermic or endothermic reaction are

proportional to the reaction enthalpy and the number of biorecognition events during the reaction. As complex strategies and long experimental procedures are needed to discriminate effectively between specific and non-specific heat changes, the application of thermal biosensors is quite limited. However, they have demonstrated great performance in analyzing enzymatic catalytic reactions of clinically interesting metabolites.[86]

Gravimetric biosensors measure changes in the mass of the biolayer during a biorecognition process on the surface of a mechanical sensor like a cantilever or a crystal resonator.[69] The increment of mass can be determined by measuring the bending of a cantilever or changes in the resonant wave of a piezoelectric crystal. Among all the gravimetric biosensing approaches in the state-of-art, quartz crystal microbalance constitutes the most employed technique for dynamic studies.[87]

Finally, optical biosensors are rooted in the measurement of variations in electromagnetic magnitudes (amplitude, wavelength, polarization, etc), as a consequence of light-matter phenomena (absorption, emission, transmission, etc) induced by biorecognition events.[1] The great performance of optical biosensors compared to those based on other physical magnitudes rely on their better sensitivity, immunity to external disturbance, stability, and low noise of the optical signals.[88] Given the scope of this thesis, the following sections will focus on optical biosensing.

2. Optical biosensors

The detection of biointeractions is grounded on the generation of analytical signals that are proportional to chemical parameters such as target concentration or binding affinity.[89] In most bioanalytical systems, these signals cannot be generated by the biorecognition events themselves and require to be assisted by signaling elements (known as labels) that produce measurable signals. These labels are typically bound (or conjugated) to one of the species involved in the biochemical reaction, to secondary reagents that interact with targets, or to target analogs. The main labels employed in optical biosensing are fluorophores, enzymes, and metallic nanoparticles.

Fluorophores are typically conjugated to biological species and used as labels that generate fluorescent signals when properly excited. It is available a wide variety of fluorophores that can be employed for biosensing.[90] The development of new fluorophores and light-emitting particles (quantum dots, upconversion particles, perovskites, etc.) is still a dynamic field in the scientific literature.[91–98] Enzymes are also extensively employed as labels for optical biosensing, where detectable optical changes are induced by adding a colorimetric enzymatic substrate.[99] One of the most exploited enzymatic labels is the horseradish peroxidase (HRP), which together with the substrate 3,3',5,5'-tetramethylbenzidine (TMB) produces a blue color liquid or precipitate that can be detected by the naked eye and quantified by spectroscopic techniques. Colorful micro and nanoparticles (i.e. gold nanoparticles) are also typically conjugated to biomolecules and employed for naked-eye detection in biorecognition assays, such as lateral flow tests.[100] In addition, gold nanoparticles are also able to catalyze the reduction of silver ions to metallic silver that precipitates in presence of a reducing agent. These metallic precipitates absorb, scatter, and reflect light, improving by several orders of magnitude the sensitivity in biosensing approaches when compared to the direct colorimetric detection of gold nanoparticles.[101]

Label-based optical strategies have demonstrated to provide many possibilities to afford the ongoing demand for highly sensitive and cost-effective biosensing systems. However, they inevitably require bioconjugation and signal development steps that may imply an important drawback in terms of simplicity and reliability of the results due to signal artifacts of the labels (i.e. quenching or photobleaching). In addition, labels can also interfere with the biorecognition process under study by steric occlusion of the binding sites.[102] Moreover, in most bioconjugation processes it is challenging to control properly the ratio of bioreceptors that are linked to label particles.

Alternatively, the rise of nanoscience and nanotechnology has made it possible to exploit nanoscopic light-matter phenomena capable of transducing biorecognition events without using labels. Label-free optical systems deal with species in their native state, thus reducing costs and complexity, and avoiding signal artifacts from the labels.[89,103] Moreover, label-free systems favor real-time measurements, providing high-throughput kinetic data of the biorecognition processes under study.[104,105] However,

these systems are not yet able to reach sensitivities comparable to those achieved with labels and they typically require expensive nanofabrication processes and materials difficult to be produced at a large scale. Therefore, a key aspect of label-free biosensing relies on discovering new transduction strategies capable of overcoming these limitations.[106] In the next sections, considering the state-of-the-art and the scope of this thesis, some of the most relevant physicochemical phenomena exploited for optical label-free approaches for biosensing are discussed.

2.1. Plasmonic biosensing

Surface plasmon resonance (SPR) is a landmark technic in label-free biosensing. The physicochemical phenomenon behind SPR relies on the resonant oscillation of electrons of a metallic surface (plasmons) generated by incident light.[107] Plasmons can be detected as spectrophotometric absorptions, and their spectral features are defined by the geometry and the nature of the metallic surface, as well as the wavelength and angle of the incident light. In SPR biosensing approaches, the bioreceptors are immobilized onto the metallic layer, which acts as the sensing surface. Basically, when target molecules interact with the immobilized bioreceptors, the amount of biological matter at the biolayer is modified and produces a change in the refractive index that affects the surface plasmons. Exploiting this phenomenon, it is possible to detect and quantify these interactions by measuring the shift of the plasmon resonant frequency.[108]

In the last decades, the basic and applied research on SPR has resulted in many scientific innovations that have been implemented in commercial systems.[109] Paradigmatic examples of this progress are imaging surface plasmon resonance (iSPR) and localized surface plasmon resonance (LSPR). iSPR combines the SPR biosensing principle with an imaging or scanning system and microarrays of bioreceptors to analyze simultaneously multiple assays.[110] LSPR enables greater confinement of plasmons in the surroundings of noble metals nanostructures (i.e. single nanoparticles,[111] nanoparticle arrays,[112] nanopillars,[113]) with geometrical features smaller than the incident wavelength.[114,115] Therefore, light-matter interactions are enhanced in LSPR, which increases the sensitivity to refractive index variations triggered by biorecognition events.[114,116,117]

LSPR also plays a key role in improving the performance of Raman spectroscopy, a molecule-specific optical technique based on the scattering of light. Scattering occurs when incident photons collide with matter and propagate in different directions than the ones defined by the transmission and reflection conditions. Most collisions are elastic (Rayleigh scattering), whereas 1 of every 10^7 photons collide inelastically (Raman scattering),[118] and are propagated with a different wavelength. Since Raman scattering is defined by the chemical species in the sample, the Raman spectra provide their characteristic vibrational fingerprint. However, Raman signals are inherently weak due to the low population of photons that undergo inelastic scattering. Surface-enhanced Raman Spectroscopy (SERS) boosts Raman signals using nanostructured LSPR substrates.[118] As a consequence, the light-matter interaction with chemical species close to the metallic surface increases, and the Raman performance becomes enhanced by a factor of 10^2-10^5.[119] Thanks to its excellent sensitivity and its ability to provide useful compositional information, many SERS-based systems with special potential to sense biorecognition events in label-free format have been developed.[118,120,121]

Finally, the new trend in plasmonic biosensing moves towards achieving narrower resonances to improve the sensitivity when measuring biorecognition events. Along these lines, Fano resonators and metamaterials have led to attractive high-sensitive biosensing approaches.[122–127] However, their applicability is still restricted by the nanostructuration techniques and the expensive materials that are required for their production.

2.2. Interferometric biosensing

Interferometry englobes a great number of label-free biosensing techniques that are grounded on measuring the amplification or cancellation of propagating waves that overlap in different phases as a result of biorecognition events.[128] One of the most paradigmatic approaches is reflectometric interference spectroscopy. In this approach, a white light beam propagates through a material composed of superimposed nanolayers with different refractive indexes (typically SiO_2 and Ta_2O_5) and undergoes interferometric phenomena due to successive reflections at each layer.[129] When the

nanolayered substrate acts as a sensing surface, changes in the biolayer as a consequence of binding events produce a change in the refractive index that modify the optical path of the light beams and produce a proportional displacement in the reflected interferometric spectra.[130,131]

In the last decades, the ongoing search for miniaturized and compact biosensors has led to many relevant interferometric systems based on waveguiding conditions, which are commented in section 3.3.2.

2.3. Diffractive biosensing

Exploiting light diffraction constitutes a new trend that is pushing for innovative developments in the biosensing field. As compared to other optical detection approaches, diffractive biosensors are considered to be in an early development stage.[132] Nevertheless, the new and improved functionalities provided by diffractive biosensing in terms of miniaturization and integration, and their unique ability to minimize undesired signals from non-specific binders, are promoting the development of novel diffraction-based biosensing approaches. Given the special relevance of light diffraction in this thesis, the physicochemical basics behind this phenomenon and the main diffractive biosensing developments in the state-of-the-art are described in the next subsections.

2.3.1. Diffraction basics

Light diffraction is an interferometric phenomenon that occurs when electromagnetic waves hit a set of slits that are distributed periodically in the same order of magnitude as the wavelength of the incident light. In the case of a single slit, light suffers a spheric bending and the aperture acts as a point source of circular waves (Figure 5A). For a periodic set of slits, the circular waves that emerge from each aperture overlap in different phases, which generate constructive and destructive interferences that result in an interferometric pattern, known as diffraction pattern, composed of a set of bright and dark regions (Figure 5A).

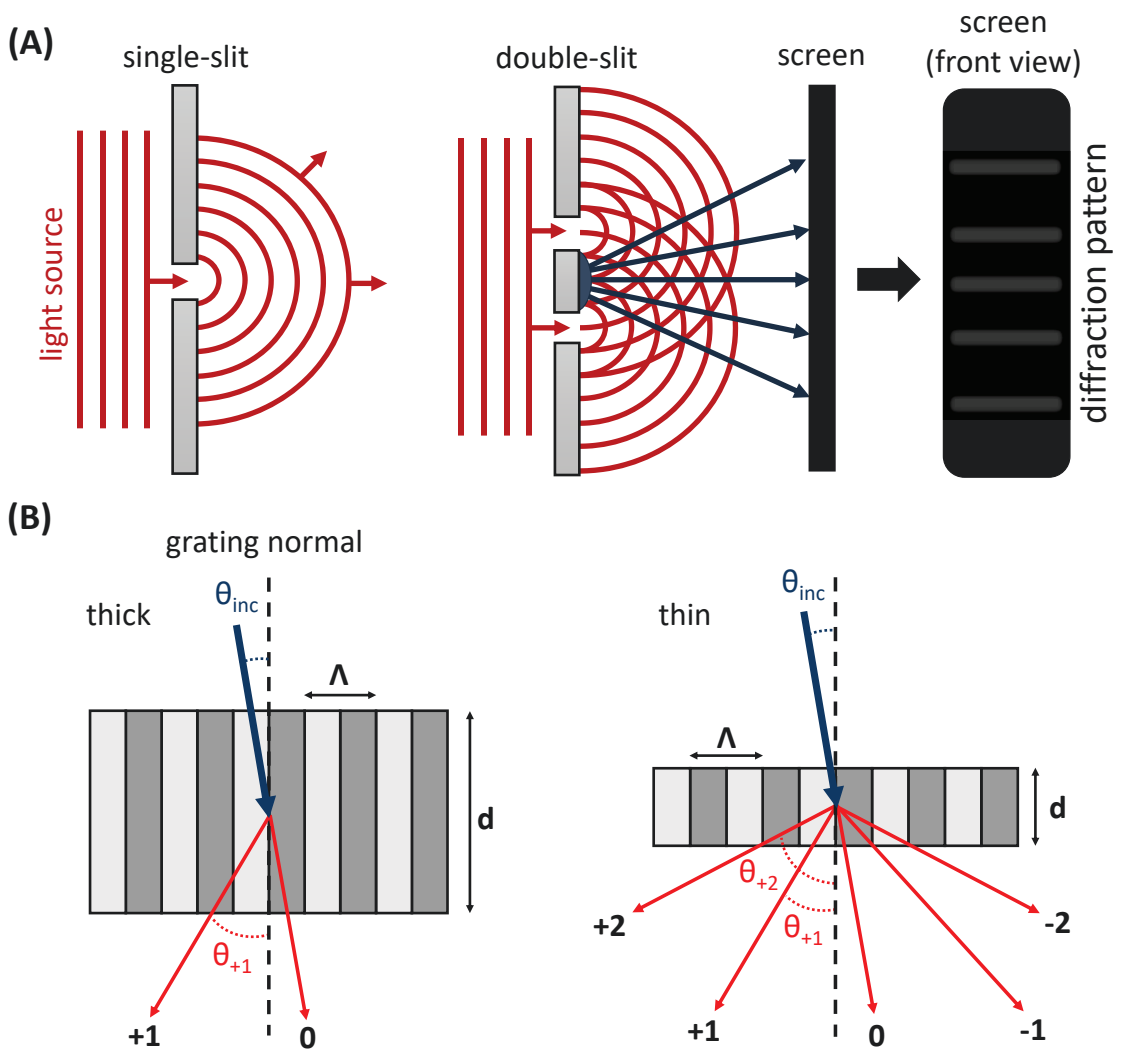

Figure 5. **(A)** Visualization of the diffraction phenomena on a single and a double slit. **(B)** Structural and optical parameters of a thick (left) and a thin (right) diffraction grating.

Diffraction gratings are materials that present optical and structural periodic modulations that can diffract an incident monochromatic or polychromatic light into discrete directions and distribute the power among them. Depending on the direction of the diffracted light, diffraction gratings are classified as transmission or reflection gratings. Moreover, according to the periodicity dimensions they can also be classified as one-dimensional, two-dimensional, and three-dimensional gratings. In this thesis, only one-dimensional transmission gratings will be discussed.

Diffraction gratings are considered thick (volume) or thin (relief) gratings depending on their regime of operation (Figure 5B). Thick gratings operate in the Bragg regime and

they only produce a single diffracted wavefront at the Bragg angle of incidence (θ_B). This behaviour is described by the Bragg equation (Eq. 1).[133]

$$\lambda_0 = 2 \cdot n \cdot \Lambda \cdot sin(\theta_B) \qquad \text{Eq. 1}$$

where λ_0 is the wavelength of the incident light, n is the refractive index and Λ is the period of the grating.

On the other hand, thin gratings produce multiple diffracted wavefronts at almost any angle of incidence. They operate in the Raman-Nath regime and their general behavior is described by the Fraunhofer equation (Eq. 2).[134,135]

$$n_{trans} \cdot sin(\theta_m) = n_{inc} \cdot sin(\theta_{inc}) - m \cdot \frac{\lambda_0}{\Lambda} \qquad \text{Eq. 2}$$

In this equation, the refractive index of the propagating medium of the incident and transmitted light are denoted as n_{inc} and n_{trans}, respectively. The integer numbers that satisfy the grating equation (m) are called diffraction orders and define several discrete angles (θ_m) that fulfill the condition of constructive interferences.

Two different approaches are employed to predict wether a diffraction grating operates as a thick or a thin grating. The Klein-Cook Q parameter[136] (Eq. 3) considers the thickness of the grating (d), the grating period, the average refractive index, and the incident wavelength.

$$Q = \frac{2 \cdot \pi \cdot \lambda_0 \cdot d}{n \cdot \Lambda^2} \qquad \text{Eq. 3}$$

Q values >10 indicate that the grating behaves as a thick grating, whereas Q values < 1 correspond to thin gratings.

The second approach is based on the calculation of the ρ parameter,[137] which considers the refractive index modulation (Δn) of the grating instead of its thickness (Eq. 4).

$$\rho = \frac{\lambda_0^2}{\Lambda^2 \cdot n \cdot \Delta n} \qquad \text{Eq. 4}$$

In this case, ρ values > 10 are for thick gratings and ρ values ≤ 1 are for thin gratings. Beyond this point and given the scope of this thesis, only thin gratings will be considered.

The Fraunhofer equation that defines thin gratings deals with refractive indexes, wavelengths, and propagation angles but does not predict how the power of the incident beam is distributed among the diffraction orders. The grating performance can be determined experimentally using the intensity of each diffracted spot (I_m) compared to the one of the incident beam (I_0). This ratio is called diffraction efficiency (η) and it can be described mathematically as outlined in Eq. 5.

$$\eta = \frac{I_m}{I_0} \qquad \text{Eq.5}$$

Complex mathematical models are needed to predict η.[135] However, in thin diffraction gratings, the calculation of η can be simplified by applying the Bessel function (Eq. 6).[138]

$$\eta = J_m^2 \cdot \left(\frac{\varphi}{2}\right) \qquad \text{Eq.6}$$

where J_m are the Bessel coefficients for each diffracted order and φ is the grating phase. The grating phase is described as follows (Eq. 7):

$$\varphi = \frac{2 \cdot \pi \cdot \Delta n \cdot d}{\lambda_0 \cdot \cos\left(\theta_{inc}\right)} \qquad \text{Eq. 7}$$

Therefore, according to this model, the diffraction efficiency of a thin grating for a given wavelength and angle of incidence will be ultimately determined by its refractive index modulation and thickness.

2.3.2. Diffractive biosensing approaches

Some paradigmatic examples that employ light diffraction for biosensing are those based on diffractive hydrogels and MIPs, and are englobed in a growing and fertile field known as holographic biosensing.[139–142] The concept behind diffractive biosensing is still expanding and other strategies are emerging in this field.

Along these lines, the patterning of biological probes (antibodies and other proteins, nucleic acids, tissues, etc.) onto solid substrates according to a grating structure enables another attractive strategy for diffractive biosensing. In this approach, the patterned biomolecules introduce a modulation of the refractive index and the thickness of the

biolayer, known as biograting, that can diffract an incident laser beam. These biogratings will act as a thin diffraction grating with a periodic modulation of its topography (Figure 6). When specific targets bind to the bioreceptors that compose these biogratings, the amount of biological matter increases selectively in the strips of the structure, resulting in an increment of Δn_g and d that enhances η (Eq.7). As a result, η can be employed to quantify bioanalytical interactions and it can be experimentally determined by monitoring the intensity of the incident laser and diffracted beams.

Over other existing label-free diffractive biosensing approaches, biogratings present a unique potential to minimize the effect of non-specific bindings (NSB). NSB are defined as the binding of undesired biological species to other biomolecules or surfaces when analyzing biological samples.[143] This is an important issue since the concentration of non-specific binders in biological samples is frequently much higher than the one of the targets of interest. In most label-free optical biosensing techniques, this phenomenon restricts their application in undiluted or unprocessed samples because the accumulation of non-specific binders on the sensing surface produces a significant change in the optical signal that cannot be discriminated from the one produced by the specific biorecognition event. In biograting-based systems, NSB is a random process that takes place equally in the strips and the gaps of the structure, whereas biorecognition events only take place on the strips of the grating structure where bioreceptors are present. Therefore, if the biograting is well-designed and fabricated, only the presence of specific biorecognition events will promote the generation of diffracted signals.

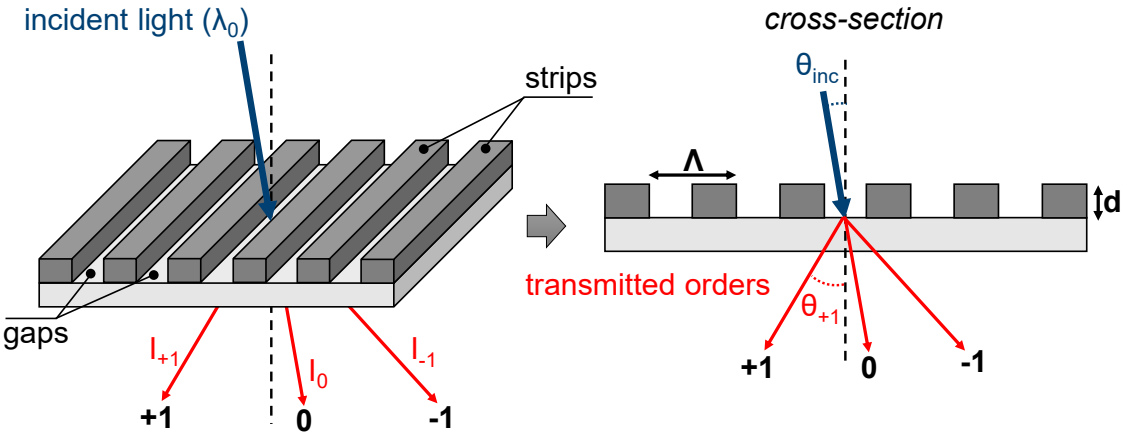

Figure 6. Scheme of a one-dimensional thin diffraction grating represented in a three-dimensional (left) and bi-dimensional (right) perspective.

The implementation of biogratings for biosensing is not extensively reported in the state of the art. This concept was first explored by Goh and coworkers,[144,145] demonstrating their potential for multiplexing and real-time analysis of protein-protein interactions. Later, Wang and coworkers employed MIPs as patterned receptors to detect dichlorophenoxyacetic acid.[146] In another approach called focal molography bioreceptors are patterned according to a submicron structure (mologram) that diffracts light into a focal spot whose intensity depends on the magnitude of biorecognition events.[147–153] Also, previous works of our group developed diffractive immunoassays to quantify low-molecular organic compounds and exploited the compact disk technology to create arrays of biogratings to sense antibodies.[154,155]

The strategy typically employed to fabricate biogratings is μCP due to its simplicity and great performance to pattern biological species. However, the fabrication of biogratings through μCP is restricted by the intrinsic limitations of this technique, which are commented in section 1.4. A key aspect to expand the scope of biogratings to the label-free optical biosensing field and NSB relies on finding alternative fabrication strategies that point toward homogeneous and scalable functional biogratings with improved capabilities.

Besides the abovementioned approaches, bioanalytical systems that employ light diffraction for the transduction of biorecognition events in waveguiding structures hold great relevance in the biosensing field. Therefore, according to the scope and the investigations presented in this thesis, the next section focuses on describing the most relevant aspects of waveguiding biosensing.

3. Waveguiding biosensing

Optical biosensors are in continuous progress to move from working laboratory prototypes to compact and integrated versions that can be deployed outside the lab. In the last two decades, the great scientific activity behind the telecommunication sector has provided vast knowledge for the integration of optical detection systems in waveguiding structures.

The ultimate goal of obtaining high-performance miniaturized optical biosensing devices relies on the monolithic integration of both passive (waveguides) and active (laser sources, detectors, couplers, polarizers, etc) components.[156,157] These devices, known as photonic integrated circuits (PICs), present appealing perspectives to develop lab-on-a-chip biosensing devices thanks to their capability to integrate chemical, optical, microfluidic, and electronic functionalities in one single platform.

Given the relevance of waveguides in this doctoral thesis, the physicochemical principles behind waveguiding and their implementation in the most common biosensing configurations are described below.

3.1. Fundamentals of waveguiding.

Waveguides are dielectric structures that confine and guide electromagnetic waves through the material.[158] When a light beam that propagates through a medium with a high refractive index hits obliquely the interface with a medium with a low refractive index at an incident angle (θ_1), a great portion of the light is propagated in the medium with the low refractive index at a greater angle (θ_2) according to the Snell's law (Figure 7A). Under these conditions, as θ_1 increases, a higher amount of light is reflected in the high-refractive medium. Upon a certain incident angle, also called critical angle (θ_c), the reflected beam becomes tangential to the interface ($\theta_2 = 90°$).[159] Therefore, for θ_1 greater than θ_C, all the light that reaches the interface becomes totally reflected in the high refractive medium (Figure 7A). This phenomenon, called total internal reflection (TIR), provides spatial confinement of electromagnetic waves in waveguiding structures and enables their propagation inside them.[160] In waveguides, the high-index medium is denoted as core, and the low-index medium that coats the core is denoted as cladding or substrate when it acts as a support to the core material (Figure 7B).

A critical parameter for the propagation of electromagnetic waves is the core thickness, which needs to be defined considering the geometrical parameters of the waveguide, the refractive index of each material, and the wavelength of the guided light. The waveguiding phenomenon exclusively takes place through a small discrete set of states called propagation modes.[161] When these requirements are not satisfied, light only

propagates through radiative modes through the cladding or the substrate, which involves high optical losses. (Figure 7B). The whole waveguide design also defines the effective refractive index associated to each mode, which characterizes them and describes how they propagate through the core material.

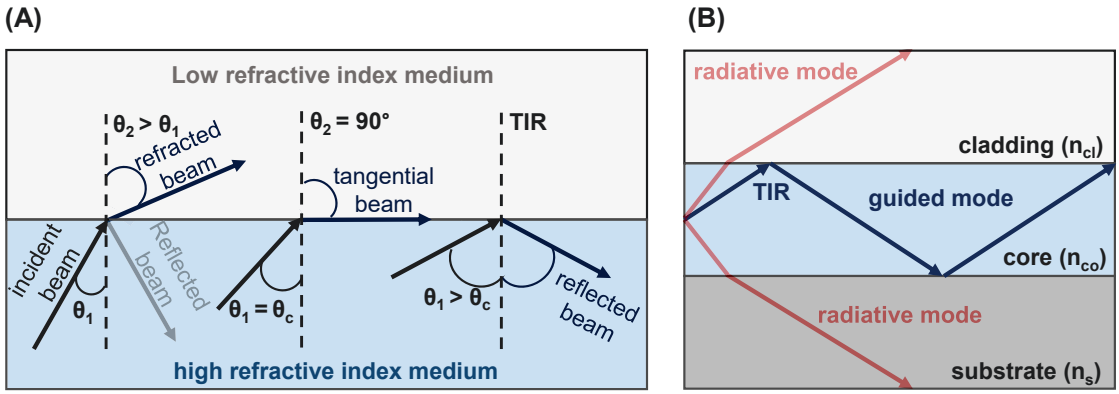

Figure 7. Two-dimensional representation of **(A)** Snell's law and **(B)** light propagation in a typical planar waveguide. n_{cl}, n_{co}, and n_s define the refractive index of the cladding, core, and substrate, respectively.

Waveguides can be classified into planar and channel waveguides according to the number of spatial dimensions that provide confinement.[162] In planar waveguides, light is only confined in one dimension, and therefore the refractive index only changes in one transverse coordinate. In contrast, in channel waveguides the confinement is produced in two dimensions, and its refractive index changes in both transverse coordinates. Depending on the structure of the waveguiding layer, channel waveguides are classified as buried, ridge, diffused, strip-loaded, rib, and ARROW waveguides.[161] Fiber optics are cylindrical structures that are also considered channel waveguides (Figure 8).

Depending on the number of the guided modes, waveguides can be classified as single-mode and multi-mode.[162] In single-mode waveguides, the core thickness is in the order of the wavelength of the guided light and only one mode is propagated. The propagation in these waveguides presents minimum optical losses because intermodal interferences do not take place. In contrast, multi-mode waveguides present a thicker core (from 10 to 100 μm^2) and are capable of guiding simultaneously fundamental and higher modes.

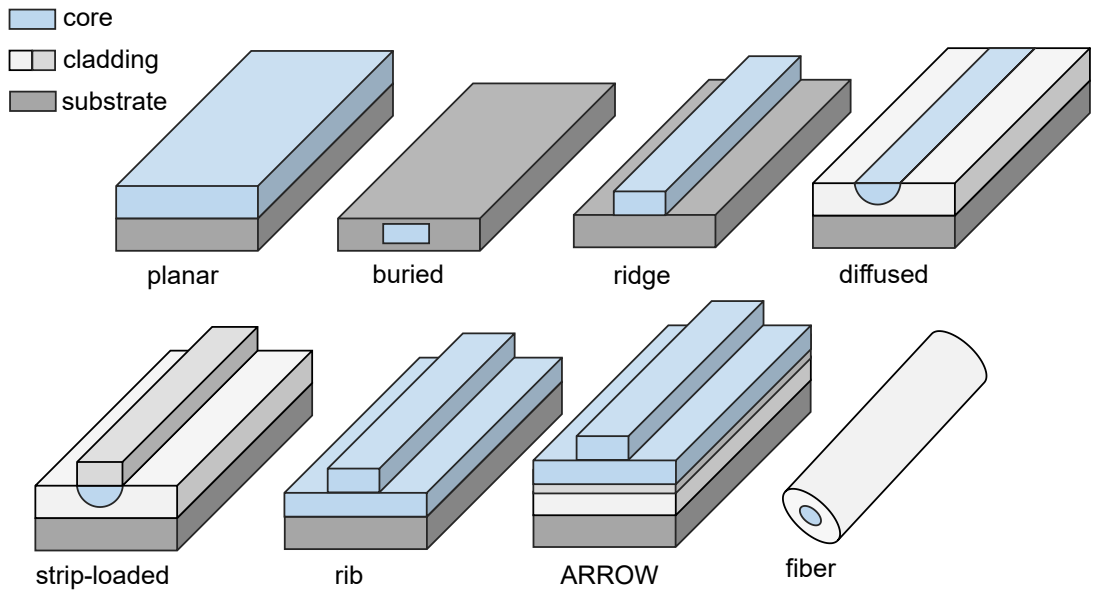

Figure 8. Examples of planar and channel waveguides.

Waveguides can also be classified according to their chemical composition as silicon-based, polymeric, and semiconductor waveguides. Silicon dioxide (SiO_2), silicon nitride (Si_3N_4), and silicon oxynitrides (SiO_xN_y) are the main components of silica-based waveguides. Due to the low cost of the materials and the manufacturing processes, these waveguides offer the possibility of mass manufacturing with a high level of integration in photonic devices. The high contrast between the refractive index of glass materials and biomolecules makes them ideal for biosensing applications.[163] However, they are only intended as passive components for waveguiding, since they cannot add optical functionalities such as emission, amplification, attenuation, etc. Also, these waveguides are fragile, present high mechanical stress,[164] and high absorption at wavelengths in the 830 nm band, which restricts their use to applications that require wavelengths between 1310 and 1550 nm.[165]

Polymeric waveguides are mainly composed of polymethylmethacrylate, polycarbonate, polystyrene, copolymers from cyclic olefins, and amorphous fluoropolymers. These waveguides show better mechanical performance and have attracted special attention for the development of several applications due to their potential to add optical functionality together with their low production costs.[166,167]

Semiconductor waveguides are composed of materials such as lithium niobate ($LiNbO_3$) and indium phosphide (InP). These materials are typically employed to fabricate active components such as light sources and detectors that are embedded into PICs.[165]

3.2. Principles of waveguide-based sensing

When an electromagnetic wave is confined in the core of a waveguide by TIR, a small portion of light goes beyond the core/cladding-substrate interfaces and generates an electromagnetic field, called evanescent field, that propagates through the interface in the same direction as the guided mode (Figure 9A).[168] The intensity of the evanescent field decays exponentially as it penetrates the surrounding medium with a lower refractive index and it is characterized by its penetration depth (δ),[169] which is defined as the distance at which the evanescent field extends beyond the core-cladding/substrate interface. The penetration depth is described mathematically for the surrounding medium as follows (Eq. 8):

$$\delta_{medium} = \frac{\lambda}{2\pi\sqrt{n_{core}^2 sin^2\theta_1 - n_{medium}^2}} \qquad \textbf{Eq. 8}$$

Waveguides were originally designed to transfer information in the telecommunications sector, which requires a maximum degree of confinement to minimize losses at interfaces. In the late 60s and early 70s, the first evanescent wave-based chemical sensors and biosensors were developed.[170] In these biosensors, both the cladding and the core of waveguiding structures can act as sensing surfaces to transduce biorecognition events as long as the evanescent field reaches the biolayer. When targets interact with the immobilized probes, they induce a local change in the optical properties of the biolayer that modify the propagation of the guided mode (Figure 9B).[161]

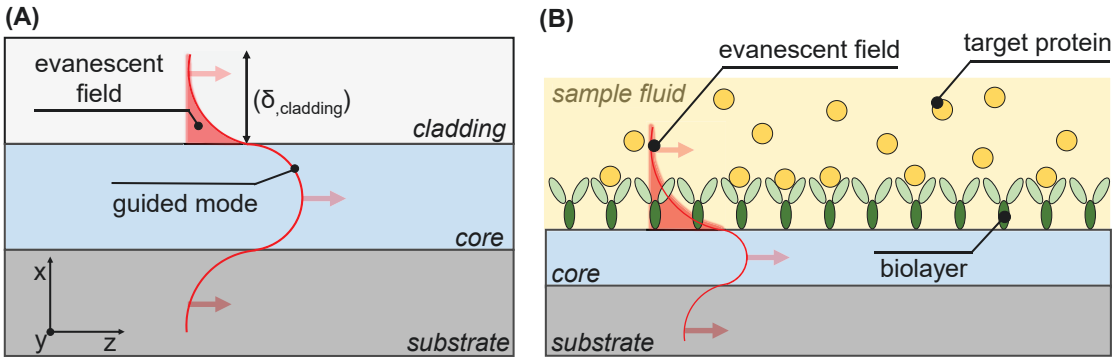

Figure 9. (A) Representation of a waveguide mode and its associated evanescent field at the core-cladding/substrate interfaces. **(B)** Representation of evanescent-wave sensing.

The magnitude of the penetration depth contributes to the performance of the evanescent-field biosensors, and many strategies are reported to maximize the amount of evanescent field in the surroundings of waveguides. These strategies essentially rely on modifying the geometry of the guide by removing a section of the cladding using mechanical and chemical processes (side polishing,[171–174] wet etching,[175] etc) or reducing the guide dimensions until they become comparable to the wavelength of the guided light.[176–178]

Another way to enhance the evanescent field is based on inscribing periodic refractive index modulations in the core of optical fibers.[179] The core and cladding in most optical fibers are both composed of silicon dioxide, and to achieve a higher refractive index in the core it is typically doped with elements such as germanium, erbium, and boron that absorb UV light (≈244 nm). Within this context, the irradiation of the fiber in discrete and periodic areas with UV light generates permanent changes in the chemical structure of the core material that results in an increment of the refractive index.[180] These periodic modulations are known as fiber Bragg gratings (FBGs) and present two main advantages compared to geometrically-modified fibers: the mechanical resistance of the fiber is minimally altered, and the redirection of light to the cladding becomes a resonant effect that only takes place at certain wavelengths. In the next section, different evanescent-wave biosensing configurations are presented with special emphasis on FBGs, since they are a particularly relevant background for this thesis.

3.3. Biosensing approaches in waveguides

The great variety and versatility of waveguides in terms of geometries, materials, and configurations has made it possible to adapt these components to different optical transduction mechanisms,[178] and even to discover new ones. The main waveguide-based approaches in the state-of-art of biosensing are briefly described below.

3.3.1. Nanoplasmonic biosensors

Considering the classic SPR approaches (see section 2.1), in 1993 Jorgenson and Yee proposed to adapt this concept to optical fibers to develop miniaturized sensor systems with low manufacturing costs and with remote sensing and multiplexing possibilities.[181,182] In these systems, the evanescent wave coupled to the guided mode is employed to excite plasmons of a metallic coating on the guide (Figure 10A). The plasmon wave generated is highly lossy and causes a damping of the guided mode, thus small variations in the refractive index caused by biorecognition events on the metallic coating can be detected as attenuations of the guided mode and displacements of the resonant wavelength.[183,184] Nowadays, nanoplasmonic biosensors have evolved to more sophisticated designs with a great variety of configurations with improved miniaturization and on-chip integration capabilities, and they have demonstrated potential application in the industrial, environmental, and clinical sectors (Table 1). However, although plasmonic biosensors are considered to be in a mature stage, their low robustness and reproducibility when analyzing complex biological samples and the need for user-friendly readouts have limited their performance as point-of-care devices.[30]

3.3.2. Interferometers

Interferometric sensors usually consist of an input waveguide that is divided into two arms: one in direct contact with the measuring solution (measuring arm) and an unaltered arm (reference arm) (Figure 10B). The biomolecular interactions that take place at the measuring arm within the evanescent field change the refractive index at the interface, which produces a phase shift in the light that propagates through the

reference arm. As this interference is proportional to the change of the refractive index in the measuring arm, a quantitative analysis of biorecognition events can be performed.[161]

Interferometric sensors such as Match-Zehnder, Young, or bimodal waveguides show a wide dynamic range and excellent sensitivity for the direct, label-free, and real-time detection of biorecognition events.[30] Compared to other strategies, interferometric sensors are the simplest configurable devices and exhibit a high dynamic range and exceptional sensitivity. A wide myriad of interferometric sensors has been developed for different biosensing applications. As an example, some approaches for the detection of small molecules, toxins, nucleic acids, proteins and antibodies, and viruses or bacterias, are summarized in Table 1. Note that, as the sensitivity scales with the length of the sensing arm, these devices usually need lengths around 5-10 mm, which restricts the number of sensors that can be integrated into a miniaturized chip for multiplex detection.

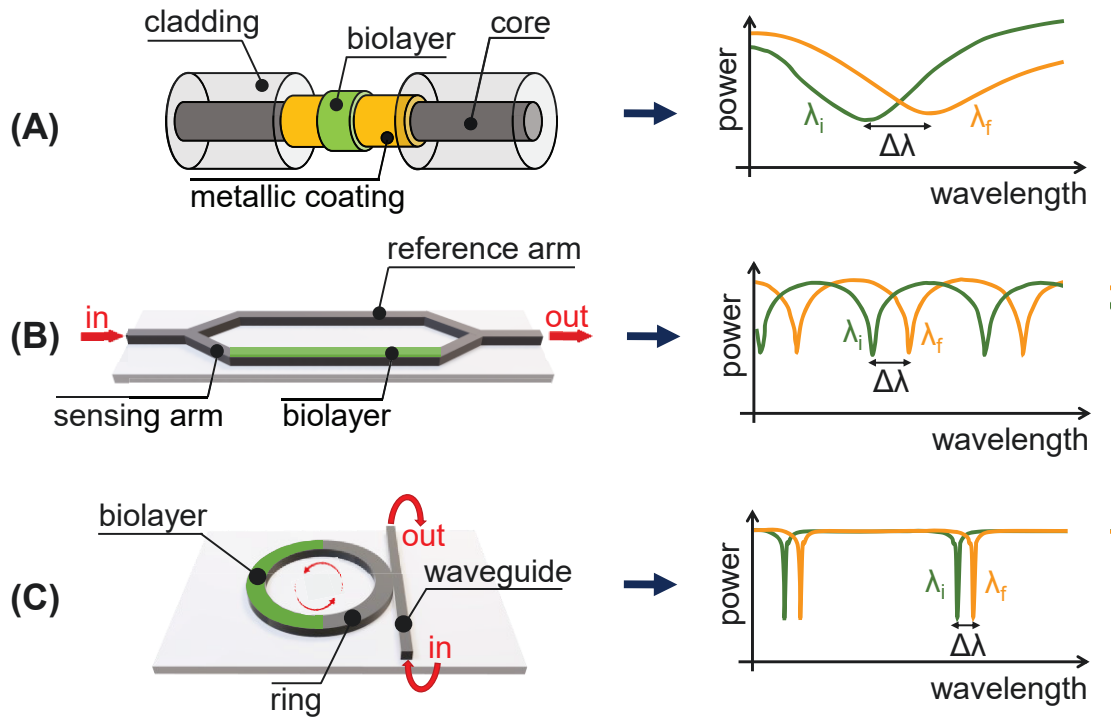

Figure 10. Schematic representation of **(A)** an etched optical fiber coated with a gold layer for SPR biosensing, **(B)** a Mach-Zehnder interferometer, and **(C)** a ring resonator. The graphs show representative transmission spectra before (green lines) and after (orange) biorecognition events.

3.3.3. Ring resonators

Ring resonators are one of the most employed photonic structures for label-free biosensing thanks to their great sensitivity and multiplexing capabilities,[185,186] Essentially, these optical structures typically comprise a loop-shaped optical waveguide (ring), and a straight guide used to couple and uncouple light from the loop. The coupling of light within the ring occurs only at certain wavelengths, which are called resonant wavelengths.[187] These resonant wavelengths mainly depend on the radius of the ring and the effective refractive index of the propagating mode. Finally, when the light is uncoupled from the loop, it interacts with the input beam and produces a destructive interference that acts as a spectral filter at the resonant wavelength (Figure 10C).

The propagation of the coupled mode in the ring is extremely sensitive to changes in the refractive index on its surface. When a biolayer is deposited on the ring, the refractive index changes locally and produces an increment of the optical path of the ring, resulting in a shift of the resonant wavelength. Therefore, variations in the resonant wavelength can provide quantitative information of biorecognition events that take place on the ring surface. Thanks to the high accuracy in the measurement of these variations (picometer range), excellent sensitivities can be achieved for label-free biosensing of proteins, nucleic acids, toxins, hormones, bacteria and viruses, among others (Table 1). Moreover, due to their small size and scalable mass-production, an on-chip high-efficient sensor integration can be implemented to create high-throughput arrays for the simultaneous analysis of multiple biological species.[186,188,189] However, their low thermal stability, and limited selectivity when analyzing complex biological samples have restricted their implementation in commercial biosensing devices.

3.3.4. Bragg gratings

Bragg gratings (BG) are periodic modulations of the refractive index in the core of the waveguides that produce a reflection of the guided light at specific wavelengths. BGs generated in fiber optics (FBGs) have attracted great attention for biosensing due to their easy fabrication and the low price of the materials. According to the periodicity of the modulations, FBGs can be classified into short-period and long-period.[178]

Short-period FBGs present periodic modulations of the refractive index below 100 µm and can be further divided into standard FBGs and tilted FBGs (TFBG). For standard FBGs, the modulation is perpendicular to the longitudinal axis of the fiber (Figure 11A). This configuration allows the coupling of the fundamental propagating mode to a mode that is propagated in the opposite direction through the fiber core at the wavelengths that fulfill the fundamental Bragg condition (Eq. 9).

$$\lambda_B = 2 \cdot n_{eff} \cdot \Lambda \qquad \textbf{Eq. 9}$$

where λ_B is the resonant wavelength and n_{eff} is the effective refractive index.[190]

When FBGs are employed to sense biorecognition events, bioreceptors are typically immobilized on the fiber surface creating a continuous biolayer. Therefore, biorecognition events that take place within the penetration depth of the evanescent field produce changes in the optical properties of the biolayer that are detected as a shift of the resonant wavelength in the transmission or reflection spectra. However, in standard FBGs the light is confined only in the core layer and the evanescent field does not reach the fiber surface, where the biolayer is deposited. To assess this issue, etched and tapered fibers are commonly employed to enhance the evanescent wave in the fiber surroundings and use it to sense biorecognition events.[191]

In TFBGs the modulation direction forms a certain angle with the longitudinal axis and the resonant wavelengths of the guided modes are reflected and coupled to cladding modes that propagate in the opposite direction (Figure 11B).[192] In this configuration, the evanescent field reaches the cladding surface of the fiber without geometrical modification and the propagating modes are sensitive to changes in the refractive index produced by biorecognition events on the cladding.

Finally, long-period FBGs (LPFBGs) present periodic modulations between 100 and 1000 µm that are perpendicular to the longitudinal axis. Unlike their short-period counterparts, the resonant wavelengths in LPFBGs are coupled to cladding modes that are propagated in the same direction of the fundamental mode (Figure 11C).[191] Analogously to TFBGs, the evanescent field also reaches the fiber surface, and the propagating modes are sensitive to changes of biolayers on the fiber cladding without modifying the geometry of the fiber.

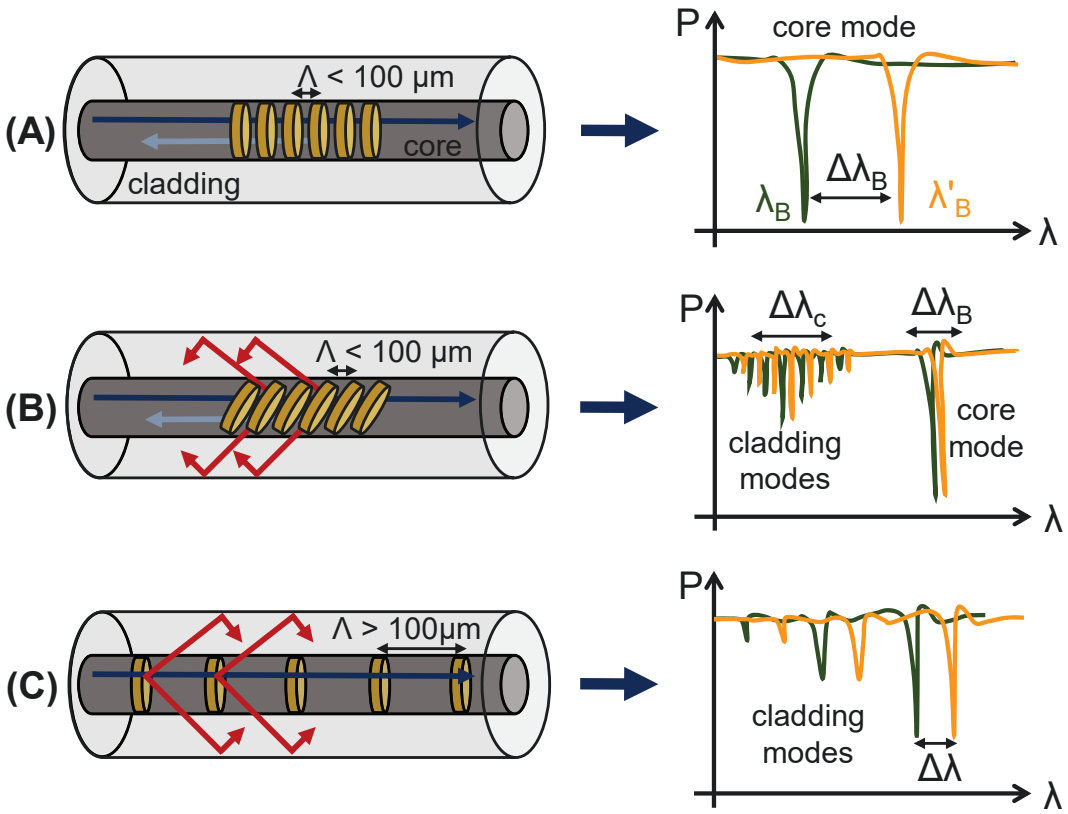

Figure 11. Schematic view of a model **(A)** standard FBG, **(B)** TFBG, and **(C)** LPFBG. Blue and red lines represent propagating core and cladding modes, respectively. The graphs show representative transmission spectra before (green lines) and after (orange) biorecognition events.

The great success of fiber-based biosensors is due to their high sensitivity, robustness, remote monitoring, and potential to perform multiplexed assays on a single fiber. Moreover, they can be used in harsh environments, are immune to electromagnetic interferences, and can be easily miniaturized at a low cost to fabricate compact and lightweight biosensing devices.[170] As a result, a multitude of biosensing approaches based on classical FBGs have been reported in recent years (Table 2). Most of these strategies were developed using only the potential transducing capabilities of FBGs, whereas some works also combine FBGs with other optical phenomena such as SPR to improve their bioanalytical performance.[193]

Although the use of classical FBGs with periodic modulations in the fiber core is widespread, creating this kind of modulations directly on the fiber surface and exploiting them for biosensing, remains rather unexplored. In this sense, the implementation of

biogratings in the fiber surface represents a turning point to investigate new label-free biosensing transduction mechanisms that can provide greater versatility, miniaturization, and compactness to the optical systems. In addition, this strategy can be transferred to waveguides embedded in a silicon platform, combining active and passive components monolithically integrated into PICs, to conceive new lab-on-a-chip devices.

Table 1. Recent and representative examples of biosensing approaches based on nanoplasmonics, ring resonators, and interferometric structures.

Technique	Target	Bioreceptor	Detection limit	Reference
Nanoplasmonics	CRP	antibody	0.1 µg·mL^{-1}*	194
	antimouse antibody	antibody	0.01 mg·L^{-1}*	195
	thrombin	aptamer	1 nM	196
	ssDNA	ssDNA	1000 nM*	197
	naphtalene	antibody	0.76 ng·mL^{-1}	198
	ammonium perfluorooctanoate	MIPs	0.13 ng·mL^{-1}	199
Ring resonators	carcinoembryonic antigen	antibody	2 ng·mL^{-1}	200
	goat and rabbit antibodies	antigoat and antirrabbit antibodies	20 pM*	201
	ssDNA M. tuberculosis	ssDNA	5 fg·µL	202
	ssDNA	ssDNA	500 nM	203
	testosterone	MIPs	48.7 pg·mL^{-1}	204
	aflatoxin M1	aptamer	12.5 nM*	205
	bean pod mottle virus	antibody	10 ng·mL^{-1}	206
	e.coli	antibody	10^5 cfu·mL^{-1}*	207
Mach-Zehnder interferometer	allergens	antibodies	0.04-1 µg·mL^{-1}	208
	biotin	streptavidin	0.07 nM$^{\#}$	209
	aflatoxin M1	antibody fragment	10 nM*	210
	ochratoxin A	antibody	3 ng·mL^{-1}	211
	listeria monocytogenes	antibody	10^5 cfu·mL	212
Bimodal waveguides	microRNA-181a probe	microRNA-181a	23 aM	213
	B. cereus/E.coli	antibody	12 cfu·mL^{-1} / 4 cfu·mL^{-1}	214
Young interferometer	herpes simplex virus type 1	antibody	850 VP·mL^{-1}*	215

Table 2. Recent and representative examples of biosensing approaches based onFBGs.

Technique	Target	Bioreceptor	Detection limit	Reference
FBG	CRP	antibody	0.01 $mg \cdot L^{-1}$*	216
	thrombin	aptamere	10 nM*	217
	ssDNA probe	ssDNA	$0.5 \cdot 10^{-6}$ M	218
	maltol	MIPs	1 $\mu g \cdot L^{-1}$	219
TFBG	thrombin	aptamere	0.110 nM	220
	cytokeratine 17	antibody	10^{-9} $g \cdot L^{-1}$	221
	glucose	glucose oxidase	1 mM*	222
LPFBG	mouse antibody	antibody	70 $\mu g \cdot mL^{-1}$	223
	biotynilated BSA	streptavidin	0.2 aM	224
	oligonucleotides	oligonucleotides	62 nM	225
	DNA strand	DNA strand	10 nM*	226
	T7 phage	antibody	$5 \cdot 10^{3}$ $cfu \cdot mL^{-1}$	227
	E. coli	T4-phage	10^{3} $cfu \cdot mL^{-1}$	228

**lowest concentration detected* *# instrumental noise level* *VP: Virus particle* *cfu: colony former units*

4. References

1. Naresh, V. & Lee, N. A Review on Biosensors and Recent Development of Nanostructured Materials-Enabled Biosensors. *Sensors* **21**, 1109 (2021).

2. Ensafi, A. A. An introduction to sensors and biosensors. in *Electrochemical Biosensors*, pp. 1–10 (Elsevier, 2019).

3. Askim, J. R., Mahmoudi, M. & Suslick, K. S. Optical sensor arrays for chemical sensing: the optoelectronic nose. *Chem. Soc. Rev.* **42**, 8649 (2013).

4. Patel, G. M., Shah, V. R., Bhatt, G. J. & Deota, P. T. Humidity nanosensors for smart manufacturing. in *Nanosensors for Smart Manufacturing*, pp. 555–580 (Elsevier, 2021).

5. Chen, H. *et al.* Nanomaterials as optical sensors for application in rapid detection of food contaminants, quality and authenticity. *Sensors Actuators B Chem.* **329**, 129135 (2021).

6. Krämer, J. *et al.* Molecular Probes, Chemosensors, and Nanosensors for Optical Detection of Biorelevant Molecules and Ions in Aqueous Media and Biofluids. *Chem. Rev.* **122**, 3459–3636 (2022).

7. Liu, R., Li, Z., Huang, Z., Li, K. & Lv, Y. Biosensors for explosives: State of art and future trends. *TrAC Trends Anal. Chem.* **118**, 123–137 (2019).

8. Lichtenstein, A. *et al.* Supersensitive fingerprinting of explosives by chemically modified nanosensors arrays. *Nat. Commun.* **5**, 4195 (2014).

9. Yang, T. & Duncan, T. V. Challenges and potential solutions for nanosensors intended for use with foods. *Nat. Nanotechnol.* **16**, 251–265 (2021).

10. Jafarizadeh-Malmiri, H., Sayyar, Z., Anarjan, N. & Berenjian, A. Nano-sensors in Food Nanobiotechnology. in *Nanobiotechnology in Food: Concepts, Applications and Perspectives*, pp. 81–94 (Springer International Publishing, 2019).

11. Castillo-Cambronero, G., Cascante-Matarrita, M., Mora-Chacón, A., Castillo-Henríquez, L. & Vega-Baudrit, J. R. Use of nanosensor technologies in the food industry. in *Nanosensors for Smart Agriculture*, pp. 643–655 (Elsevier, 2022).

12. Verdian, A. Apta-nanosensors for detection and quantitative determination of acetamiprid – A pesticide residue in food and environment. *Talanta* **176**, 456–464 (2018).

13. Vikesland, P. J. Nanosensors for water quality monitoring. *Nat. Nanotechnol.* **13**, 651–660 (2018).

14. Quesada-González, D. & Merkoçi, A. Nanomaterial-based devices for point-of-care diagnostic applications. *Chem. Soc. Rev.* **47**, 4697–4709 (2018).

15. Alba-Patiño, A. *et al.* Micro- and nanosensors for detecting blood pathogens and biomarkers at different points of sepsis care. *Microchim. Acta* **189**, 74 (2022).

16. Jouyban, A. & Rahimpour, E. Sensors/nanosensors based on upconversion materials for the determination of pharmaceuticals and biomolecules: An overview. *Talanta* **220**, 121383 (2020).

17. Gonçalves, J. M., Martins, P. R., Santos, B. G., Araki, K. & Angnes, L. Sensing Materials: Metals Oxides. in *Encyclopedia of Sensors and Biosensors*, pp. 93-113 (Elsevier, 2023).

18. Thévenot, D. R., Toth, K., Durst, R. A. & Wilson, G. S. Electrochemical biosensors: recommended definitions and classification. 1st International Union of Pure and Applied Chemistry: Physical Chemistry Division, Commission I.7 (Biophysical Chemistry); Analytical Chemistry Division, Commission V.5 (Electroanalytical). *Biosens. Bioelectron.* **16**, 121–131 (2001).

19. Hulanicki, A., Glab, S. & Ingman, F. Chemical sensors: definitions and classification. *Pure Appl. Chem.* **63**, 1247–1250 (1991).

20. Markets and Markets™ (March 3rd,2022). *Biosensors Market by Type, Product (Wearable, Non-wearable), Technology, Application (POC, Home Diagnostics, Research Lab, Environmental Monitoring, Food & Beverages, Biodefense) and Region 2026.* https://www.marketsandmarkets.com/Market-Reports/biosensors-market-798.html.

21. Excler, J.-L., Saville, M., Berkley, S. & Kim, J. H. Vaccine development for emerging infectious diseases. *Nat. Med.* **27**, 591–600 (2021).

22. Kirtane, A. R. *et al.* Nanotechnology approaches for global infectious diseases. *Nat. Nanotechnol.* **16**, 369–384 (2021).

23. Wang, C. *et al.* Point-of-care diagnostics for infectious diseases: From methods to devices. *Nano Today* **37**, 101092 (2021).

24. Park, M. & Heo, Y. J. Biosensing Technologies for Chronic Diseases. *BioChip J.* **15**, 1–13 (2021).

25. Sharma, A., Badea, M., Tiwari, S. & Marty, J. L. Wearable Biosensors: An Alternative and Practical Approach in Healthcare and Disease Monitoring. *Molecules* **26**, 748 (2021).

26. Naik, B. N., Gupta, R., Singh, A., Soni, S. L. & Puri, G. D. Real-Time Smart Patient Monitoring and Assessment Amid COVID-19 Pandemic – an Alternative Approach to Remote Monitoring. *J. Med. Syst.* **44**, 131 (2020).

27. Antiochia, R. Developments in biosensors for CoV detection and future trends. *Biosens. Bioelectron.* **173**, 112777 (2021).

28. Kleinert, S. & Horton, R. Can COVID-19 help accelerate and transform the diagnostics agenda? *Lancet* **398**, 1945–1947 (2021).

29. Shaffaf, T. & Ghafar-Zadeh, E. COVID-19 Diagnostic Strategies Part II: Protein-Based Technologies. *Bioengineering* **8**, 54 (2021).

30. Soler, M., Estevez, M. C., Cardenosa-Rubio, M., Astua, A. & Lechuga, L. M. How Nanophotonic Label-Free Biosensors Can Contribute to Rapid and Massive Diagnostics of Respiratory Virus Infections: COVID-19 Case. *ACS Sensors* **5**, 2663–2678 (2020).

31. Mayer, M. & Baeumner, A. J. A Megatrend Challenging Analytical Chemistry: Biosensor and Chemosensor Concepts Ready for the Internet of Things. *Chem. Rev.* **119**, 7996–8027 (2019).

32. Thevenot, D. R., Tóth, K., Durst, R. A. & Wilson, G. S. Electrochemical Biosensors: Recommended Definitions and Classification. *Pure Appl. Chem.* **71**, 2333–2348 (1999).

33. Sinha, A. S. & Aakeröy, C. B. Design of Molecular Crystals: Supramolecular Synthons. in *Comprehensive Supramolecular Chemistry II*, pp. 3–24 (Elsevier, 2017).

34. Morales, M. A. & Halpern, J. M. Guide to Selecting a Biorecognition Element for Biosensors. *Bioconjug. Chem.* **29**, 3231–3239 (2018).

35. Clark, L. C. & Lyons, C. Electrode systems for continuous monitoring in cardiovascular surgery. *Ann. N. Y. Acad. Sci.* **102**, 29–45 (2006).

36. Justino, C. I. L., Rocha-Santos, T. A., Duarte, A. C. & Rocha-Santos, T. A. Review of analytical figures of merit of sensors and biosensors in clinical applications. *TrAC Trends Anal. Chem.* **29**, 1172–1183 (2010).

37. Mauriz, E., Dey, P. & Lechuga, L. M. Advances in nanoplasmonic biosensors for clinical applications. *Analyst* **144**, 7105–7129 (2019).

38. Yoo, S. M. & Lee, S. Y. Optical Biosensors for the Detection of Pathogenic Microorganisms. *Trends Biotechnol.* **34**, 7–25 (2016).

39. Lan, L., Yao, Y., Ping, J. & Ying, Y. Recent advances in nanomaterial-based biosensors for antibiotics detection. *Biosens. Bioelectron.* **91**, 504–514 (2017).

40. Abolhasan, R., Mehdizadeh, A., Rashidi, M. R., Aghebati-Maleki, L. & Yousefi, M. Application of hairpin DNA-based biosensors with various signal amplification strategies in clinical diagnosis. *Biosens. Bioelectron.* **129**, 164–174 (2019).

41. Kirchhain, A., Bonini, A., Vivaldi, F., Poma, N. & Di Francesco, F. Latest developments in non-faradic impedimetric biosensors: Towards clinical applications. *TrAC Trends Anal. Chem.* **133**, 116073 (2020).

42. Kundu, M., Krishnan, P., Kotnala, R. K. & Sumana, G. Recent developments in biosensors to combat agricultural challenges and their future prospects. *Trends Food Sci. Technol.* **88**, 157–178 (2019).

43. Adetunji, C. O., Nwankwo, W., Ukhurebor, K. E., Olayinka, A. S. & Makinde, A. S. Application of Biosensor for the Identification of Various Pathogens and Pests Mitigating Against the Agricultural Production: Recent Advances. in *Biosensors in Agriculture: Recent Trends and Future Perspectives*, pp. 169–189 (Springer, 2021).

44. Griesche, C. & Baeumner, A. J. Biosensors to support sustainable agriculture and food safety. *TrAC Trends Anal. Chem.* **128**, 115906 (2020).

45. Sena-Torralba, A., Pallás-Tamarit, Y., Morais, S. & Maquieira, Á. Recent advances and challenges in food-borne allergen detection. *TrAC Trends Anal. Chem.* **132**, 116050 (2020).

46. McLamore, E. S. *et al.* FEAST of biosensors: Food, environmental and agricultural sensing technologies (FEAST) in North America. *Biosens. Bioelectron.* **178**, 113011 (2021).

47. Hua, Z., Yu, T., Liu, D. & Xianyu, Y. Recent advances in gold nanoparticles-based biosensors for food safety detection. *Biosens. Bioelectron.* **179**, 113076 (2021).

48. Balbinot, S., Srivastav, A. M., Vidic, J., Abdulhalim, I. & Manzano, M. Plasmonic biosensors for food control. *Trends Food Sci. Technol.* **111**, 128–140 (2021).

49. Thakur, M., Wang, B. & Verma, M. L. Development and applications of nanobiosensors for sustainable agricultural and food industries: Recent developments, challenges and perspectives. *Environ. Technol. Innov.* **26**, 102371 (2022).

50. Vinoth, S., Shalini Devi, K. S. & Pandikumar, A. A comprehensive review on graphitic carbon nitride based electrochemical and biosensors for environmental and healthcare applications. *TrAC Trends Anal. Chem.* **140**, 116274 (2021).

51. Liu, X. *et al.* A One-Step Homogeneous Immunoassay for Cancer Biomarker Detection Using Gold Nanoparticle Probes Coupled with Dynamic Light Scattering. *J. Am. Chem. Soc.* **130**, 2780–2782 (2008).

52. Chan, D. W. Automation of immunoassays. in *Immunoassay*, pp. 483–504 (Academic Press, 1996).

53. Schrittwieser, S. *et al.* Homogeneous Biosensing Based on Magnetic Particle Labels. *Sensors* **16**, 828 (2016).

54. Hu, S., Chen, T. H., Zhao, Y., Wang, Z. & Lam, R. H. W. Protein-Substrate Adhesion in Microcontact Printing Regulates Cell Behavior. *Langmuir* **34**, 1750–1759 (2018).

55. Bañuls, M.-J., Puchades, R. & Maquieira, Á. Chemical surface modifications for the development of silicon-based label-free integrated optical (IO) biosensors: A review. *Anal. Chim. Acta* **777**, 1–16 (2013).

56. Hoyle, C. E. & Bowman, C. N. Thiol-Ene Click Chemistry. *Angew. Chemie Int. Ed.* **49**, 1540–1573 (2010).

57. Hermanson, G. T. The Reactions of Bioconjugation. in *Bioconjugate Techniques*, pp. 229–258 (Academic Press, 2013).

58. Blawas, A. S. & Reichert, W. M. Protein patterning. *Biomaterials* **19**, 595–609 (1998).

59. You, C., Bhagawati, M., Brecht, A. & Piehler, J. Affinity capturing for targeting proteins into micro and nanostructures. *Anal. Bioanal. Chem.* **393**, 1563–1570 (2009).

60. Laitinen, O. H., Nordlund, H. R., Hytönen, V. P. & Kulomaa, M. S. Brave new (strept)avidins in biotechnology. *Trends Biotechnol.* **25**, 269–277 (2007).

61. Bickerstaff, G. F. Immobilization of Enzymes and Cells: Some Practical Considerations. in *Immobilization of Enzymes and Cells*, pp. 1–12 (Humana Press, 1997).

62. Barbulovic-Nad, I. *et al.* Bio-Microarray Fabrication Techniques—A Review. *Crit. Rev. Biotechnol.* **26**, 237–259 (2006).

63. Gresham, D., Dunham, M. J. & Botstein, D. Comparing whole genomes using DNA microarrays. *Nat. Rev. Genet.* **9**, 291–302 (2008).

64. Sassolas, A., Leca-Bouvier, B. D. & Blum, L. J. DNA Biosensors and Microarrays. *Chem. Rev.* **108**, 109–139 (2008).

65. Templin, M. F. *et al.* Protein microarrays: Promising tools for proteomic research. *Proteomics* **3**, 2155–2166 (2003).

66. Wilson, D. S. & Nock, S. Recent Developments in Protein Microarray Technology. *Angew. Chemie Int. Ed.* **42**, 494–500 (2003).

67. Syu, G.-D., Dunn, J. & Zhu, H. Developments and Applications of Functional Protein Microarrays. *Mol. Cell. Proteomics* **19**, 916–927 (2020).

68. Fathi, F., Rashidi, M.-R., Pakchin, P. S., Ahmadi-Kandjani, S. & Nikniazi, A. Photonic crystal based biosensors: Emerging inverse opals for biomarker detection. *Talanta* **221**, 121615 (2021).

69. Jayanthi, V. S. P. K. S. A., Das, A. B. & Saxena, U. Recent advances in biosensor development for the detection of cancer biomarkers. *Biosens. Bioelectron.* **91**, 15–23 (2017).

70. van Assenbergh, P., Meinders, E., Geraedts, J. & Dodou, D. Nanostructure and Microstructure Fabrication: From Desired Properties to Suitable Processes. *Small* **14**, 1703401 (2018).

71. Gates, B. D. *et al.* New Approaches to Nanofabrication: Molding, Printing, and Other Techniques. *Chem. Rev.* **105**, 1171–1196 (2005).

72. Zhao, X.-M., Xia, Y. & Whitesides, G. M. Soft lithographic methods for nano-fabrication. *J. Mater. Chem.* **7**, 1069–1074 (1997).

73. Perl, A., Reinhoudt, D. N. & Huskens, J. Microcontact printing: Limitations and achievements. *Adv. Mater.* **21**, 2257–2268 (2009).

74. Alom Ruiz, S. & Chen, C. S. Microcontact printing: A tool to pattern. *Soft Matter* **3**, 168–177 (2007).

75. Khadpekar, A. J., Khan, M., Sose, A. & Majumder, A. Low Cost and Lithography-free Stamp fabrication for Microcontact Printing. *Sci. Rep.* **9**, 1024 (2019).

76. Wang, B., Koo, B., Huang, L. W. & Monbouquette, H. G. Microbiosensor fabrication by polydimethylsiloxane stamping for combined sensing of glucose and choline. *Analyst* **143**, 5008–5013 (2018).

77. Bernard, A., Renault, J. P., Michel, B., Bosshard, H. R. & Delamarche, E. Microcontact Printing of Proteins. *Adv. Mater.* **12**, 1067–1070 (2000).

78. Wendeln, C. & Ravoo, B. J. Surface patterning by microcontact chemistry. *Langmuir* **28**, 5527–5538 (2012).

79. Ravoo, B. J. Microcontact chemistry: surface reactions in nanoscale confinement. *J. Mater. Chem.* **19**, 8902 (2009).

80. Lamping, S., Buten, C. & Ravoo, B. J. Functionalization and Patterning of Self-Assembled Monolayers and Polymer Brushes Using Microcontact Chemistry. *Acc. Chem. Res.* **52**, 1336-1346 (2019).

81. Wendeln, C., Heile, A., Arlinghaus, H. F. & Ravoo, B. J. Carbohydrate microarrays by microcontact printing. *Langmuir* **26**, 4933–4940 (2010).

82. Buhl, M., Vonhören, B. & Ravoo, B. J. Immobilization of Enzymes via Microcontact Printing and Thiol-Ene Click Chemistry. *Bioconjug. Chem.* **26**, 1017–1020 (2015).

83. Cho, I.-H., Kim, D. H. & Park, S. Electrochemical biosensors: perspective on functional nanomaterials for on-site analysis. *Biomater. Res.* **24**, 6 (2020).

84. Menon, S., Mathew, M. R., Sam, S., Keerthi, K. & Kumar, K. G. Recent advances and challenges in electrochemical biosensors for emerging and re-emerging infectious diseases. *J. Electroanal. Chem.* **878**, 114596 (2020).

85. Ramanathan, K. & Danielsson, B. Principles and applications of thermal biosensors. *Biosens. Bioelectron.* **16**, 417–423 (2001).

86. Yakovleva, M., Bhand, S. & Danielsson, B. The enzyme thermistor—A realistic biosensor concept. A critical review. *Anal. Chim. Acta* **766**, 1–12 (2013).

87. Lim, H. J., Saha, T., Tey, B. T., Tan, W. S. & Ooi, C. W. Quartz crystal microbalance-based biosensors as rapid diagnostic devices for infectious diseases. *Biosens. Bioelectron.* **168**, 112513 (2020).

88. Chen, C. & Wang, J. Optical biosensors: an exhaustive and comprehensive review. *Analyst* **145**, 1605–1628 (2020).

89. Khansili, N., Rattu, G. & Krishna, P. M. Label-free optical biosensors for food and biological sensor applications. *Sensors Actuators B Chem.* **265**, 35–49 (2018).

90. Hermanson, G. T. Fluorescent Probes. in *Bioconjugate Techniques*, pp. 395–463 (Academic Press, 2013).

91. Gallo, E. Fluorogen-Activating Proteins: Next-Generation Fluorescence Probes for Biological Research. *Bioconjug. Chem.* **31**, 16–27 (2020).

92. Su, D., Li, H., Yan, X., Lin, Y. & Lu, G. Biosensors based on fluorescence carbon nanomaterials for detection of pesticides. *TrAC Trends Anal. Chem.* **134**, 116126 (2021).

93. Tian, X., Murfin, L. C., Wu, L., Lewis, S. E. & James, T. D. Fluorescent small organic probes for biosensing. *Chem. Sci.* **12**, 3406–3426 (2021).

94. Wegner, K. D. & Hildebrandt, N. Quantum dots: bright and versatile in vitro and in vivo fluorescence imaging biosensors. *Chem. Soc. Rev.* **44**, 4792–4834 (2015).

95. Ma, F., Li, C. & Zhang, C. Development of quantum dot-based biosensors: principles and applications. *J. Mater. Chem. B* **6**, 6173–6190 (2018).

96. Peltomaa, R., Benito-Peña, E., Gorris, H. H. & Moreno-Bondi, M. C. Biosensing based on upconversion nanoparticles for food quality and safety applications. *Analyst* **146**, 13–32 (2021).

97. Solhi, E. & Hasanzadeh, M. Recent advances on the biosensing and bioimaging based on polymer dots as advanced nanomaterial: Analytical approaches. *TrAC Trends Anal. Chem.* **118**, 840–852 (2019).

98. Avugadda, S. K. *et al.* Highly Emitting Perovskite Nanocrystals with 2-Year Stability in Water through an Automated Polymer Encapsulation for Bioimaging. *ACS Nano* **16**, 13657–13666 (2022).

99. Hermanson, G. T. Enzyme Modification and Conjugation. in *Bioconjugate Techniques*, pp. 951–957 (Academic Press, 2013).

100. Quesada-González, D. & Merkoçi, A. Nanoparticle-based lateral flow biosensors. *Biosens. Bioelectron.* **73**, 47–63 (2015).

101. Liu, R., Zhang, Y., Zhang, S., Qiu, W. & Gao, Y. Silver Enhancement of Gold Nanoparticles for Biosensing: From Qualitative to Quantitative. *Appl. Spectrosc. Rev.* **49**, 121–138 (2014).

102. Wadhera, T., Kakkar, D., Wadhwa, G. & Raj, B. Recent Advances and Progress in Development of the Field Effect Transistor Biosensor: A Review. *J. Electron. Mater.* **48**, 7635–7646 (2019).

103. Zanchetta, G., Lanfranco, R., Giavazzi, F., Bellini, T. & Buscaglia, M. Emerging applications of label-free optical biosensors. *Nanophotonics* **6**, 627–645 (2017).

104. Chen, Y., Liu, J., Yang, Z., Wilkinson, J. S. & Zhou, X. Optical biosensors based on refractometric sensing schemes: A review. *Biosens. Bioelectron.* **144**, 111693 (2019).

105. Peltomaa, R., Glahn-Martínez, B., Benito-Peña, E. & Moreno-Bondi, M. Optical Biosensors for Label-Free Detection of Small Molecules. *Sensors* **18**, 4126 (2018).

106. Sang, S. *et al.* Progress of new label-free techniques for biosensors: a review. *Crit. Rev. Biotechnol.* 1–17 (2015).

107. Homola, J., Yee, S. S. & Gauglitz, G. Surface plasmon resonance sensors: review. *Sensors Actuators B Chem.* **54**, 3–15 (1999).

108. Nguyen, H., Park, J., Kang, S. & Kim, M. Surface Plasmon Resonance: A Versatile Technique for Biosensor Applications. *Sensors* **15**, 10481–10510 (2015).

109. Ho, A. H.-P., Wu, S.-Y., Kong, S.-K., Zeng, S. & Yong, K.-T. SPR Biosensors. in *Handbook of Photonics for Biomedical Engineering*, pp. 123–145 (Springer Netherlands, 2017).

110. Spoto, G. & Minunni, M. Surface Plasmon Resonance Imaging: What Next? *J. Phys. Chem. Lett.* **3**, 2682–2691 (2012).

111. Amendola, V., Pilot, R., Frasconi, M., Maragò, O. M. & Iatì, M. A. Surface plasmon resonance in gold nanoparticles: a review. *J. Phys. Condens. Matter* **29**, 203002 (2017).

112. Sui, M., Kunwar, S., Pandey, P. & Lee, J. Strongly confined localized surface plasmon resonance (LSPR) bands of Pt, AgPt, AgAuPt nanoparticles. *Sci. Rep.* **9**, 16582 (2019).

113. Vestri, A. *et al.* LSPR immuno-sensing based on iso-Y nanopillars for highly sensitive and specific imidacloprid detection. *J. Mater. Chem. B* **9**, 9153–9161 (2021).

114. Mayer, K. M. & Hafner, J. H. Localized Surface Plasmon Resonance Sensors. *Chem. Rev.* **111**, 3828–3857 (2011).

115. Xu, T. & Geng, Z. Strategies to improve performances of LSPR biosensing: Structure, materials, and interface modification. *Biosens. Bioelectron.* **174**, 112850 (2021).

116. Bonyár, A. Maximizing the Surface Sensitivity of LSPR Biosensors through Plasmon Coupling—Interparticle Gap Optimization for Dimers Using Computational Simulations. *Biosensors* **11**, 527 (2021).

117. Lednický, T. & Bonyár, A. Large Scale Fabrication of Ordered Gold Nanoparticle–Epoxy Surface Nanocomposites and Their Application as Label-Free Plasmonic DNA Biosensors. *ACS Appl. Mater. Interfaces* **12**, 4804–4814 (2020).

118. Cialla-May, D. *et al.* Raman Spectroscopy and Imaging in Bioanalytics. *Anal. Chem.* **94**, 86–119 (2022).

119. Lee, H. K. *et al.* Designing surface-enhanced Raman scattering (SERS) platforms beyond hotspot engineering: emerging opportunities in analyte manipulations and hybrid materials. *Chem. Soc. Rev.* **48**, 731–756 (2019).

120. Muhammad, M. & Huang, Q. A review of aptamer-based SERS biosensors: Design strategies and applications. *Talanta* **227**, 122188 (2021).

121. Zheng, X.-S., Jahn, I. J., Weber, K., Cialla-May, D. & Popp, J. Label-free SERS in biological and biomedical applications: Recent progress, current challenges and opportunities. *Spectrochim. Acta Part A Mol. Biomol. Spectrosc.* **197**, 56–77 (2018).

122. Zhu, X., Cao, N., Thibeault, B. J., Pinsky, B. & Yanik, A. A. Mechanisms of Fano-resonant biosensing: Mechanical loading of plasmonic oscillators. *Opt. Commun.* **469**, 125780 (2020).

123. Lee, K.-L., Huang, J.-B., Chang, J.-W., Wu, S.-H. & Wei, P.-K. Ultrasensitive Biosensors Using Enhanced Fano Resonances in Capped Gold Nanoslit Arrays. *Sci. Rep.* **5**, 8547 (2015).

124. Khanikaev, A. B., Wu, C. & Shvets, G. Fano-resonant metamaterials and their applications. *Nanophotonics* **2**, 247–264 (2013).

125. Zhang, J. *et al.* Highly sensitive detection of malignant glioma cells using metamaterial-inspired THz biosensor based on electromagnetically induced transparency. *Biosens. Bioelectron.* **185**, 113241 (2021).

126. Hassan, M. M., Sium, F. S., Islam, F. & Choudhury, S. M. A review on plasmonic and metamaterial based biosensing platforms for virus detection. *Sens. Bio-Sensing Res.* **33**, 100429 (2021).

127. Ahmadivand, A. & Gerislioglu, B. Photonic and Plasmonic Metasensors. *Laser Photon. Rev.* **16**, 2100328 (2022).

128. Nolte, D. D. Interferometry. in *Optical Interferometry for Biology and Medicine*, pp. 3–48 (Springer New York, 2012).

129. Proll, G., Markovic, G., Steinle, L. & Gauglitz, G. Reflectometric Interference Spectroscopy. in *Biosensors and Biodetection. Methods in Molecular Biology*, pp. 167–178 (Humana Press, 2009).

130. Sancho-Fornes, G., Avella-Oliver, M., Carrascosa, J., Puchades, R. & Maquieira, Á. Interferometric multilayered nanomaterials for imaging unlabeled biorecognition events. *Sensors Actuators, B Chem.* **331**, (2021).

131. Rau, S. & Gauglitz, G. Reflectometric interference spectroscopy (RIfS) as a new tool to measure in the complex matrix milk at low analyte concentration. *Anal. Bioanal. Chem.* **402**, 529–536 (2012).

132. Yetisen, A. K., Naydenova, I., da Cruz Vasconcellos, F., Blyth, J. & Lowe, C. R. Holographic Sensors: Three-Dimensional Analyte-Sensitive Nanostructures and Their Applications. *Chem. Rev.* **114**, 10654–10696 (2014).

133. Cody, D. & Naydenova, I. Theoretical modeling and design of photonic structures in zeolite nanocomposites for gas sensing Part II: volume gratings. *J. Opt. Soc. Am. A* **35**, 12 (2018).

134. Barnes, N. P. Transition Metal Solid-State Lasers. in *Tunable Lasers Handbook*, pp. 219–291 (Academic Press, 1995).

135. Neipp, C., Márquez, A., Hernandez, A., Alvarez, M. L. & Beléndez, A. Thin and thick diffraction gratings: Thin matrix decomposition method. *Optik (Stuttg).* **115**, 385–392 (2004).

136. Klein, W. R. & Cook, B. D. Unified Approach to Ultrasonic Light Diffraction. *IEEE Trans. Sonics Ultrason.* **14**, 123–134 (1967).

137. Moharam, M. G. & Young, L. Criterion for Bragg and Raman-Nath diffraction regimes. *Appl. Opt.* **17**, 1757 (1978).

138. Cody, D. & Naydenova, I. Theoretical modeling and design of photonic structures in zeolite nanocomposites for gas sensing Part I: surface relief gratings. *J. Opt. Soc. Am. A* **34**, 2110 (2017).

139. Davies, S. *et al.* Holographic Sensors in Biotechnology. *Adv. Funct. Mater.* **31**, 2105645 (2021).

140. Lucío, M. I. *et al.* Label-free detection of C-Reactive protein using bioresponsive hydrogel-based surface relief diffraction gratings. *Biosens. Bioelectron.* **193**, 113561 (2021).

141. Lucío, M. I., Cubells-Gómez, A., Maquieira, Á. & Bañuls, M.-J. Hydrogel-based holographic sensors and biosensors: past, present, and future. *Anal. Bioanal. Chem.* **414**, 993–1014 (2022).

142. Yetisen, A. K. *et al.* Photonic hydrogel sensors. *Biotechnol. Adv.* **34**, 250–271 (2016).

143. Frutiger, A. *et al.* Nonspecific Binding—Fundamental Concepts and Consequences for Biosensing Applications. *Chem. Rev.* **121**, 8095–8160 (2021).

144. Goh, J., Loo, R., McAloney, R. & Goh, C. Diffraction-based assay for detecting multiple analytes. *Anal. Bioanal. Chem.* **374**, 54–56 (2002).

145. Goh, J. B., Loo, R. W. & Goh, M. C. Label-free monitoring of multiple biomolecular binding interactions in real-time with diffraction-based sensing. *Sensors Actuators, B Chem.* **106**, 243–248 (2005).

146. Wang, X., Liu, X. & Wang, X. Surface-relief-gratings based on molecularly imprinted polymer for 2,4-dichlorophenoxyacetic acid detection. *Sensors Actuators B Chem.* **220**, 873–879 (2015).

147. Gatterdam, V. *et al.* Focal molography is a new method for the in situ analysis of molecular interactions in biological samples. *Nat. Nanotechnol.* **12**, 1089–1095 (2017).

148. Fattinger, C. Focal Molography: Coherent Microscopic Detection of Biomolecular Interaction. *Phys. Rev. X* **4**, 031024 (2014).

149. Frutiger, A. *et al.* Principles for Sensitive and Robust Biomolecular Interaction Analysis: The Limits of Detection and Resolution of Diffraction-Limited Focal Molography. *Phys. Rev. Appl.* **11**, 1 (2019).

150. Blickenstorfer, Y. *et al.* Total internal reflection focal molography (TIR-M). *Sensors Actuators B Chem.* **349**, 130746 (2021).

151. Frutiger, A. *et al.* Image reversal reactive immersion lithography improves the detection limit of focal molography. *Opt. Lett.* **43**, 5801 (2018).

152. Reichmuth, A. M. *et al.* Quantification of Molecular Interactions in Living Cells in Real Time using a Membrane Protein Nanopattern. *Anal. Chem.* **92**, 8983–8991 (2020).

153. Reichmuth, A. M. *et al.* Investigating Complex Samples with Mologrames of Low-Affinity Binders. *ACS Sensors* **6**, 1067–1076 (2021).

154. Avella-Oliver, M., Ferrando, V., Monsoriu, J. A., Puchades, R. & Maquieira, A. A label-free diffraction-based sensing displacement immunosensor to quantify low molecular weight organic compounds. *Anal. Chim. Acta* **1033**, 173–179 (2018).

155. Avella-Oliver, M., Carrascosa, J., Puchades, R. & Maquieira, Á. Diffractive Protein Gratings as Optically Active Transducers for High-Throughput Label-free Immunosensing. *Anal. Chem.* **89**, 9002–9008 (2017).

156. Artundo, I. Photonic Integration: New Applications Are Visible. *Opt. Photonik* **12**, 22–25 (2017).

157. Chandrasekar, R., Lapin, Z. J., Nichols, A. S., Braun, R. M. & Fountain, A. W. Photonic integrated circuits for Department of Defense-relevant chemical and biological sensing applications: state-of-the-art and future outlooks. *Opt. Eng.* **58**, 1 (2019).

158. Schmitt, K. & Hoffmann, C. High-Refractive-Index Waveguide Platforms for Chemical and Biosensing. in *Optical Guided-wave Chemical and Biosensors I*, pp. 21–54 (Springer Berlin Heidelberg, 2010).

159. Kao, K. C. Optical and Electro-Optic Processes. in *Dielectric Phenomena in Solids*, pp. 115–212 (Academic Press, 2004).

160. Zhang, J. X. J. & Hoshino, K. Optical transducers: Optical molecular sensing and spectroscopy. in *Molecular Sensors and Nanodevices*, pp. 231–309 (Academic Press, 2019).

161. Kozma, P., Kehl, F., Ehrentreich-Förster, E., Stamm, C. & Bier, F. F. Integrated planar optical waveguide interferometer biosensors: A comparative review. *Biosens. Bioelectron.* **58**, 287–307 (2014).

162. Kobayashi, M. Guided-wave Optical Interconnect Techniques. in *Photonics in Switching*, pp. 271–317 (Academic Press, 1993).

163. Mukundan, H. *et al.* Waveguide-Based Biosensors for Pathogen Detection. *Sensors* **9**, 5783–5809 (2009).

164. Shukla, S. K., Kushwaha, C. S., Guner, T. & Demir, M. M. Chemically modified optical fibers in advanced technology: An overview. *Opt. Laser Technol.* **115**, 404–432 (2019).

165. Tong, X. C. Fundamentals and Design Guides for Optical Waveguides. in *Advanced Materials for Integrated Optical Waveguides. Springer Series in Advanced Microelectronics*, pp. 1–51 (Springer, 2014).

166. Zubia, J. & Arrue, J. Plastic Optical Fibers: An Introduction to Their Technological Processes and Applications. *Opt. Fiber Technol.* **7**, 101–140 (2001).

167. Luo, Y. *et al.* Fabrication of Polymer Optical Fibre (POF) Gratings. *Sensors* **17**, 511 (2017).

168. Narayanaswamy, R. Photometric sensors. in *Encyclopedia of Analytical Science*, pp. 262–269 (Academic Press, 2005).

169. Sapsford, K. E. Total-Internal-Reflection Platforms for Chemical and Biological Sensing Applications. in *Optical Guided-wave Chemical and Biosensors I. Springer Series on Chemical Sensors and Biosensors*, pp. 3–20 (Springer Berlin Heidelberg, 2010).

170. Marazuela, M. & Moreno-Bondi, M. Fiber-optic biosensors – an overview. *Anal. Bioanal. Chem.* **372**, 664–682 (2002).

171. Gaston, A., Lozano, I., Perez, F., Auza, F. & Sevilla, J. Evanescent wave optical-fiber sensing (temperature, relative humidity, and ph sensors). *IEEE Sens. J.* **3**, 806–811 (2003).

172. Tseng, S.-M. & Chen, C.-L. Side-polished fibers. *Appl. Opt.* **31**, 3438 (1992).

173. Teng, C. *et al.* Intensity-Modulated Polymer Optical Fiber-Based Refractive Index Sensor: A Review. *Sensors* **22**, 81 (2021).

174. Liu, G. & Feng, D. Evanescent wave analysis and experimental realization of refractive index sensor based on D-shaped plastic optical fiber. *Optik (Stuttg).* **127**, 690–693 (2016).

175. Pissadakis, S. Lab-in-a-fiber sensors: A review. *Microelectron. Eng.* **217**, 111105 (2019).

176. Birks, T. A. & Li, Y. W. The shape of fiber tapers. *J. Light. Technol.* **10**, 432–438 (1992).

177. Korposh, S., James, S., Lee, S.-W. & Tatam, R. Tapered Optical Fibre Sensors: Current Trends and Future Perspectives. *Sensors* **19**, 2294 (2019).

178. Jiao, L. *et al.* Recent advances in fiber-optic evanescent wave sensors for monitoring organic and inorganic pollutants in water. *TrAC Trends Anal. Chem.* **127**, 115892 (2020).

179. Bashan, G., London, Y., Hagai Diamandi, H. & Zadok, A. Distributed cladding mode fiber-optic sensor. *Optica* **7**, 85 (2020).

180. Przhiialkovskii, D. V. & Butov, O. V. High-precision point-by-point fiber Bragg grating inscription. *Results Phys.* **30**, 104902 (2021).

181. Jorgenson, R. C. & Yee, S. S. A fiber-optic chemical sensor based on surface plasmon resonance. *Sensors Actuators B Chem.* **12**, 213–220 (1993).

182. Ahn, J. H. *et al.* Fiber-optic waveguide coupled surface plasmon resonance sensor. *Opt. Express* **20**, 21729 (2012).

183. Hoa, X. D., Kirk, A. G. & Tabrizian, M. Towards integrated and sensitive surface plasmon resonance biosensors: A review of recent progress. *Biosens. Bioelectron.* **23**, 151–160 (2007).

184. Odacı, C. & Aydemir, U. The surface plasmon resonance-based fiber optic sensors: A theoretical comparative study with 2D TMDC materials. *Results Opt.* **3**, 100063 (2021).

185. De Vos, K. *et al.* Multiplexed Antibody Detection With an Array of Silicon-on-Insulator Microring Resonators. *IEEE Photonics J.* **1**, 225–235 (2009).

186. Steglich, P., Hülsemann, M., Dietzel, B. & Mai, A. Optical Biosensors Based on Silicon-On-Insulator Ring Resonators: A Review. *Molecules* **24**, 519 (2019).

187. Iqbal, M. *et al.* Label-Free Biosensor Arrays Based on Silicon Ring Resonators and High-Speed Optical Scanning Instrumentation. *IEEE J. Sel. Top. Quantum Electron.* **16**, 654–661 (2010).

188. Luan, E., Shoman, H., Ratner, D., Cheung, K. & Chrostowski, L. Silicon Photonic Biosensors Using Label-Free Detection. *Sensors* **18**, 3519 (2018).

189. Carlborg, C. F. *et al.* A packaged optical slot-waveguide ring resonator sensor array for multiplex label-free assays in labs-on-chips. *Lab Chip* **10**, 281–290 (2010).

190. Kersey, A. D. *et al.* Fiber grating sensors. *J. Light. Technol.* **15**, 1442–1463 (1997).

191. Chiavaioli, F., Baldini, F., Tombelli, S., Trono, C. & Giannetti, A. Biosensing with optical fiber gratings. *Nanophotonics* **6**, 663–679 (2017).

192. Albert, J., Shao, L.-Y. & Caucheteur, C. Tilted fiber Bragg grating sensors. *Laser Photon. Rev.* **7**, 83–108 (2013).

193. Lee, B., Roh, S. & Park, J. Current status of micro- and nano-structured optical fiber sensors. *Opt. Fiber Technol.* **15**, 209–221 (2009).

194. Wang, W. *et al.* A label-free fiber optic SPR biosensor for specific detection of C-reactive protein. *Sci. Rep.* **7**, 16904 (2017).

195. Cennamo, N. *et al.* A Complete Optical Sensor System Based on a POF-SPR Platform and a Thermo-Stabilized Flow Cell for Biochemical Applications. *Sensors* **16**, 196 (2016).

196. Cennamo, N. *et al.* D-shaped plastic optical fibre aptasensor for fast thrombin detection in nanomolar range. *Sci. Rep.* **9**, 18740 (2019).

197. Rahman, M. S. *et al.* Modeling of a highly sensitive MoS2-Graphene hybrid based fiber optic SPR biosensor for sensing DNA hybridization. *Optik (Stuttg).* **140**, 989–997 (2017).

198. Cennamo, N. *et al.* Detection of naphthalene in sea-water by a label-free plasmonic optical fiber biosensor. *Talanta* **194**, 289–297 (2019).

199. Cennamo, N. *et al.* A Molecularly Imprinted Polymer on a Plasmonic Plastic Optical Fiber to Detect Perfluorinated Compounds in Water. *Sensors* **18**, 1836 (2018).

200. Washburn, A. L., Gunn, L. C. & Bailey, R. C. Label-Free Quantitation of a Cancer Biomarker in Complex Media Using Silicon Photonic Microring Resonators. *Anal. Chem.* **81**, 9499–9506 (2009).

201. Xu, D.-X. *et al.* Label-free biosensor array based on silicon-on-insulator ring resonators addressed using a WDM approach. *Opt. Lett.* **35**, 2771 (2010).

202. Liu, Q. *et al.* Label-free, real-time and multiplex detection of Mycobacterium tuberculosis based on silicon photonic microring sensors and asymmetric isothermal amplification technique (SPMS-AIA). *Sensors Actuators B Chem.* **255**, 1595–1603 (2018).

203. Lo, S. M. *et al.* Photonic crystal microring resonator for label-free biosensing. *Opt. Express* **25**, 7046 (2017).

204. Chen, Y. *et al.* Ultrasensitive Detection of Testosterone Using Microring Resonator with Molecularly Imprinted Polymers. *Sensors* **15**, 31558–31565 (2015).

205. Guider, R. *et al.* Design and Optimization of SiON Ring Resonator-Based Biosensors for Aflatoxin M1 Detection. *Sensors* **15**, 17300–17312 (2015).

206. McClellan, M. S., Domier, L. L. & Bailey, R. C. Label-free virus detection using silicon photonic microring resonators. *Biosens. Bioelectron.* **31**, 388–392 (2012).

207. Ramachandran, A. *et al.* A universal biosensing platform based on optical micro-ring resonators. *Biosens. Bioelectron.* **23**, 939–944 (2008).

208. Angelopoulou, M. *et al.* Ultrafast Multiplexed-Allergen Detection through Advanced Fluidic Design and Monolithic Interferometric Silicon Chips. *Anal. Chem.* **90**, 9559–9567 (2018).

209. Goodwin, M. J. *et al.* Highly Sensitive Protein Detection by Asymmetric Mach–Zehnder Interferometry for Biosensing Applications. *ACS Appl. Bio Mater.* **3**, 4566–4572 (2020).

210. Chalyan, T. *et al.* Asymmetric Mach–Zehnder Interferometer Based Biosensors for Aflatoxin M1 Detection. *Biosensors* **6**, 1 (2016).

211. Pagkali, V. *et al.* Detection of ochratoxin A in beer samples with a label-free monolithically integrated optoelectronic biosensor. *J. Hazard. Mater.* **323**, 75–83 (2017).

212. Sarkar, D., Gunda, N. S. K., Jamal, I. & Mitra, S. K. Optical biosensors with an integrated Mach-Zehnder Interferometer for detection of Listeria monocytogenes. *Biomed. Microdevices* **16**, 509–520 (2014).

213. Huertas, C. S., Fariña, D. & Lechuga, L. M. Direct and Label-Free Quantification of Micro-RNA-181a at Attomolar Level in Complex Media Using a Nanophotonic Biosensor. *ACS Sensors* **1**, 748–756 (2016).

214. Maldonado, J., González-Guerrero, A. B., Domínguez, C. & Lechuga, L. M. Label-free bimodal waveguide immunosensor for rapid diagnosis of bacterial infections in cirrhotic patients. *Biosens. Bioelectron.* **85**, 310–316 (2016).

215. Ymeti, A. *et al.* Fast, Ultrasensitive Virus Detection Using a Young Interferometer Sensor. *Nano Lett.* **7**, 394–397 (2007).

216. Sridevi, S., Vasu, K. S., Asokan, S. & Sood, A. K. Sensitive detection of C-reactive protein using optical fiber Bragg gratings. *Biosens. Bioelectron.* **65**, 251–256 (2015).

217. Bekmurzayeva, A. *et al.* Etched fiber bragg grating biosensor functionalized with aptamers for detection of thrombin. *Sensors (Switzerland)* **18**, (2018).

218. Sun, D., Guo, T., Ran, Y., Huang, Y. & Guan, B.-O. In-situ DNA hybridization detection with a reflective microfiber grating biosensor. *Biosens. Bioelectron.* **61**, 541–546 (2014).

219. Lépinay, S., Ianoul, A. & Albert, J. Molecular imprinted polymer-coated optical fiber sensor for the identification of low molecular weight molecules. *Talanta* **128**, 401–407 (2014).

220. Sypabekova, M. *et al.* Functionalized etched tilted fiber Bragg grating aptasensor for label-free protein detection. *Biosens. Bioelectron.* **146**, 1–9 (2019).

221. Loyez, M., Albert, J., Caucheteur, C. & Wattiez, R. Cytokeratins Biosensing Using Tilted Fiber Gratings. *Biosensors* **8**, 74 (2018).

222. Jiang, B. *et al.* Label-free glucose biosensor based on enzymatic graphene oxide-functionalized tilted fiber grating. *Sensors Actuators B Chem.* **254**, 1033–1039 (2018).

223. Chiavaioli, F. *et al.* Towards sensitive label-free immunosensing by means of turn-around point long period fiber gratings. *Biosens. Bioelectron.* **60**, 305–310 (2014).

224. Esposito, F. *et al.* Ultrasensitive biosensor based on long period grating coated with polycarbonate-graphene oxide multilayer. *Sensors Actuators B Chem.* **274**, 517–526 (2018).

225. Gonçalves, H. M. R. *et al.* Biosensor for label-free DNA quantification based on functionalized LPGs. *Biosens. Bioelectron.* **84**, 30–36 (2016).

226. Delgado-Pinar, M. *et al.* Oligonucleotide-Hybridization Fiber-Optic Biosensor Using a Narrow Bandwidth Long Period Grating. *IEEE Sens. J.* **17**, 5503–5509 (2017).

227. Janczuk-Richter, M. *et al.* Long-period fiber grating sensor for detection of viruses. *Sensors Actuators B Chem.* **250**, 32–38 (2017).

228. Tripathi, S. M. *et al.* Long period grating based biosensor for the detection of Escherichia coli bacteria. *Biosens. Bioelectron.* **35**, 308–312 (2012).

OBJECTIVES

This doctoral thesis aims to innovate and extend the scope of diffractive biosensing. For that, this investigation explores diverse strategies to fabricate biogratings, evaluates their bioanalytical potential with immunological model systems, and addresses their further implementation in waveguiding structures to develop compact and miniaturized optical devices for label-free biosensing.

This main goal is subdivided into the following objectives:

- To explore and characterize the strengths and limitations of microcontact printing technique to fabricate diffractive structures of bioreceptors, with a special interest in the immobilization and functionality of the patterned biological probes **(Chapter 1)**.
- To assess and develop novel strategies to fabricate diffractive structures of bioreceptors that overcome the intrinsic limitations of microcontact printing **(Chapter 2)**.
- To implement biogratings in waveguiding structures to prove the concept of this novel diffractive transduction mechanism and to materialize it in technologies that aim to integrate all the optical functionalities in one single platform **(Chapter 3)**.

RESULTS

Chapter 1

Microcontact printing to pattern biogratings

Chapter 1: Microcontact printing to pattern biogratings.

Microcontact printing (μCP) has become a preferential technique to fabricate biogratings due basically to its simplicity, versatility, and great performance. However, μCP also presents some restricting features such as a moderate reproducibility of the resulting patterns and long inking times, together with other important effects in the scope of these techniques reported for the first time in this chapter. In this sense, the patterning of macromolecules by μCP may involve conformational changes that lead to a loss in the biological activity of the patterned bioreceptors.

The first part of this chapter **(Chapter 1.1)** demonstrates this phenomenon and provides an alternative strategy to overcome this issue, keeping the advantages of μCP. From a general perspective, this study introduces and assesses this new approach, and discusses its potential in immunosensing.

On the other hand, the transfer of bioreceptors in most μCP approaches reported in the state-of-the-art is driven by physical forces. Alternatively, μCP can be also tailored to incorporate chemical reactions between the bioreceptors and the surface chemical groups to improve the immobilization strength. The second part of the chapter **(Chapter 1.2)** explores different chemistries coupled to μCP for patterning functional biogratings. As a proof of concept, the resulting protein patterns are applied to the immunosensing of specific IgGs related to cow's milk allergy.

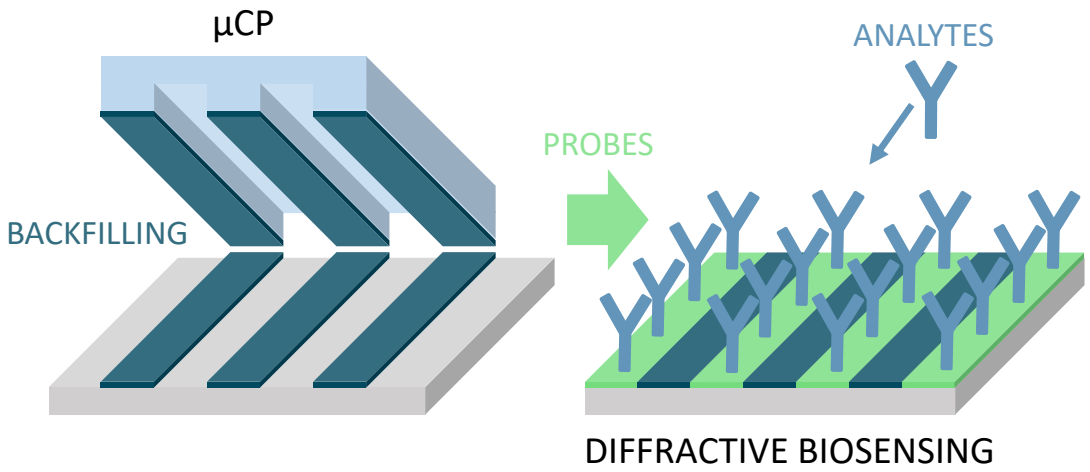

Chapter 1.1: Indirect Microcontact Printing to Create Functional Patterns of Physisorbed Antibodies

Sensors **2018**, 18(9), 3163

sensors

INDIRECT MICROCONTACT PRINTING TO CREATE FUNCTIONAL PATTERNS OF PHYSISORBED ANTIBODIES

Augusto Juste-Dolz[1], Miquel Avella-Oliver[1], Rosa Puchades[1,2] and Angel Maquieira[1,2,] *

[1]*Instituto Interuniversitario de Investigación de Reconocimiento Molecular y Desarrollo Tecnológico (IDM), Universitat Politècnica de València, Universitat de València, 46022 Valencia, Spain.*

[2]*Departamento de Química, Universitat Politècnica de València, 46022 Valencia, Spain*

*Correspondence: amaquieira@qim.upv.es (Ángel Maquieira)

ABSTRACT

Microcontact printing (µCP) is a practical and versatile approach to create nanostructured patterns of biomolecular probes, but it involves conformational changes on the patterned bioreceptors that often lead to a loss on the biological activity of the resulting structures. Herein we introduce indirect µCP to create functional patterns of bioreceptors on solid substrates. This is a simple strategy that relies on physisorbing biomolecular probes of interest in the nanostructured gaps that result after patterning backfilling agents by standard µCP. This study presents the approach, assesses bovine serum albumin as backfilling agent for indirect µCP on different materials, reports the limitations of standard µCP on the functionality of patterned antibodies, and demonstrates the capabilities of indirect µCP to solve this issue. Bioreceptors were herein structured as diffractive gratings and used to measure biorecognition events in label-free conditions. Besides, as a preliminary approach towards sensing biomarkers, this work also reports the implementation of indirect µCP in an immunoassay to detect human immunoglobulin E.

Keywords: microcontact printing; physisorption; diffraction-based sensing; label-free; antibody; immunoglobulin E; allergy; soft lithography; denaturation; paratope.

1. Introduction

Creating nanostructures of bioreceptors (proteins, nucleic acids, cells, etc.) nowadays plays an important role in biosensing, and it constitutes a significant trend in advances in nanoscience and nanotechnology [1, 2]. Classical approaches to fabricating nanostructures for bioanalysis rely on placing biomolecular probes on solid nanomaterials [3-7]. Alternatively, developing nanostructures constituted by the bioreceptors themselves patterned on unstructured substrates is an appealing option in terms of simplicity, multiplexing, label-free capabilities, and cost-effectiveness, among others [8-12].

Contact techniques (pin printing, flow printing, dip pen nanolithography, etc.) enable well-defined and homogenous patterning, and they are typically employed to produce these structures of bioactive molecules [13, 14]. Among these techniques, micro-contact printing (μCP) holds an important scientific relevance from its development. It relies on "inking" the probes on the surface of a nanostructured elastomeric stamp (typically made of polydimethylsiloxane) and then precisely transferring them to a solid material just by contact (Figure 1a). This versatile technique allows for the creation of large-scale patterns of probes of different natures (small molecules, proteins, nucleic acids, etc.) in standard biochemical lab settings [15-17], and with a resolution of up to about 50 nm [18]. Thanks to all these strengths, μCP holds a great popularity [19-22]. Nanometric patterns of bioreceptors fabricated by μCP have found many applications, such as microarraying and neuronal cells guidance among others [12, 15, 23]. Besides, these nanostructures also allow us to exploit nanoscopic light-matter phenomena to transduce biorecognition events, as is the case for diffraction-based sensing (DBS).

DBS relies on patterning biological probes as diffractive gratings on solid substrates, and then quantifying biorecognition events by the means of changes in their diffracted pattern. These changes come from variations in the mass that conforms the gratings (generated by probe–target interactions), and they can be easily quantified by measuring the intensity of a diffracted order [24-27]. This strategy allows for label-free sensing and real-time biorecognition assays of different natures [24, 25], using simple assay setups [27], and in a multiplexed and high-throughput fashion [26]. Besides, μCP

has shown to be a powerful technique to create functional nanostructures of bioreceptors for DBS [25-29].

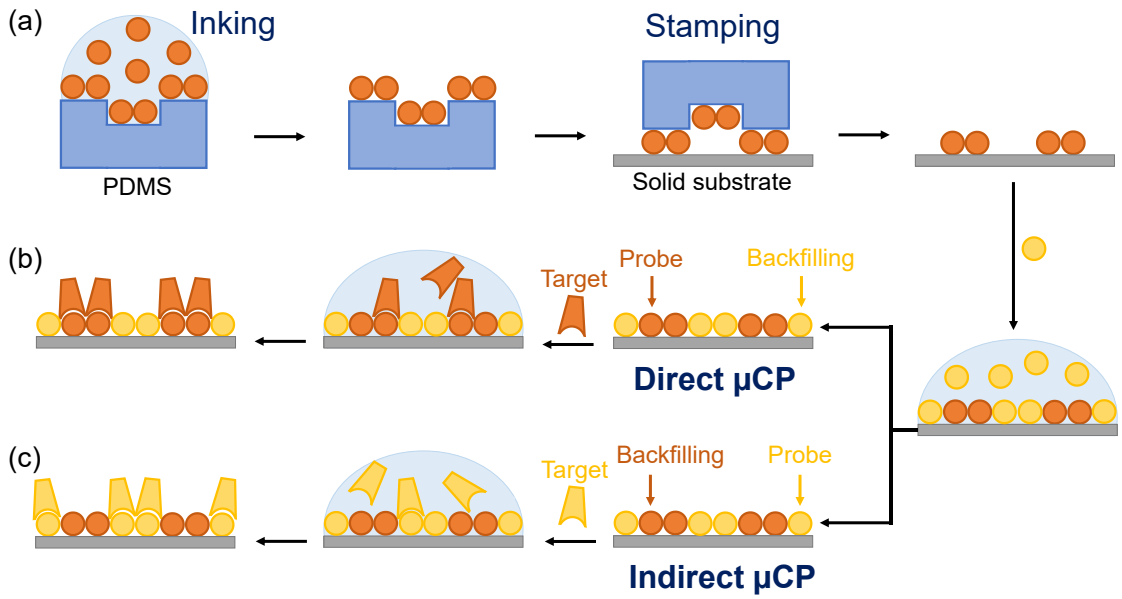

Figure 1. Schematic illustration of the fabrication and biorecognition processes, including **(a)** inking and stamping, **(b)** standard microcontact printing (µCP), and **(c)** indirect µCP. Note that in standard µCP, probes are patterned by stamping, whereas in indirect µCP, backfilling agents are stamped first and then the probes are physisorbed on the gaps just by incubation.

µCP also enables direct patterning of proteins by physisorption. However, while this fact presents advantages in terms of simplicity, the conformational changes experimented by the patterned proteins along the physisorption process may lead to an important loss on their activity [30]. The conformation of physisorbed proteins on solid surfaces is governed by a complex interplay of different forces (Van der Waals, electrostatic, hydrogen bonding, conformational entropy, etc.) [14, 31], which makes it extremely difficult to predict the functionality of a particular protein that is adsorbed on a given surface. This complexity increases even more when the proteins are patterned by standard µCP, since it involves two sequential adsorption processes, and the transfer to the final surface takes place in a rather dry state. This phenomenon was already observed in the early stages of µCP [32], and it is still an issue nowadays as it reduces

the range of applications for this approach. An interesting alternative found in the state-of-the-art relies on mediating the patterning of proteins by self-assembled monolayers of reactive ligands structured by μCP [20, 33, 34]. This ligand-based strategy can provide solutions in terms of activity of the patterned proteins and introduces appealing options towards more stable immobilization chemistries, whereas on the other hand, it also limits the characteristic simplicity of μCP by introducing additional reagents and experimental stages.

The present study addresses this issue and focuses on creating functional structures of physisorbed antibodies by μCP. Given their central role in biosensing, antibodies were herein used as both, probes, and targets. Also, since the functionality of their binding sites may be specially susceptible to the conformational changes involved in the structural rearrangements during the adsorption processes, these bioreceptors are highly suitable for the scope of this work. In fact, the results presented below highlight a substantial functionality difference between the paratopes and the epitopes of antibodies patterned by standard μCP. In this study, we explore this phenomenon on different materials using two model immunochemical systems and assessing by DBS and AFM the molecular-scale events taking place at the interface that holds the biomolecular pattern. From these results, this work proposes indirect μCP as a novel alternative to create functional structures of capture antibodies. This strategy keeps the characteristic simplicity of μCP, relies on physisorption, and provides a practical solution for those cases in which standard μCP leads to patterns of biomolecular probes with a reduced functionality. Herein we present indirect μCP and demonstrate it in a model immunochemical system, as well as in a label-free immunoassay to detect human immunoglobulin E.

2. Materials and Methods

2.1. Materials

Sodium phosphate buffer (PBS, 8 mM Na_2HPO_4, 2 mM KH_2PO_4, 137 mM NaCl, 2.7 mM KCl, pH 7.4), PBS-T (PBS with polysorbate 20 0.05% v/v), and carbonate buffer (50 mM sodium carbonate, pH 9.6) were prepared with purified water (Milli-Q, Millipore Iberica,

Darmstadt, Germany) and filtered through 0.2 µm polyethersulfone membranes (Merck, Darmstadt, Germany). Polydimethylsiloxane (PDMS) Sylgard 184 was from Dow Corning (Wiesbaden, Germany). Bovine serum albumin (BSA), polysorbate 20 (Tween 20), polyclonal rabbit anti-BSA antibodies, polyclonal goat anti-rabbit antibodies (anti-RIgGs), and allyltrimethoxysilane were supplied by Sigma-Aldrich (Madrid, Spain). Rabbit antibodies (RIgGs) were purified from rabbit antiserum by affinity chromatography. Human immunoglobulins E (IgE) were from NIBSC (South Mimms, UK), and anti-IgE antibodies from Dr. Fooke (Neuss, Germany). Glass slides were purchased from Labbox (Mataró, Spain), polystyrene slides from Evergreen (Ted Pella Inc., Redding, CA, USA), and polymethyl methacrylate and polyester substrates were kindly supplied by Plexi (Valencia, Spain). Polycarbonate substrates were easily obtained from regular compact disks (MediaRange, MPO Iberica, Madrid, Spain) as described elsewhere [35]. The silicon grooved nanostructure (555.5 nm period, 100 nm groove depth, duty cycle 50%) used as a master for µCP was from LightSmyth (Eugene, OR, USA).

2.2. Patterning

Periodic nanostructures of biomolecular probes (proteins and antibodies) were fabricated on flat solid substrates by µCP. For that, PDMS (elastomer:curing agent, 10:1 w/w) was poured onto the nanogrooved side of the silicon master, degassed in a vacuum chamber for about 5 min, polymerized overnight at 60 °C, peeled off from the master, cut in 5 × 5 mm squared pieces, washed three times by sonication in ethanol (30% in water, 5 min), and dried under a stream of air. Then, as schematized in Figure 1, probe solutions in PBS (40 µL, 200 µg mL^{-1}) were incubated on the structured side of the PDMS stamps during 160 min, the stamps were then rinsed with deionized water, dried by air stream, and stamped on the substrate. Finally, the chips containing the stamped structures were rinsed with water and dried as before.

Prior to stamping, the substrate materials were washed three times by sonication in ethanol (30% in water, 5 min), and dried under a stream of air. Gold surfaces were created by sputtering (EM SCD005, Leica Microsystems, Madrid, Spain) a 50 nm thick layer of metal on polycarbonate chips. Functionalized glass was obtained by immersing

slides in allyltrimethoxysilane (2% v/v in toluene) for 2 h under orbital agitation, rinsing the slides with toluene, drying them by air, and curing at 110 °C for 30 min. This silanization was monitored by contact angle measurements (Figure A1).

Two patterning strategies were performed in this work: standard (Figure 1b) and indirect (Figure 1c) μCP. The first one consists of the conventional state-of-the-art μCP process and it is based on an initial patterning of the probes as described in the paragraph above, and then incubating a backfilling agent to minimize non-specific binding during subsequent biorecognition assays. Conversely, indirect μCP relies on patterning first, backfilling (blocking) agent by standard μCP, and then incubating the bioreceptors on the patterned area (40 μg mL^{-1} in carbonate buffer, 2 h, 37 °C) in order to immobilize them by physisorption on the remaining gaps of the structure. In both cases, the resulting patterns were rinsed with deionized water and dried under a stream of air. A specific incubation of a backfilling agent was omitted in standard μCP, since previous reports showed that similar performances can be obtained in this case by just including polysorbate 20 in the incubation solution during the biorecognition steps [27].

2.3. Biorecognition Assays

To perform the biorecognition assays, 70–100 μL of sample containing target antibodies (0–100 μg·mL^{-1}) in PBS-T were incubated on the bioreceptor nanostructures over 30 min at room temperature. Then, the chips were rinsed with PBS-T and deionized water, and they were dried under a stream of air. Custom circular incubation masks made of adhesive polymeric film were used to incubate the samples on glass. Three replicates for each condition were assayed and measured, and then used to calculate averaged and standard deviation values. Noise was estimated as the standard deviation from the measurement of 10 blank structures and employed to infer signal-to-noise ratios (SNR). Limits of detection were calculated as the concentrations associated with SNR = 3 from the linear interpolation in the experimental dose-response curves.

2.4. DBS Measurements

In essence, DBS responds to nanoscopic contrasts between the mass, constituting both parts of the diffractive structure (ridges and gaps in this case). This technique was herein employed to quantify biorecognition events, as well as to assess the characteristics of the developed nanometric patterns along the fabrication process. All the measurements were performed in air at endpoint conditions. Bioreceptor structures on transparent substrates (glass, functionalized glass, polystyrene, polycarbonate, polymethyl methacrylate, and polyester) were assessed by transmission, and by reflection on non-transparent materials (gold).

Transmission DBS measurements were performed using a simple optomechanical setup, as illustrated in Figure 2a. Basically, the chips containing protein structures were set to be orthogonally irradiated by a collimated and attenuated (95%) 532 nm laser source (100 mW, MGL-III-532, CNI, Changchun, China). This configuration generates a diffracted order whose intensity was measured using a monochromatic CMOS camera (1 ms of exposure time, Edmund eo-1312 m, York, UK). For reflection measurements, the setup was arranged to irradiate the surface at 80 °C and to collect the intensity of the diffracted order reflected from the surface, as illustrated in Figure 2b.

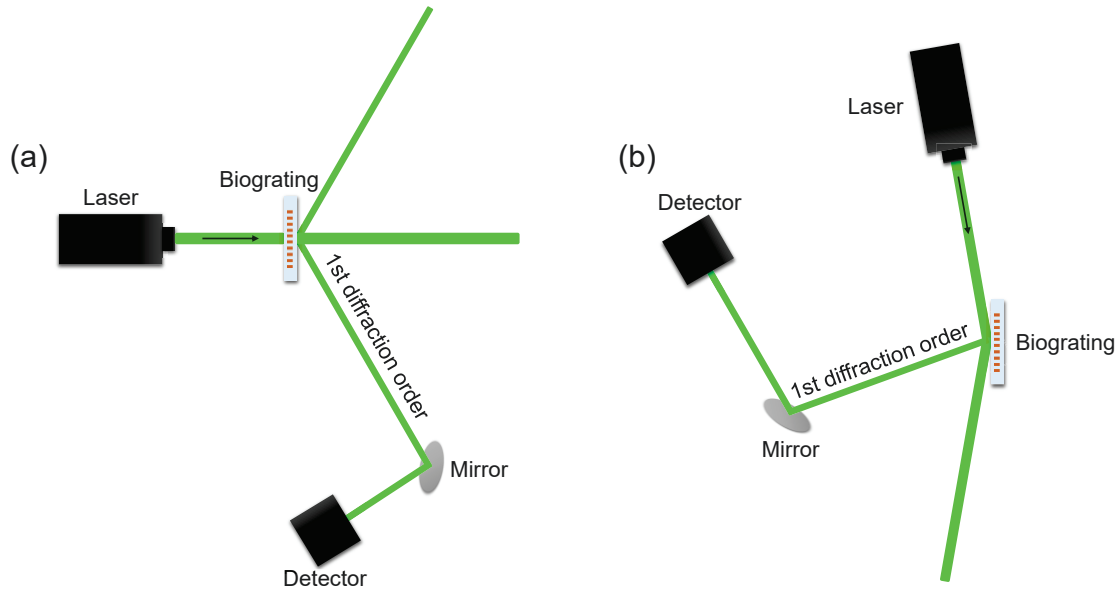

Figure 2. Schematic illustration of the experimental setups employed in this study to perform DBS measurements by **(a)** transmission and **(b)** reflection.

2.5. AFM Characterization

The topography of the developed bioreceptor structures was analyzed by atomic force microscopy (AFM), using tapping mode in air in a Multimode 8 microscope (Bruker) with RFESPA probes (MPP-21120-10 Bruker). AFM images were analyzed using Nanoscope software, and a first order polynomial flatten was applied in all the cases. To calculate the averaged cross section profiles, the area of interest was selected and the height of every data row along the longitudinal direction of the rides was averaged and plotted.

3. Results and Discussion

3.1. Substrate Materials

The nature of the substrate material is a key parameter for the performance of the physisorbed bioreceptors patterned by μCP. Regarding topography, suitable substrates must be flat enough to ensure maximal and homogeneous contact during the stamping stage. More importantly within the scope of this work, the chemical composition of the solid surface plays a crucial role on the conformational rearrangements undergone by proteins to become physisorbed, and therefore this parameter strongly affects their resulting functionality.

To explore this issue, this section evaluates (by DBS) the experimental dose-response curves of protein patterns fabricated by standard μCP on materials of different natures. For that, we first used a model system based on BSA as a probe and anti-BSA antibodies as targets. This is a reference immunoassay in the field of biosensing, herein selected to extend the scope of this assessment and to set up BSA patterning for its subsequent use as backfilling agent in this study (Section 3.2).

BSA patterns were fabricated on materials presenting different compositions and hydrophilicity (Figure A1), and a range of anti-BSA concentrations were incubated on them. Glass is a widely used substrate, and its functionalization (silanization) introduces interesting options to modulate surface properties [36]. Polystyrene is a well-known material for biosensing, and polycarbonate is interesting due to its good immobilization features and its compatibility with lab-on-a-disk biosensors [35]. Polymethyl

methacrylate and polyester were selected as polymers for broadening the scope of this comparison. Regarding gold, it presents well-known probe immobilization features, and it is involved in many other label-free biosensing techniques (SPR, SERS, QCM, etc.).

As observed in Figure 3, rather similar responses were obtained with all the different materials, and antibody concentrations of at least 0.5 μg mL^{-1} were detected in all the cases. More importantly, all dose-response curves display good correlations between the diffracted intensity and the target concentration. Although many processes may be involved in these responses (such as different physisorption densities, desorption processes, or non-specific binding, among others), this trend indicates that the conformations of the patterned protein are suitable to be recognized by the target IgG.

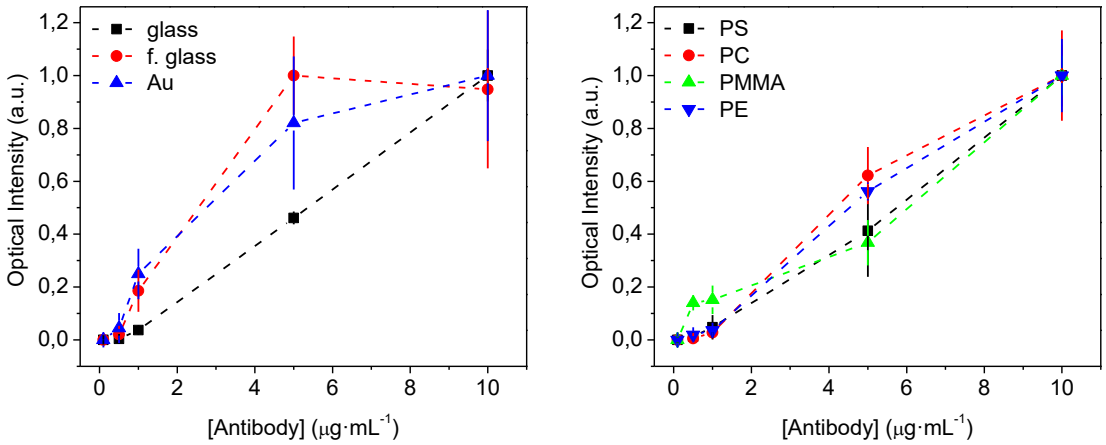

Figure 3. Dose-response curves for bovine serum albumin (BSA) probes and anti-BSA targets on different materials. Optical intensities in the vertical axes are normalized to the maximum intensity observed.

Beyond using BSA as probes, we extended this study to antibodies, since they play a central role in biosensing and their functionality may be highly dependent on the conformation of their physisorbed state. For that, we first patterned rabbit antibodies (RIgG) on glass, to be recognized by anti-rabbit antibodies (anti-RIgG). As observed in Figure 4a (upper curve), the response displayed by this system also indicates a suitable conformation of the patterned antibodies to be recognized by anti-RIgGs in solution. However, when these anti-RIgGs were patterned as probes, they were not able to bind their target RIgG anymore, and the corresponding dose-response curve displayed a

negligible signal-concentration correlation (Figure 4a, lower curve). This observation indicates that the resulting conformation of these antibodies after the patterning process on glass strongly disrupts the functionality of their binding sites.

Then, the same experiment was conducted on polycarbonate. Since this polymer presents different compositional and hydrophilicity characteristics compared to glass (Figure A1), the patterned probes may lead to distinct conformations in their physisorbed state, which may change their functionality. However, equivalent results to glass were obtained with polycarbonate. A good correlation between concentration and diffracted signals was only obtained for patterned RIgGs on the substrate (Figure 4b, upper curve), but the dose-response for patterned anti-RIgG presents a rather flat trend (Figure 4b, lower curve).

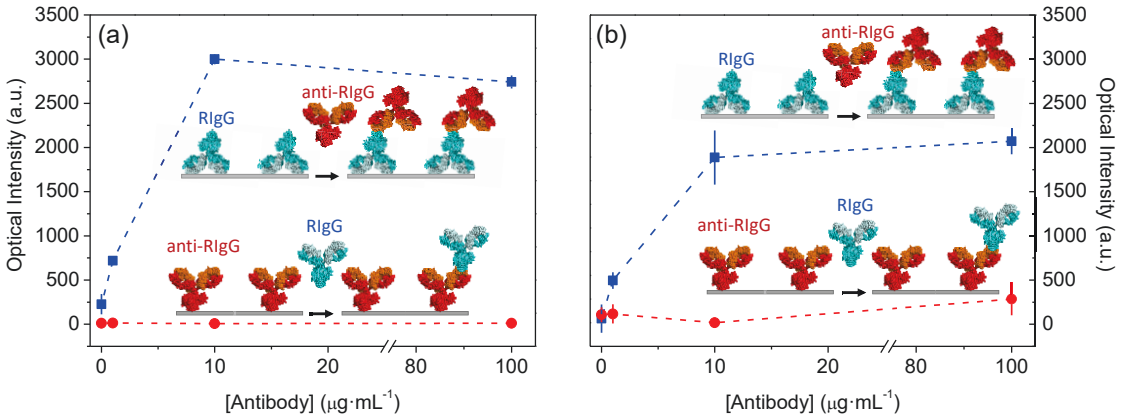

Figure 4. Dose-response curves of the immunochemical system based on rabbit antibodies (RIgG) and anti-rabbit antibodies (anti-RIgG) on **(a)** glass and **(b)** polycarbonate surfaces. In both cases, upper curves correspond to patterned RIgGs and anti-RIgG targets, and lower curves display the response of patterned anti-RIgGs and RIgG targets.

Therefore, the results suggest that the functionality of these IgGs is much more sensitive to the conformational changes undergone during μCP if the patterned antibodies are the ones that recognize targets than if they are the ones being recognized (anti-RIgGs and RIgGs in this system, respectively). In other words, these conformational changes make paratopes (IgG regions that recognizes the antigen) become inactive when

patterned, whereas the patterned epitopes (regions recognized by the paratopes) keep their ability to be recognized. Another potential explanation for these observations is that both paratopes and epitopes become strongly denatured when patterned, so paratopes become completely inactive, whereas some conformational epitopes remain unaltered and some lineal epitopes results accessible and can be recognized by certain paratopes within the polyclonal distribution of IgGs. In any case, it is interesting to highlight that this phenomenon may also potentially hinder the functionality of other biosensing configurations beyond this particular system, which would be interesting to explore in future investigations involving different biorecognition assays and patterning techniques.

3.2. Indirect μCP

As highlighted from the results in the section above, the paratopes of the antibodies patterned by standard μCP can undergo a dramatic decrease in their binding functionality. This problem is hard to predict and it constitutes an important limitation of μCP that may arise when developing new biosensing systems based on the nanostructured patterns of bioreceptors. Along these lines, in this section we introduce indirect μCP as a patterning alternative to address this issue.

As illustrated in Figure 1, indirect μCP relies on first patterning a backfilling agent by standard μCP. The denaturation of this agent does not affect on the performance of the assay, since it is merely used for backfilling. More importantly, this initial step leads to structured gaps on the surface, in which the desired bioreceptors can be immobilized by physisorption just by incubating them in solution. As a result, the biomolecular probes of interest can be immobilized in a structured fashion without undergoing all the conformational changes involved in μCP (only the ones in standard physisorption), thus experimenting milder processes and therefore presenting a lower potential to denature their binding sites and decrease their functionality. Furthermore, this strategy provides bioreceptor networks that already comprises an effective backfilling, which is very important to minimize potential artifacts coming from non-specific binding in the prospective use of these structures to analyze targets in complex matrixes [37].

To assess indirect μCP, we patterned BSA as a backfilling agent on glass, and then immobilized anti-RIgG as binding probes to subsequently recognize the RIgG targets in solution. As demonstrated in the section above, BSA presents great capabilities to be patterned by μCP on different materials and measured by DBS, and this fact, together with its inexpensiveness, makes this protein a highly suitable backfilling agent for this indirect printing. The experimental topographic characterization after this BSA patterning shows that the resulting structure is constituted by parallel, periodic, and straight ridges (Figure B1a), whose definition is affected by some smears and heterogeneities. These ridges present an averaged height difference (ridges-grooves) of about 4 nm (Figures B1d). Considering the prolate ellipsoid shape of BSA (14 nm for the polar axis and 4 nm for the equatorial axis), this height suggests that the protein tends to form a monolayer with its equatorial axis oriented orthogonally to the surface.

Figure 5b shows that the incubation of probes led to a dramatic decrease on the diffraction intensity, compared to the one of the initial BSA gratings. This fact points out that this incubation diminishes the difference in the mass that constitutes both parts of the grooved structure, which matches with the proper physisorption of the probes in the gaps, by a lot. This observation is also supported by the topographic characterization of the structure in this stage, where the averaged height difference decreases from 4.4 to 2 nm (Figures B1b,d). The not-null-diffracted signal obtained after incubating the probe must be generated by a greater mass in the anti-RIgG ridges, which agrees with the higher molecular weight of antibodies versus BSA (150 and 66.5 kDa, respectively). In fact, the AFM images also showed that the BSA ridges were narrower than the resulting gaps (Figure B1a), whereas the higher ridges after incubating the probe were actually the wider ones (Figure B1b).

Then, we studied the biosensing capabilities of these backfilled antibody structures by incubating different concentrations of target RIgGs in solution. Figure 5c shows the rising trend in the diffracted intensity obtained for increasing concentrations of target. This observation indicates that the conformation of the patterned paratopes preserve enough functionality to recognize the target epitopes. This proper recognition is also observed in the topographic measurements, which reaches an averaged height increase of 1.5 nm in the wider ridges (Figure B1c,d). A limit of detection of about 0.4 $\mu g \cdot mL^{-1}$ is

inferred from the experimental dose-response curve in Figure 5c for this particular immunochemical system. Although higher diffracted intensities were registered when patterning RIgGs by standard µCP (Figure 4b, upper curve), it must be took into account that the indirect approach involves stronger backfilling conditions. Therefore, it results in much smaller contrasts between the mass conforming the probe and the mass in the backfilled ridges, which generates lower signals along the dose-response curve. However, what is important to highlight from these findings is that the presented indirect patterning strategy keeps the advantages of µCP and allows for the easy creation of functional structures of physisorbed antibodies that preserve the functionality of their paratopes, even for IgGs with a negligible functionality when patterned by standard µCP (lower curves in Figures 4b,c).

3.3. IgEs Immunosensing

To provide insights into the potential of indirect µCP for label-free biosensing, we implemented this approach in an immunochemical system to quantify human IgEs by DBS. IgEs are an isotype of immunoglobulins found in mammals, whose concentration in human blood serum is low at normal levels. This kind of immunoglobulins can be used as biomarkers for the diagnosis of allergies, parasitosis, immunoregulatory diseases, infections, and inflammatory disorders [38-41].

We developed diffractive nanometric patterns of anti-IgE antibodies on glass by indirect µCP, with BSA backfilling as before. The results presented in Figure 5c illustrate that the incubation of these antibodies on the BSA patterns also leads to an important decrease of the diffracted signal, which indicates the proper immobilization of the antibodies on the structure gaps, as discussed in the section above (Figure 5a,b). Furthermore, these results show that the diffracted signal increases together with the target IgE concentration, which indicates that the paratopes of the resulting anti-IgE nanostructures are also functional for this immunochemical system. From the results shown at Figure 5c, an experimental limit of detection of 0.2 $\mu g \cdot mL^{-1}$ of IgEs was inferred. Given the rather low SNR values obtained in this curve, this assay would be more suitable for qualitative analysis. For the particular application of this system in the

diagnosis of allergies, this sensitivity enables for the detection of IgE concentrations in the range of ultra high levels of allergy, according to the radioallergosorbent test scores.

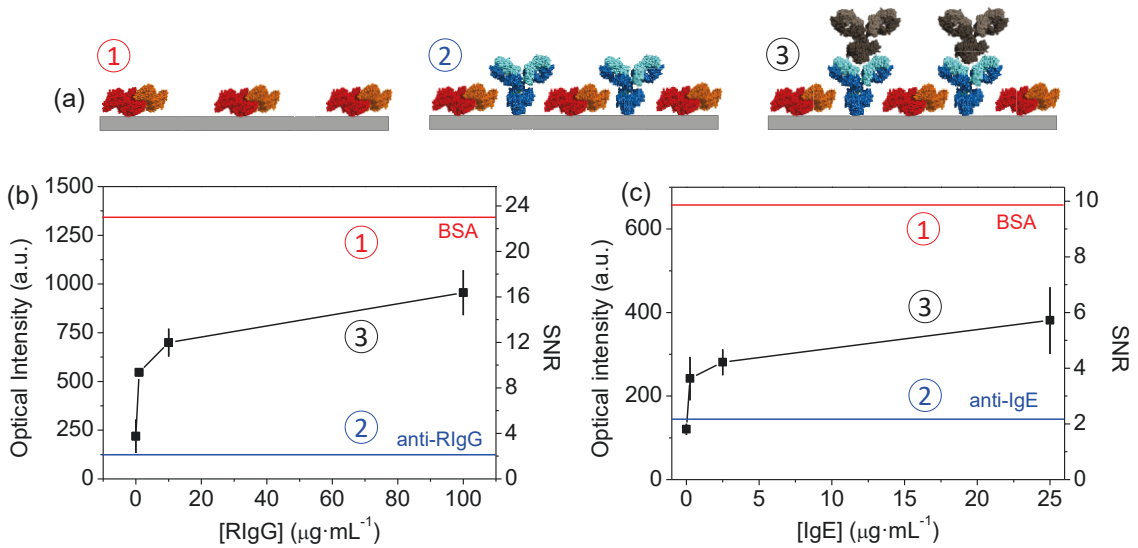

Figure 5. Experimental results for indirect μCP. **(a)** Schematic illustration of the state of the nanostructures ① after patterning the backfilling agent, ② after incubating the probe, and ③ after binding target antibodies. **(b,c)** Dose-response curves obtained from antibody structures patterned by indirect μCP for **(b)** anti-RIgG probes and RIgG targets, and **(c)** anti-IgE probes and human IgE targets. Upper and lower horizontal lines show the signal levels before and after incubating probe antibodies, respectively. The numbering of the curves indicates the state of the patterns at each stage, according to Figure 5a.

4. Conclusions

This work introduces indirect μCP as a strategy to create functional nanostructures of antibodies immobilized by physisorption. The experimental evidences herein presented demonstrate that, in some instances (typically hard to predict), these functional antibody gratings cannot be obtained by standard μCP. The results also suggest that the paratopes of immobilized antibodies are more prone to loose their activity after μCP patterning, with respect to their epitopes. Along these lines, BSA is a suitable protein as a backfilling agent for indirect μCP on a wide range of materials. When used to mediate the patterning of IgGs, antibody nanostructures with functional paratopes can be

successfully fabricated by indirect μCP. This approach has proved its capabilities to create functional patterns of antibodies in a model system based on IgGs as probes and analytes, as well as in an immunoassay to detect human IgEs in label-free conditions by DBS. From these results, this study aims to introduce indirect μCP as a practical alternative for those cases in which standard μCP leads to patterns of non-functional biomolecular probes.

Author Contributions

Conceptualization, A.J.-D. and M.A.-O.; Investigation, A.J.-D. and M.A.-O.; Writing—Original Draft Preparation, A.J.-D. and M.A.-O.; Writing—Review & Editing, A.J.-D., M.A.-O., R.P., and A.M.; Supervision, R.P. and A.M.; Funding Acquisition, M.A.-O., R.P., and A.M.

Funding

This research was funded by the Spanish Ministry of Economy and Competitiveness (CTQ2016-75749-R), FEDER, Generalitat Valenciana (PROMETEO II/2014/040), and Universitat Politècnica de Valencia (FPI program).

Conflicts of Interest

The authors declare no conflict of interest. The funders had no role in the design of the study; in the collection, analyses, or interpretation of data; in the writing of the manuscript, and in the decision to publish the results.

Appendix A

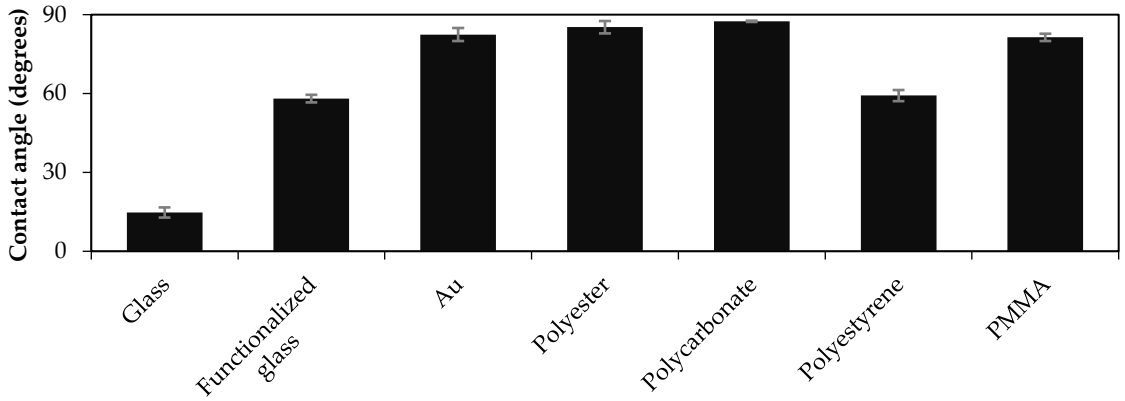

Figure A1. Contact angles of the different substrate materials studied in this work. Measured in water (2 µL droplets).

Appendix B

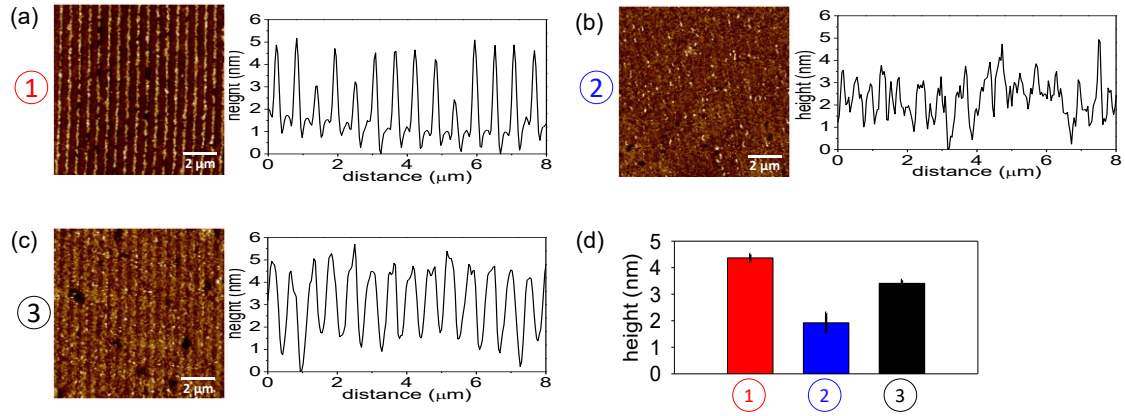

Figure B1. AFM topographic characterization along the different stages of indirect µCP: **(a)** Initial BSA patterning, **(b)** probe anti-IgG patterning, and **(c)** incubation of target IgG (100 µg mL^{-1}). Left figures are the experimental AFM images and right graphs are their corresponding averaged cross section profiles. **(d)** Averaged height differences (ridges–grooves) obtained from the AFM scans above. The numbers in circles indicate the state of the patterns at each stage, according to Figure 5a.

References

1. Holzinger, M.; Le Goff, A.; Cosnier, S., Synergetic Effects of Combined Nanomaterials for Biosensing Applications. Sensors **2017**, 17, 1010, doi: 10.3390/s17051010.

2. Lee, J.; Takemura, K.; Park, E., Plasmonic Nanomaterial-Based Optical Biosensing Platforms for Virus Detection. Sensors **2017**, 17, 2332, doi: 10.3390/s17102332.

3. Kahraman, M.; Mullen, E. R.; Korkmaz, A.; Wachsmann-Hogiu, S., Fundamentals and applications of SERS-based bioanalytical sensing. Nanophotonics **2017**, 6, 831-852, doi: 10.1515/nanoph-2016-0174.

4. Barrios, C. A.; Canalejas-Tejero, V.; Herranz, S.; Moreno-Bondi, M. C.; Avella-Oliver, M.; Puchades, R.; Maquieira, A., Aluminum Nanohole Arrays Fabricated on Polycarbonate for Compact Disc-Based Label-Free Optical Biosensing. Plasmonics **2014**, 9, 645-649, doi: 10.1007/s11468-014-9676-5.

5. Inan, H.; Poyraz, M.; Inci, F.; Lifson, M. A.; Baday, M.; Cunningham, B. T.; Demirci, U., Photonic crystals: emerging biosensors and their promise for point-of-care applications. Chem. Soc. Rev. **2017**, 46, 366-388, doi: 10.1039/c6cs00206d.

6. Avella-Oliver, M.; Puchades, R.; Wachsmann-Hogiu, S.; Maquieira, A., Label-free SERS analysis of proteins and exosomes with large-scale substrates from recordable compact disks. Sens. Actuators, B **2017**, 252, 657-662, doi: 10.1016/j.snb.2017.06.058.

7. Gavela, A. F.; Garcia, D. G.; Ramirez, J. C.; Lechuga, L. M., Last Advances in Silicon-Based Optical Biosensors. Sensors **2016**, 16, 285, doi: 10.3390/s16030285.

8. Goh, J. B.; Loo, R. W.; Goh, M. C., Label-free monitoring of multiple biomolecular binding interactions in real-time with diffraction-based sensing. Sens. Actuators, B **2005**, 106, 243-248, doi: 10.1016/j.snb.2004.08.003.

9. Kussrow, A.; Enders, C. S.; Bornhop, D. J., Interferometric Methods for Label-Free Molecular Interaction Studies. Anal. Chem. **2012**, 84, 779-792, doi: 10.1021/ac202812h.

10. Wang, X.; Wang, X., Aptamer-functionalized hydrogel diffraction gratings for the human thrombin detection. Chem. Commun. **2013**, 49, 5957-5959, doi: 10.1039/c3cc41827h.

11. Barrios, C. A.; Zhenhe, C.; Navarro-Villoslada, F.; López-Romero, D.; Moreno-Bondi, M. C., Molecularly imprinted polymer diffraction grating as label-free optical bio(mimetic)sensor. Biosens. Bioelectron. **2011**, 26, 2801-2804, doi: 10.1016/j.bios.2010.11.009.

12. Gupta, S.; Manubhai, K. P.; Kulkarni, V.; Srivastava, S., An overview of innovations and industrial solutions in Protein Microarray Technology. Proteomics **2016**, 16, 1297-1308, doi: 10.1002/pmic.201500429.

13. Romanov, V.; Davidoff, S. N.; Miles, A. R.; Grainger, D. W.; Gale, B. K.; Brooks, B. D., A critical comparison of protein microarray fabrication technologies. Analyst **2014**, 139, 1303-1326, doi: 10.1039/C3AN01577G.

14. Ekblad, T.; Liedberg, B., Protein adsorption and surface patterning. Curr. Opin. Colloid Interface Sci. **2010**, 15, 499-509, doi: 10.1016/j.cocis.2010.07.008.

15. Voskuhl, J.; Brinkmann, J.; Jonkheijm, P., Advances in contact printing technologies of carbohydrate, peptide and protein arrays. Curr. Opin. Chem. Biol. **2014**, 18, 1-7, doi: 10.1016/j.cpba.2013.10.022.

16. Kane, R. S.; Takayama, S.; Ostuni, E.; Ingber, D. E.; Whitesides, G. M., Patterning proteins and cells using soft lithography. Biomaterials **1999**, 20, 2363-2376, doi: https://doi.org/10.1016/S0142-9612(99)00165-9.

17. Castagna, R.; Bertucci, A.; Prasetyanto, E. A.; Monticelli, M.; Conca, D. V.; Massetti, M.; Sharma, P. P.; Damin, F.; Chiari, M.; De Cola, L.; Bertacco, R., Reactive Microcontact Printing of DNA Probes on (DMA-NAS-MAPS) Copolymer-Coated Substrates for Efficient Hybridization Platforms. Langmuir **2016**, 32, 3308-3313, doi: 10.1021/acs.langmuir.5b04669.

18. Sauer, U., Analytical Protein Microarrays: Advancements Towards Clinical Applications. Sensors **2017**, 17, 256, doi: 10.3390/s17020256.

19. Xuexin, D.; Yiping, Z.; András, P.; Erwin, B.; N., R. D.; Jurriaan, H., Nanopatterning by an Integrated Process Combining Capillary Force Lithography and Microcontact Printing. Adv. Funct. Mater. **2010**, 20, 663-668, doi: 10.1002/adfm.200901700.

20. Wendeln, C.; Ravoo, B. J., Surface Patterning by Microcontact Chemistry. Langmuir **2012**, 28, 5527-5538, doi: 10.1021/la204721x.

21. Ricoult, S. G.; Nezhad, A. S.; Knapp-Mohammady, M.; Kennedy, T. E.; Juncker, D., Humidified Microcontact Printing of Proteins: Universal Patterning of Proteins on Both Low and High Energy Surfaces. Langmuir **2014**, 30, 12002-12010, doi: 10.1021/la502742r.

22. Andrews, A. M.; Liao, W.-S.; Weiss, P. S., Double-Sided Opportunities Using Chemical Lift-Off Lithography. Acc. Chem. Res. **2016**, 49, 1449-1457, doi: 10.1021/acs.accounts.6b00034.

23. Offenhausser, A.; Bocker-Meffert, S.; Decker, T.; Helpenstein, R.; Gasteier, P.; Groll, J.; Moller, M.; Reska, A.; Schafer, S.; Schulte, P.; Vogt-Eisele, A., Microcontact printing of proteins for neuronal cell guidance. Soft Matter **2007**, 3, 290-298, doi: 10.1039/b607615g.

24. Loget, G.; Corn, R. M., Silica Nanowire Arrays for Diffraction-Based Bioaffinity Sensing. Chem. Eur. J. **2014**, 20, 10802-10810, doi: 10.1002/chem.201304800.

25. Wang, X.; Liu, X.; Wang, X., Surface-relief-gratings based on molecularly imprinted polymer for 2,4-dichlorophenoxyacetic acid detection. Sens. Actuators, B **2015**, 220, 873-879, doi: 10.1016/j.snb.2015.05.112.

26. Avella-Oliver, M.; Carrascosa, J.; Puchades, R.; Maquieira, Á., Diffractive Protein Gratings as Optically Active Transducers for High-Throughput Label-free Immunosensing. Anal. Chem. **2017**, 89, 9002-9008, doi: 10.1021/acs.analchem.7b01649.

27. Avella-Oliver, M.; Ferrando, V.; Monsoriu, J. A.; Puchades, R.; Maquieira, A., A label-free diffraction-based sensing displacement immunosensor to quantify low molecular weight organic compounds. Anal. Chim. Acta **2018**, 1033, 173-179, doi: 10.1016/j.aca.2018.05.060.

28. Egea, A. M. C.; Mazenq, L.; Trevisiol, E.; Paveau, V.; Vieu, C., Optical label free biodetection based on the diffraction of light by nanoscale protein gratings. Microelectron. Eng. **2013**, 111, 425-427, doi: 10.1016/j.mee.2013.05.002.

29. Lee, J.; Icoz, K.; Roberts, A.; Ellington, A. D.; Savran, C. A., Diffractometric detection of proteins using microbead-based rolling circle amplification. Anal. Chem. **2010**, 82, 197-202, doi: 10.1021/ac901716d.

30. Bernard, A.; Renault, J. P.; Michel, B.; Bosshard, H. R.; Delamarche, E., Microcontact Printing of Proteins. Adv. Mater. **2000**, 12, 1067-1070, doi: doi:10.1002/1521-4095(200007)12:14<1067::AID-ADMA1067>3.0.CO;2-M.

31. Yano, Y. F., Kinetics of protein unfolding at interfaces. J. Phys. Condens. Matter **2012**, 24, 503101, doi: 10.1088/0953-8984/24/50/503101.

32. Bernard, A.; Delamarche, E.; Schmid, H.; Michel, B.; Bosshard, H. R.; Biebuyck, H., Printing Patterns of Proteins. Langmuir **1998**, 14, 2225-2229, doi: 10.1021/la980037l.

33. Wasserberg, D.; Nicosia, C.; Tromp, E. E.; Subramaniam, V.; Huskens, J.; Jonkheijm, P., Oriented Protein Immobilization using Covalent and Noncovalent Chemistry on a Thiol-Reactive Self-Reporting Surface. J. Am. Chem. Soc. **2013**, 135, 3104-3111, doi: 10.1021/ja3102133.

34. Coyle, B. L.; Baneyx, F., Direct and reversible immobilization and microcontact printing of functional proteins on glass using a genetically appended silica-binding tag. Chem. Commun. **2016**, 52, 7001-7004, doi: 10.1039/C6CC02660E.

35. Avella-Oliver, M.; Morais, S.; Carrascosa, J.; Puchades, R.; Maquieira, Á., Total Analysis Systems with Thermochromic Etching Discs Technology. Anal. Chem. **2014**, 86, 12037-12046, doi: 10.1021/ac502640j.

36. Escorihuela, J.; Banuls, M. J.; Castello, J. G.; Toccafondo, V.; Garcia-Ruperez, J.; Puchades, R.; Maquieira, A., Chemical silicon surface modification and bioreceptor attachment to develop competitive integrated photonic biosensors. Anal. Bioanal. Chem. **2012**, 404, 2831-2840, doi: 10.1007/s00216-012-6280-4.

37. Halpern, A. R.; Nishi, N.; Wen, J.; Yang, F.; Xiang, C.; Penner, R. M.; Corn, R. M., Characterization of Electrodeposited Gold and Palladium Nanowire Gratings with Optical Diffraction Measurements. Anal. Chem. **2009**, 81, 5585-5592, doi: 10.1021/ac900938t.

38. Heimall, J.; Freeman, A.; Holland, S. M., Pathogenesis of Hyper IgE Syndrome. Clin. Rev. Allerg. Immu. **2010**, 38, 32-38, doi: 10.1007/s12016-009-8134-1.

39. Sato, S.; Yanagida, N.; Ohtani, K.; Koike, Y.; Ebisawa, M., A review of biomarkers for predicting clinical reactivity to foods with a focus on specific immunoglobulin E antibodies. Curr. Opin. Allergy. Clin. Immunol. **2015**, 15, 250-258, doi: 10.1097/aci.0000000000000162.

40. Carballeda-Sangiao, N.; Rodríguez-Mahillo, A. I.; Careche, M.; Navas, A.; Moneo, I.; González-Muñoz, M., Changes over Time in IgE Sensitization to Allergens of the Fish Parasite Anisakis spp. Plos Negl. Trop. Dis. **2016**, 10, e0004864, doi: 10.1371/journal.pntd.0004864.

41. Tay, T. R.; Bosco, J.; Aumann, H.; O'Hehir, R.; Hew, M., Elevated total serum immunoglobulin E (>1000 IU/mL): implications? Intern. Med. J. **2016**, 46, 846-849, doi: 10.1111/imj.13073.

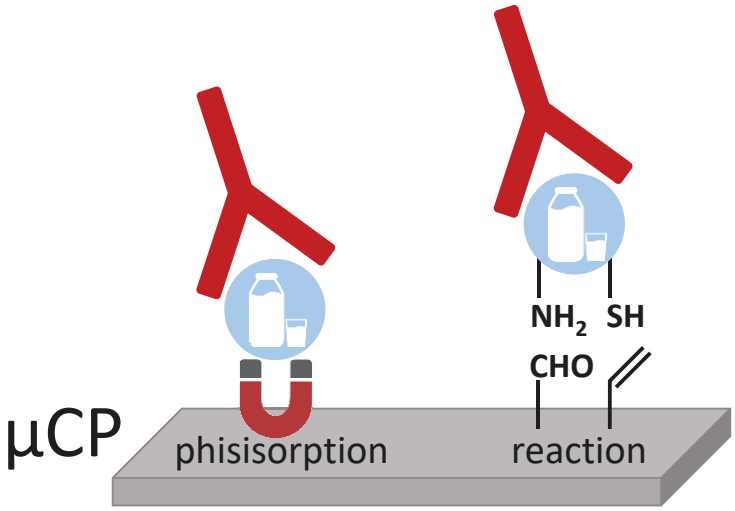

Chapter 1.2: Patterned Biolayers of Protein Antigens for Label free Biosensing in Cow Milk Allergy

Biosensors **2023**, 13(2), 214

biosensors

PATTERNED BIOLAYERS OF PROTEIN ANTIGENS FOR LABEL FREE BIOSENSING IN COW MILK ALLERGY

Augusto Juste-Dolz[1], Estrella Fernández[1], Rosa Puchades[1,2], Miquel Avella Oliver[1,2,*] and Ángel Maquieira[1,2,*]

[1]*Instituto Interuniversitario de Investigación de Reconocimiento Molecular y Desarrollo Tecnológico (IDM), Universitat Politècnica de València, Universitat de València, 46022 Valencia, Spain.*

[2]*Departamento de Química, Universitat Politècnica de València, 46022 Valencia, Spain.*

**Correspondence: miavol@upv.es (Miquel Avella-Oliver), amaquieira@qim.upv.es (Ángel Maquieira).*

ABSTRACT

This paper focuses on creating one-dimensional diffractive grooved structures of antigen proteins on glass substrates for the label-free detection of antibodies to dairy allergens. In particular, the fabrication of protein structures is carried out by combining microcontact printing with physisorption, imines coupling, and thiol-ene click chemistry. The work first sets up these patterning methods and discusses and compares the main aspects involved in them (structure, biolayer thickness, functionality, stability). Homogeneous periodic submicron structures of proteins are created and characterized by diffractive measurements, AFM, FESEM, and fluorescence scanning. Then, this patterning method is applied to proteins involved in cow milk allergy, and the resulting structures are implemented as optical transducers to sense specific immunoglobulins G. In particular, gratings of bovine serum albumin, casein, and β-lactoglobulin are created and assessed, reaching limits of detection in the range of 30–45 ng·mL^{-1} of unlabeled antibodies by diffractive biosensing.

Keywords: diffraction; grating; microcontact printing; casein; bovine serum albumin; β-lactoglobulin; covalent; immunoglobulin G; dairy; beef

1. Introduction

Developing new strategies for patterning biological layers entails nowadays a major scientific interest that leads to appealing bioanalytical developments in a wide range of scenarios [1–4]. Microcontact printing (μCP), often known also as soft lithography, has emerged as a practical method to create functional patterns of biomolecules [5,6]. This is a widely used technique thanks to its simplicity, versatility, and minimal requirements for microfabrication facilities.

As schematized in Figure 1A, μCP relies on a selective transfer of biomolecules using patterned stamps made of an elastomer (typically PDMS), which is usually obtained by replica molding from a pre-patterned master [7,8]. The biomacromolecules incubated on the stamp during the inking stage become adsorbed on the PDMS surface, and in the subsequent stamping step, they are only transferred in the contact areas, thus obtaining a pattern on a solid substrate. The patterning of biological species by μCP is typically mediated by physisorption (Figure 1A) [9,10]. In this case, the transfer efficiency of the biomolecules ultimately depends on their affinity for the substrate material, which should be higher than that for the stamp [11].

μCP can be customized by incorporating functional groups tailored to undergo linking reactions between the inked biomolecules and the surface of the substrates. This strategy introduces patterning alternatives where the transfer during the stamping stage is mainly driven by chemical reactions [12–15]. Developing ways to pattern and control even smaller structures is a crucial aspect of the worldwide focus on nanoscience and nanotechnology. However, despite the extensive attention that μCP has received in the scientific literature, to the best of our knowledge, the implementation of covalent chemistries for patterning submicron (from 0.1 to 1 μm) structures of biomacromolecules remains unexplored [16–21].

Within the biosensing scenario, the fabrication of protein nanostructures points towards exploiting new light-matter phenomena to transduce biorecognition events [22–25]. The increasing incidence of chronic and inflammatory diseases such as allergies supports the development of this kind of nanobiosensors [26]. Particularly, allergies to dairy products are acquiring a special concern since they are prevalent food products in

human nutrition, representing 14% of the caloric intake in developed countries [27]. Among all the constituents present in dairy products, casein and β-lactoglobulin (BLG) are important proteins in cow milk allergy [28,29]. Bovine serum albumin (BSA) is a relevant protein in beef allergy that is also involved in the allergic response to cow milk [29,30]. Along these lines, in addition to their general relevance in immunosensing, immunoglobulins G (IgGs) may also play a key role in allergic diseases [30–33]. IgGs are considered to be part of the normal immune response to foreign antigens [34]. Although the evaluation of specific IgGs in serum has not yet been revealed as having a predictive value in food allergy diagnosis [34], the relation between the IgGs and IgEs levels can be employed to distinguish between persistent and transient food allergies, and it is also considered a predictor for future tolerance [35]. Moreover, the higher levels of IgGs in IgE-mediated allergic processes, together with their long persistence in serum, make them an interesting alternative to study allergies to cow milk.

This work firstly focuses on key aspects in the fabrication of submicron diffractive patterns of protein allergens by μCP on glass surfaces. The role of UV-ozone treatments typically employed to improve protein transfer and the implementation of different patterning chemistries are thoroughly explored, compared, and characterized. Then, from these results, diffractive gratings of three important proteins in cow milk allergy (BSA, casein, and BLG) are fabricated and employed as optical transducers for biosensing. Along these lines, the biorecognition events between the patterned antigens and their target IgGs in solution are characterized and sensed in a label-free format. Insights into the selectivity of the resulting biosensing system, and its potential to avoid non-specific binding issues in the analysis of serum samples, are also provided in this study.

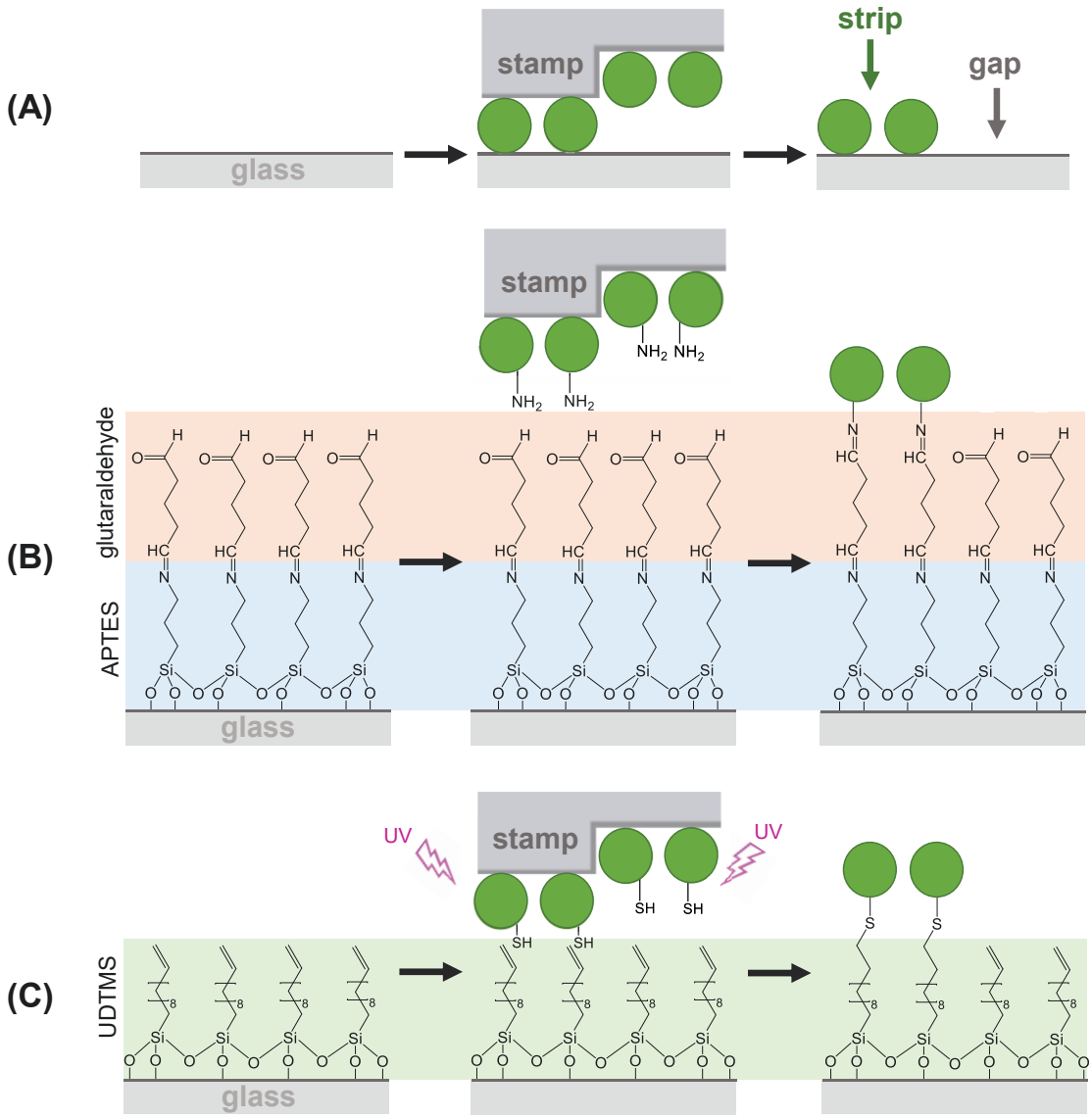

Figure 1. Schemes of the µCP routes investigated in this study for patterning proteins by combining µCP with: **(A)** physisorption, **(B)** imine coupling reaction, and **(C)** thiol-ene click reaction.

2. Materials and Methods

2.1. Materials

Bovine serum albumin (BSA), whole antiserum with anti BSA antibodies produced in rabbit (antiBSA IgG, 3.8 mg·mL^{-1} of specific IgGs), casein and BLG from bovine milk, human serum (male, AB plasma), polysorbate 20 (Tween 20), (3-

aminopropyl)triethoxysilane (APTES), glutaraldehyde, N-hydroxysuccinimide (NHS), N-(3-Dimethylaminopropyl)-N′ -ethylcarbodiimide (EDC), and ethanolamine were supplied by Sigma-Aldrich (Madrid, Spain). Anticasein antibodies (0.33 $mg \cdot mL^{-1}$ of specific IgGs) and antiBLG antibodies (1 $mg \cdot mL^{-1}$ of specific IgGs) were from Ingenasa (Madrid, Spain). 10-undecenyltrimethoxysilane (UDTMS) was purchased from Gelest (Morrisville, Pennsylvania, USA). Toluene was from Scharlau (Barcelona, Spain). Polydimethylsiloxane (PDMS) Sylgard 184 was acquired from Dow Corning (Wiesbaden, Germany) and glass slides (standard line, 25 × 75 × 1.2 mm) were from Labbox (Mataró, Spain). Alexa Fluor 647 antibody labeling kit was from Thermo Fischer (Waltham, Massachusetts, USA). The silicon grooved structure (555.5 nm period, 100 nm groove depth, duty cycle 50%) used as a master for µCP was supplied by LightSmyth (Eugene, OR, USA). Sodium phosphate buffer (PBS, 8 mM Na_2HPO_4, 2 mM KH_2PO_4, 137 mM NaCl, 2.7 mM KCl, pH 7.4) and PBS-T (PBS with polysorbate 20 0.05% *v/v*), were prepared with ultrapure water (Milli-Q, Millipore Iberica, Darmstadt, Germany) and filtered with 0.2 µm polyethersulfone membranes (Merck, Darmstadt, Germany).

2.2. PDMS stamps

To create the PDMS stamps, the Sylgard 184 elastomer was mixed with its curing agent (10 to 1 mix ratio). This mixture was thoroughly homogenized, dispensed onto the structured side of the silicon master, degassed in a vacuum chamber for 30 min, and then polymerized overnight at 60 °C. Next, the cured PDMS was peeled off from the master and cut into 5 × 5 mm squared pieces. The resulting stamps were sonicated three times for 5 min in ethanol (30% in MilliQ water) and dried under an air stream before use.

For the ozone treatment, PDMS stamps were oxidized in an ozone atmosphere generated with a 347 nm UV lamp (UVOH 150 lab, FHR Anlagenbaum GmbH, Ottendorf-Okrilla, Germany).

2.3. Characterization

Static contact angles were measured to evaluate the surface wettability of the glass and PDMS surfaces under study. For that, an optical tensiometer (Attention Theta Lite, Biolin Scientific, Sweden) was employed to calculate the values of purified water droplets (4 μL). Averaged and standard deviation values were calculated from three replicates measured for 10 s.

Fluorescence measurements were carried out by incubating target IgGs labeled with a fluorophore (Alexa Fluor 647) onto the protein patterns. A custom setup consisting of a charge-coupled device camera (Retiga, EXi, Qimaging Inc., Burnaby, Canada) as the detector, and light-emitting diodes (Toshiba TLOH157P, Tokyo, Japan) as the light source was employed to acquire the fluorescence images. The image analysis for fluorescence quantification was performed with the GenePix Pro 4.0 software (Molecular Devices, San José, CA, USA). Averaged and standard deviation values were calculated from the three parallel measurements of each condition.

The topographic characterizations were performed by Field Emission Scanning Electron Microscopy (FESEM) and atomic force microscopy (AFM). For FESEM measurements, PDMS stamps were first coated with a 10 nm layer of palladium using a high vacuum coater (Leica EM MED020, Leica Microsystems, Wetzlar, Germany) and then they were analyzed using a ZEISS ULTRA-55 scanning electron microscope (ZEISS, Oxford instruments). AFM measurements of both PDMS stamps and protein patterns were performed with a Bruker Multimode 8 microscope (Bruker, Massachusetts, USA) using RFESPA probes (MPP-21120–10, Bruker). Averaged cross-section profiles were calculated from the resulting AFM images employing the Nanoscope Software. A second-order polynomial flattening was applied to each image and the height was averaged along the longitudinal direction of the pattern strips. The period of the structures was calculated as the sum of the average width of the strips and the average width of the gaps between them. The duty cycle was calculated as the average width of the strips, multiplied by 100, and divided by the period.

2.4. Diffractive measurements

In this study, diffractive measurements were performed to assess the structural features of the PDMS stamps and the protein patterns. This detection principle (herein called diffractive biosensing) requires that the measured structures are periodic and that they fulfill the Bragg condition to diffract an incident laser beam. In this case, one-dimensional diffraction grating structures with a submicron-range periodicity (555 nm) were employed, since they split incident laser beams of visible light into multiple beams (called diffraction orders) distributed in a single row, which simplifies the detection setup and the optical measurements. The intensity of the diffraction orders decreases if the periodic features of the measured structure worsen. Moreover, this intensity increases together with the contrast in height and/or refractive index between the strips and gaps of the grooved structures (Figure 1A). Along these lines, the binding events between the patterned protein and specific antibodies increase the amount of biological matter in the grating strips, which enhances this contrast and increments the intensity of the diffraction orders. As a result, this detection principle provides useful information on the thickness and periodic features of the measured structures and enables quantifying biorecognition assays.

The diffractive response was evaluated using a custom optomechanical setup arranged as illustrated in Figure 2A. It comprises a collimated and attenuated (95%) 532 nm diode laser (100 mW, MGL-III-532, CNI, Changchun, China), and a holder which clamps the diffractive samples (PDMS stamps and protein patterns on glass slides) and fixthem to be orthogonally irradiated by the laser beam. The setup also includes a monochromatic CMOS camera (1 ms of exposure time, Edmund eo-1312m, York, UK) and planar silicon photodiodes (SLC-61N2, Silonex Inc., Montreal, Canada) to measure the intensity of the zeroth and the first diffraction orders coming from the diffractive structures. The diffraction efficiency was calculated as the light intensity of the first diffracted order divided by the light intensity of the incident laser beam. Averaged and standard deviation values were calculated from the measurement of three different replicates of each sample.

2.5. Surface functionalization

The glass slides used as substrates were washed by sonication (5 min) in ethanol (30% in milli-Q water) and dried under a stream of air. To functionalize their surface, they were irradiated with a 347 nm UV-lamp (UVOH 150 lab, FHR Anlagenbaum GmbH, Ottendorf-Okrilla, Germany) for ten minutes to generate hydroxyl groups (Figure S1A). Then, the hydroxyl-activated substrates were immersed into 1% (*v/v*) solutions of organosilanes (UDTMS or APTES) in toluene for 30 min and under orbital agitation. After silanization, the substrates were rinsed with acetone and air-dried. Thereafter, substrates were cured at 80 °C for 30 min, rinsed with acetone, and dried as before.

Before protein patterning, aminated substrates (functionalized with APTES) were immersed into a 2.5% solution of glutaraldehyde in PBS for 30 min (Figure S2) [16]. After immersion, the substrates were rinsed with MilliQ water and air-dried.

2.6 Protein patterning

Submicron structures of BSA, casein, and BLG were fabricated by microcontact printing (Figure 2B). The inking and stamping conditions were adapted from previous studies [9]. For the inking, solutions of BSA, casein, and BLG in PBS (250 $\mu g \cdot mL^{-1}$, 40 µL) were incubated for 160 min at room temperature (22 °C) onto the structured side of the stamps. Then, the stamps were rinsed with Milli-Q water and dried under a stream of air. To perform the stamping stage, the structured side of the inked stamps was placed in contact with the surface of the glass substrates (unmodified or functionalized) for 20 min. In the substrates modified with UDTMS, the stamps were then irradiated with the UV lamp during the stamping stage to conduct the thiol-ene click reaction. Finally, the stamps were removed, and the substrates were rinsed with MilliQ water and dried as before.

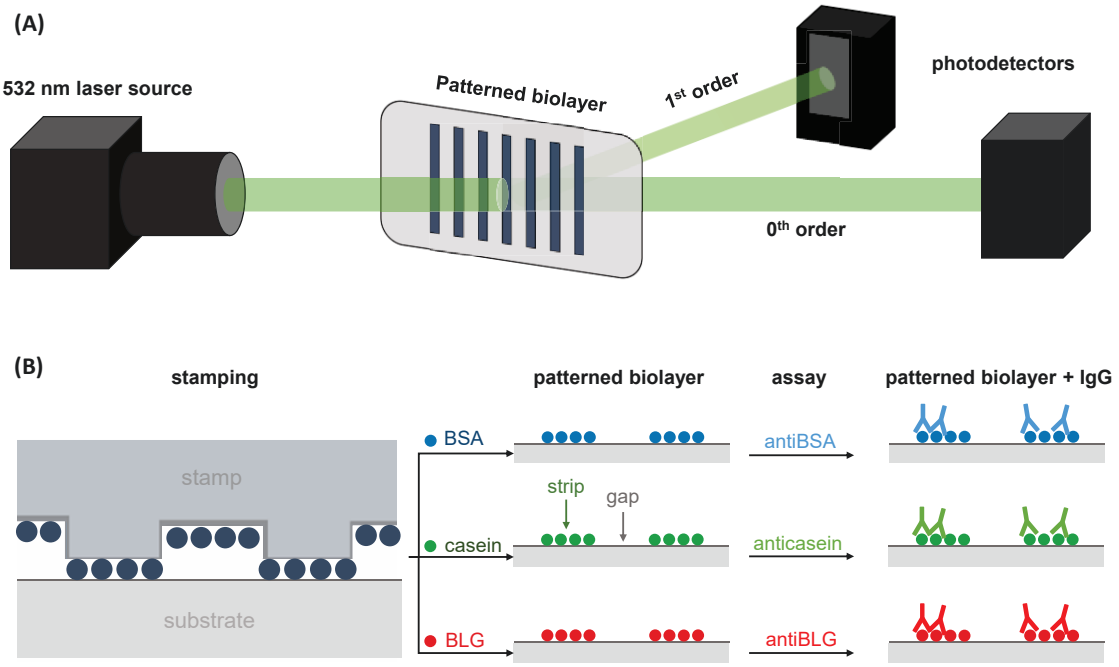

Figure 2. Schemes of **(A)** the optical setup employed to perform the diffraction measurements and **(B)** the fabrication by µCP of the BSA, casein, and BLG patterns employed for the quantification of specific IgG.

2.7. Biorecognition assays

Custom adhesive polymeric masks were adhered to the glass substrates to create open cells to incubate 50 µL of IgG solutions in PBS-T to perform the assays (Figure 2B). In addition, Alexa 647-labeled anti-BSA rabbit IgGs were incubated to assess the protein patterns by fluorescence. After 20 min of incubation, the substrates were rinsed with PBS-T and MiliQ water and dried under a stream of air. Limits of detection (LOD) and quantification (LOQ) were calculated from the trend fitted to the experimental data of the dose-response curves. The LOD was determined as the concentration associated to the mean signal of ten blank measurements plus three times their standard deviation. The LOQ was determined as the concentration related to the mean signal of ten blank measurements plus ten times their standard deviation. The linear range was calculated as the concentration interval above the LOQ that displays a correlation coefficient value (R^2) of at least 0.99 when the experimental results are fitted to a linear trend

3. Results and Discussion

3.1. PDMS activation

The hydrophilicity of the PDMS surface is an important aspect of the performance of μCP [21], and the UV-ozone treatment of PDMS is a well-established strategy to modulate this parameter. It is reported that the ozone produced by UV-irradiation of molecular oxygen reacts with the non-polar methyl groups at the PDMS surface and increases its hydrophilicity by introducing polar SiO_x groups [36,37]. The incorporation of this oxidation stage has demonstrated to be an effective way to improve the transfer rate of biomacromolecules for creating biolayer patterns constituted by features above the micron range [38]. However, this UV irradiation involves critical aspects to pattern biomacromolecules by μCP in the submicron range and below. In addition, characterizing this surface transformation is important to introduce UV-mediated chemical couplings in μCP, as investigated in the next section.

PDMS stamps were created from a grooved silicon master defined by a period of 555.5 nm, a groove depth of 100 nm, and a duty cycle of 50%. To assess the effect of the UV-ozone treatment on these submicrometric patterns, the PDMS stamps were exposed to different irradiation times, and the resulting surfaces were characterized by different techniques. First, we studied the static contact angle of water droplets on the grooved surface to quantify the changes in surface hydrophilicity. As shown in Figure 3A (top), the contact angle of the PDMS stamps decreases linearly from 130 ± 2° to 87 ± 3° when the exposure time increases. This trend indicates that the hydrophilicity of this surface increases together with its exposure to ozone, as is expected to improve the protein transfer by μCP. Note that the grooved structure of this surface confers a higher contact angle (130 ± 2°) than that reported in the literature for untreated PDMS (105°) [36].

Then, the effect of this treatment on the submicron features of the PDMS was assessed by diffractive measurements. The grooved pattern on these PDMS surfaces diffracts when irradiated with a 532 nm laser beam, and the efficiency of this diffraction ultimately depends on the features that define the grooved pattern (period, depth, homogeneity, etc.). Therefore, changes in the overall structural features can be monitored through the diffraction efficiency. The experimental results (Figure 3A,

bottom) show that the stamps keep their original surface topography for exposure times of up to one minute since the PDMS structures display the maximal diffractive response. However, a dropping trend in the diffraction efficiency is observed beyond this exposure time, which indicates a substantial modification of the pattern.

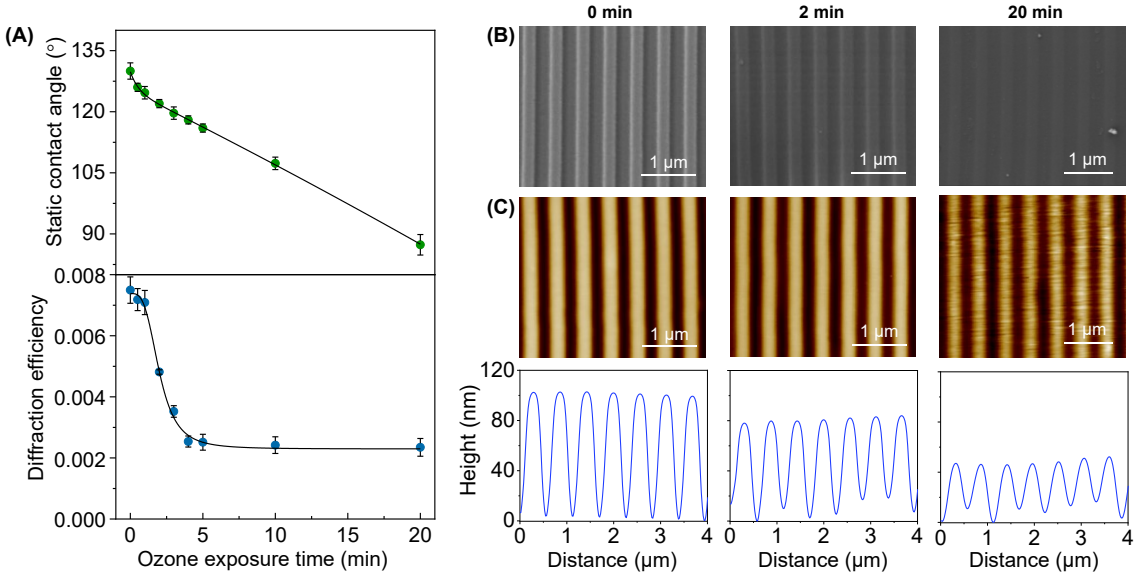

Figure 3. Effect of the UV-ozone exposure on the PDMS grooved structure. **(A)** Evolution of the surface hydrophobicity (top) and the diffractive response (bottom) for increasing exposure times. **(B)** FESEM images (see Figure S3 for larger scans). **(C)** AFM images (top) and their corresponding height profiles (bottom).

The FESEM images of the resulting PDMS stamps reveal that they keep their structural homogeneity even after 20 min of exposure (Figure 3B), and both the period and the duty cycle correlate well with the original values (Table S1). However, these images suggest a decrease in the groove depth, which was confirmed and quantified by AFM. As observed in Figure 3C, the grooves on untreated PDMS stamps display a depth of 99 ± 1 nm. However, the UV-ozone treatment progressively decreases this depth, reaching a value of 39 ± 6 nm at 20 min (Table S1).

Therefore, these results reveal that the UV-ozone exposure times that introduce substantial hydrophilicity changes that favor the protein transfer, also lead to structural losses on the submicron relief needed for the biolayer patterning. This depth decrease

favors undesired roof collapse deformations during the stamping stage [39], and its negative effect on the resulting submicron patterns of biolayers is proved in the next section (Figure 4). From these results, exposure times below two minutes were selected in the next steps of this study.

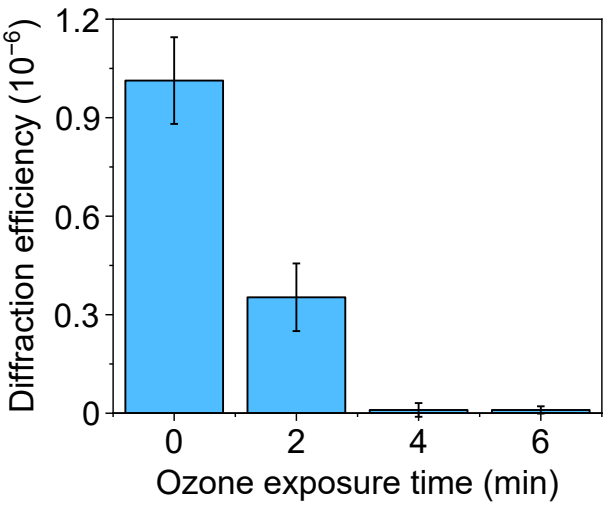

Figure 4. Diffraction efficiency of protein patterns fabricated by µCP on glass, with PDMS stamps treated by different UV-ozone exposure times before the inking.

3.2. Patterning chemistries

In addition to classical µCP strategies based on physisorption, alternative chemical couplings can also be implemented to attach the patterned biomolecules to the host substrate. In this section, we explore and compare different physisorption and covalent ways to create submicron one-dimensional patterns of proteins by µCP, using BSA as a representative model system.

In physisorption, the transfer of inked proteins is mainly driven by weak forces such as electrostatic and Van der Waals interactions [18]. As reported above, UV-ozone treatments of the PDMS may lead to structural changes that compromise the µCP performance in submicron patterning. In addition to decreasing the depth of the grooves (Figure 3C), the submicron BSA patterns obtained with treated stamps deteriorate when the UV-ozone exposure time increases, since their diffraction efficiency decays drastically with the exposure time (Figure 4). From these results, we

addressed this patterning using untreated stamps. As shown in Figure 5, a grooved structure that matches the structural features of the employed stamp is obtained (Tables S1 and S2). The resulting thickness of the patterned proteins (3.3 ± 0.4 nm) suggests a surface density close to a monolayer in the grating strips and agrees with the magnitude of the diffracted efficiencies measured (Figure 4) [40,41].

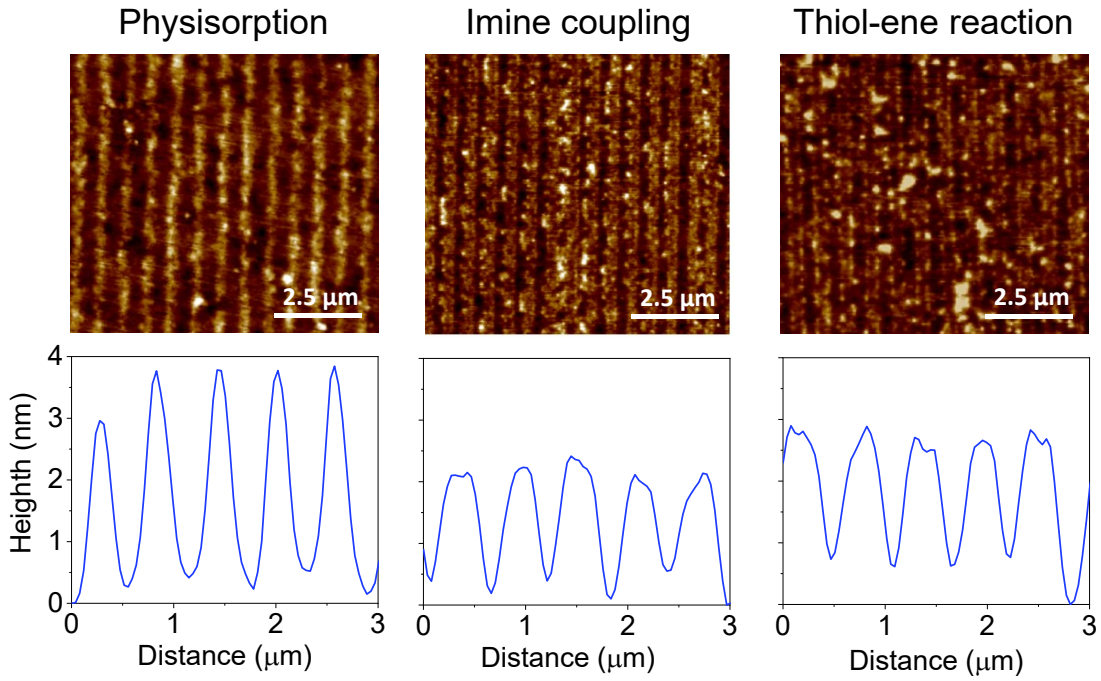

Figure 5. AFM images and height profiles of protein patterns fabricated by µCP combined with physisorption, imine coupling, and thiol-ene reaction.

Then, we explored the combination of µCP with the imine formation between amines and aldehydes to covalently attach submicron patterns of proteins on the surfaces (Figure 1B). First, we observed that the inking stage with organosilanes degrades the submicron structure of the stamp (Figure S4). Therefore, BSA proteins were stamped on glass substrates previously treated with APTES, together with glutaraldehyde as a crosslinking reagent (Figure 1B). As shown in Figure 5, the aimed striped pattern is obtained by this approach, whose averaged strip thickness (2.0 ± 0.3 nm) indicates a slightly lower surface density of the patterned proteins than that obtained by physisorption (Table S2). A potential biosensing drawback of this imine coupling is that part of the aldehyde groups remains active after the patterning, and this issue is

successfully solved by treating the protein patterns with aminated blocking agents before the incubation of the sample (Figure S5).

We also explored the combination of µCP with the thiol-ene click reaction by stamping BSA proteins on glass surfaces silanized with UDTMS, and then irradiating UV light during the stamping (Figure 1C). We observed that this irradiation involves three key phenomena in the resulting structures: the magnitude of the coupling, the loss of the stamp relief, and the denaturation of the patterned proteins. As shown in Figure S6, 1 min of UV irradiation is a suitable condition for the µCP thiol-ene patterning. The desired stripped protein patterns are obtained in these conditions and display an averaged thickness (2.1 ± 0.3 nm) similar to that achieved by imine coupling (Figure 5 and Table S2). Besides, the patterns fabricated without irradiation (Figure 6, 0 min) involve negligible diffraction efficiencies, revealing minor protein physisorption on the glass surfaces treated with UDTMS.

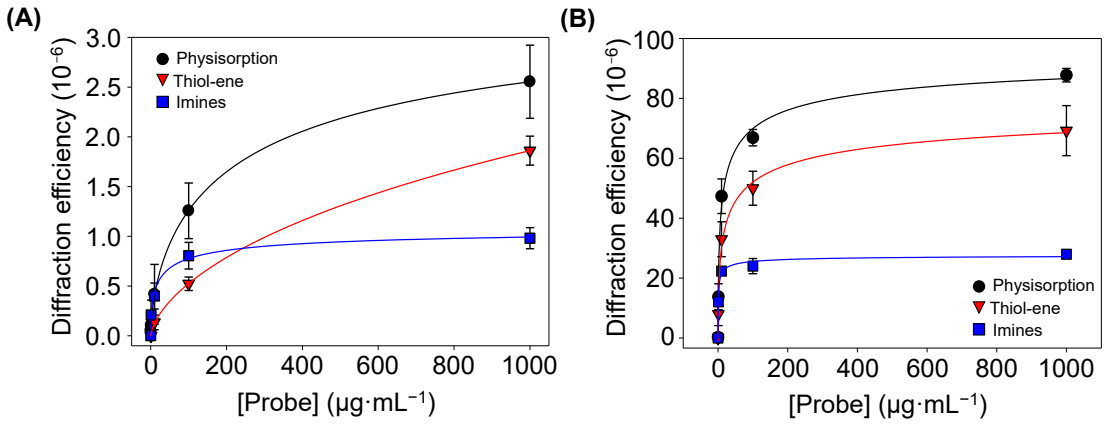

Figure 6. Diffraction efficiencies of the BSA patterns (A) before and (B) after incubating specific antiBSA IgG (10 µg·mL^{-1}), created by increasing concentrations of BSA in the inking solutions. All trends correlated well with 4-parameter logistic curves (R^2 = 0.998). See Figure S7 for a zoomed view of both graphs in their low concentration range.

Finally, the amount of BSA proteins patterned by physisorption, imine coupling, and thiol-ene reaction were compared. For that, increasing concentrations of BSA were employed as inking solutions, and then the diffraction efficiency of each pattern was measured (Figure 6A). At low concentrations (0–10 µg·mL^{-1}), the physisorption and

imine approaches displayed similar responses (Figure S7). However, for higher protein concentrations, the diffraction efficiency of the patterns fabricated by physisorption was about 2.5 and 1.5 times greater than that for imine coupling and thiol-ene reaction, respectively. These results suggest that a higher number of proteins is transferred to the substrate by μCP combined with physisorption, which also correlates with the strip thicknesses observed in Figure 5.

3.3. Bioanalytical performance

Proteins can undergo significant conformational changes during the inking and stamping steps of μCP. Moreover, their native conformational structure can also be considerably altered when patterned in the host surface, even leading to functionality losses [11]. This issue can be especially critical in covalent attachment, given that the chemical composition of the proteins is also affected. This section first assesses the functionality of the BSA structures fabricated by the different μCP approximations through their binding capacity with specific antiBSA IgGs. A polyclonal whole antiserum is used in this study as antiBSA, which provides insights into the applicability of these diffractive protein patterns in biological samples.

The diffractive response after incubating specific IgGs onto patterns fabricated with different inking concentrations of protein was measured. In this experiment (Figure 6B), the diffraction efficiency is significantly higher than that observed without IgGs incubation (Figure 6A), being maximal for the patterns fabricated by passive adsorption. It may be due to the fact that albumins, such as BSA, present high immobilization strengths when physisorbed in both hydrophilic and hydrophobic surfaces [40]. These results demonstrate that these proteins keep their functionality after the patterning and they bind their target IgGs, which increases the biolayer thickness (Figure S8) and enhances the diffraction efficiency.

These results also highlight the potential of these patterns to become diffractive transducers to quantify biorecognition events in label-free format. To explore the biosensing capabilities of this approach, the diffractive response of BSA patterns fabricated by μCP combined with passive adsorption was analyzed after incubating with

increasing concentrations of specific IgGs. As shown in Figure 7, well-correlated trends were obtained in the dose-response curve of this immunoassay. A limit of detection of 30 ng·mL^{-1} and a limit of quantification of 68 ng·mL^{-1} of unlabelled IgGs, and a linear range between 68 and 870 ng·mL^{-1}, are inferred from these results (Table 1).

Then, the same patterning procedure as before was applied to create diffractive gratings of the casein and BLG (Figure 2B). Those proteins are present at high concentrations in cow milk, about 32 mg·mL^{-1} for casein and 2 mg·mL^{-1} for BLG [42], being important allergens in dairy products [28,29]. Well-correlated dose-response curves in the application of these protein patterns for immunosensing specific anticasein and antiBLG IgGs are also obtained in these cases (Figure 7A). On the other hand, slightly higher limits of detection and quantification, 35 and 111 ng·mL^{-1} for anticasein together with 44 and 302 ng·mL^{-1} for antiBLG, are displayed by these systems (Table 1). This higher sensitivity obtained in the antiBSA immunoassay may be favored by the intrinsic great immobilization properties of albumins on solid substrates [40]. As observed in Table 2, representative LOD values in the state-of-the-art for the quantification of specific IgGs cover concentrations from 0.1 to 280 ng·mL^{-1} in immunoassays based on different labelling and signal development strategies. On the other hand, label-free approaches introduce important analytical advantages, while higher LODs are typically reached with these systems. The detection and quantification limits reported in this work are in the range of other recent optical immunosensing development for IgGs (Table 2), especially those that enable label-free detection. Those are promising sensitivities considering that the detection system in this study is still in its first steps of development, even though there are highly sensitive label-based and label-free approaches for the detection of specific IgGs in the state-of-the-art.

An important issue when analyzing biological samples in label-free conditions is the presence of eventual unspecific interactions (adsorption, cross-reactivity, etc) in the sensing surface. These interactions are prone to introduce undesired signal contributions that cannot be discriminated from the specific biorecognition events. To explore this phenomenon in our biosensing approach, we first evaluated potential cross-reactivities by assessing the diffractive response of the patterns upon the incubation of high concentrations (10 µg·mL^{-1}) of antiBSA, anticasein, and antiBLG IgGs. As shown in

Figure 7B, the incubation of anticasein and antiBLGA IgGs in BSA patterns displayed a negligible enhancement of the diffracted signals, reaching values in the same order as the one obtained after the incubation of buffer solution. Besides, the incubation of antiBSA IgG produced a substantial increment in the diffraction efficiency. In the same line, the diffraction efficiency of casein and BLG patterns was only enhanced after incubating their specific antibodies, which points out the analytical selectivity of this system.

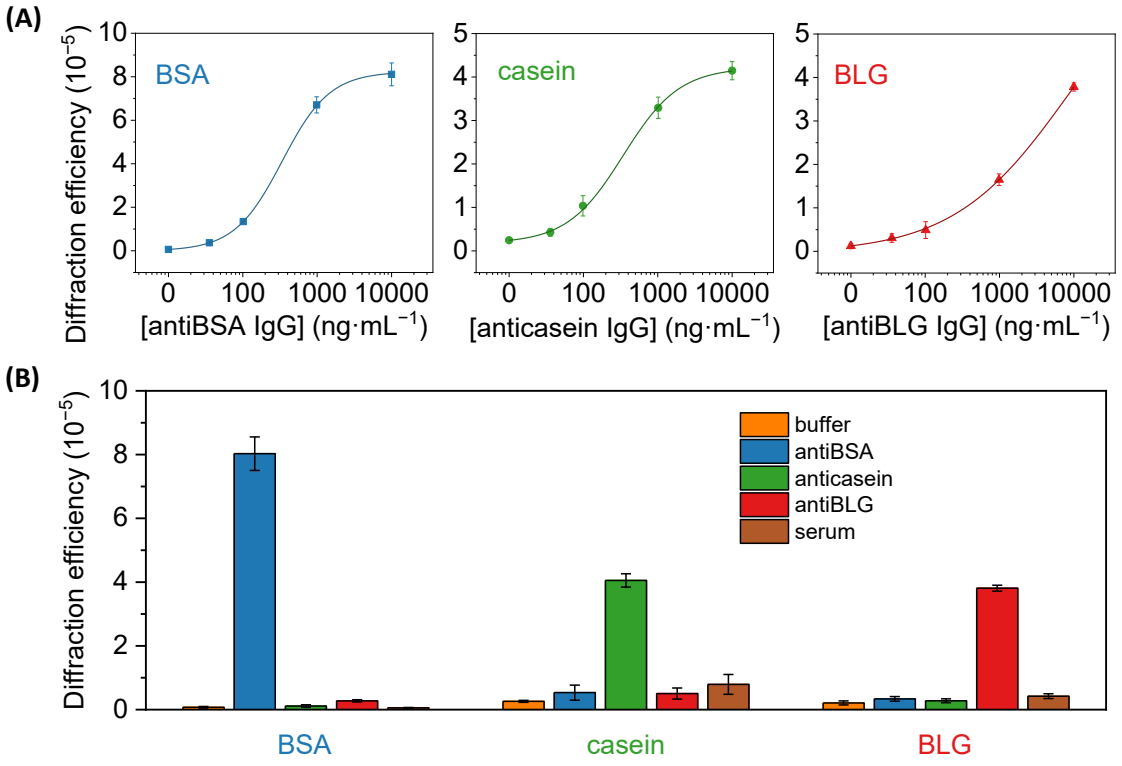

Figure 7. (A) Dose-response immunoassay curves obtained with diffractive patterns of BSA, casein, and BLG, after the incubation of a range of concentrations of specific IgG solutions (antiBSA, anticasein, and antiBLG, respectively). Experimental data were fitted to a sigmoidal regression (4-parameter logistic, $R^2 = 0.999$ in all cases). See Figure S9 for a zoomed view of the graphs in their low concentration range. **(B)** Diffraction efficiencies achieved in BSA, casein and BLG patterns after incubating PBST (buffer), 10 µg·mL^{-1} of specific antiBSA, anticasein and antiBLG antibodies in buffer, and human serum.

The signal contribution due to non-specific adsorptions of undesired species that can be present in real samples was also assessed for this biosensing system. A unique feature

of diffractive biosensing is the ability to minimize the signal contribution of non-specific bindings since the adsorption of non-specific species is a random process prone to take place evenly in the strips and the gaps of the protein patterns [23,43]. Therefore, even if non-specific adsorption takes place onto the protein structures, it does not increase the periodic modulation that conforms the gratings and the contribution of the non-specific binding to the diffraction efficiency is minimal. To explore this issue, we incubated pure human serum with a high concentration of non-specific species onto the protein patterns. As observed in Figure 7B, these serum incubations generated diffracted signals 0.8, 3 and 2 times higher than their corresponding incubations of blank solutions in the anti-BSA, anti-casein and anti-BLG assays, respectively. Those results offer promising insights into solving non-specific binding issues in the prospective application of these antigen patterns to analyze target biomolecules present in serum samples.

From a general perspective, these biomolecular gratings can sense different kinds of immunoglobulins (G, E, M, and A) present in a sample. In this first approximation, the analytical results can quantify the concentration of a mix of immunoglobulin classes. However, note that this biosensing approach is compatible with the discrimination of IgGs, for example by including an additional incubation of secondary antibodies (antiIgG, antiIgE, antiIgA, etc.) in the assay. This work also introduces the basis to exploit the high versatility of µCP to fabricate patterns of a broad range of biomolecules. For example, diffractive structures of antibodies can be patterned by µCP to detect the presence of allergens in dairy products. This configuration should take into account the potential activity loss undergone by antibodies when patterned by µCP, together with the introduction of alternative stamping strategies to overcome this issue [11]

Table 1. Limits of detection and quantification calculated from the experimental trends.

IgG	LOD (ng·mL^{-1})	LOQ (ng·mL^{-1})	Linear range (ng·mL^{-1})
antiBSA	30	68	68-425
anticasein	35	111	111-450
antiBLG	44	302	302-1525

* see Table S3 for the linear relationships between the antigens and the antibodies.

Table 2. Comparative table of limits of detection reported by recent optical bioanalytical developments in the scientific literature for sensing IgGs.

Technique	label	target	LOD (ng·mL^{-1})	Ref.
microarray	HRP/TMB	anticasein IgG	129	[44]
ELISA	HRP/TMB	human antiN antigen IgG	16	[45]
ELISA	HRP/TMB	human antiS antigen IgG	12.5	[45]
PMNIA[a]	Gold NPs[a]	human antiS antigen IgG	7	[46]
		human antiN antigen IgG	17	
		human antiInfluenza A IgG	30	
microarray	HRP/TMB	human antiInfluenza B IgG	280	[47]
		human anti adenovirus IgG	110	
		Human antiRSV[a] IgG	12	
ELISA	HRP/TMB	anti Sap2[a] IgG	0.0011	[48]
SERS-based LFIA[a]	GERTs[a]	human antiSARS-CoV-2 IgG	0.1	[49]
LFIA	Gold NPs[a]	human antiEbola Virus IgG	200	[50]
LSPR[a]	free	human antiS antigen IgG	0.08	[51]
focal molography	free	antiBSA IgG	200	[23]
1D photonic crystal	free	antihuman IgG	28	[52]
diffractive biosensing	free	antiBSA IgG	30	this work
diffractive biosensing	free	anticasein IgG	35	this work
diffractive biosensing	free	antiBLG IgG	44	this work

[a] PMNIA: porous MNs and immunochromatographic assay, NPs: nanoparticles, RSV: respiratory sinctial virus, Sap2: secreted aspartyl proteinase 2, SERS: surface-enhanced Raman spectroscopy,

LFIA: lateral flow immunoassay, GERTs: gap-enhanced Raman tags, LSPR: localized surface plasmon resonance.

4. Conclusions

This investigation focuses on submicron patterns of allergen proteins created by different microcontact printing (μCP) chemistries and their application to detect antibodies involved in dairy allergies. The study demonstrates that exposing the PDMS stamps to UV-ozone before the inking may compromise their performance when patterning at the submicron scale. Moreover, the conditions required to pattern organosilanes by μCP also damage the relief of the stamp, whereas marrying μCP with physisorption, imines reaction, and thiol-ene coupling is a successful strategy to pattern proteins at this scale. In the thiol-ene approach, the irradiation time is a critical parameter to reach maximal couplings, keep the pattern structure, and avoid protein denaturation. Homogeneous patterns of periodic protein strips (about 280 nm wide and 2–3 nm tall) are obtained in all the cases, which present great potential as diffractive transducers for label-free biosensing. Functional submicron patterns of allergen proteins involved in cow milk allergy can be created and used to sense specific immunoglobulins G in solution. In particular, this work provides insights into their implementation in bovine serum albumin, casein, and β-lactoglobulin, displaying limits of detection of 30, 35, and 44 $ng \cdot mL^{-1}$, respectively. In addition to IgGs, these results introduce the basis for the prospective fabrication and application of these diffractive structures to sense other immunoglobulins and macromolecules involved in dairy and other food allergies.

Author contributions

Conceptualization, A.J.-D. and M.A.-O.; Investigation, A.J.-D. and M.A.-O.; Writing—Original Draft Preparation, A.J.-D., E.F. and M.A.-O. Writing—Review & Editing, A.J.-D., E.F., R.P., M.A.-O. and A.M.; Supervision, R.P. and A.M.; Funding Acquisition, R.P., M.A.-O. and A.M.

Funding

Grant PID2019-110713RB-I00 funded by MCIN/AEI/10.13039/501100011033 and cofunded by ‘‘ERDF A way of making Europe’’, Generalitat Valenciana (PROMETEO/2020/094), and Universitat Politècnica de València (PAID-06-22).

Institutional review board statement

Not applicable

Informed consent statement

Not applicable

Data availability statement

The data presented in this study are available on request from the corresponding author. The data are not publicly available due to privacy restrictions.

Conflicts of interest

The authors declare no conflict of interest.

References

1. Shukla, A.; Slater, J.H.; Culver, J.C.; Dickinson, M.E.; West, J.L. Biomimetic Surface Patterning Promotes Mesenchymal Stem Cell Differentiation. *ACS Appl. Mater. Interfaces* **2016**, *8*, 21883–21892. https://doi.org/10.1021/acsami.5b08978.
2. Martinez-Rivas, A.; González-Quijano, G.K.; Proa-Coronado, S.; Séverac, C.; Dague, E. Methods of Micropatterning and Manipulation of Cells for Biomedical Applications. *Micromachines* **2017**, *8*, 347. https://doi.org/10.3390/mi8120347.

3. Wang, L.S.; Gopalakrishnan, S.; Rotello, V.M. Tailored Functional Surfaces Using Nanoparticle and Protein "Nanobrick" Coatings. *Langmuir* **2019**, *35*, 10993–11006. https://doi.org/10.1021/acs.langmuir.8b03235.

4. Kolodziej, C.M.; Maynard, H.D. Electron-Beam Lithography for Patterning Biomolecules at the Micron and Nanometer Scale. *Chem. Mater.* **2012**, *24*, 774–780. https://doi.org/10.1021/cm202669f.

5. Voskuhl, J.; Brinkmann, J.; Jonkheijm, P. Advances in Contact Printing Technologies of Carbohydrate, Peptide and Protein Arrays. *Curr. Opin. Chem. Biol.* **2014**, *18*, 1–7. https://doi.org/10.1016/j.cbpa.2013.10.022.

6. Sauer, U. Analytical Protein Microarrays: Advancements towards Clinical Applications. *Sensors* **2017**, *17*, 256. https://doi.org/10.3390/s17020256.

7. Khadpekar, A.J.; Khan, M.; Sose, A.; Majumder, A. Low Cost and Lithography-Free Stamp Fabrication for Microcontact Printing. *Sci. Rep.* **2019**, *9*, 1024. https://doi.org/10.1038/s41598-018-36521-x.

8. Wang, B.; Koo, B.; Huang, L.W.; Monbouquette, H.G. Microbiosensor Fabrication by Polydimethylsiloxane Stamping for Combined Sensing of Glucose and Choline. *Analyst* **2018**, *143*, 5008–5013. https://doi.org/10.1039/c8an01343h.

9. Avella-Oliver, M.; Ferrando, V.; Monsoriu, J.A.; Puchades, R.; Maquieira, A. A Label-Free Diffraction-Based Sensing Displacement Immunosensor to Quantify Low Molecular Weight Organic Compounds. *Anal. Chim. Acta* **2018**, *1033*, 173–179. https://doi.org/10.1016/j.aca.2018.05.060.

10. Offenhäusser, A.; Böcker-Meffert, S.; Decker, T.; Helpenstein, R.; Gasteier, P.; Groll, J.; Möller, M.; Reska, A.; Schäfer, S.; Schulte, P.; et al. Microcontact Printing of Proteins for Neuronal Cell Guidance. *Soft Matter* **2007**, *3*, 290–298. https://doi.org/10.1039/b607615g.

11. Juste-Dolz, A.; Avella-Oliver, M.; Puchades, R.; Maquieira, A. Indirect Microcontact Printing to Create Functional Patterns of Physisorbed Antibodies. *Sensors* **2018**, *18*, 3163. https://doi.org/10.3390/s18093163.

12. Wendeln, C.; Ravoo, B.J. Surface Patterning by Microcontact Chemistry. *Langmuir* **2012**, *28*, 5527–5538. https://doi.org/10.1021/la204721x.

13. Ravoo, B.J. Microcontact Chemistry: Surface Reactions in Nanoscale Confinement. *J. Mater. Chem.* **2009**, *19*, 8902–8906. https://doi.org/10.1039/b908564e.

14. Lamping, S.; Buten, C.; Ravoo, B.J. Functionalization and Patterning of Self-Assembled Monolayers and Polymer Brushes Using Microcontact Chemistry. *Acc. Chem. Res.* **2019**, *52*, 1336–1346. https://doi.org/10.1021/acs.accounts.9b00041.

15. Bañuls, M.J.; González-Martínez, M.Á.; Sabek, J.; García-Rupérez, J.; Maquieira, Á. Thiol-Click Photochemistry for Surface Functionalization Applied to Optical Biosensing. *Anal. Chim. Acta* **2019**, *1060*, 103–113. https://doi.org/10.1016/j.aca.2019.01.055.

16. Sancho-Fornes, G.; Avella-Oliver, M.; Carrascosa, J.; Fernandez, E.; Brun, E.M.; Maquieira, Á. Disk-Based One-Dimensional Photonic Crystal Slabs for Label-Free Immunosensing. *Biosens. Bioelectron.* **2019**, *126*, 315–323. https://doi.org/10.1016/j.bios.2018.11.005.

17. Rozkiewicz, D.I.; Kraan, Y.; Werten, M.W.T.; De Wolf, F.A.; Subramaniam, V.; Ravoo, B.J.; Reinhoudt, D.N. Covalent Microcontact Printing of Proteins for Cell Patterning. *Chem. A Eur. J.* **2006**, *12*, 6290–6297. https://doi.org/10.1002/chem.200501554.

18. Hu, S.; Chen, T.H.; Zhao, Y.; Wang, Z.; Lam, R.H.W. Protein-Substrate Adhesion in Microcontact Printing Regulates Cell Behavior. *Langmuir* **2018**, *34*, 1750–1759. https://doi.org/10.1021/acs.langmuir.7b02935.

19. Buhl, M.; Vonhören, B.; Ravoo, B.J. Immobilization of Enzymes via Microcontact Printing and Thiol-Ene Click Chemistry. *Bioconjug. Chem.* **2015**, *26*, 1017–1020. https://doi.org/10.1021/acs.bioconjchem.5b00282.

20. Wendeln, C.; Rinnen, S.; Schulz, C.; Arlinghaus, H.F.; Ravoo, B.J. Photochemical Microcontact Printing by Thiol−Ene and Thiol−Yne Click Chemistry. *Langmuir* **2010**, *26*, 15966–15971. https://doi.org/10.1021/la102966j.

21. Trimbach, D.C.; Stapert, H.; Van Orselen, J.; Jandt, K.D.; Bastiaansen, C.W.M.; Broer,

D.J. Improved Microcontact Printing of Proteins Using Hydrophilic Thermoplastic Elastomers as Stamp Materials. *Adv. Eng. Mater.* **2007**, *9*, 1123–1128. https://doi.org/10.1002/adem.200700282.

22. Juste-Dolz, A.; Delgado-Pinar, M.; Avella-Oliver, M.; Fernández, E.; Pastor, D.; Andrés, M. V.; Maquieira, Á. BIO Bragg Gratings on Microfibers for Label-Free Biosensing. *Biosens. Bioelectron.* **2021**, *176*, 112916. https://doi.org/10.1016/j.bios.2020.112916.

23. Gatterdam, V.; Frutiger, A.; Stengele, K.P.; Heindl, D.; Lübbers, T.; Vörös, J.; Fattinger, C. Focal Molography Is a New Method for the in Situ Analysis of Molecular Interactions in Biological Samples. *Nat. Nanotechnol.* **2017**, *12*, 1089–1095. https://doi.org/10.1038/nnano.2017.168.

24. Blickenstorfer, Y.; Borghi, L.; Reichmuth, A.M.; Fattinger, C.; Vörös, J.; Frutiger, A. Total Internal Reflection Focal Molography (TIR-M). *Sens. Actuators B Chem.* **2021**, *349*, 130746. https://doi.org/10.1016/j.snb.2021.130746.

25. Avella-Oliver, M.; Carrascosa, J.; Puchades, R.; Maquieira, Á. Diffractive Protein Gratings as Optically Active Transducers for High-Throughput Label-Free Immunosensing. *Anal. Chem.* **2017**, *89*, 9002–9008. https://doi.org/10.1021/acs.analchem.7b01649.

26. Aquino, A.; Conte-Junior, C.A. A Systematic Review of Food Allergy: Nanobiosensor and Food Allergen Detection. *Biosensors* **2020**, *10*, 194. https://doi.org/10.3390/bios10120194.

27. Muehlhoff, E.; Bennet, A.; McMahon, D. (Eds.) *Milk and Dairy Products in Human Nutrition*; Food and Agriculture Organization of the United Nations: Rome, Italy, 2013; ISBN 978-92-5-107863-1.

28. Bartuzi, Z.; Cocco, R.R.; Muraro, A.; Nowak-Węgrzyn, A. Contribution of Molecular Allergen Analysis in Diagnosis of Milk Allergy. *Curr. Allergy Asthma Rep.* **2017**, *17*, 46. https://doi.org/10.1007/s11882-017-0716-z.

29. El-Agamy, E.I. The Challenge of Cow Milk Protein Allergy. *Small Rumin. Res.* **2007**, *68*, 64–72. https://doi.org/10.1016/j.smallrumres.2006.09.016.

30. Fuc, E.; Złotkowska, D.; Wróblewska, B. Milk and Meat Allergens from Bos Taurus β-Lactoglobulin, α-Casein, and Bovine Serum Albumin: An In-Vivo Study of the Immune Response in Mice. *Nutrients* **2019**, *11*, 2095. https://doi.org/10.3390/nu11092095.

31. Shamji, M.H.; Valenta, R.; Jardetzky, T.; Verhasselt, V.; Durham, S.R.; Würtzen, P.A.; van Neerven, R.J.J. The Role of Allergen-specific IgE, IgG and IgA in Allergic Disease. *Allergy* **2021**, *76*, 3627–3641. https://doi.org/10.1111/all.14908.

32. Fuc, E.; Złotkowska, D.; Stachurska, E.; Wróblewska, B. Immunoreactive Properties of α-Casein and κ-Casein: Ex Vivo and in Vivo Studies. *J. Dairy Sci.* **2018**, *101*, 10703–10713. https://doi.org/10.3168/jds.2018-14915.

33. Wong, K.H.; Horwitz, R.; Soffer, G.K. Immunoglobulin G Food Testing. *Ann. Allergy Asthma Immunol.* **2021**, *126*, 611–612. https://doi.org/10.1016/j.anai.2021.01.022.

34. Ansotegui, I.J.; Melioli, G.; Canonica, G.W.; Gómez, R.M.; Jensen-Jarolim, E.; Ebisawa, M.; Luengo, O.; Caraballo, L.; Passalacqua, G.; Poulsen, L.K.; et al. A WAO—ARIA—GA2LEN Consensus Document on Molecular-Based Allergy Diagnosis (PAMD@): Update 2020. *World Allergy Organ. J.* **2020**, *13*, 100091. https://doi.org/10.1016/j.waojou.2019.100091.

35. McKendry, R.T.; Kwok, M.; Hemmings, O.; James, L.K.; Santos, A.F. Allergen-specific IgG Show Distinct Patterns in Persistent and Transient Food Allergy. *Pediatr. Allergy Immunol.* **2021**, *32*, 1508–1518. https://doi.org/10.1111/pai.13567.

36. Francis, G.; Stuart, B.W.; Assender, H.E. Selective Ozone Treatment of PDMS Printing Stamps for Selective Ag Metallization: A New Approach to Improving Resolution in Patterned Flexible/Stretchable Electronics. *J. Colloid Interface Sci.* **2020**, *568*, 273–281. https://doi.org/10.1016/j.jcis.2020.02.008.

37. Ma, K.; Rivera, J.; Hirasaki, G.J.; Biswal, S.L. Wettability Control and Patterning of PDMS Using UV-Ozone and Water Immersion. *J. Colloid Interface Sci.* **2011**, *363*, 371–378. https://doi.org/10.1016/j.jcis.2011.07.036.

38. Kaufmann, T.; Ravoo, B.J. Stamps, Inks and Substrates: Polymers in Microcontact Printing. *Polym. Chem.* **2010**, *1*, 371–387. https://doi.org/10.1039/b9py00281b.

39. Perl, A.; Reinhoudt, D.N.; Huskens, J. Microcontact Printing: Limitations and Achievements. *Adv. Mater.* **2009**, *21*, 2257–2268. https://doi.org/10.1002/adma.200801864.

40. Jeyachandran, Y.L.; Mielczarski, E.; Rai, B.; Mielczarski, J.A. Quantitative and Qualitative Evaluation of Adsorption/Desorption of Bovine Serum Albumin on Hydrophilic and Hydrophobic Surfaces. *Langmuir* **2009**, *25*, 11614–11620. https://doi.org/10.1021/la901453a.

41. Barden, S.C.; Arns, J.A.; Colburn, W.S. Volume-Phase Holographic Gratings and Their Potential for Astronomical Applications. *Proc. SPIE Opt. Astron. Instrum.* **1998**, *3355*, 866–876.

42. Franzoi, M.; Niero, G.; Visentin, G.; Penasa, M.; Cassandro, M.; De Marchi, M. Variation of Detailed Protein Composition of Cow Milk Predicted from a Large Database of Mid-Infrared Spectra. *Animals* **2019**, *9*, 176. https://doi.org/10.3390/ani9040176.

43. Frutiger, A.; Tanno, A.; Hwu, S.; Tiefenauer, R.F.; Vörös, J.; Nakatsuka, N. Nonspecific Binding—Fundamental Concepts and Consequences for Biosensing Applications. *Chem. Rev.* **2021**, *121*, 8095–8160. https://doi.org/10.1021/acs.chemrev.1c00044.

44. Sancho-Fornes, G.; Avella-Oliver, M.; Carrascosa, J.; Morais, S.; Puchades, R.; Maquieira, Á. Enhancing the Sensitivity in Optical Biosensing by Striped Arrays and Frequency-Domain Analysis. *Sens. Actuators B Chem.* **2019**, *281*, 432–438. https://doi.org/10.1016/j.snb.2018.10.130.

45. Djaileb, A.; Hojjat Jodaylami, M.; Coutu, J.; Ricard, P.; Lamarre, M.; Rochet, L.; Cellier-Goetghebeur, S.; Macaulay, D.; Charron, B.; Lavallée, É.; et al. Cross-Validation of ELISA and a Portable Surface Plasmon Resonance Instrument for IgG Antibody Serology with SARS-CoV-2 Positive Individuals. *Analyst* **2021**, *146*, 4905–4917. https://doi.org/10.1039/D1AN00893E.

46. Bao, L.; Park, J.; Qin, B.; Kim, B. Anti-SARS-CoV-2 IgM/IgG Antibodies Detection Using a Patch Sensor Containing Porous Microneedles and a Paper-Based Immunoassay. *Sci. Rep.* **2022**, *12*, 10693. https://doi.org/10.1038/s41598-022-14725-6.

47. Teixeira, W.; Pallás-Tamarit, Y.; Juste-Dolz, A.; Sena-Torralba, A.; Gozalbo-Rovira, R.; Rodríguez-Díaz, J.; Navarro, D.; Carrascosa, J.; Gimenez-Romero, D.; Maquieira, Á.; et al. An All-in-One Point-of-Care Testing Device for Multiplexed Detection of Respiratory Infections. *Biosens. Bioelectron.* **2022**, *213*, 114454. https://doi.org/10.1016/j.bios.2022.114454.

48. Wang, Y.; Ju, Z.; Cao, B.; Gao, X.; Zhu, Y.; Qiu, P.; Xu, H.; Pan, P.; Bao, H.; Wang, L.; et al. Ultrasensitive Rapid Detection of Human Serum Antibody Biomarkers by Biomarker-Capturing Viral Nanofibers. *ACS Nano* **2015**, *9*, 4475–4483. https://doi.org/10.1021/acsnano.5b01074.

49. Chen, S.; Meng, L.; Wang, L.; Huang, X.; Ali, S.; Chen, X.; Yu, M.; Yi, M.; Li, L.; Chen, X.; et al. SERS-Based Lateral Flow Immunoassay for Sensitive and Simultaneous Detection of Anti-SARS-CoV-2 IgM and IgG Antibodies by Using Gap-Enhanced Raman Nanotags. *Sens. Actuators B Chem.* **2021**, *348*, 130706. https://doi.org/10.1016/j.snb.2021.130706.

50. Brangel, P.; Sobarzo, A.; Parolo, C.; Miller, B.S.; Howes, P.D.; Gelkop, S.; Lutwama, J.J.; Dye, J.M.; McKendry, R.A.; Lobel, L.; et al. A Serological Point-of-Care Test for the Detection of IgG Antibodies against Ebola Virus in Human Survivors. *ACS Nano* **2018**, *12*, 63–73. https://doi.org/10.1021/acsnano.7b07021.

51. Funari, R.; Chu, K.-Y.; Shen, A.Q. Detection of Antibodies against SARS-CoV-2 Spike Protein by Gold Nanospikes in an Opto-Microfluidic Chip. *Biosens. Bioelectron.* **2020**, *169*, 112578. https://doi.org/10.1016/j.bios.2020.112578.

52. Sinibaldi, A.; Occhicone, A.; Munzert, P.; Danz, N.; Sonntag, F.; Michelotti, F. Label-Free Monitoring of Human IgG/Anti-IgG Recognition Using Bloch Surface Waves on 1D Photonic Crystals. *Biosensors* **2018**, *8*, 71. https://doi.org/10.3390/bios8030071.

Supplementary Material

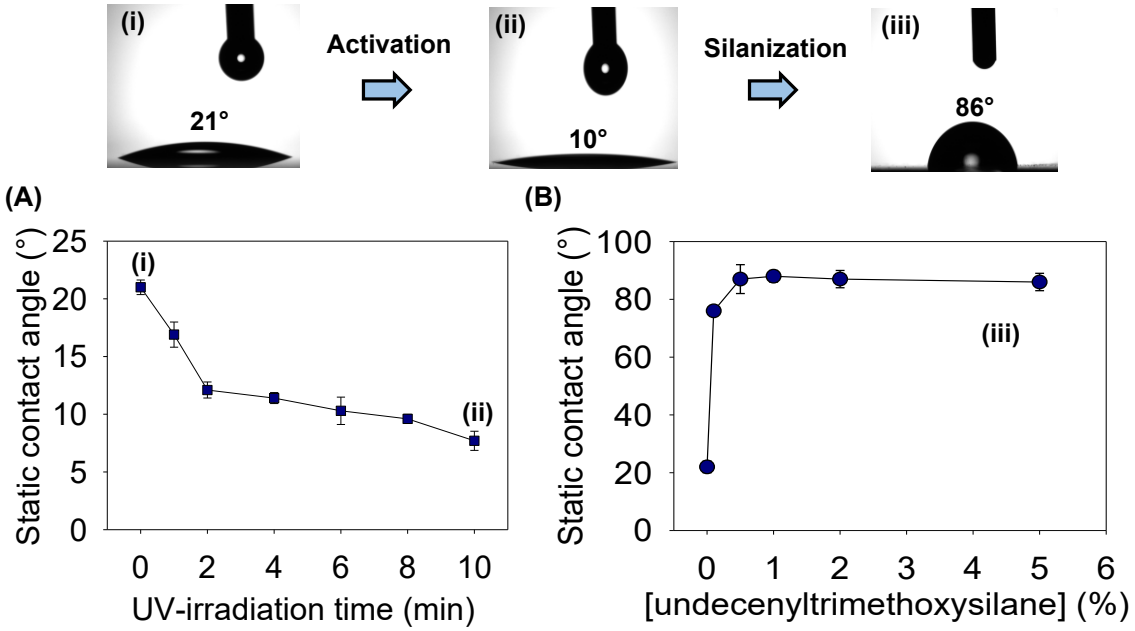

Figure S1. Static contact angle values of glass substrates **(A)** irradiated with UV-light for increasing times and **(B)** treated with increasing concentrations of 10-undecenyltrimethoxysilane after the ozone activation.

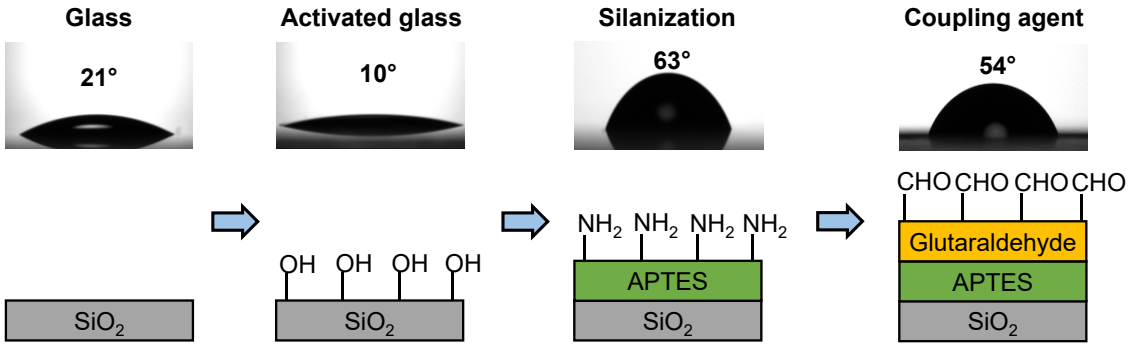

Figure S2. Static contact angles values measured after each functionalization step for the imine coupling.

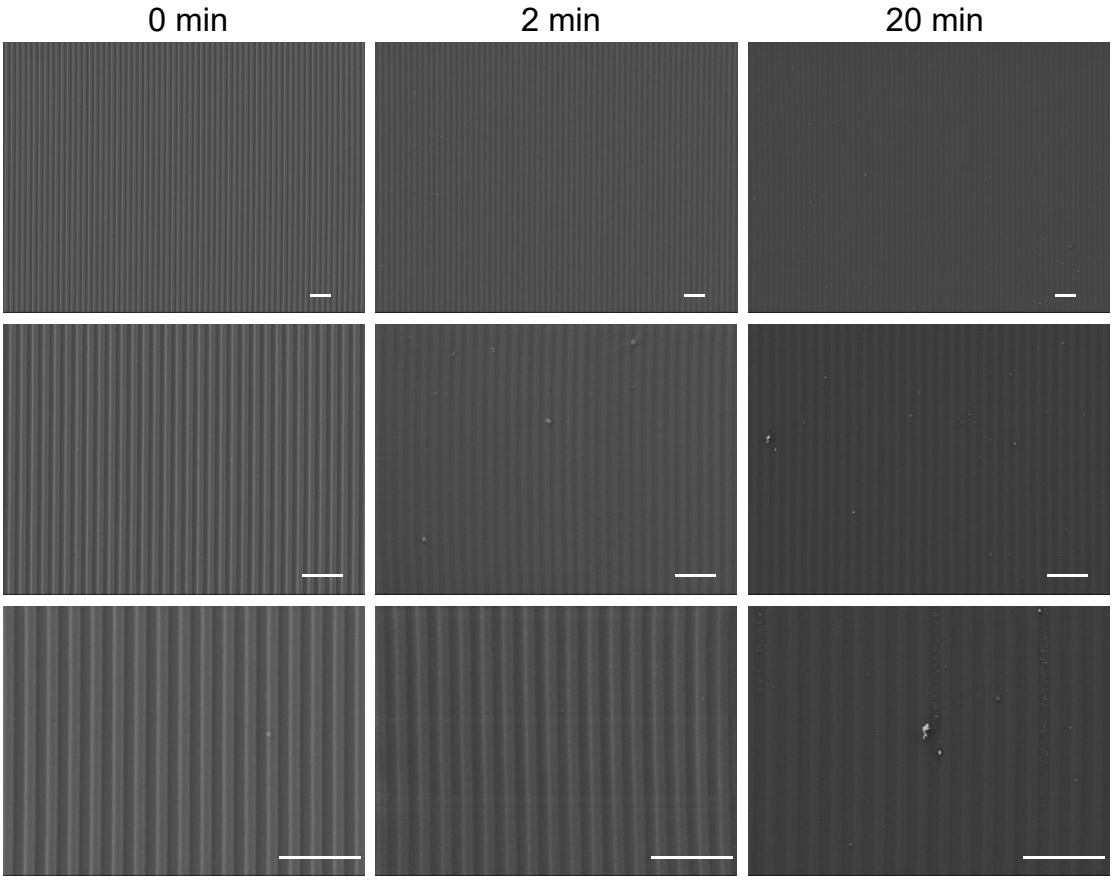

Figure S3. FESEM images of the PDMS grooved structure after different UV-ozone exposure times. Scale bars correspond to 2 µm.

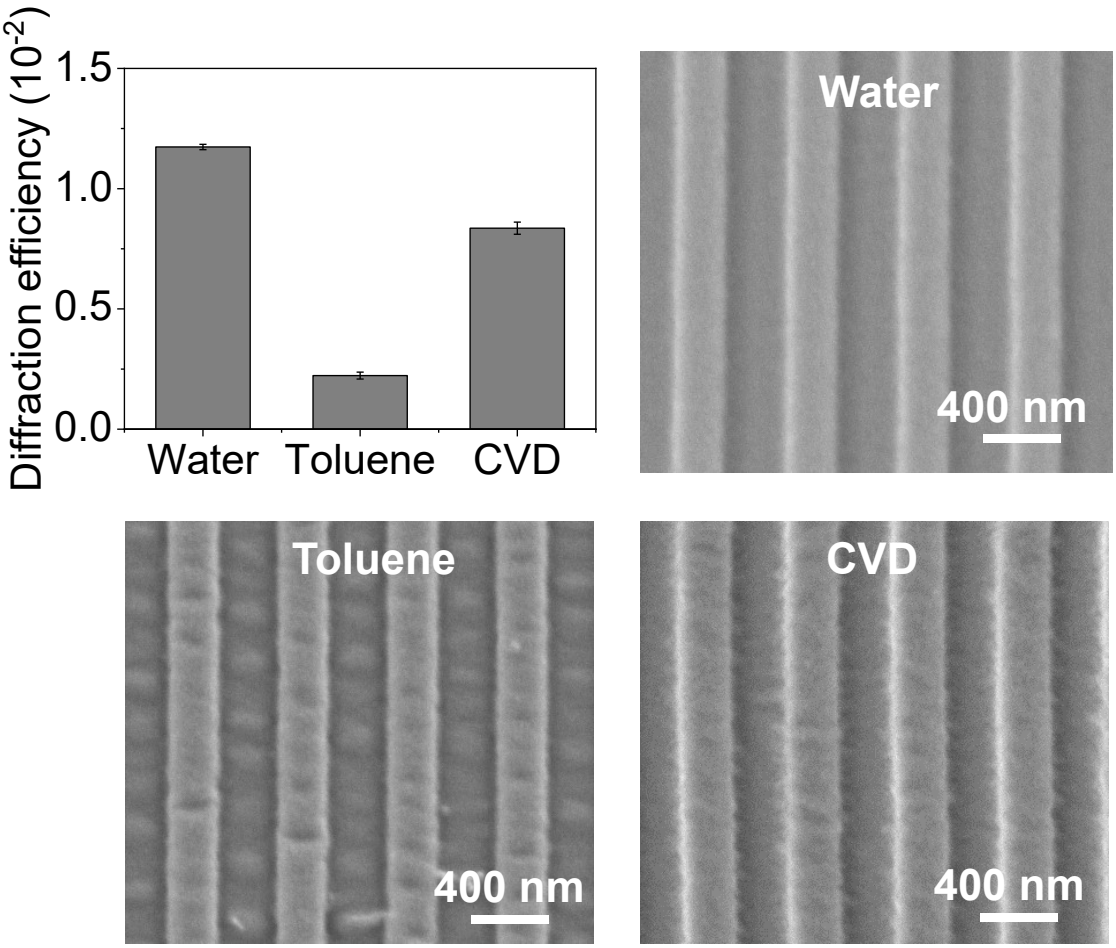

Figure S4. Diffraction efficiency and FESEM images of the PDMS stamps after their immersion in water and toluene for 160 min, and after their exposition to chemical vapor deposition (CVD) of APTES.

Organosilanes need to be diluted and solved in organic and aprotic solvents (typically toluene) that avoid their polymerization (*Anal. Bioanal. Chem. 2021, 414, 5071-5085*). But the results in Figure S4 show that this incubation introduces structural heterogeneities that lead to a significant drop in the diffraction efficiency (from 1.22 to 0.22) compared to the incubation of water used as a control.

Chemical vapor deposition (CVD) is a solventless alternative also commonly used to create monolayers of organolsilanes, where the surface to be silanized is directly exposed to the vapor of the selected organosilane (*Langmuir 2018, 34, 1400-1409*). However, the resulting stamps also display structural heterogeneities in the FESEM images as well as an important decrease in the diffraction efficiency.

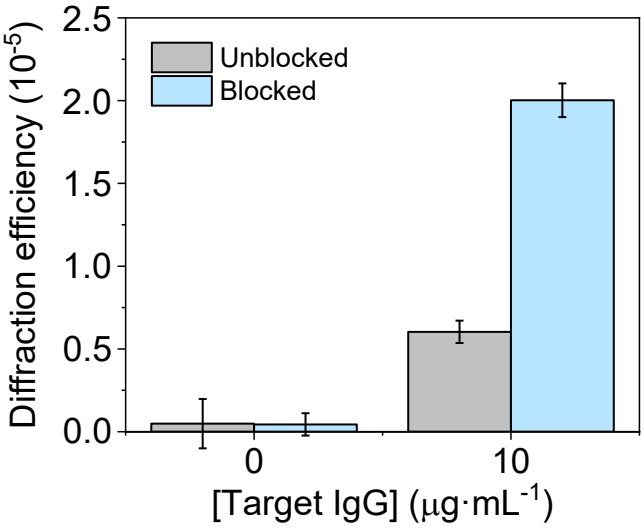

Figure S5. Diffraction efficiency measured after incubating different concentrations of antiBSA IgG in PBS-T onto BSA patterns unblocked (grey) and blocked (blue) with ethanolamine, fabricated through the imine route.

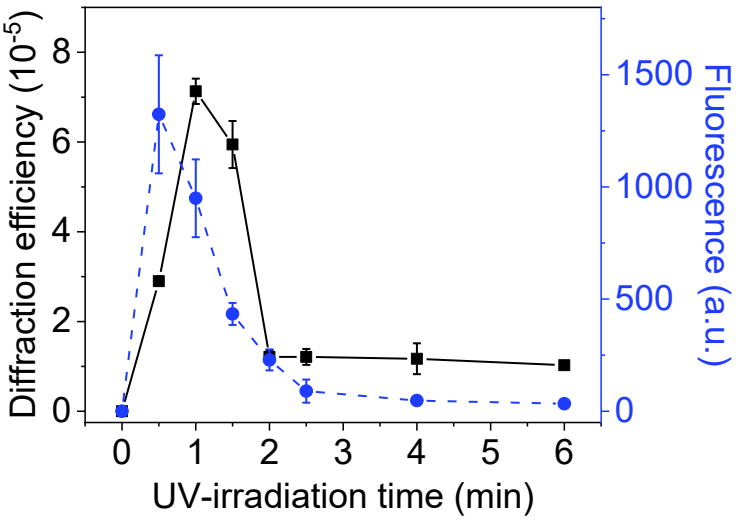

Figure S6. Diffraction efficiency (black squares and continuous line) and fluorescence signals (blue dots and dashed line) of BSA patterns after incubating fluorophore-labeled antiBSA (10 μg·mL^{-1}), fabricated by μCP coupled to thiol-ene reaction by increasing the UV-irradiation times.

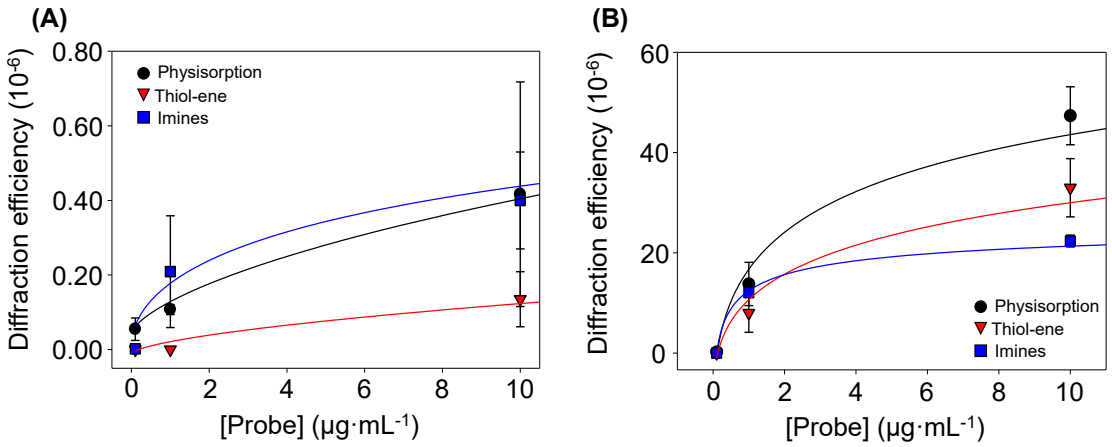

Figure S7. Zoomed view of the low concentration range of both representations in Figure 6 of the main manuscript.

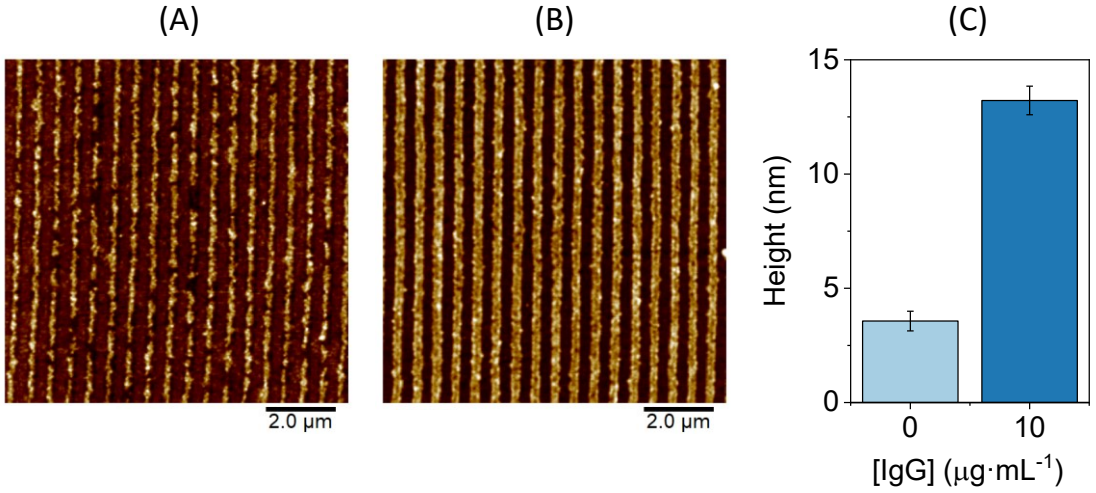

Figure S8. AFM images of BSA patterns after incubating a solution of antiBSA in PBS-T at **(A)** 0 µg·mL^{-1} and **(B)** 10 µg·mL^{-1}, and **(C)** the corresponding height of the protein strips measured from these scans.

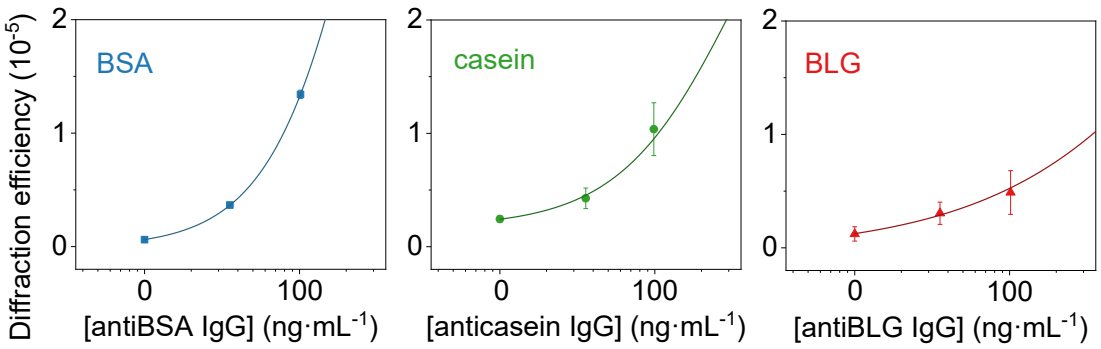

Figure S9. Zoomed view of the low concentration range of the graphs presented in Figure 7 of the main manuscript.

Table S1. Characterization results of the PDMS stamps after different ozone exposure times.

Ozone exposure time (min)	0	2	20
Diffraction efficiency (·10^{-3})	7.5 ± 0.4	4.8 ± 0.1	2.3 ± 0.3
Static contact angle (°)	130 ± 2	122 ± 1	87 ± 3
Pattern period (nm) *	563 ± 4	557 ± 2	544 ± 3
Duty cycle *	50 ± 1	53 ± 1	54 ± 1
Groove height (nm) *	99 ± 1	72 ± 6	39 ± 6

** Measured from AFM scans (Figure 3C).*

Table S2. Structural parameters measured from the AFM images in Figure 5.

Strategy	Period (nm)	Duty cycle (%)	Height (nm)
Physisorption	564 ± 8	43 ± 2	3.3 ± 0.4
Imines	580 ± 10	58 ± 3	2.0 ± 0.3
Thiol-ene	582 ± 7	60 ± 3	2.1 ± 0.2

Table S3. Parameters of the linear fittings employed to infer the linear range of the immunoassays (*Diffraction efficiency = a + b [IgG]).*

	a	b	R^2
BSA	$3 \cdot 10^{-6}$	$1 \cdot 10^{-7}$	0.99
casein	$6 \cdot 10^{-6}$	$4 \cdot 10^{-8}$	0.99
BLG	$7 \cdot 10^{-6}$	$9 \cdot 10^{-9}$	0.99

Chapter 2

Fabrication of biogratings by local and periodic deactivation of biolayers

Chapter 2: Fabrication of biogratings by local and periodic deactivation of biolayers.

As commented in the introduction (section 1.4), and demonstrated in chapter 1, μCP is a powerful and versatile technique to pattern biogratings. Some issues related to the μCP performance (loss of the biological activity and immobilization strength of the bioreceptors) have been addressed in chapter 1. However, other limitations, such as moderate reproducibilities of the patterns, high concentrations of inking molecules needed, long inking times, and limited scalability, still hinder its scope in the biosensing scenario.

Standard light-based nanofabrication techniques (photolithography, e-beam lithography, etc.) have demonstrated to be fast and scalable approaches to create nanostructures. They typically rely on the fabrication of nanostructured substrates by ablation or by curing photoresists, but they are rather unexplored to pattern biomolecules. In this chapter, a new photopatterning method based on the periodic denaturation of protein biolayers assisted by UV-laser, is presented. The hypothesis relies on generating an interference pattern in a continuous biolayer, in order to make proteins exposed to constructive interferences to become deactivated but not removed from the substrate, whereas those exposed to destructive interferences will keep their activity. Therefore, this approach aims to generate a periodic modulation without topographic contributions and only based on the protein activity. If these patterns are periodic at the nanoscale, they will interact with incident light beams and diffract them, allowing to transduce biorecognition events in the same way that the biogratings fabricated by μCP. The investigation herein presented reports the design and characterization of this photopatterning method, compares the resulting biogratings with their counterparts fabricated by μCP, and addresses their bioanalytical features with a model immunoassay tested in complex samples.

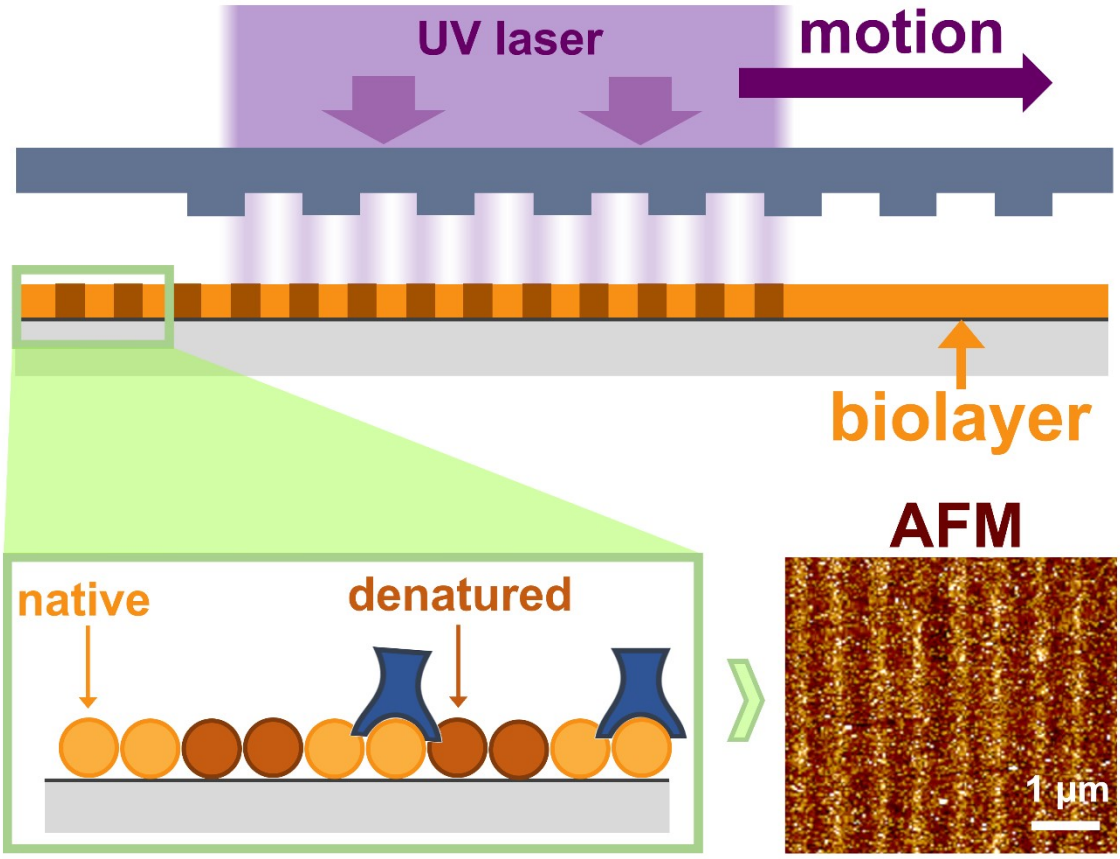

Denaturing for Nanoarchitectonics: Local and Periodic UV-laser Photodeactivation of Protein Biolayers to Create Functional Patterns for Biosensing

ACS Applied Materials and Interfaces **2022**, 14, 41640-41648

ACS APPLIED MATERIALS & INTERFACES

DENATURING FOR NANOARCHITECTONICS: LOCAL AND PERIODIC UV-LASER PHOTODEACTIVATION OF PROTEIN BIOLAYERS TO CREATE FUNCTIONAL PATTERNS FOR BIOSENSING

Augusto Juste-Dolz,[1] Martina Delgado-Pinar,[2,*] Miquel Avella-Oliver,[1,3,*] Estrella Fernández,[1] Jose Luís Cruz,[2] Miguel V. Andrés,[2] Ángel Maquieira[1,3,*]

[1]*Instituto Interuniversitario de Investigación de Reconocimiento Molecular y Desarrollo Tecnológico (IDM), Universitat Politècnica de València, Universitat de València, 46022 Valencia, Spain.*

[2]*Department of Applied Physics and Electromagnetism-ICMUV, Universitat de València, Burjassot 46100, Spain.*

[3]*Departamento de Química, Universitat Politècnica de València, 46022 Valencia, Spain.*

**Corresponding autor: amaquieira@qim.upv.es (Á. Maquieira), miavol@upv.es (M. Avella-Oliver), Martina.Delgado@uv.es (M. Delgado-Pinar).*

Abstract

The nanostructuration of biolayers has become a paradigm for exploiting nanoscopic light-matter phenomena for biosensing, among other biomedical purposes. In this work, we present a photopatterning method to create periodic structures of biomacromolecules, based on a local and periodic mild denaturation of protein biolayers mediated by UV-laser irradiation. These nanostructures are constituted by a periodic modulation of the protein activity, so they are free of topographic and compositional changes along the pattern. Herein we introduce the approach, explore the patterning parameters, characterize the resulting structures, and assess their overall homogeneity. This UV-based patterning principle has proven to be an easy, cost-effective, and fast way to fabricate large areas of homogeneous one-dimensional protein patterns (2 min, 15 x 1.2 mm, relative standard deviation ≃ 16%). This work also investigates the implementation of these protein patterns as transducers for diffractive biosensing. Using a model immunoassay, these patterns have demonstrated negligible signal

contributions from non-specific bindings and comparable experimental limits of detection in buffer medium and in human serum (53 and 36 ng·mL^{-1} of unlabelled IgG, respectively).

Keywords: biosensor, UV denaturation, Immunoassay, non-specific binding, label-free, diffraction

1. Introduction

Nanoscience and nanotechnology are nowadays a fertile groundwork of materials and nanoscopic light-matter phenomena that provide unique solutions in endless scenarios. Within this field, the patterning of biomacromolecules points towards a promising scope in biomedical applications such as organ-on-a-chip,[1,2] neuronal networks,[3–6] drug delivery,[7] and implant coatings[8] among others. It also involves a particularly high impact in biosensing, where the biomolecular patterns are tailored to display nanoscopic phenomena to transduce biorecognition events.[9,10] A crucial aspect in this scenario is the development of fast and large-scale methods to fabricate active nanostructures with a high geometrical accuracy.

A classical approach for structuring biomacromolecules is to place continuous biolayers onto prepatterned solid substrates,[11–13] typically fabricated by photolithography,[14] electron-beam lithography,[15] dip-pen lithography,[16] and laser interference.[17] An alternative approach is to create nanostructures constituted by the biomacromolecules themselves on unstructured substrates. This strategy has been widely used to create microarrays for biosensing, using techniques as contact and non-contact printing,[18] photochemical surface chemistries[19] or using patterned incubation masks.[20] Among these nanostructuration techniques, microcontact printing (μCP) holds a noteworthy popularity for patterning biomolecules of different natures (proteins, nucleic acids, small molecules, etc).[21] μCP relies on the selective transfer of biomolecules from a nanostructured elastomeric stamp (typically made of polydimethylsiloxane) to a solid substrate just by contact. Even though μCP has demonstrated to be an excellent

nanostructuration technique for biolayers in terms of versatility, simplicity, and cost effectiveness, it presents some limitations, such as a moderate homogeneity of the resulting structures,[22] and a limited functionality of the patterned biomolecules.[23]

In this work, we present a method to create 1D periodic nanostructures of biomacromolecules on flat surfaces, based on the local deactivation of protein biolayers assisted by UV-laser. As schematized in Figure 1, the hypothesis behind this patterning strategy relies on irradiating surface-bound protein monolayers through a phase mask that generates an interferometric pattern of light on the biolayer. Proteins exposed to constructive interferences undergo a mild denaturation that impede their functionality (without reaching ablation), and those exposed to the destructive interference keep their activity. Unlike standard UV photopatterning techniques typically based on photoresists, ablation, and inscribing refractive index variations on inorganic substrates,[26–28] this approach aims to create patterns constituted by a periodic modulation of protein functionality and free of topographic contributions.

If these patterns of biomacromolecules are periodic at the nanoscale they can interact with incident light beams and diffract them. Assessing this diffractive response provides useful information for the characterization of the structures. In addition, diffractive patterns of biomacromolecules have demonstrated to be a promising transduction system for biosensing.[29–34] Among other features, they enable the development of miniaturized bioanalytical systems for real-time and label-free sensing, with a unique potential to minimize non-specific binding issues in the analysis of complex biological samples.[35]

Herein we report the design and development of this patterning method for biomacromolecules based on periodic UV deactivation. First, the photofabrication parameters are explored and the structural features of the resulting protein patterns are characterized by microscopy and by assessing their diffractive response. Then, the homogeneity of the structures is investigated and compared with their counterparts fabricated by micro-contact printing. Finally, this work studies and reports the bioanalytical performance of these protein patterns for diffractive biosensing, investigates their potential to minimize non-specific binding contributions in biological samples, and provides insights into their multiplexing capabilities.

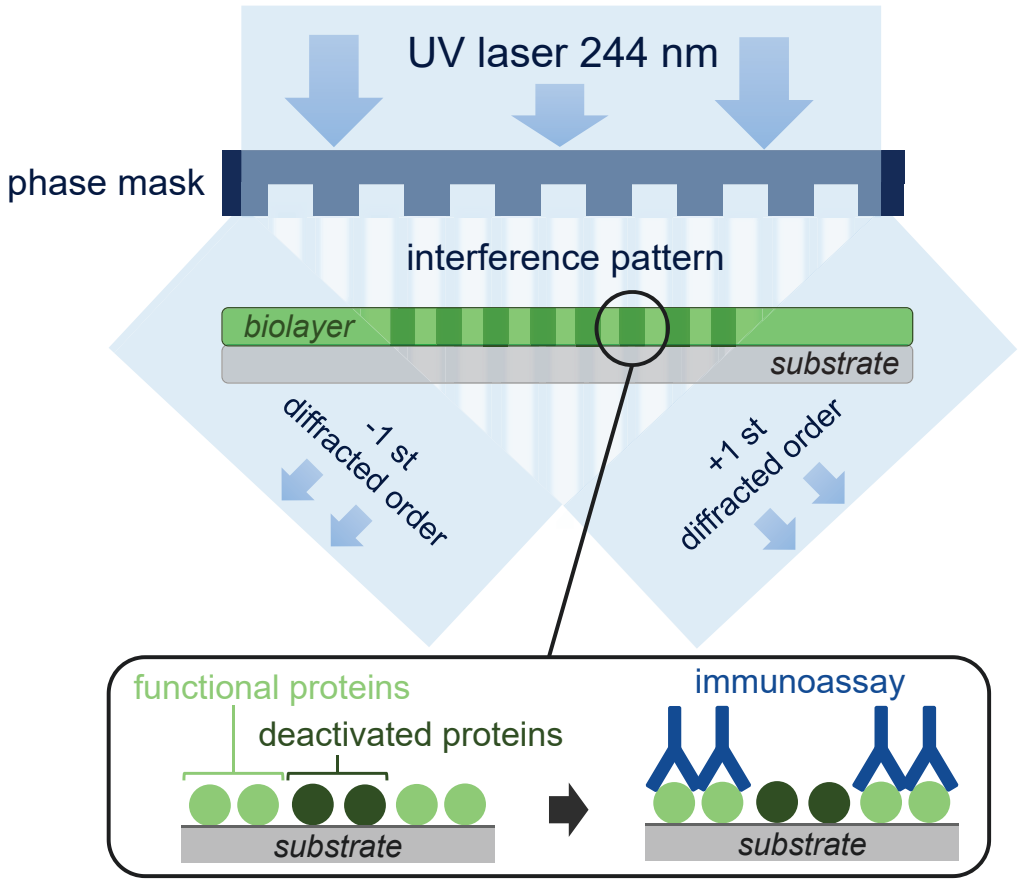

Figure 1. Scheme of the UV-induced selective protein deactivation process.

2. Results and discussion

2.1. Photopatterning

The amount of light applied to the surface-bound bioreceptors is a key parameter in this photopatterning strategy, since it will ultimately determine the rate of proteins that become deactivated and the magnitude of their denaturation.[25] This aspect is herein investigated using a model immunoassay based on bovine serum albumin (BSA) protein probes and specific antiBSA IgGs targets.

After optimizing the surface concentration of the BSA protein biolayer (Figure S1), a range of UV fluences were experimentally assessed to explore their effect and to set-up optimal conditions to create functional nanostructures. To modulate the fluences, both the emission power of the UV-laser and the time of exposure on the protein surface

were investigated. The time of exposure was controlled by the scan velocity of the UV laser along the phase mask, and the structural features of the resulting protein patterns were assessed by means of their diffractive response and their atomic force microscopy (AFM) profile.

Regarding the diffractive characterization, note that these patterns are periodic one-dimensional nanostructures conformed by alternated strips of active and inactive BSA proteins, where the active proteins will be able to bind their target IgGs but the photodeactivated ones will not. As the relative amount of matter in the activated strips selectively increases because of the interaction with the target IgG, the periodic modulation becomes greater, and the diffraction efficiency increases too. As expected, neglectable diffraction efficiencies are experimentally observed in all the biolayers right after the photopatterning, regardless the irradiation fluence. Also, unstructured flat topographies are observed by AFM (Figure S2), suggesting that these fluences neither reach the threshold to create a periodic ablation of the biolayer or the glass surface, nor lead to a severe protein denaturation that would introduce a significant periodic modulation of the refractive index. Instead, the results match the expected periodic mild denaturation of the surface proteins.

Then, to assess the deactivation profile, the irradiated biolayers were investigated after incubating a solution of specific target antiBSA IgG (10 $\mu g \cdot mL^{-1}$) on them. Therefore, these IgG should bind the proteins of the active strips, but not the deactivated ones. A diffractive response is observed in all the cases (Figure 2A), which indicates the selective IgG binding according to the expected stripped pattern. The experimental results show different diffractive trends, and topographic features for low, medium, and high irradiation fluences as discussed below.

As shown in Figure 2A, the low-fluence range (from 0 to about 1.5 $J \cdot cm^{-2}$) displays a low diffractive response that increases together with the fluence. It indicates that the aimed periodic protein deactivation takes also place at these fluences, although it involves a lower height modulation. In fact, irradiation fluences as low as $62 \cdot mJ \cdot cm^{-2}$ are enough to create a pattern. On the other hand, the diffractive response of the patterns created by different laser powers (27.5 and 55 mW) overlap in this low-fluence range, whereas this is not the case for the rest of the curve. This observation suggests that the biolayer

presents non-linear response to the laser power and the scan velocity, and therefore both parameters must by optimized simultaneously.

An optimal range is shown at medium fluence of 1.5-4 $J \cdot cm^{-2}$ (Figure 2A). In particular, the maximal diffractive response is obtained in protein patterns created at 2.5 $J \cdot cm^{-2}$ with a laser power of 55 mW, and a dropping trend in the diffraction efficiency is observed beyond this medium range in all the cases.

These results indicate that the highest rate of denaturation between active and deactivated strips corresponds to medium irradiation fluences, and this observation is supported by the topographic characterization. The biolayer exposed to medium fluences display greater height modulations after the immunoassay than those created at low and high fluences (Table S1). Also, as shown in Figures 2B(i) and (ii), the target antiBSA IgGs selectively bind to active protein strips generating a homogeneous, periodic, and grooved structure.

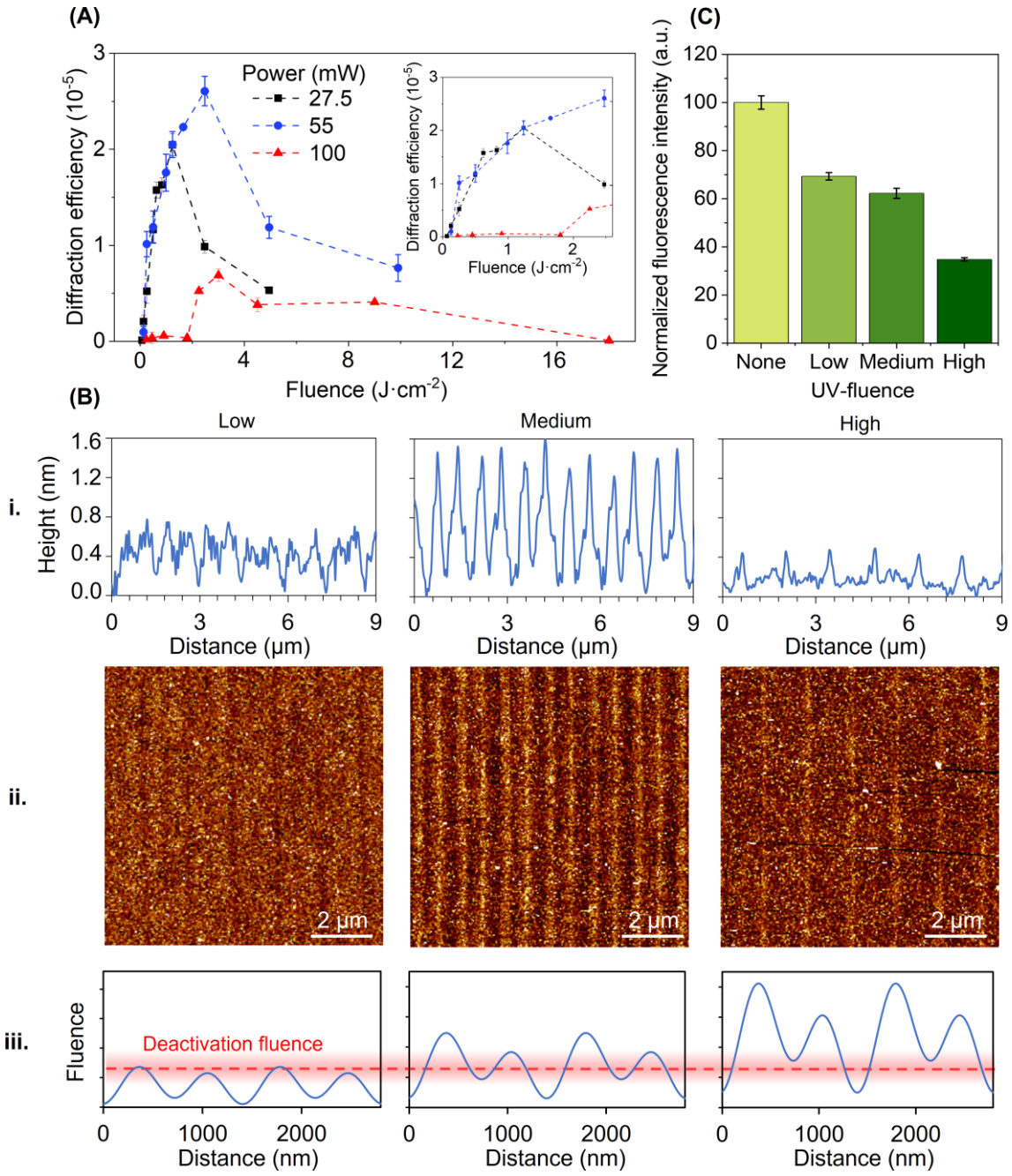

Figure 2. (A) Representation of the diffraction response of the BSA gratings obtained at different irradiation conditions. The inset shows a detail of the lower fluences range. **(B)** i. Cross section profiles of the ii. AFM images after incubating target anti BSA IgG (10 $\mu g \cdot mL^{-1}$) onto protein layers irradiated with a low (55 mW and 4.4 $mm \cdot s^{-1}$, 0.1 $J \cdot cm^{-2}$), medium (55 mW and 0.2 $mm \cdot s^{-1}$, 2.5 $J \cdot cm^{-2}$) and high (55 mW and 0.1 $mm \cdot s^{-1}$, 9.9 $J \cdot cm^{-2}$) fluences. Dark and bright colors indicate deep and high areas, respectively. See Table S1 for the corresponding topographic data. iii. Scheme of the threshold deactivation fluence and the light profiles generated from the interference between the 0^{th} and 1^{st}

diffraction orders. **(C)** Fluorescence intensities from non-irradiated and UV-irradiated protein biolayers with low, medium, and high fluences after incubating fluorophore-labelled specific anti BSA IgGs (10 $\mu g \cdot mL^{-1}$).

Regarding the period of the biolayer patterns, the one expected for the employed phase mask (710 nm) is obtained in all the cases, as measured by AFM (Figures 2A and Table S1). A contribution of a double-length period (around 1420 nm) is also observed in the diffractive response and in the AFM scans and comes from the two effects schematized in Figure 2B (iii). One of them is a deactivation fluence of a relatively wide range, rather than a narrow value. The other one is a non-negligible contribution of the zeroth diffraction order of the phase mask, which interferes with the first orders and generates a sinusoidal light profile on the biolayer constituted by alternated lobes of higher and lower intensity. Although only a power contribution of about 3% is expected from the zeroth order,[36] the experimental results show that it can involve a significant impact in the resulting protein pattern. The interaction of these two effects can also explain the deviation in the duty cycle measured by AFM (Table S1), around 60% and 40% for low and high fluences, respectively. This issue can be minimized by selecting proper irradiation parameters (laser power and scan velocity), and our experimental results show that a minimal presence of this double period and an optimal duty cycle of around 50% are simultaneously obtained in the structures fabricated at medium fluence.

Regarding the changes undergone by the surface-bound proteins due to the irradiation, proteins absorb UV light thanks to the side chain of the aromatic amino acids. This excitation can generate an electron flux that induces the breakage of disulfide bridges and irreversibly modify the three-dimensional conformation of the protein.[24,25] On the one hand, the formation of disulfide bridges requires two nearby cysteines for their side chains to interact. On the other, among the aromatic amino acids, tryptophan has de highest absorption coefficient in the near UV region and plays a central role in the electron transfer for the photolytic cleavage of nearby disulfide bridges.[24,37] In the case of the BSA proteins used in this study, they are constituted by 607 aminoacids, with 34 couples of nearby cysteins and 10 of them with close spatial proximity to a tryptofan (Figure S3), who are the main responsible for the photopatterning process herein studied.[37,38]

This UV-induced disulfide bridge disruption may modify the three-dimensional conformation of the protein. However, these periodic conformational changes are not experimentally detected in the AFM topographic characterization (Figure S2), presumably given their negligible contribution in the resulting height modulation of the pattern. On the other hand, it must be highlighted that, after the irradiation at medium fluence the patterned protein biolayers do display a minute diffractive signal. Although this diffraction efficiency is about three orders of magnitude lower than the corresponding one after binding target antibodies ($1.1 \cdot 10^{-8}$ before and $2.8 \cdot 10^{-5}$ after the incubation of 10 $\mu g \cdot mL^{-1}$ of specific IgGs), these results suggest that irradiated proteins undergo a conformational change that slightly modifies their refractive index.

To assess the protein deactivation rate, we also measured the fluorescence intensity after incubating specific antiBSA IgGs labelled with a fluorophore. Instead of structural information of the patterns, these measurements provide information about the overall deactivation rate of the biolayer, where a higher fluorescence intensity indicates a greater amount of bound targets and therefore a lower deactivation. As shown in Figure 2C, the higher fluence is applied, the greater overall deactivation is obtained and therefore a lower fluorescence signal is acquired. This observation complements the abovementioned characterization and supports the hypothesis of this structuration strategy.

From these results, protein patterns fabricated by a fluence of 2.5 $J \cdot cm^{-2}$ (55 mW laser power and 0.2 $mm \cdot s^{-1}$ scan velocity) were selected to further investigate this patterning method. It is worth highlighting that, for this patterning conditions, about 20 mm^2 of optically-active structures can be patterned in less than two minutes. Furthermore, once fabricated and stored at 4°C, these protein patterns have shown to keep their optical and binding functionality for more than 30 days (Figure S4).

2.2. Structural homogeneity

Once fabricated, the overall homogeneity of the obtained protein patterns was assessed by means of their diffractive response. Herein these results are experimentally compared with those obtained by micro-contact printing (μCP), since this is an

important technique widely employed to pattern biomacromolecules and also used to create diffractive protein structures.[9,23,29,32]

First, the repeatability of the gratings was assessed by means of the relative standard deviation (RSD) of the diffraction efficiency obtained after the incubation of specific antiBSA IgG targets. As shown in Figure 3A, RSD values for the photopatterned biolayers is about two-fold better than the one displayed by μCP. This improvement is especially significant in blank samples (0 $\mu g \cdot mL^{-1}$ of IgG) since the diffracted signals of the photopatterned BSA gratings are negligible (Figure 3B and 3C). Therefore, this effect impacts on the experimental noise rates and will ultimately affect the detection and quantification limits for biosensing.

Then, the overall homogeneity of the patterned biolayers was also assessed by means of the shape of the diffracted light spots. Structural irregularities and deformations scatter the incident light and even lead to period changes that distribute the diffracted beam on a wider and more irregular area.[39] As shown in Figures 3B and 3C, the diffracted spots from biomolecular gratings obtained by μCP are typically defined by an uneven and wider distribution. On the other hand, the diffracted spots generated by the biolayers patterned by this photodeactivation strategy are constituted by a well-defined gaussian-like profile that concentrates the diffracted light in a regular area, which provides insights into the great homogeneity of these structures.

The homogeneity of the resulting biomolecular structures was assessed by mapping their diffractive response along the patterned area (Figure S5). As shown in Figure 3D, large areas of optically-active protein nanostructures can be patterned with this method. The horizontal (x) dimension in this plot corresponds to the motion direction of the laser during the patterning, and the other (y) one corresponds to the vertical expansion of the laser beam by a cylindrical lens included in the patterning setup (Figure S6). In this first approach, an RSD of 16% is obtained from the diffractive mapping of the patterned strip of 15 x 1.2 mm, which will be selected as the sensing area in the next steps of this study.

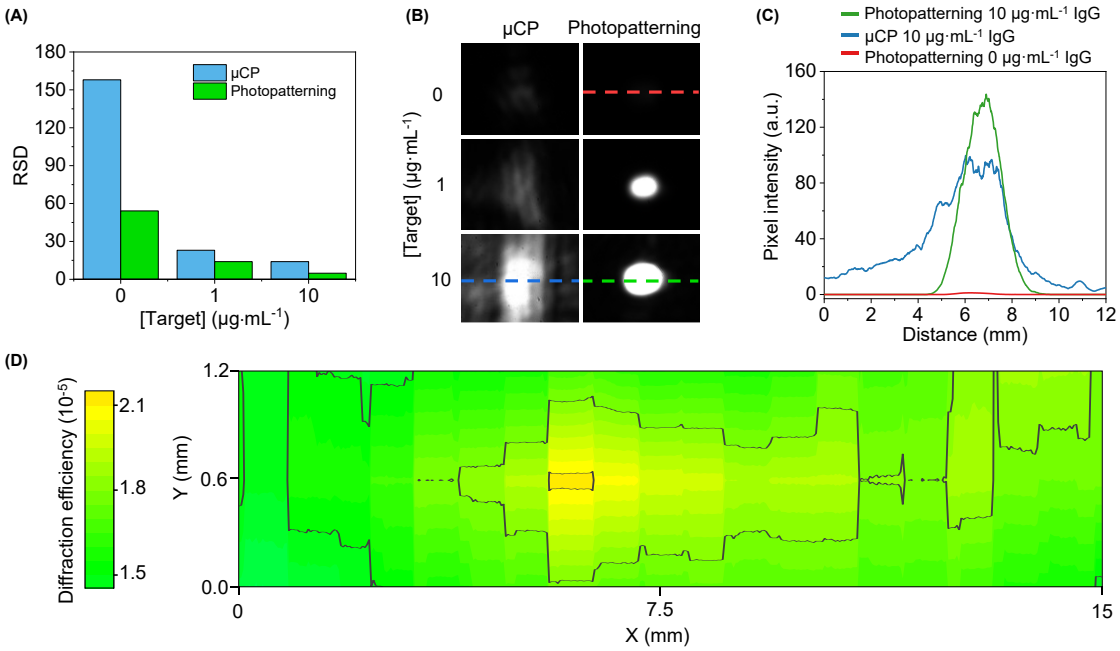

Figure 3. (A) Homogeneity assessment. RSD values of the diffraction efficiency (three replicates), and **(B)** images of the first-order diffracted spots obtained with BSA patterns fabricated by photodeactivation and μCP after the incubation of different concentrations of specific antiBSA IgG in buffer solution. **(C)** Cross-section profiles of the first-order diffracted spots, where the profile direction along the spot is indicated by the dashed line in Figure 3B. See Figure S5 for a zoomed view of the cross-section for the photopatterned biolayer after the incubation of 0 μg mL^{-1} of antiBSA. **(D)** Diffraction efficiency mapping of the 1st diffracted order of a photopatterned biolayer incubated with 10 μg mL^{-1} of specific antiBSA IgGs and the corresponding cross-section indicated as a dashed line.

2.3. Immunosensing

The abovementioned disulphide bridge cleavages undergone by the surface-bound biolayers exposed to constructive UV interferences can modify the protein parts that act as epitopes in antibody-mediated biorecognition events, and these changes can affect the subsequent binding processes of specific antibodies. To explore the biosensing capabilities of this approach we used a representative immunoassay based on BSA probes and specific antiBSA IgGs as targets. A whole antiserum is used as antiBSA in this study, which provides more insights into the applicability of these photopatterned

biolayers. This antiserum contains many non-specific proteins, and specific antibodies that are polyclonal, thus involving a wide range of paratopes for different lineal and conformational epitopes.

To assess the effect of the UV irradiation on the binding process, BSA patterns were created, and their response was experimentally measured after the incubation of a single concentration of antiBSA (10 $\mu g \cdot mL^{-1}$). Using labelled secondary antibodies, it is observed that strong irradiations substantially hinder the subsequent binding of specific antibodies (Figure S7), and this effect increases together with the fluence applied in the photopatterning (Figure 2C). Furthermore, when comparing the topography before (Figure S2) and after (Figure 2B, medium fluence) the antibody incubation, a selective height growth following the photopatterned striped structure is observed. This local and periodic antibody binding is also confirmed by the dramatic increase of the diffraction efficiency observed after the incubation (Figure 3C). All these results confirm that the UV-induced modifications undergone by the surface-bound proteins hampers its activity as epitopes for the subsequent biorecognition events with antibodies, and that this binding follows the periodic structure created in the photopatterning.

To further characterize the capabilities of these photopatterned biolayers as diffractive transducers for biosensing, their diffractive response upon the incubation of a range of antibody concentrations was investigated. As shown in Figure 4A, the system displays a well-correlated calibration curve (R^2 = 0.999) that fits the expected trend for this biorecognition event. From these results, experimental detection, and quantification limits (LOD and LOQ) of 53 ng mL^{-1} (0.4 nM) and 164 ng mL^{-1} (1.1 nM) of antiBSA IgG are inferred, respectively. Those are promising values for this novel patterning approach, determined in experimental and label-free conditions, which are in the range of other recent label-free optical approaches in the state-of-art (Table S2).

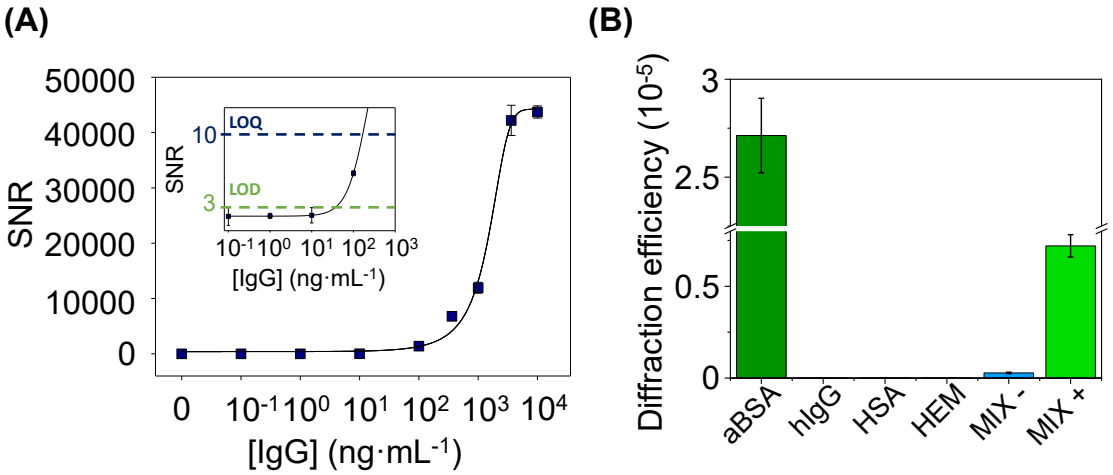

Figure 4. (A) Immunoassay calibration curve. Experimental data fitted to a sigmoidal regression (4-parameter logistic). The inset zooms in on the detection and quantification limits. **(B)** Diffraction efficiencies achieved after incubating 10 µg·mL^{-1} of specific IgG targets (aBSA), human IgGs (hIgG), human serum albumin (HSA), haemoglobin (HEM), and a mixture of hIgG, HSA and HEM without (MIX-) and with (MIX+) 10 µg·mL^{-1} of antiBSA in PBS-T buffer.

An important issue in label-free biosensing is the signal contribution of non-specific bindings (NSB), an undesired phenomenon that takes place specially in the analysis of biological or other complex samples,[35,40] which contain many molecules at different concentrations that are prone to adsorb non-specifically on the sensing surface and generate signals that cannot be discriminated from the probe-target biorecognition events. A particular feature of diffractive biosensing approaches is their potential to avoid signal contributions from NSB. It relies on the fact that only the binding events that meet the periodicity of the patterned biolayer create a periodic modulation that modifies the diffraction efficiency of the nanostructure, as it happens for the recognition between the patterned active probes and their targets. However, the adsorption of non-specific binders on the biolayer follows a random and not periodic distribution, and therefore do not modify the diffraction efficiency.[30]

A positive aspect to favour the randomness of the NSB process is to keep the same chemical composition on both kinds of strips of the patterned biolayer. So that non-specific binders present the same tendency for both parts of the pattern and they become evenly distributed as desired to avoid NSB signal contributions. This is the case for the structures herein investigated, where activated and deactivated strips are constituted by the same biomacromolecule, only differentiated by a mild modification that changes its binding capability.

As a first step to explore the ability of this approach to minimize NSB signal contributions, the diffractive response upon the incubation of high concentrations (10 $\mu g \cdot mL^{-1}$ in buffer solution) of non-specific binders typically found in serum, was assessed. As observed in Figure 4B, negligible signals compared to the one for the binding of specific antiBSA IgG at the same concentration are obtained. In addition to the NSB issue, note that this experiment also points out the analytical selectivity of the assay.

Then, we explored the response of the system under a range of dilutions of a commercial human serum containing $6.5 \cdot 10^4$ $\mu g \cdot mL^{-1}$ of non-specific proteins, 1025 $\mu g \cdot mL^{-1}$, of triglycerides and 1600 $\mu g \cdot mL^{-1}$ of cholesterol, which are potential non-specific binders. On the one hand, all these serum incubations displayed negligible changes in the diffractive response of the biomolecular pattern, which points out that unwanted additive signal contributions from NSB are avoided. On the other hand, the diffraction efficiency decays with the concentration of non-specific binders when target antiBSA IgGs are spiked in these serum dilutions, as shown in Figure 5A. Note that the concentration of non-specific binders in this real sample is many orders of magnitude larger than the one of specific targets. It may lead to steric clashes and hindered diffusive processes that decrease the availability of free patterned probes to interact with the specific targets. Interestingly, the results show that together with this signal decrease, the experimental noise value undergo a dramatic decay too, and as a result favourable signal-to-noise ratios are obtained also in these high NSB conditions. As shown in Figure 5B, great signal-to-noise ratios (SNR) and a well-correlated calibration curve ($R^2 = 0.998$) are obtained in pure human serum. From these results, the experimental detection and quantification limits reached similar values to those obtained in buffer.

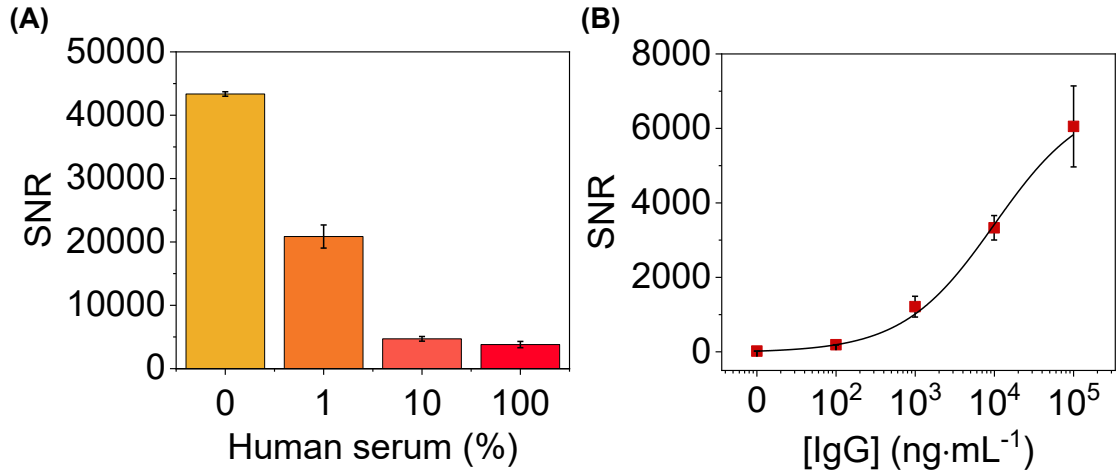

Figure 5. (A) SNR values achieved after incubating different dilutions of human serum (in PBS-T) spiked with specific IgG (10 µg·mL^{-1}). **(B)** Immunoassay calibration curve performed in pure human serum. Experimental data fitted to a sigmoidal regression (4-parameter logistic).

As an exemplary approach to provide preliminary insights into the implementation of these photopatterned biolayers in detection schemes for multiplexed biosensing, the mapping setup commented above (Figure S6) was employed to automatically scan the diffractive response of different assays in a single measurement. For that, incubation masks of adhesive film were attached on the slides after the photopatterning and used to create several sensing areas where different target concentrations were incubated. As shown in Figure 6, an array of multiple sensing spots can be easily created, and their response measured in less than 40 s. Beyond this first approximation, arrays containing a larger number of sensing spots can be easily arranged to automatically quantify many targets in a single assay with these photopatterned biolayers.

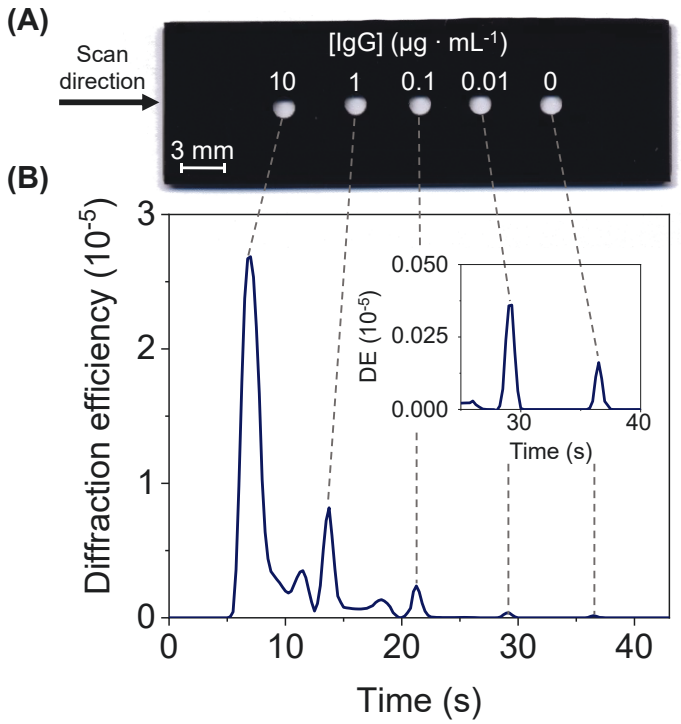

Figure 6. Multiplexed scanning. **(A)** Top-view photograph of a glass slide with a patterned protein biolayer after attaching the incubation mask. **(B)** Cross-section of the signal profile acquired with the diffractive scanning after incubating the IgG concentrations indicated above on each spot in buffer.

3. Conclusions

This work introduces a patterning method for biolayers based on the local deactivation of surface-bound proteins by UV-laser irradiation. The results support the design, optimization, characterization, and fabrication of one-dimensional periodic distributions of biomacromolecules with label-free biosensing capabilities. The proteins that are exposed to that UV-radiation conditions become deactivated but not removed from the substrate, thus producing protein patterns free of topographic contributions, but constituted by a periodic deactivation of the protein activity. This method enables a fast fabrication of large areas of homogeneous protein patterns, whose analytical capabilities as diffractive optical transducers for biosensing are demonstrated by calibration curves with a representative immunoassay in label-free format. The resulting photopatterned protein nanostructures present a particular potential to avoid non-

specific binding issues in the direct analysis of complex biological environments. In addition to provide insights into multiplexed biosensing, these results also introduce the basis for the prospective implementation of this photodenaturation-based patterning principle in alternative laser technologies and applications.

4. Experimental section

4.1. Materials

Sodium phosphate buffer (PBS, 8 mM Na_2HPO_4, 2 mM, 137 mM NaCl, 2.7 mM KCl, pH 7.4), PBS-T (PBS with polysorbate 20 0.05% v/v) and carbonate-bicarbonate buffer (15 mM Na_2CO_3, 34 mM $NaHCO_3$, pH 9.6) were prepared with purified water (Milli-Q, Millipore Iberica, Darmstadt, Germany) and filtered through 0.2 µm polyethersulfone membranes (Merck, Darmstadt, Germany). Bovine serum albumin (BSA), polysorbate 20 (Tween 20), antiBSA IgG produced in rabbit (whole antiserum), human serum albumin (HSA), human IgG, haemoglobin, goat anti-rabbit antibodies labelled with 5 nm gold nanoparticles, and silver enhancers were supplied by Sigma-Aldrich (Madrid, Spain). Alexa Fluor® 647 conjugation kit was from abcam (Cambridge, United Kingdom). Polydimethylsiloxane (PDMS) Sylgard 184 was supplied by Dow Corning (Wiesbaden, Germany). Human serum obtained by centrifugation of a pool of blood samples (type AB) from male donors was provided by Sigma-Aldrich (Madrid, Spain). Glass slides (25 x 75 x 1 mm) were purchased from Labbox (Barcelona, Spain).

Glass slides were washed three times by sonication in ethanol (30% in water, 5 min) and dried under a stream of air. Then, protein solutions in carbonate buffer (500 µL, 25 $\mu g \cdot mL^{-1}$) were incubated overnight on the glass slides at 4°C (Figure S1). Finally, glass slides were rinsed with deionized water and dried by air stream.

4.2. Patterning

The periodic deactivation of the protein layers was performed by an optical setup described in Figure S6. Basically, it consists of a continuous wave UV laser (Fred doubled argon laser, 244nm, 100mW adjustable power) (Coherent, Santa Clara, California, USA)

that, after passing through a phase mask (±1 order working principle, 1420 nm period, 2.5 cm length, duty cycle 50%) (Ibsen Photonics, Farum, Denmark), irradiates a protein biolayer created on glass slides. The interference of the $+1^{st}$ and -1^{st} order creates a light intensity pattern which interacts with the biolayer. A cylindrical lens (divergent lens, 2cm focal length) (OptoSigma, Santa Ana, California, USA) is included between the laser and the phase mask to expand the beam along the vertical direction. The power of the laser is measured with an optical power meter Mentor M10 (Scientech-Inc,Boulder, Colorado, USA). In this setup, the glass slide with the biolayer together with the phase mask are placed onto an automatic positioning system (Physik Instrumente GmbH , Karlsruhe, Germany) that moves the incident beam over the samples to be irradiated along the horizontal direction at a controllable velocity.

The irradiation fluence is calculated as (P·W)/(A·V), where P is the power of the laser (27.5, 55, and 100 mW), W is the width of the laser spot on the biolayer along the translational direction of the positioning system (0.1 cm), A is the area of the laser spot on the biolayer (0.1 cm^2), and V is the velocity of the positioning system (from $6 \cdot 10^{-3}$ to 0.4 $cm \cdot s^{-1}$).

4.3. Characterization

The diffractive measurements were performed in a transmission configuration using a simple optomechanical setup illustrated in Figure S6. The glass slides with protein nanopatterns were set to be orthogonally irradiated by a collimated and attenuated (50%) 532 nm laser source (100 mW, MGL-III-532/1, CNI, Changchun, China). The intensity of the diffracted beams was registered using a monochromatic CMOS camera (Edmund eo-1312m, York, UK) and photosensors created from planar silicon photodiodes (SLC-61N2, Silonex Inc., Montreal, Canada). The diffraction efficiency of the protein patterns, i.e. analytical signal, was calculated as the quotient between the intensity of the 1^{st} and 0^{th} diffraction orders. RSD values for each sample were calculated as the ratio between the standard deviation and mean values of three diffraction measurements performed within the patterned area.

These results were compared to protein nanopatterns fabricated by microcontact printing as described elsewhere.[34] Basically, BSA solutions (250 µg·mL^{-1} in PBS) were incubated onto the nanostructured surface of the PDMS stamps for 160 minutes, and after washing them with deionized water and drying them under air stream, they were stamped onto glass slides for 20 minutes. Finally, the glass slides were washed and dried as before.

The mapping of the diffraction efficiency along the whole area was performed with a custom scanning system that sequentially moves the surface and collects the optical signals, as described elsewhere.[41] Two photosensors were incorporated in this case to measure the transmitted 0th and 1st orders (Figure S5) and RSD values were calculated from the diffraction efficiency of all the pixels within the sensing area (20 x 1.2 mm).

For the fluorescence measurements, IgG targets were labelled with Alexa Fluor 647 and incubated on the patterned biolayers. Then, fluorescence images were acquired with a custom fluorescence CCD camera (Retiga EXi camera, Qimaging Inc., Burnaby, Canada) and an oblique LED source (Toshiba TLOH157PToshiba, Tokyo, Japan). The resulting data was analysed with the Genepix Pro 6.0 software (Molecular Devices, San José, California, USA).

The topography of the nanostructures was analyzed by Atomic Force Microscopy (AFM), using a Bruker Multimode 8 microscope (Bruker, Massachusetts, USA) and with RFESPA probes (MPP-21120-10 Bruker), before and after incubating specific targets. AFM images were analyzed using Nanoscope software. To calculate the averaged cross-section profiles, all images were flattened using a first-order polynomial fitting and the height of every data row along the longitudinal direction of the pattern strips was averaged. From these cross-sections, the height modulation is calculated as the average height of the deactivated strips subtracted to the one of the active strips. The duty cycle is calculated as the percentage of the averaged width of the active strips with respect to the period.

4.4. Biorecognition assays

To perform the immunoassays, 500 µL of target IgG (antiBSA) solutions in PBS-T and human serum were incubated onto the photopatterned protein (BSA) biolayers for 15

minutes at room temperature. Then, each slide was rinsed with PBS-T, deionized water, and dried under air stream. That same procedure was followed for the fluorescence assays, but in this case the target IgGs were labelled with a fluorophore (Alexa Fluor® 647) before the assay.

Three replicates of each condition were measured to calculate averaged and standard deviation values. Noise was appraised as the standard deviation from 10 blank measurements (0 $\mu g \cdot mL^{-1}$ of target IgG incubated on 10 different nanostructures) and employed to determine signal-to-noise ratios (SNR). The limits of detection (LOD) and quantification (LOQ) were calculated as the concentrations associated to SNR = 3 and SNR = 10, respectively, from the linear interpolation in the experimental calibration curves.

Acknowledgements

This work was financially supported by the Ministerio de Ciencia e Innovación/Agencia Estatal de Investigación (MCIN/AEI/10.13039/501100011033), co-funded by the European Union ‘‘ERDF A way of making Europe,’’ under grants PID2019-110713RB-I00 and PDI2019-104276RB-I00, and Generalitat Valenciana (PROMETEO/2020/094 and PROMETEO/2019/048). A.J.-D. acknowledges the FPI-UPV 2017 grant program. The authors thank Ángel López Muñoz for the construction of the scanning system.

References

(1) Arrabito, G.; Ferrara, V.; Bonasera, A.; Pignataro, B. Artificial Biosystems by Printing Biology. *Small* **2020**, *16* (27), 1–30. https://doi.org/10.1002/smll.201907691.

(2) Park, J. Y.; Jang, J.; Kang, H. W. 3D Bioprinting and Its Application to Organ-on-a-Chip. *Microelectron. Eng.* **2018**, *200* (August), 1–11. https://doi.org/10.1016/j.mee.2018.08.004.

(3) Lantoine, J.; Procès, A.; Villers, A.; Halliez, S.; Bueé, L.; Ris, L.; Gabriele, S.

Inflammatory Molecules Released by Mechanically Injured Astrocytes Trigger Presynaptic Loss in Cortical Neuronal Networks. *ACS Chem. Neurosci.* **2021**, *12* (20), 3885–3897. https://doi.org/10.1021/acschemneuro.1c00488.

(4) Koroleva, A.; Deiwick, A.; El-Tamer, A.; Koch, L.; Shi, Y.; Estévez-Priego, E.; Ludl, A. A.; Soriano, J.; Guseva, D.; Ponimaskin, E.; Chichkov, B. In Vitro Development of Human IPSC-Derived Functional Neuronal Networks on Laser-Fabricated 3D Scaffolds. *ACS Appl. Mater. Interfaces* **2021**, *13* (7), 7839–7853. https://doi.org/10.1021/acsami.0c16616.

(5) Zierold, R.; Harberts, J.; Fendler, C.; Teuber, J.; Siegmund, M.; Silva, A.; Rieck, N.; Wolpert, M.; Blick, R. H. Toward Brain-on-a-Chip: Human Induced Pluripotent Stem Cell-Derived Guided Neuronal Networks in Tailor-Made 3d Nanoprinted Microscaffolds. *ACS Nano* **2020**, *14* (10), 13091–13102. https://doi.org/10.1021/acsnano.0c04640.

(6) Aebersold, M. J.; Dermutz, H.; Forró, C.; Weydert, S.; Thompson-Steckel, G.; Vörös, J.; Demkó, L. "Brains on a Chip": Towards Engineered Neural Networks. *TrAC - Trends Anal. Chem.* **2016**, *78*, 60–69. https://doi.org/10.1016/j.trac.2016.01.025.

(7) Qiu, S.; Ji, J.; Sun, W.; Pei, J.; He, J.; Li, Y.; Li, J. J.; Wang, G. Recent Advances in Surface Manipulation Using Micro-Contact Printing for Biomedical Applications. *Smart Mater. Med.* **2021**, *2* (November 2020), 65–73. https://doi.org/10.1016/j.smaim.2020.12.002.

(8) Yang, W.; qin, Y.; Wang, Z.; Yu, T.; Chen, Y.; Ge, Z. Recent Advance in Cell Patterning Techniques: Approaches, Applications and Future Prospects. *Sensors Actuators A Phys.* **2021**, No. xxxx, 113229. https://doi.org/10.1016/j.sna.2021.113229.

(9) Delamarche, E.; Pereiro, I.; Kashyap, A.; Kaigala, G. V. Biopatterning: The Art of Patterning Biomolecules on Surfaces. *Langmuir* **2021**, *37* (32), 9637–9651. https://doi.org/10.1021/acs.langmuir.1c00867.

(10) Banerjee, A.; Maity, S.; Mastrangelo, C. H. Nanostructures for Biosensing, with a

Brief Overview on Cancer Detection, IoT, and the Role of Machine Learning in Smart Biosensors. *Sensors* **2021**, *21* (4), 1253. https://doi.org/10.3390/s21041253.

(11) Breault-Turcot, J.; Masson, J. F. Nanostructured Substrates for Portable and Miniature SPR Biosensors. *Anal. Bioanal. Chem.* **2012**, *403* (6), 1477–1484. https://doi.org/10.1007/s00216-012-5963-1.

(12) Kim, D. M.; Park, J. S.; Jung, S. W.; Yeom, J.; Yoo, S. M. =Biosensing Applications Using Nanostructure-Based Localized Surface Plasmon Resonance Sensors. *Sensors* **2021**, *21* (9), 1–27. https://doi.org/10.3390/s21093191.

(13) Wang, Z.; Zong, S.; Wu, L.; Zhu, D.; Cui, Y. SERS-Activated Platforms for Immunoassay: Probes, Encoding Methods, and Applications. *Chem. Rev.* **2017**, *117* (12), 7910–7963. https://doi.org/10.1021/acs.chemrev.7b00027.

(14) Fruncillo, S.; Su, X.; Liu, H.; Wong, L. S. Lithographic Processes for the Scalable Fabrication of Micro- And Nanostructures for Biochips and Biosensors. *ACS Sensors* **2021**, *6* (6). https://doi.org/10.1021/acssensors.0c02704.

(15) Lau, U. Y.; Saxer, S. S.; Lee, J.; Bat, E.; Maynard, H. D. Direct Write Protein Patterns for Multiplexed Cytokine Detection from Live Cells Using Electron Beam Lithography. *ACS Nano* **2016**, *10* (1), 723–729. https://doi.org/10.1021/acsnano.5b05781.

(16) Liu, G.; Petrosko, S. H.; Zheng, Z.; Mirkin, C. A. Evolution of Dip-Pen Nanolithography (DPN): From Molecular Patterning to Materials Discovery. *Chem. Rev.* **2020**, *120* (13), 6009–6047. https://doi.org/10.1021/acs.chemrev.9b00725.

(17) Lucío, M. I.; Montoto, A. H.; Fernández, E.; Alamri, S.; Kunze, T.; Bañuls, M. J.; Maquieira, Á. Label-Free Detection of C-Reactive Protein Using Bioresponsive Hydrogel-Based Surface Relief Diffraction Gratings. *Biosens. Bioelectron.* **2021**, *193* (August). https://doi.org/10.1016/j.bios.2021.113561.

(18) Barbulovic-Nad, I.; Lucente, M.; Sun, Y.; Zhang, M.; Wheeler, A. R.; Bussmann, M. Bio-Microarray Fabrication Techniques - A Review. *Crit. Rev. Biotechnol.* **2006**, *26*

(4), 237–259. https://doi.org/10.1080/07388550600978358.

(19) Bhatt, M.; Shende, P. Surface Patterning Techniques for Proteins on Nano- and Micro-Systems: A Modulated Aspect in Hierarchical Structures. *J. Mater. Chem. B* **2022**, *10* (8), 1176–1195. https://doi.org/10.1039/D1TB02455H.

(20) Sancho-Fornes, G.; Avella-Oliver, M.; Carrascosa, J.; Morais, S.; Puchades, R.; Maquieira, Á. Enhancing the Sensitivity in Optical Biosensing by Striped Arrays and Frequency-Domain Analysis. *Sensors Actuators, B Chem.* **2019**, *281* (October 2018), 432–438. https://doi.org/10.1016/j.snb.2018.10.130.

(21) Alom Ruiz, S.; Chen, C. S. Microcontact Printing: A Tool to Pattern. *Soft Matter* **2007**, *3* (2), 168–177. https://doi.org/10.1039/b613349e.

(22) Perl, A.; Reinhoudt, D. N.; Huskens, J. Microcontact Printing: Limitations and Achievements. *Adv. Mater.* **2009**, *21* (22), 2257–2268. https://doi.org/10.1002/adma.200801864.

(23) Juste-Dolz, A.; Avella-Oliver, M.; Puchades, R.; Maquieira, A. Indirect Microcontact Printing to Create Functional Patterns of Physisorbed Antibodies. *Sensors (Switzerland)* **2018**, *18* (9). https://doi.org/10.3390/s18093163.

(24) Correia, M.; Snabe, T.; Thiagarajan, V.; Petersen, S. B.; Campos, S. R. R.; Baptista, A. M.; Neves-Petersen, M. T. Photonic Activation of Plasminogen Induced by Low Dose UVB. *PLoS One* **2015**, *10* (1), 1–34. https://doi.org/10.1371/journal.pone.0116737.

(25) Heinz, W. F.; Hoh, M.; Hoh, J. H. Laser Inactivation Protein Patterning of Cell Culture Microenvironments. *Lab Chip* **2011**, *11* (19), 3336–3346. https://doi.org/10.1039/c1lc20204a.

(26) Li, Y.; Hong, M. Parallel Laser Micro/Nano-Processing for Functional Device Fabrication. *Laser Photon. Rev.* **2020**, *14* (3), 1900062. https://doi.org/10.1002/lpor.201900062.

(27) Mulko, L.; Soldera, M.; Lasagni, A. F. Structuring and Functionalization of Non-Metallic Materials Using Direct Laser Interference Patterning: A Review.

Nanophotonics **2022**, *11* (2), 203–240. https://doi.org/10.1515/nanoph-2021-0591.

(28) He, J.; Xu, B.; Xu, X.; Liao, C.; Wang, Y. Review of Femtosecond-Laser-Inscribed Fiber Bragg Gratings: Fabrication Technologies and Sensing Applications. *Photonic Sensors* **2021**, *11* (2), 203–226. https://doi.org/10.1007/s13320-021-0629-2.

(29) Juste-Dolz, A.; Delgado-Pinar, M.; Avella-Oliver, M.; Fernández, E.; Pastor, D.; Andrés, M. V.; Maquieira, Á. BIO Bragg Gratings on Microfibers for Label-Free Biosensing. *Biosens. Bioelectron.* **2021**, *176* (December 2020). https://doi.org/10.1016/j.bios.2020.112916.

(30) Gatterdam, V.; Frutiger, A.; Stengele, K.-P.; Heindl, D.; Lübbers, T.; Vörös, J.; Fattinger, C. Focal Molography Is a New Method for the in Situ Analysis of Molecular Interactions in Biological Samples. *Nat. Nanotechnol.* **2017**, *12* (11), 1089–1095. https://doi.org/10.1038/nnano.2017.168.

(31) Incaviglia, I.; Frutiger, A.; Blickenstorfer, Y.; Treindl, F.; Ammirati, G.; Lüchtefeld, I.; Dreier, B.; Plückthun, A.; Vörös, J.; Reichmuth, A. M. An Approach for the Real-Time Quantification of Cytosolic Protein–Protein Interactions in Living Cells. *ACS Sensors* **2021**, *6* (4), 1572–1582. https://doi.org/10.1021/acssensors.0c02480.

(32) Goh, J. B.; Loo, R. W.; Goh, M. C. Label-Free Monitoring of Multiple Biomolecular Binding Interactions in Real-Time with Diffraction-Based Sensing. *Sensors Actuators, B Chem.* **2005**, *106* (1 SPEC. ISS.), 243–248. https://doi.org/10.1016/j.snb.2004.08.003.

(33) Zhou, Z.; Shi, Z.; Cai, X.; Zhang, S.; Corder, S. G.; Li, X.; Zhang, Y.; Zhang, G.; Chen, L.; Liu, M.; Kaplan, D. L.; Omenetto, F. G.; Mao, Y.; Tao, Z.; Tao, T. H. The Use of Functionalized Silk Fibroin Films as a Platform for Optical Diffraction-Based Sensing Applications. *Adv. Mater.* **2017**, *29* (15), 1605471. https://doi.org/10.1002/adma.201605471.

(34) Avella-Oliver, M.; Ferrando, V.; Monsoriu, J. A.; Puchades, R.; Maquieira, A. A Label-Free Diffraction-Based Sensing Displacement Immunosensor to Quantify Low Molecular Weight Organic Compounds. *Anal. Chim. Acta* **2018**, *1033*, 173–

179. https://doi.org/10.1016/j.aca.2018.05.060.

(35) Frutiger, A.; Tanno, A.; Hwu, S.; Tiefenauer, R. F.; Vörös, J.; Nakatsuka, N. Nonspecific Binding - Fundamental Concepts and Consequences for Biosensing Applications. *Chem. Rev.* **2021**, *121* (13), 8095–8160. https://doi.org/10.1021/acs.chemrev.1c00044.

(36) Xiong, Z.; Peng, G. D.; Wu, B.; Chu, P. L. Effects of the Zeroth-Order Diffraction of a Phase Mask on Bragg Gratings. *J. Light. Technol.* **1999**, *17* (11), 2361–2365. https://doi.org/10.1109/50.803031.

(37) Parracino, A.; Gajula, G. P.; di Gennaro, A. K.; Correia, M.; Neves-Petersen, M. T.; Rafaelsen, J.; Petersen, S. B. Photonic Immobilization of Bsa for Nanobiomedical Applications: Creation of High Density Microarrays and Superparamagnetic Bioconjugates. *Biotechnol. Bioeng.* **2011**, *108* (5), 999–1010. https://doi.org/10.1002/bit.23015.

(38) Bujacz, A. Structures of Bovine, Equine and Leporine Serum Albumin. *Acta Crystallogr. Sect. D Biol. Crystallogr.* **2012**, *68* (10), 1278–1289. https://doi.org/10.1107/S0907444912027047.

(39) Goodman, J. W. *Introduction to Fourier Optics*, 4th editio.; WH Freeman, 2017.

(40) Visentin, J.; Couzi, L.; Dromer, C.; Neau-Cransac, M.; Guidicelli, G.; Veniard, V.; Coniat, K. N. le; Merville, P.; Di Primo, C.; Taupin, J. L. Overcoming Non-Specific Binding to Measure the Active Concentration and Kinetics of Serum Anti-HLA Antibodies by Surface Plasmon Resonance. *Biosens. Bioelectron.* **2018**, *117* (June), 191–200. https://doi.org/10.1016/j.bios.2018.06.013.

(41) Sancho-Fornes, G.; Avella-Oliver, M.; Carrascosa, J.; Puchades, R.; Maquieira, Á. Interferometric Multilayered Nanomaterials for Imaging Unlabeled Biorecognition Events. *Sensors Actuators, B Chem.* **2021**, *331* (November 2020). https://doi.org/10.1016/j.snb.2020.129289.

Supporting Information

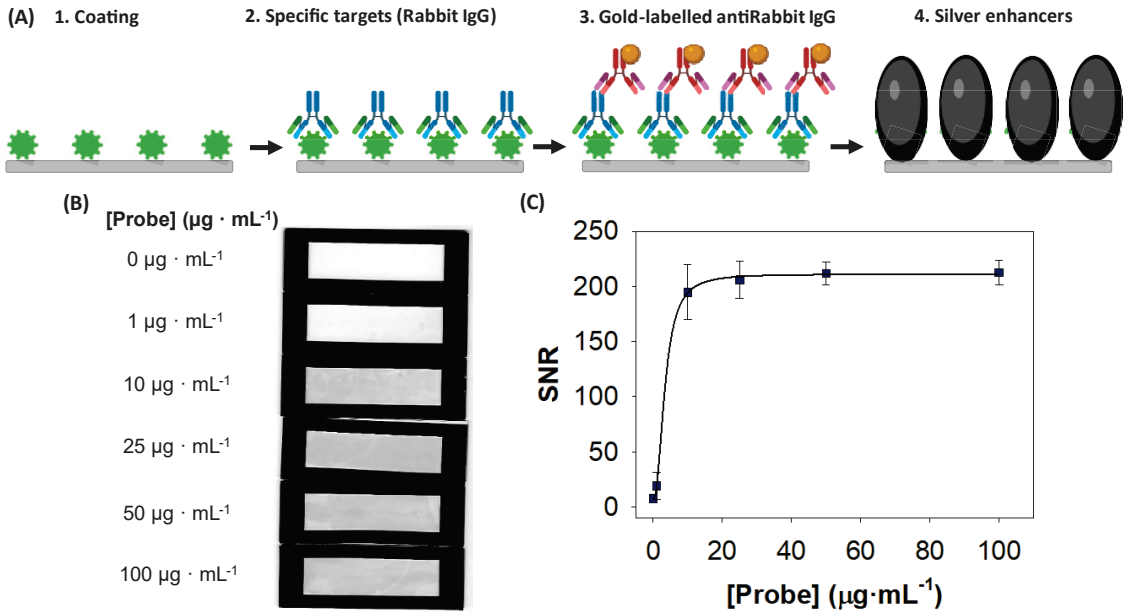

Figure S1. Optimization of the concentration of bioreceptors for surface coating. **(A)** Scheme of the biorecognition assays performed. First, glass slides were coated with different concentrations of BSA (0-100 µg·mL^{-1}) and then incubated with a fixed concentration (10 µg·mL^{-1}) of specific IgGs produced in rabbit. Next, gold-labelled antiRabbit IgGs were incubated to promote the precipitation of metallic silver from a silver solution. **(B)** Coating concentrations and scanned images of the silver-coated slides. **(C)** Signal-to-noise ratios calculated after quantifying the mean grayscale intensity from the scanned images.

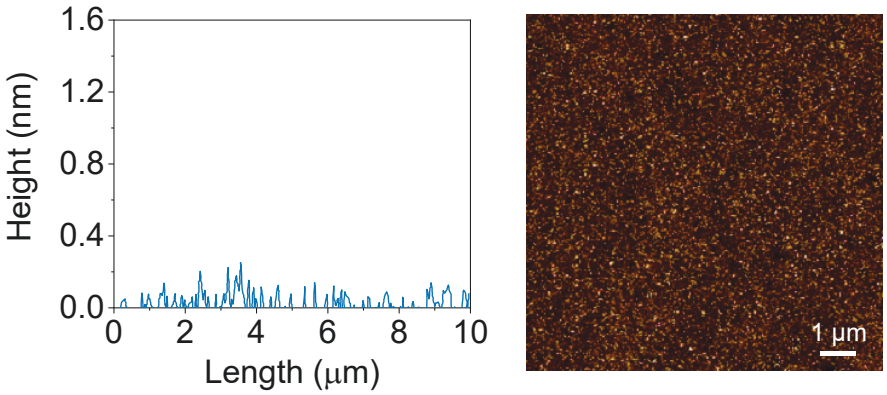

Figure S2. AFM image and height profile of a protein-coated slide after photopatterning with a medium fluence (55 mW, 0.022 cm·s^{-1}).

(A)

10	20	30	40	50
MKWVTFISLL	LLFSSAYSRG	VFRRDTHKSE	IAHRFKDLGE	EHFKGLVLIA
60	70	80	90	100
FSQYLQQCPF	DEHVKLVNEL	TEFAKTCVAD	ESHAGCEKSL	HTLFGDELCK
110	120	130	140	150
VASLRETYGD	MADCCEKQEP	ERNECFLSHK	DDSPDLPKLK	PDPNTLCDEF
160	170	180	190	200
KADEKKFWGK	YLYEIARRHP	YFYAPELLYY	ANKYNGVFQE	CCQAEDKGAC
210	220	230	240	250
LLPKIETMRE	KVLASSARQR	LRCASIQKFG	ERALKAWSVA	RLSQKFPKAE
260	270	280	290	300
FVEVTKLVTD	LTKVHKECCH	GDLLECADDR	ADLAKYICDN	QDTISSKLKE
310	320	330	340	350
CCDKPLLEKS	HCIAEVEKDA	IPENLPPLTA	DFAEDKDVCK	NYQEAKDAFL
360	370	380	390	400
GSFLYEYSRR	HPEYAVSVLL	RLAKEYEATL	EECCAKDDPH	ACYSTVFDKL
410	420	430	440	450
KHLVDEPQNL	IKQNCDQFEK	LGEYGFQNAL	IVRYTRKVPQ	VSTPTLVEVS
460	470	480	490	500
RSLGKVGTRC	CTKPESERMP	CTEDYLSLIL	NRLCVLHEKT	PVSEKVTKCC
510	520	530	540	550
TESLVNRRPC	FSALTPDETY	VPKAFDEKLF	TFHADICTLP	DTEKQIKKQT
560	570	580	590	600
ALVELLKHKP	KATEEQLKTV	MENFVAFVDK	CCAADDKEAC	FAVEGPKLVV
607				
STQTALA				

(B)

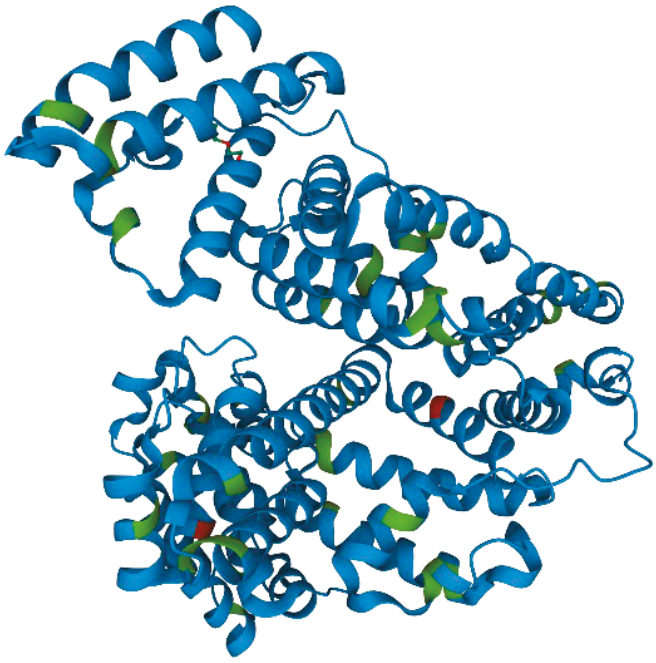

Figure S3. (A) Amino acid sequence of the BSA.[1,2] **(B)** Three-dimensional conformation of the BSA (protein data bank entry 4F5S). In both figures cysteines are represented in green and tryptophans in red color.

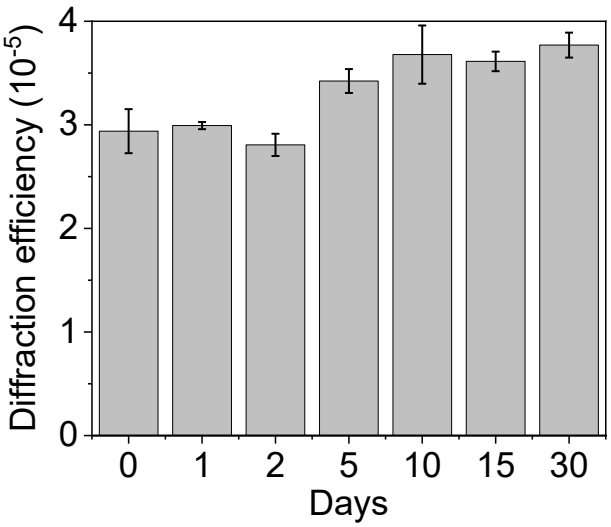

Figure S4. Stability over time. In this experiment, all the BSA patterns were fabricated at the same time (day 0). Then, the diffraction efficiency after incubating specific IgG (antiBSA, 10 µg·mL^{-1} in buffer) was measured after different days.

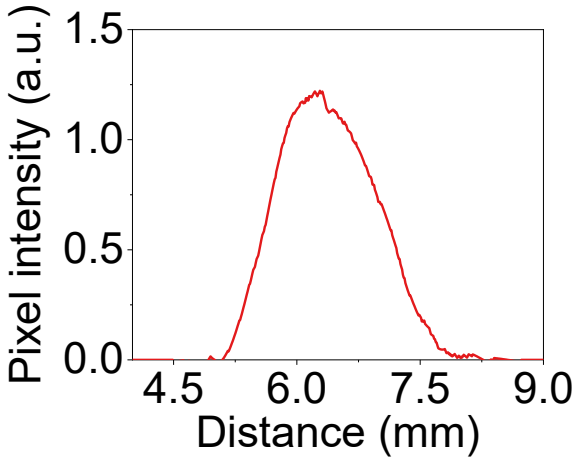

Figure S5. Zoomed view of the cross-section profile of the first-order diffracted spots for a photopatterned BSA biolayer after the incubation of 0 µg mL^{-1} of antiBSA. Note the difference in the vertical scale versus Figure 3C in the main manuscript.

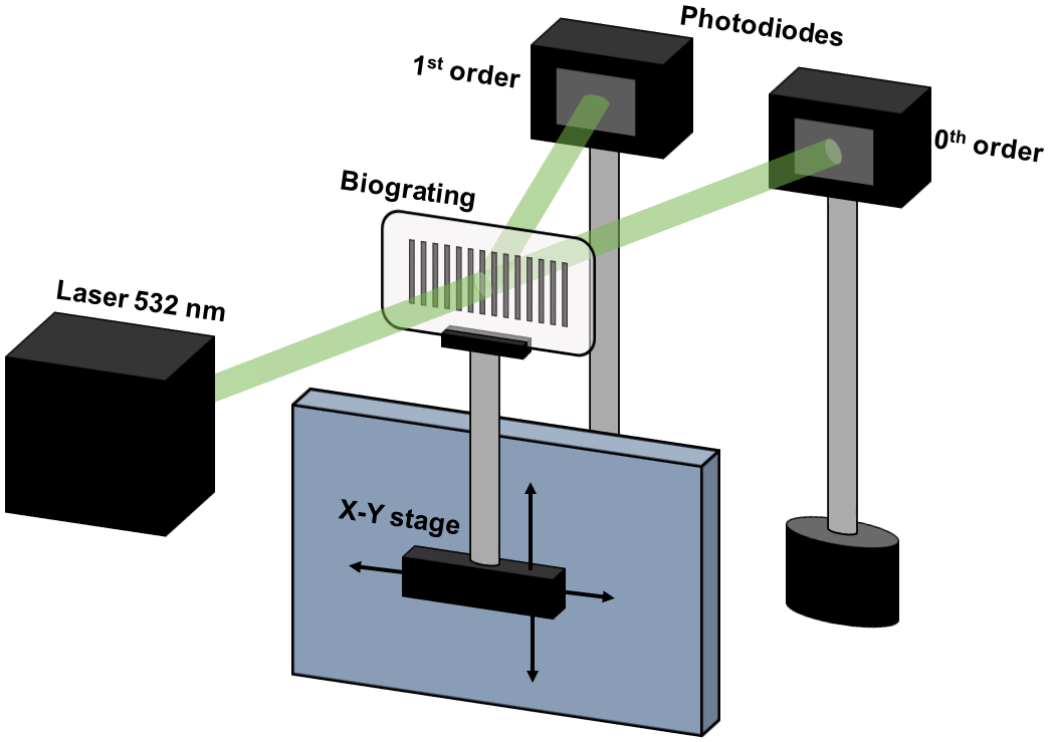

Figure S6. Scheme of the optical setup employed to map the diffraction efficiency of the nanostructures along the patterned area. Glass slides containing the protein patterns were placed in a custom X-Y stage with minimum displacement of 0.5 mm and then irradiated with a 532 nm laser source. The intensity of the zeroth and first diffracted orders was measured employing two photodiodes.

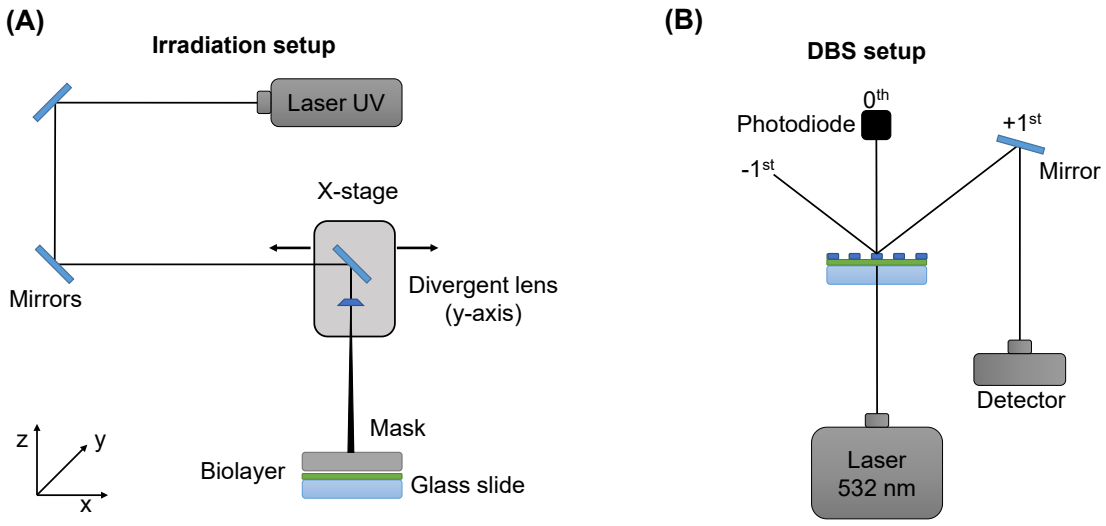

Figure S7. Schemes of **(A)** the irradiation setup for selective protein deactivation and **(B)** the optical setup to quantify the diffraction efficiency of the nanostructures.

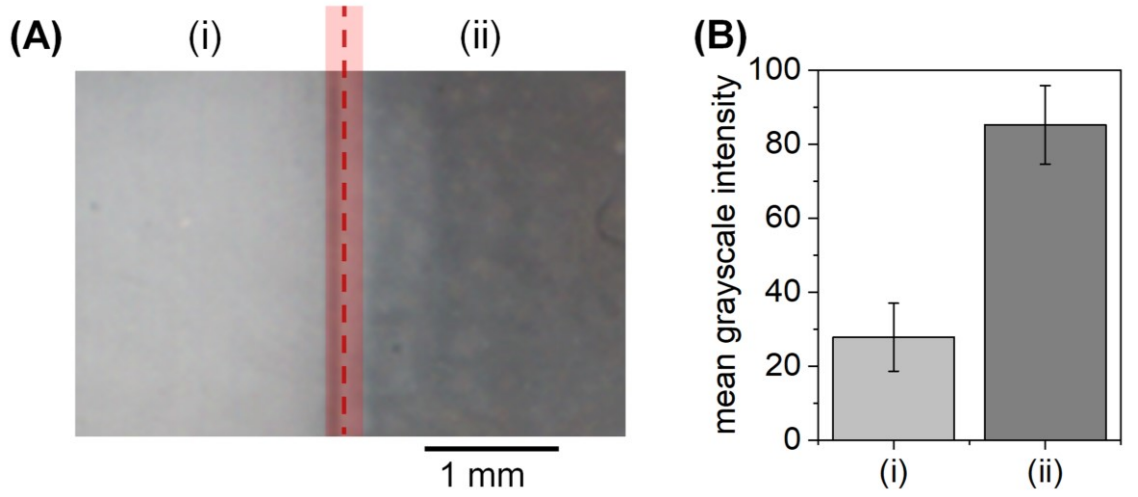

Figure S8. **(A)** Scaned image and **(B)** the resulting grayscale intensity of a BSA biolayer (i) irradiated with a strong fluence (about 66 J·cm^{-2}) and (ii) not irradiated, after perfoming the gold-labelled immunoassay described in the legend of Figure S1. Note that an important contribution of the grayscale intensity measured in the irradiated area may be generated by inspecific precipitation of silver in the signal development stage of this labelled assay.

Table S1. Fabrication conditions and topographic features of the protein patterns measured by AFM.

	Fluence (J·cm^{-2})	**Laser power (mW)**	**Motion velocity (cm·s^{-1})**	**Height modulation (nm)**	**Period (nm)**	**Duty cycle (%)**
Low	0.1	55	0.44	0.49 ± 0.10	711 ± 3	60 ± 3
Medium	2.5	55	0.022	1.25 ± 0.13	709 ± 2	49 ± 3
High	9.9	55	0.011	0.31 ± 0.12	710 ± 2	38 ± 6

Table S2. Comparative table of recent diffractive and non-diffractive label-free biosensing approaches in the state-of-art.

Technique	Target	Limit of detection	Matrix	Reference
SPR	ssDNA	0.1 nM	Buffer	(1)
SPR	kanamycin	285 nM	Buffer	(2)
SPR	HSA	100 ng·mL^{-1}	Buffer	(3)
Focal mology raphy	IgG	1.3 nM	Human plasma	(4)
Diffractive hydrogels	CRP	300 ng·mL^{-1}	Human serum	(5)
Diffractive reflectance	streptavidin	25 nM	Buffer	(6)
Bio Bragg Gratings	IgG	100 ng·mL^{-1}	Buffer	(7)
Diffraction-based sensing	IgG	53 ng·mL^{-1}/ 0.4 nM	Buffer	This work
Diffraction-based sensing	IgG	36 ng·mL^{-1}/ 0.3 nM	Human serum	This work

References

(1) An, N.; Li, K.; Zhang, Y.; Wen, T.; Liu, W.; Liu, G.; Li, L.; Jin, W. A Multiplex and Regenerable Surface Plasmon Resonance (MR-SPR) Biosensor for DNA Detection of Genetically Modified Organisms. *Talanta* **2021**, *231*, 122361. https://doi.org/10.1016/j.talanta.2021.122361.

(2) Écija-Arenas, Á.; Kirchner, E.-M.; Hirsch, T.; Fernández-Romero, J. M. Development of an Aptamer-Based SPR-Biosensor for the Determination of Kanamycin Residues in Foods. *Anal. Chim. Acta* **2021**, *1169*, 338631. https://doi.org/10.1016/j.aca.2021.338631.

(3) Makhneva, E.; Farka, Z.; Pastucha, M.; Obrusník, A.; Horáčková, V.; Skládal, P.; Zajíčková, L. Maleic Anhydride and Acetylene Plasma Copolymer Surfaces for SPR Immunosensing. *Anal. Bioanal. Chem.* **2019**, *411* (29), 7689–7697. https://doi.org/10.1007/s00216-019-01979-9.

(4) Gatterdam, V.; Frutiger, A.; Stengele, K.-P.; Heindl, D.; Lübbers, T.; Vörös, J.; Fattinger, C. Focal Molography Is a New Method for the in Situ Analysis of Molecular Interactions in Biological Samples. *Nat. Nanotechnol.* **2017**, *12* (11), 1089–1095. https://doi.org/10.1038/nnano.2017.168.

(5) Lucío, M. I.; Montoto, A. H.; Fernández, E.; Alamri, S.; Kunze, T.; Bañuls, M. J.; Maquieira, Á. Label-Free Detection of C-Reactive Protein Using Bioresponsive Hydrogel-Based Surface Relief Diffraction Gratings. *Biosens. Bioelectron.* **2021**, *193* (August). https://doi.org/10.1016/j.bios.2021.113561.

(6) Chen, W. T.; Li, S. S.; Chu, J. P.; Feng, K. C.; Chen, J. K. Fabrication of Ordered Metallic Glass Nanotube Arrays for Label-Free Biosensing with Diffractive Reflectance. *Biosens. Bioelectron.* **2018**, *102* (September 2017), 129–135. https://doi.org/10.1016/j.bios.2017.10.023.

(7) Juste-Dolz, A.; Delgado-Pinar, M.; Avella-Oliver, M.; Fernández, E.; Pastor, D.; Andrés, M. V.; Maquieira, Á. BIO Bragg Gratings on Microfibers for Label-Free Biosensing. *Biosens. Bioelectron.* **2021**, *176* (December 2020). https://doi.org/10.1016/j.bios.2020.112916.

Chapter 3

Biogratings on waveguides

Chapter 3: Biogratings on waveguides.

The implementation of optical phenomena in waveguiding structures, such as optical fibers and PICs, introduces new perspectives to conceive miniaturized and compact bioanalytical systems. Thanks to the fertile scientific activity behind the telecommunication sector, a great progress has been achieved in integrating different optical phenomena (SPR, interferometry, diffraction, etc) on waveguides to transduce biorecognition events.

A paradigmatic diffractive approach for biosensing in waveguides relies on inscribing periodic modulations of refractive index in the core material of the guides to sense biorecognition events on their surface (FBG, TFBG, LPFBG). However, creating these periodic modulations on the waveguide surface is rather unexplored, and it has never been reported with biomacromolecules. This doctoral thesis aims to establish an innovative perspective on the existing optical systems by assessing for the first time the implementation of biogratings on waveguides, herein called Bio Bragg gratings (BBG). The potential strengths behind the BBG concept rely on combining the benefits of using waveguides (miniaturization, remote measurements, etc.) with the unique potential of biogratings to avoid the signal contribution from non-specific bindings in real biosensing scenarios.

For that, this chapter first introduces a proof of concept of BBGs using optical fibers as waveguides employing a representative immunoassay together with human serum samples **(Chapter 3.1)**. Then, this thesis explores the implementation of BBGs in photonic integrated platforms constituted by rib waveguides thus pointing towards integrated photonic biosensors based on biogratings **(Chapter 3.2)**.

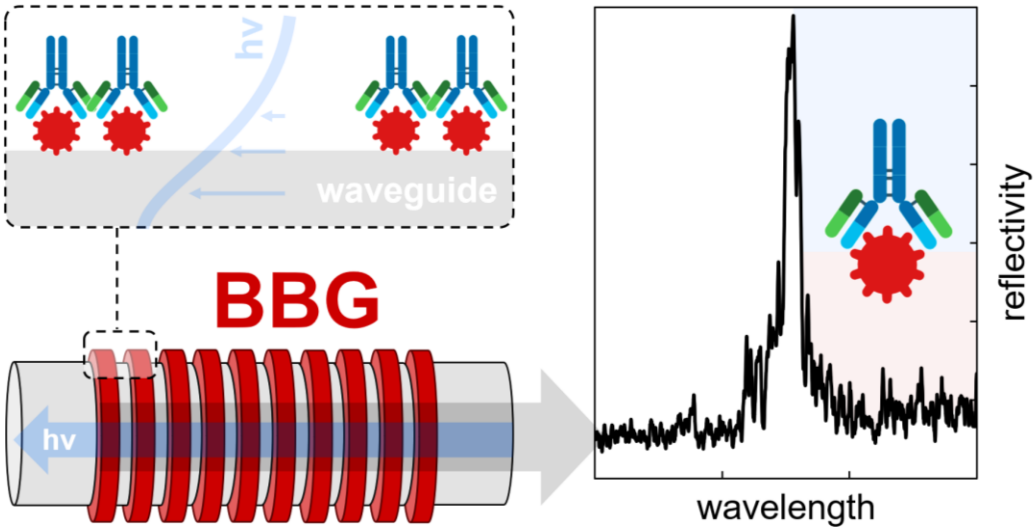

Chapter 3.1: Bio Bragg gratings on microfibers for label-free biosensing

Biosensors and Bioelectronics **2021**, 176, 112916

BIO BRAGG GRATINGS ON MICROFIBERS FOR LABEL-FREE BIOSENSING

Augusto Juste-Dolz[1], Martina Delgado-Pinar[2], Miquel Avella-Oliver[1,4,*], Estrella Fernández[1], Daniel Pastor[3], Miguel V. Andrés[2], Ángel Maquieira[1,4,**]

[1]Instituto Interuniversitario de Investigación de Reconocimiento Molecular y Desarrollo Tecnológico (IDM), Universitat Politècnica de València, Universitat de València, 46022 Valencia, Spain.

[2]Department of Applied Physics and Electromagnetism-ICMUV, Universitat de València, Burjassot 46100, Spain.

[3]Photonics Research Labs, Universitat Politècnica de València, 46021 Valencia, Spain.

[4]Departamento de Química, Universitat Politècnica de València, 46022 Valencia, Spain.

** Corresponding author.*

*** Corresponding author.*

E-mail addresses: miavol@upv.es (M. Avella-Oliver), amaquieira@qim.upv.es (Á. Maquieira).

Abstract

Discovering nanoscale phenomena to sense biorecognition events introduces new perspectives to exploit nanoscience and nanotechnology for bioanalytical purposes. Here we present Bio Bragg Gratings (BBGs), a novel biosensing approach that consists of diffractive structures of protein bioreceptors patterned on the surface of optical waveguides, and tailored to transduce the magnitude of biorecognition assays into the intensity of single peaks in the reflection spectrum. This work addresses the design, fabrication, and optimization of this system by both theoretical and experimental studies to explore the fundamental physicochemical parameters involved. Functional biomolecular gratings are fabricated by microcontact printing on the surface of tapered optical microfibers, and their structural features were characterized. The transduction principle is experimentally demonstrated, and its quantitative bioanalytical prospects are assessed in a representative immunoassay, based on patterned protein probes and selective IgG targets, in label-free conditions. This biosensing system involves appealing perspectives to avoid unwanted signal contributions from non-specific binding, herein

investigated in human serum samples. The work also proves how the optical response of the system can be easily tuned, and it provides insights into the relevance of this feature to conceive multiplexed BBG systems capable to perform multiple label-free biorecognition assays in a single device.

Keywords: biosensor, diffraction, optical microfiber, immunoassay, non-specific binding, label-free

1. Introduction

The advances in chemistry, biotechnology and nanoscience have introduced exciting strategies to sense biomacromolecules (Mahmoudpour et al., 2019; Xu et al., 2020; Zhang et al., 2020) and the interaction events between them (Bhattacharyya et al., 2019; Escorihuela et al., 2015; Schneider and Niemeyer, 2018). Discovering new nanoscale phenomena to transduce biorecognition processes into measurable signals open new potential venues to materialize the benefits that nanoscience offers in key areas of today's society, such as medicine and pharmacology (Prasad et al., 2019; Wong et al., 2020; Zhang et al., 2020).

The implementation of some optical phenomena for biosensing such as SPR (Nootchanat et al., 2019; Zhao et al., 2019), SERS (Langer et al., 2020; Liu et al., 2020), and light interference (Chen et al., 2019; J. Wang et al., 2020) became the seed of a high scientific activity in the last decades, which have provided a great knowledge on innovative, sensitive and label-free bioanalytical systems. Along these lines, light diffraction is still a promising and rather unexplored phenomena to transduce biorecognition events, as introduced by some investigations focused on diffraction-based sensing (Avella-Oliver et al., 2017, 2018a; Goh et al., 2002, 2005) and focal molography (Frutiger et al., 2020, 2019; Gatterdam et al., 2017).

On the other hand, the integration of transduction principles in optical fibers presents a great potential to conceive miniaturized, inexpensive, low-loss, and compact systems for in-field analysis. This approach constitutes nowadays an important innovation area in the state-of-the-art, for both (bio)chemical and physical sensing (Wang and Wolfbeis, 2020; Zhao et al., 2020). A paradigmatic strategy in this context is to inscribe a periodic

modulation in the refractive index of the core material of optical fibers or microfibers, thus fabricating special fiber Bragg gratings (FBGs), microfiber Bragg gratings, long period gratings and tilted fiber Bragg gratings whose optical response is designed to be sensitive to the presence of analytes in the external medium surrounding the optical device (Bekmurzayeva et al., 2018; Cao et al., 2017; Delgado-Pinar et al., 2017; Liu et al., 2018; Loyez et al., 2020; Malachovská et al., 2015; Sridevi et al., 2015; Sypabekova et al., 2019).

In this study, we present a novel transduction principle to sense biorecognition events based on periodic networks of bioreceptors patterned on the surface of tapered optical fibers, herein called Bio Bragg Gratings (BBGs). As schematized in Fig. 1, the concept behind this idea relies on using a microfiber, whose optical modes present a significant evanescent field in the external medium, and imprinting a periodic biomolecular network along its surface. The fundamental optical mode will interact with the BBG, and it will result on a reflection peak centered at the optical wavelength that fulfills the Bragg condition. The biosensing transduction principle relies on the fact that binding events between the patterned bioreceptors and their targets in solution modify the amount of matter constituting the strips of the BBG (compared to the gaps), thus the presence of the analyte will change the modulation depth of the BBG. Consequently, this system aims to transduce the magnitude of binding events by means of the peak reflectivity. In addition to the novelty, this strategy projects potential prospects for label-free biosensing, with simple and inexpensive materials, and neglecting signal contributions generated by non-specific bindings (Gatterdam et al., 2017).

Herein we present the design, fabrication, and optimization of the BBGs in tapered microfibers, and report our investigations to explore and prove the concept of this biosensing transduction system. This work addresses an optical and functional characterization of the system by both theoretical and experimental studies using a model immunochemical assay. A custom setup is developed to fabricate the BBGs on tapered microfibers, and the structural features of the resulting bioreceptor networks are characterized by electron microscopy. Finally, this study demonstrates the bioanalytical performance of the system, provide insights into prospective biosensing properties of BBGs and discusses them.

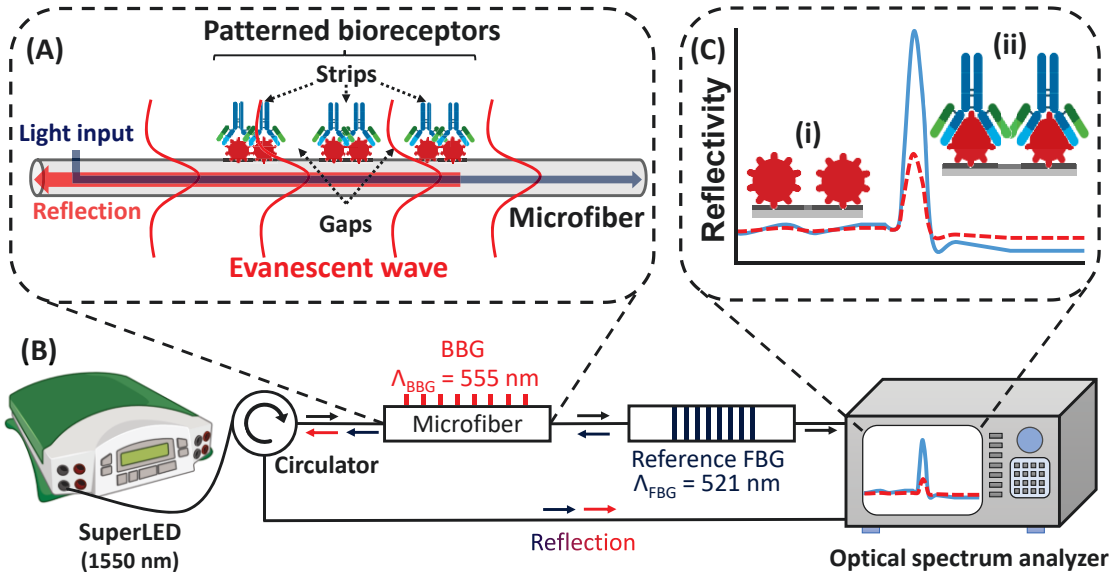

Fig. 1. General illustration of the approach. **(A)** Scheme of a BBG on a microfiber, and its interaction with the guided light. **(B)** Scheme of the detection setup. See Fig. S1 for real images and additional setup details. **(C)** Optical response in the reflection spectrum before (i, and red dashed line) and after (ii, and blue continuous line) incubation and binding of target compounds on the patterned bioreceptors of the BBG. (For interpretation of the references to colour in this figure legend, the reader is referred to the Web version of this article.)

2. Materials and methods

2.1. Materials

Sodium phosphate buffer (PBS, 8 mM Na_2HPO_4, 2 mM, 137 mM NaCl, 2.7 mM KCl, pH 7.4), PBS-T (PBS with polysorbate 20 0.05% v/v), were prepared with purified water (Milli-Q, Millipore Iberica, Darmstadt, Germany) and filtered through 0.2 µm polyethersulfone membranes (Merck, Darmstadt, Germany). Polydimethylsiloxane (PDMS) Sylgard 184 was from Dow Corning (Wiesbaden, Germany). Bovine serum albumin (BSA), polysorbate 20 (Tween 20), antiBSA rabbit IgG, C-reactive protein (CRP), casein and human serum (human male, AB plasma) were supplied by Sigma-Aldrich (Madrid, Spain). Single-mode optical fibers SMF-28 were purchased from Corning (Madrid, Spain). The silicon grooved nanostructure (555.5 nm period, 140 nm groove

depth, duty cycle 50%) used as a master to prepare the micro-contact printing stamp, was from LightSmyth (Eugene, OR, USA).

2.2. Simulations

Electromagnetic simulations to calculate the optical response of the system were carried out by means of finite difference method in the Quasi TE & TM approach, implemented on Matlab™ (Rumpf et al., 2014; Zhu and Brown, 2002). Electromagnetic fields distribution results were validated with commercial software MODE Lumerical (Finite Difference Eigenmode). The overlapping integrals (i.e. proportion of the total field interacting with the Bragg perturbation) were calculated from the obtained field distribution over the complete waveguide and compared with the field localized onto the BBG area. Then, the contradirectional coupling coefficient and the device reflectivity were calculated with the well-known closed form expressions for periodically perturbed waveguides (Erdogan, 1997; Yariv and Yeh, 2007).

An incident wavelength of 1550 nm and refractive indexes of 1.43 for biomolecules (Freeman et al., 2004; Sancho-Fornes et al., 2019) and 1.446 for silica microfibers were considered. For the simulations, the BBGs were defined as 2 mm long periodic (period = 555 nm, duty cycle = 50%) gratings of biomolecules that cover a 90° section of the total azimuthal coordinate of the fiber surface. The thickness of the printed strips in the simulations was considered 1 nm for BSA BBGs (i.e., before target incubation) and 10 nm for BSA-IgG BBGs (i.e., after target incubation) (Avella-Oliver et al., 2018).

2.3. Microfibers

Microfibers were fabricated by tapering standard single mode fibers (Corning SMF-28, 125 µm of diameter) by means of the pull-and-fuse technique. This process consists on the controlled pulling of a conventional fiber, while it is heated up to the plastic deformation temperature of the silica (Fig. S2). As described elsewhere (Birks and Li, 1992), this system allows to obtain uniform microfibers of several centimeters long, with

diameters of the waist down to 1 µm. After fabrication, microfibers were fixed in a custom holder that keep them taut (Fig. S3).

2.4. BBG patterning

Nanostructured networks of bioreceptors (BBGs), constituted by periodic parallel strips of biomacromolecules and empty gaps between them (Fig. 1A), were patterned onto the surface of microfibers by microcontact printing and immobilized. For that, PDMS (elastomer: curing agent, 10:1 w/w) was poured onto the nanogrooved side of the silicon master, degassed in a vacuum chamber for 5 min, and polymerized overnight at 60 °C. Then, the cured polymer was peeled off from the master and cut in 10 × 5 mm pieces, and these stamps were washed three times by sonication in ethanol (30% in water, 5 min) and dried under a stream of air. Probe solutions in PBS (80 µL, 250 $\mu g \cdot mL^{-1}$) were incubated on the structured side of the stamps and after 160 min they were rinsed with deionized water and dried by air stream, thus obtaining BBGs of physisorbed probes on the fiber (Juste-Dolz et al., 2018).

A custom setup was created to pattern the BBGs onto tapered fibers, based on a mechanical elevator that uplifts the inked stamps until their grooved side becomes in contact with the microfiber. A detailed description on the configuration and use of this setup is reported in Fig. S4. The optical response of the system was measured with the detection setup described below and used to monitor the stamping processes (Fig. S5).

The topography of the resulting BBGs was analyzed by Field Emission Scanning Electron Microscopy (FESEM), using a ZEISS ULTRA-55 scanning electron microscope (ZEISS, Oxford Instruments).

2.5. Biorecognition assays

First, to perform and quantify the immunoassays, once fabricated the probe BBGs their optical responses were measured in air (as described in sections 2.6 and 2.7 below). Then, the microfibers containing the BBGs were immersed in 600 µL of liquid samples and incubated for 30 min. A custom incubation chamber made of PDMS was used to

keep the fiber immersed within the liquid samples during the incubations. Subsequently, the fibers were rinsed with PBS-T and deionized water, and dried in air. Finally, the optical response of the BBGs after the biorecognition were measured in air. All the measurements and incubations were performed at room temperature.

2.6. Optical setup

The scheme of the optical setup is shown in Fig. 1B. The optical light was provided by an infrared LED source (1.3 mW continuous wave, central wavelength: 1550 nm, bandwidth > 100 nm), and it was launched to the microfiber through an optical circulator (Thorlabs, operation wavelength: 1550 nm, bandwidth: 90 nm). Thus, both transmission and reflection spectra were measured. An optical spectrum analyser AQ6370D, Yokogawa, 600–1700 nm, minimum resolution 20 p.m., was used to acquire the spectra. An additional FBG, written using UV radiation in the core of commercial photosensitive fiber (Fibercore PS1250) by means of the phase-mask technique, was included in the setup (Fig. S6). The peak intensity of this grating serves as a reference to monitor and correct potential power level changes introduced in the fabrication process and the immunoassays, as well as power level fluctuations (Supplementary Information 7).

2.7. Data acquisition and processing

Transmission and reflection spectra were acquired in each step of the BBGs fabrication and the subsequent biosensing assays. The data was analyzed in both logarithmic and linear scale, and a detailed description of this processing is provided in the Supplementary Information 10. All optical traces were registered within the range 1500–1580 nm with a spectral resolution of 50 p.m., and the variation in the peak reflectivity was used as the analytical signal. This net reflectivity was calculated as the difference between the peak reflectivity registered after patterning the probes, and after incubating the targets, as detailed in the Supplementary Information 7 and Fig. S8.

Noise was estimated as the standard deviation from 10 blank measurements (0 $\mu g \cdot mL^{-1}$ of target IgG incubated on BBGs fabricated on 10 different fibers) that we employed to

infer signal-to-noise ratios (SNR). Limits of detection and quantification were calculated from experimental dose-response curves as the concentrations associated to SNR = 3 and SNR = 10, respectively.

3. Results and discussion

3.1. Microfibers design

The diameter of the microfiber is a key parameter in this BBG concept, since it determines the fraction of light in the evanescent field of the optical mode. It will ultimately affect the magnitude of the diffractive interaction with the bioreceptors and define the performance of resulting the biosensing transduction. Hence, theoretical calculations were performed beforehand experimental assessments to set the starting working conditions.

Firstly, the overlap integral between the fundamental optical mode (LP01) and the diffractive nanostructure of bioreceptors (BBG) on the microfiber was calculated as a function of the diameter of the microfiber. As shown in Fig. 2A, as the diameter increases, the stronger confinement of the mode within the microfiber leads to a negligible overlap integral. However, when the microfiber diameter becomes comparable to the light wavelength, the evanescent field enlarges and the fraction of light overlapping the BBG displays an exponential growth. These preliminary insights are also supported by the calculations of the corresponding peak reflectivity of such BBGs (Fig. 2B), where the reflectivity increases (together with the overlap integral) when the fiber diameter decreases.

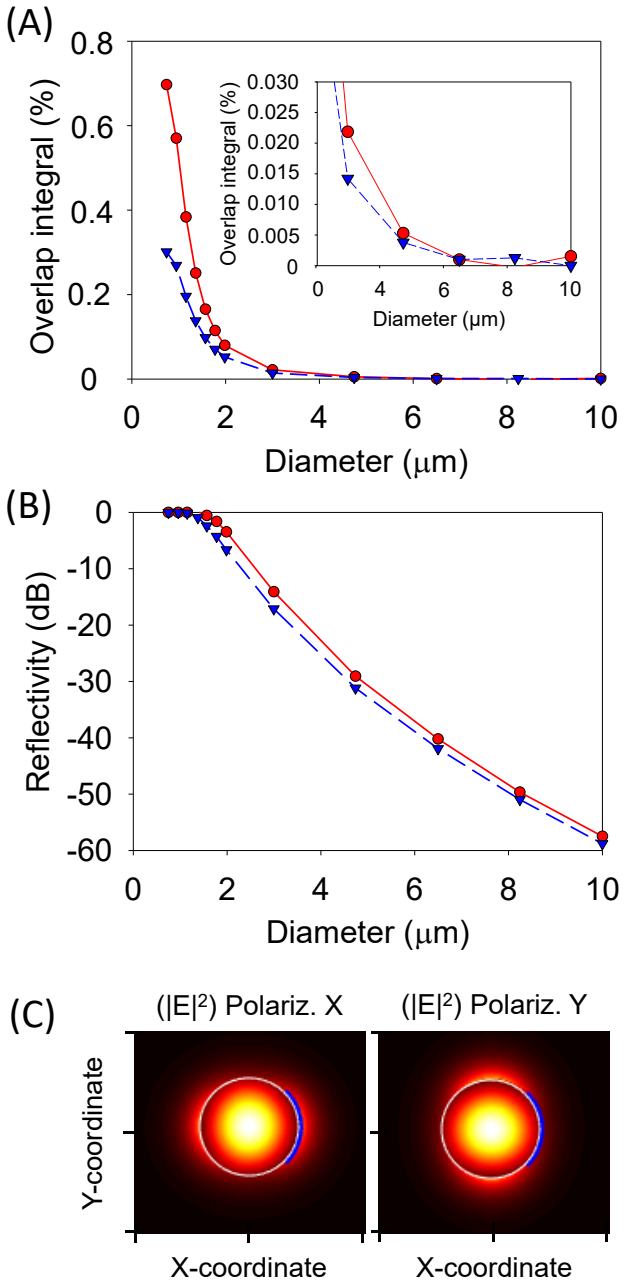

Fig. 2. Simulated optical response for different microfiber diameters. **(A)** Overlap integral and **(B)** reflectivity for the fundamental optical mode, a BBG thickness of 10 nm, and at both orientations of the linear polarization of the optical mode (red continuous line for X polarization and blue dashed line for Y polarization). The inset in Fig. 2A zooms in the overlap integral at larger diameters for a better visualization. **(C)** Electric field intensity distribution for both polarizations in a 1 μm microfiber. The blue line at the right side of both plots, represents the microfiber section covered by the BBG. (For interpretation of the references to colour in this figure legend, the reader is referred to the Web version of this article.)

The BBG is located at one side of the fiber, which leads to an anisotropic system whose optical response must be dependent on the orientation of the linear polarization of the optical mode, partly due to the different position of the evanescent tail of the mode for each polarization (see Fig. 2C). Therefore, to perform a rigorous analysis, the optical response in both linear polarizations (X and Y) were also calculated together with the overlap integral and the peak reflectivity. As observed in Fig. 2A and B, for a 3 µm diameter there is difference of around 3 dB in the peak intensity between the two polarizations, which corresponds to a reduction in the fields overlapping of about a 50% and highlights the role of the polarization in this system. However, the anisotropic behavior of the BBG was not observed in the subsequent experimental immunoassays (section 3.3).

From these results and considering the manipulation feasibility of microfibers below 1 µm, fiber diameters from 2 to 5 µm were selected to experimentally investigate the BBG concept.

3.2. Structural and functional characterization of the BBGs

A critical step in this approach is the BBG patterning, and herein we address it by microcontact printing. This is an important and versatile technique in the state-of-art (Lamping et al., 2019; Wang et al., 2020b), widely used to create functional and homogeneous patterns of biomolecules onto flat substrates of different compositions (Juste-Dolz et al., 2018). However, it remains challenging to pattern biomacromolecules onto curved, fragile, and micrometric structures as microfibers. In this work we successfully addressed this issue with a half-assisted setup that allows a practical manipulation of the microfibers and monitors the transmission spectrum of the optical device as a feedback system to control the nanoscopic patterning process taking place on the fiber surface. For this assessment, we patterned BBGs of physisorbed bovine serum albumin (BSA) probes on 5 µm microfibers.

As can be seen in Fig. 3, homogeneous periodic grooved structures are generated onto the surface of the microfiber, where darker vertical lines are the protein strips of the BBG, and the greyish ones are the gaps between them. A grating period (Λ_{BBG}) of 556 ± 1 nm was calculated from FESEM images (Fig. 3B), which agrees with the period of the

original master structure (555 nm). However, as protein strips are thinner than the gaps the duty cycle becomes slightly lower (35%), and this structural difference can be attributed to the weak contact between the stamp and the microfiber. Moreover, due to the curvature of the microfiber, a maximum angular surface coverage of 90° may be reached with this patterning method. Therefore, our results bear witness to the ability of microcontact printing for generating patterned networks of biomolecules even on fragile and non-flat micrometric surfaces.

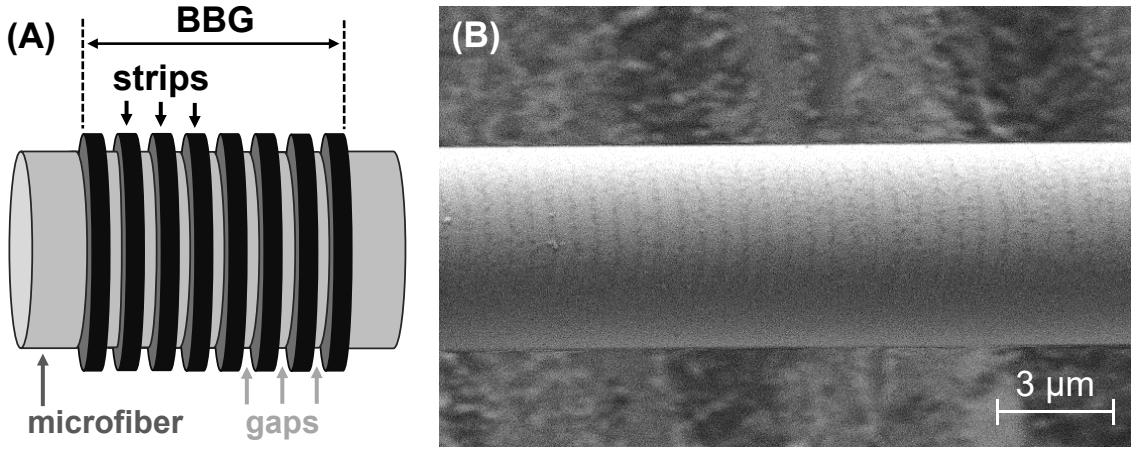

Fig. 3. (A) Scheme of a BBG fabricated on a microfiber and **(B)** FESEM image of a BSA BBG patterned onto a 5 µm microfiber.

In order to monitor and optimize the fabrication process, we measured the optical response of the BBGs by means of the collection of reflection and transmission spectra at each step of their fabrication and the subsequent biorecognition assay on a 3 µm microfiber. At first, only the reflection peak corresponding to the reference FBG (1564 nm, Fig. 4 i) is observed. An additional intense reflection peak appears at 1537 nm during the BBG stamping step (Fig. S9), which meets the Bragg condition and confirms an effective contact of the grooved stamp on the surface of the microfiber. After the stamping, this peak remains in the reflection spectrum (Fig. 4 ii), which corroborates the transfer of the stamped bioreceptor and the proper structuration of the resulting BBG. This initial BBG peak reaches a -27 dB level respect to the reference, and this reflectivity drop agrees with the lower thickness and refractive index contrast of patterned proteins, compared to the grooved PDMS stamp in the previous stage.

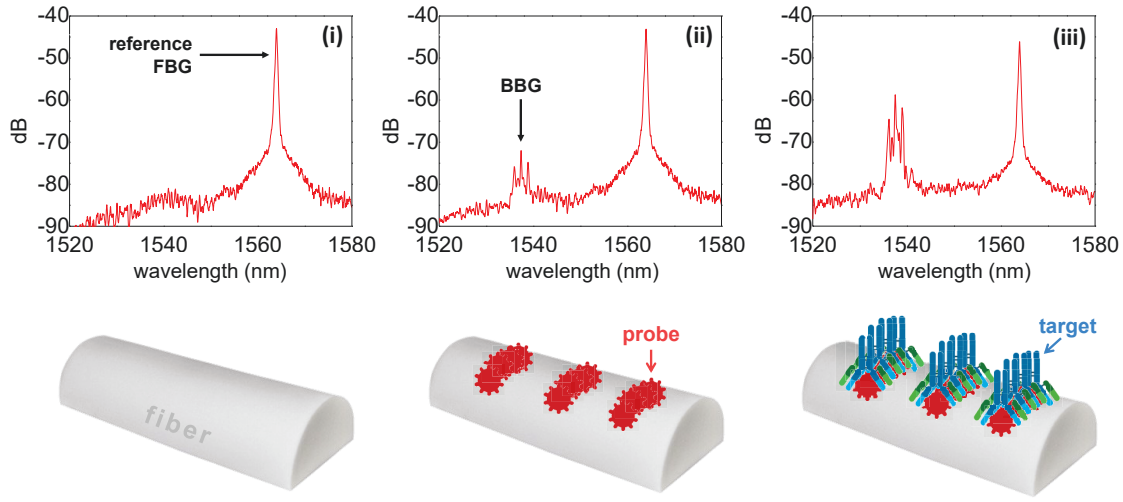

Fig. 4. Experimental reflection spectra obtained at (i) Initial step, (ii) after the patterning a BBG of BSA, and (iii) after incubating specific antiBSA IgGs (10 µg mL^{-1}). Schematic illustrations of the fiber and the BBG at each step is represented below each corresponding spectrum.

Finally, the incubation of selective IgGs on the patterned protein displays an important enhancement of the BBG reflection peak that reaches a -13 dB level respect to reference (14 dB increase), as shown in Fig. 4 iii. According to the starting hypothesis, this enhancement must come from the greater amount of biological matter in the BBG strips generated by the biorecognition between the patterned probes and their targets in solution. Furthermore, this reflectivity enhancement is not observed after incubating only PBS-T buffer (Fig. S10). It is important to highlight here that this result constitutes the first experimental proof of bioanalytical transduction principle investigated in this study. Besides, the reflectivity of the reference FBG peak was used as a reference signal along the whole process, as well as to monitor any significant optical loss in the system.

3.3. Experimental performance

As a preliminary experimental prove towards real biosensing, we explored how the thickness of the biological layer that constitutes the BBG strips affects the optical response. For that, BBGs of proteins with a range of molecular weights (from 24 to 118

kDa) were patterned on different microfibers, and the intensity of the resulting reflection peak was compared. The results of this experiment (Fig. S11) show that the resulting peak reflectivity increases together with the molecular weight of the proteins (i.e., the amount of matter on the BBG strips), as expected and necessary for the success of this transduction system.

As discussed above, the intensity of the BBG peak in the reflection spectrum is predicted to decay as the diameter of the microfiber increases (Fig. 2B), and only BBG reflectivities produced in microfibers with diameters below 5 µm may be detected with standard equipment. This is a crucial issue since greater analytical signals in the biorecognition transduction will potentially enhance the sensitivity of the resulting bioanalytical systems. As observed in Fig. 5A, the simulated trend is also observed in experimental conditions. The divergencies between both trends were attributable to the fact that simulations are unable to consider the experimental uncertainty. Although maximum reflectivities for fiber diameters of 2 µm (and below) are displayed by the theoretical calculations, we have experimentally observed that these microfibres are much more fragile and lead to higher optical losses in the BBGs patterning and the subsequent sample incubations. Hence, 3 µm microfiber diameter was considered the best option.

However, although thoroughly checked, negligible changes in the optical response (both in amplitude and wavelength position) were observed for different linear polarizations when experimentally measuring bioreceptor BBGs, even after interacting with high concentrations of their target IgGs. In particular, it was confirmed by experimental results that the Bragg wavelength splitting is only observed in high-contrast gratings, as the ones resulting from the contact between the grooved PDMS and the fiber in the first step of the BBG patterning (Fig. S4). It is possible that a random polarization conversion in the grating region is behind the lack of significant polarization effects. Therefore, the polarizing elements were omitted in the optical setup for measuring BBG biorecognition assays in experimental conditions.

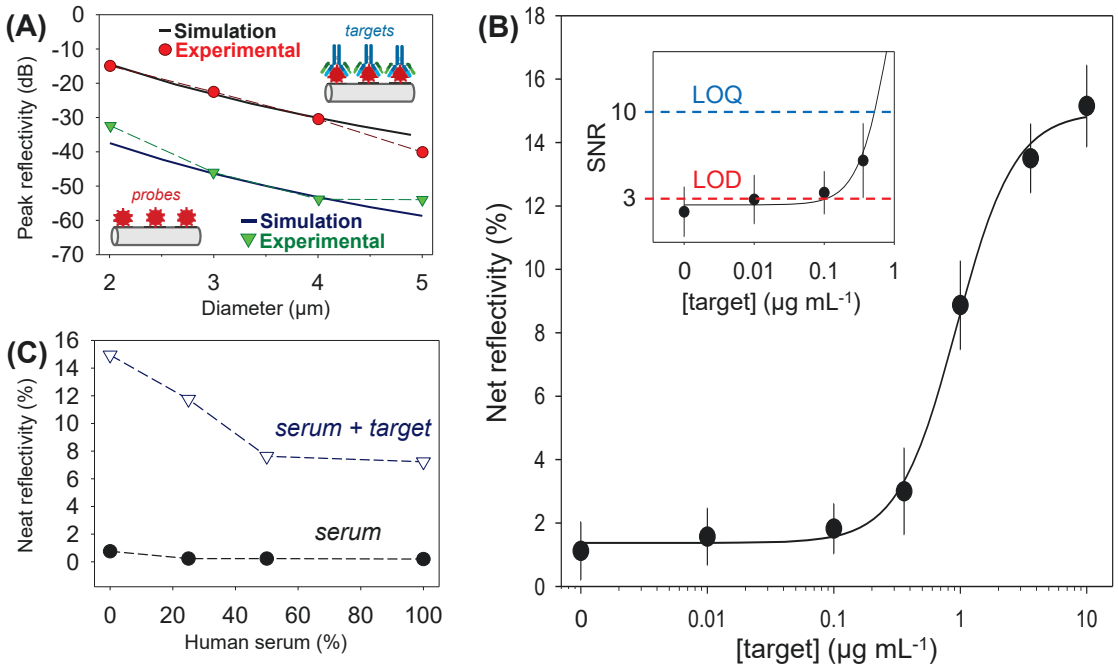

Fig. 5. (A) BBG peak reflectivities of patterned BSA probes before (green triangles) and after (red circles) incubating a solution of specific IgG (10 μg·mL^{-1}), for a range of fiber diameters. Blue and black continuous lines represent the corresponding simulated data considering BBG thicknesses of 1 and 10 nm, respectively. **(B)** Experimental dose-response immunoassay curve, fitted to a sigmoidal (logistic 4 parameters) regression. **(C)** Net reflectivity achieved after incubating different dilutions of human serum in PBS-T buffer onto BBGs without (black circles) and with specific IgG (10 μg·mL^{-1}, blue empty triangles). (For interpretation of the references to colour in this figure legend, the reader is referred to the Web version of this article.)

3.4. Immunosensing

The biosensing capabilities were studied by means of an experimental dose-response curve using a representative model immunoassay based on BBGs of patterned BSA probes and specific antiBSA IgGs as targets. A set of 3 μm microfibers were individually fabricated, patterned with the BSA probes, and incubated with different concentrations of target. As shown in Fig. 5B, the increase of the peak reflectivity is proportional to the target concentration, achieves a maximal reflectivity of 15%, and correlates well with the expected trend for a biorecognition dose-response curve (R^2 = 0.997). This indicates

that the reproducibility in the fabrication and testing processes is high. From these results, experimental detection and quantification limits of 0.1 $\mu g \cdot mL^{-1}$ and 0.4 $\mu g \cdot mL^{-1}$, respectively, of IgG in label-free conditions are inferred. This is a promising sensitivity which is in the range of other recent label-free optical approaches (Chen et al., 2018; Gatterdam et al., 2017; Juste-Dolz et al., 2018; Makhneva et al., 2019).

An important issue in biosensing are the problems associated to non-specific binding (NSB) (Hirst et al., 2008; Mittal et al., 2013). This is especially critical in label-free systems and biological samples, which commonly comprise a high content of biomacromolecules that adsorb on the sensor surface and generate signals that cannot be discriminated from the ones originated by the biorecognition of interest. A unique feature of diffractive bioanalytical systems is their potential to minimize signal contributions generated by NSB (Gatterdam et al., 2017). Unlike specific biorecognition of targets in the probe strips, NSB is a random process prone to take place evenly in the BBG strips and gaps. Therefore, in a first approximation, the reduction in the refractive index contrast generated by the unspecific adsorption on the gaps becomes compensated by the increase in the refractive index contrast caused by the NSB in the strips. To evaluate the effect of NSB, we studied the response of the system with the model immunoassay under a range of dilutions of human serum (7% of non-specific proteins, potentially interfering lipids, etc.) in PBS-T. Fig. 5C shows that reflectivity drops by half when pure human serum containing specific targets is incubated and it increases until it reaches the level of maximum reflectivity (R = 15%) for pure PBS-T (blue squares). Besides, the same serum dilutions without targets do not involve significant changes in the reflectivity achieved by the BSA pattern itself (Fig. 5C, black squares). These results demonstrate very promising perspectives for label-free detection in complex matrixes, whereas these NSB features could be improved by designing BBGs with a minimal compositional difference between the strips and the gaps. Another interesting feature of this biosensing system is the easy wavelength tunability of its optical response. The Bragg's wavelength of the BBG reflection peak can be controlled by modifying the fiber diameter, in a first approach. As represented in Fig. 6A, a change in the diameter of the fiber induces a variation of the effective refractive index of the optical mode. Thus, a change in the microfiber diameter results in a Bragg's wavelength shift according to the

Bragg condition. Our experimental results using fibers with diameters ranging from 2 to 5 µm match well with the simulations (Fig. 6B), being possible to tune the response within a range of 60 nm (from 1500 to 1560 nm). However, this approach would result in poorer sensitivities for the largest diameters.

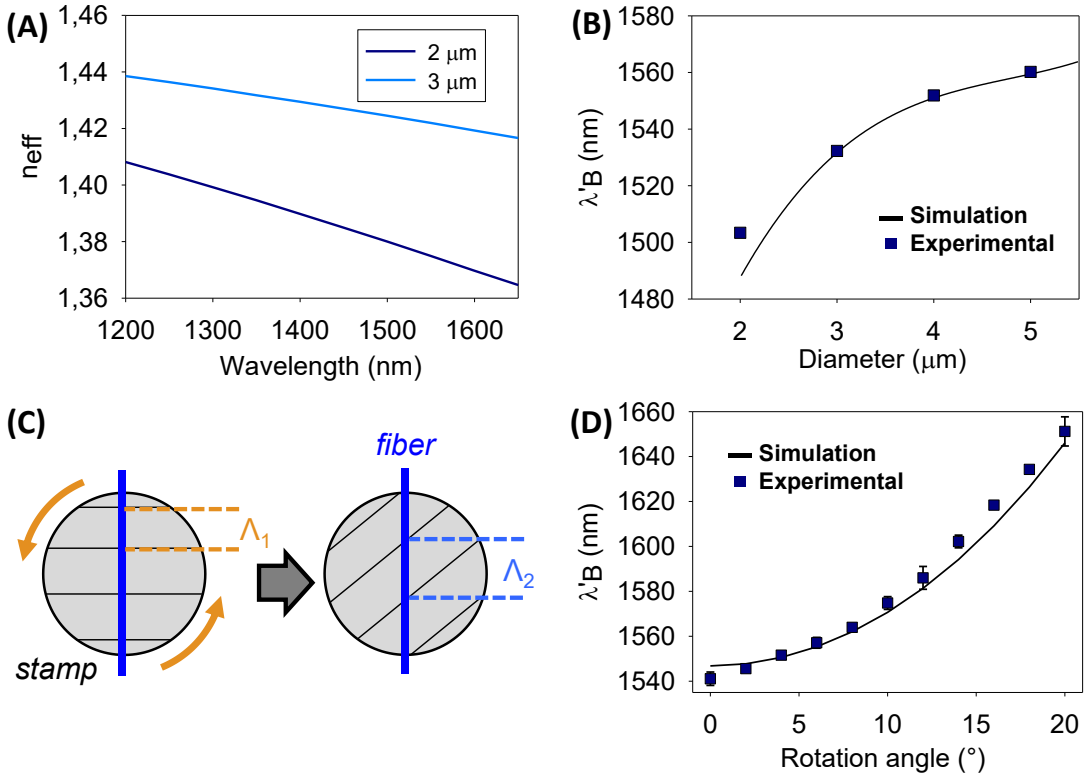

Fig. 6. Tunability of the bioanalytical response. **(A)** Calculated wavelength dispersion of LP01 n_{eff} for two microfiber diameters. **(B)** Experimental Bragg's wavelength of the BBG peaks (after incubating target IgGs at 10 µg·mL^{-1}) in a range of fiber diameters and the corresponding simulated results (strip height of 10 nm). **(C)** Scheme of the variation of the period by rotating the stamp in the BBG patterning. **(D)** Experimental Bragg's wavelength shift measured for different devices. All of them were patterned using a 555 nm period stamp in a 3-µm fiber, by changing the angle between the stamp strips and the axis of the fiber. The simulation shows a sinus trend.

Alternatively, the position of the BBG peak can also be tuned by modifying the BBG period. We found that this parameter can be easily controlled experimentally by just rotating the inked stamp in the stamping step (Fig. 6C), with respect to the longitudinal

axis of the microfiber. This approach allows tuning the Bragg's wavelength accurately, since the reflectivity peak shifts towards longer wavelengths when the rotation angle increases. Also, it involves minimal nanofabrication requirements, when compared to creating a specific master substrate for each period. As shown in Fig. 6D, this tunning strategy permits to shift the position of the BBG peak up to 120 nm in 20°.

In addition to provide versatility in terms of the optical instrumentation compatible with this bioanalytical approach, this tunability introduces interesting capabilities for performing multiplexed assays. For example, the reflection peaks of multiple assays could be acquired in a single measurement, and effectively discriminated by combining BBGs with different periods in the same microfiber (Fig. 7A). To explore it, two BBGs were created on a single microfiber with two different stamp rotation angles (5° and 15° degrees), which resulted in different Λ_{BBG} (558 nm and 575 nm, respectively), in experimental immunoassay conditions.

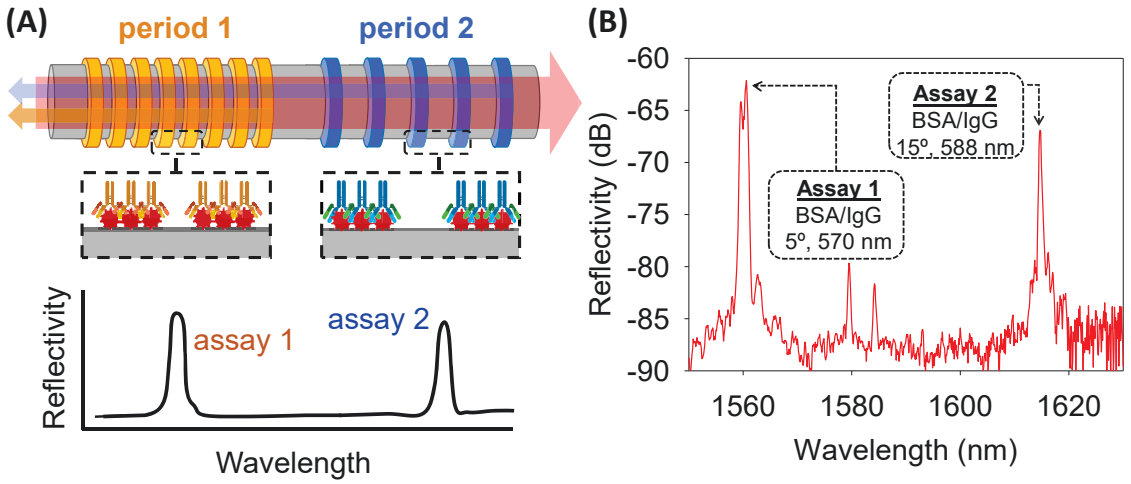

Fig. 7. Assay multiplexing by patterning different BBG periods in a single microfiber. **(A)** Schematic illustration of the approach. **(B)** Experimental reflection spectra obtained with the model immunoassay after incubating the target IgG (10 µg·mL^{-1}) in two different BBGs patterned on a single fiber.

As shown in Fig. 7B, two main peaks were obtained, each one of them transducing the biorecognition event of a different assay. The peak at 1615 nm corresponds to the immunoassay with a shorter BBG period (558 nm) and the 1650 nm peak to the longer

period one (575 nm). Both peaks can be discriminated and quantified in the reflection spectrum of a single measurement, and this prove aims to open the door for prospective BBG systems integrating multiple BBGs tuned to spread across the reflection spectrum in order to perform and quantify multiple label-free assays for different targets in a single step.

4. Conclusions

This work introduces and demonstrates Bio Bragg Gratings for biosensing, a new physicochemical principle to transduce biorecognition events, based on diffractive networks of bioreceptors patterned on optical waveguides. The results of this theoretical and experimental study support the design, optimization, characterization and fabrication of functional biosensing systems capable of transducing unlabeled immunoassays as a peak in the reflection spectra. The approach is herein implemented in microfibers (1–5 μm in diameter) fabricated from standard optical fibers, which is an extremely inexpensive material that ensures a low optical loss and projects interesting perspectives for integration in telecommunication systems. This work also demonstrates the capability of micro-contact printing to pattern biomacromolecules onto fragile and non-flat microstructures. Different devices were fabricated and tested individually in a model immunoassay based on protein probes and IgG targets, and the results display well-correlated quantitative dose-response curves in label-free conditions. This biosensing approach presents appealing perspectives to avoid signal contributions from non-specific binding in the analysis of complex biological samples, as shown in this study with human blood serum. Besides, the wavelength response of the sensor can be easily tuned by modifying the microfiber diameter or the period of the biomolecular grating, and the results demonstrate that this tunability provides an interesting solution to perform multiplexed assays on a single fiber. In addition to introduce new biosensing possibilities for fiber-based developments, this investigation provides the basis for a prospective implementation of this transduction system in other waveguide materials and devices to conceive new integrated biosensors.

Acknowledgements

Spanish Ministry of Science and Innovation (CTQ2016-75749-R and TEC2016-80385-P), Agencia Estatal de Investigación and Fondo Europeo de Desarrollo Regional (PID2019-110877 GB-I00 and PDI2019- 104276RB-I00) and Generalitat Valenciana (PROMETEO/2019/048 and PROMETEO/2017/103). A.J.-D. acknowledges the FPI-UPV 2017 grant program, M.A.-O acknowledges the APSOSTD/2019 program of the GVA.

References

Avella-Oliver, M., Carrascosa, J., Puchades, R., Maquieira, A., 2017. Diffractive protein gratings as optically active transducers for high-throughput label-free immunosensing. Anal. Chem. 89, 9002–9008. https://doi.org/10.1021/acs.analchem.7b01649.

Avella-Oliver, M., Ferrando, V., Monsoriu, J.A., Puchades, R., Maquieira, A., 2018. A label-free diffraction-based sensing displacement immunosensor to quantify low molecular weight organic compounds. Anal. Chim. Acta 1033, 173–179. https://doi. org/10.1016/j.aca.2018.05.060.

Bekmurzayeva, A., Dukenbayev, K., Shaimerdenova, M., Bekniyazov, I., Ayupova, T., Sypabekova, M., Molardi, C., Tosi, D., 2018. Etched fiber bragg grating biosensor functionalized with aptamers for detection of thrombin. Sensors 18. https://doi.org/ 10.3390/s18124298.

Bhattacharyya, I.M., Cohen, S., Shalabny, A., Bashouti, M., Akavayov, B., Shalev, G., 2019. Specific and label-free immunosensing of protein-protein interactions with silicon-based immunoFETs. Biosens. Bioelectron. 132, 143–161. https://doi.org/10.1016/j.bios.2019.03.003.

Birks, T.A., Li, Y.W., 1992. The shape of fiber tapers. J. Lightwave Technol. 10, 432–438. https://doi.org/10.1109/50.134196.

Cao, Y., Wang, W., Guo, T., Ran, Y., Feng, X., Guan, B.-O., Yao, J., 2017. High-resolution and temperature-compensational HER2 antigendetection based on microwave

photonic interrogation. Sensor. Actuator. B. 245, 583–589. https://doi.org/10.1016/j.snb.2017.01.085.

Chen, W.T., Li, S.S., Chu, J.P., Feng, K.C., Chen, J.K., 2018. Fabrication of ordered metallic glass nanotube arrays for label-free biosensing with diffractive reflectance. Biosens. Bioelectron. 102, 129–135. https://doi.org/10.1016/j.bios.2017.10.023.

Chen, Y., Liu, J., Yang, Z., Wilkinson, J.S., Zhou, X., 2019. Optical biosensors based on refractometric sensing schemes: a review. Biosens. Bioelectron. 144, 111693. https://doi.org/10.1016/j.bios.2019.111693.

Delgado-Pinar, M., Shi, Q., Poveda-Wong, L., Delgado-Pinar, E., Xu, B., Zhao, J., Cruz, J. L., Andr´es, M.V., 2017. Oligonucleotide-hybridization fiber-optic biosensor using a narrow bandwidth long period grating. IEEE Sensor. J. 17, 5503–5509. https://doi. org/10.1109/JSEN.2017.2723759.

Erdogan, T., 1997. Fiber grating spectra. J. Lightwave Technol. 15, 1277–1294. https://doi.org/10.1109/50.618322.

Escorihuela, J., Gonz´alez-Martínez, M.´A., L´opez-Paz, J.L., Puchades, R., Maquieira, A., Gimenez-Romero, D., 2015. Dual-polarization interferometry: a novel technique to light up the nanomolecular world. Chem. Rev. 115 (1), 265–294. https://doi.org/ 10.1021/cr5002063.

Freeman, N.J., Peel, L.L., Swann, M.J., Cross, G.H., Reeves, A., Brand, S., Lu, J.R., 2004. Real time, high resolution studies of protein adsorption and structure at the solid-liquid interface using dual polarization interferometry. J. Phys. Condens. Matter 16, 4. https://doi.org/10.1088/0953-8984/16/26/023.

Frutiger, A., Blickenstorfer, Y., Bischof, S., Forr´o, C., Lauer, M., Gatterdam, V., Fattinger, C., V¨or¨os, J., 2019. Principles for sensitive and robust biomolecular interaction analysis: the limits of detection and resolution of diffraction-limited focal molography. Phys. Rev. Appl. 11, 1. https://doi.org/10.1103/PhysRevApplied.11.014056.

Frutiger, A., Tschannen, C.D., Blickenstorfer, Y., Reichmuth, A.M., Fatttinger, C., V¨or¨os, J., 2020. Image reversal reactive immersion lithography improves the detection

limit of focal molography: erratum. Opt. Lett. 45, 918. https://doi.org/10.1364/ol.45.000918.

Gatterdam, V., Frutiger, A., Stengele, K.P., Heindl, D., Lübbers, T., V¨or¨os, J., Fattinger, C., 2017. Focal molography is a new method for the in situ analysis of molecular interactions in biological samples. Nat. Nanotechnol. 12, 1089–1095. https://doi.org/10.1038/nnano.2017.168.

Goh, J.B., Loo, R.W., Goh, M.C., 2005. Label-free monitoring of multiple biomolecular binding interactions in real-time with diffraction-based sensing. Sensor. Actuator. B Chem. 106, 243–248. https://doi.org/10.1016/j.snb.2004.08.003.

Goh, J.B., Loo, R.W., McAloney, R.A., Goh, M.C., 2002. Diffraction-based assay for detecting multiple analytes. Anal. Bioanal. Chem. 374, 54–56. https://doi.org/10.1007/s00216-002-1478-5.

Hirst, E.R., Yuan, Y.J., Xu, W.L., Bronlund, J.E., 2008. Bond-rupture immunosensors-A review. Biosens. Bioelectron. 23, 1759–1768. https://doi.org/10.1016/j.bios.2008.02.002.

Juste-Dolz, A., Avella-Oliver, M., Puchades, R., Maquieira, A., 2018. Indirect microcontact printing to create functional patterns of physisorbed antibodies. Sensors 18. https://doi.org/10.3390/s18093163.

Lamping, S., Buten, C., Ravoo, B.J., 2019. Functionalization and patterning of self-assembled monolayers and polymer brushes using microcontact chemistry. https://doi.org/10.1021/acs.accounts.9b00041.

Langer, J., de Aberasturi, D.J., Aizpurua, J., Alvarez-Puebla, R.A., Augui´e, B., Baumberg, J.J., Bazan, G.C., Bell, S.E.J., Boisen, A., Brolo, A.G., Choo, J., Cialla- May, D., Deckert, V., Fabris, L., Faulds, K., Javier García de Abajo, F., Goodacre, R., Graham, D., Haes, A.J., Haynes, C.L., Huck, C., Itoh, T., K¨all, M., Kneipp, J., Kotov, N.A., Kuang, H., Le Ru, E.C., Lee, H.K., Li, J.F., Ling, X.Y., Maier, S.A., Mayerh¨ofer, T., Moskovits, M., Murakoshi, K., Nam, J.M., Nie, S., Ozaki, Y., Pastoriza-Santos, I., Perez-Juste, J., Popp, J., Pucci, A., Reich, S., Ren, B., Schatz, G. C., Shegai, T., Schlücker, S., Tay, L.L., George Thomas, K., Tian, Z.Q., van Duyne, R. P., Vo-Dinh,

T., Wang, Y., Willets, K.A., Xu, C., Xu, H., Xu, Y., Yamamoto, Y.S., Zhao, B., Liz-Marz´an, L.M., 2020. Present and future of surface-enhanced Raman scattering. ACS Nano 14, 28–117. https://doi.org/10.1021/acsnano.9b04224.

Liu, J., Jalali, M., Mahshid, S., Wachsmann-Hogiu, S., 2020. Are plasmonic optical biosensors ready for use in point-of-need applications? Analyst. https://doi.org/10.1039/c9an02149c.

Liu, T., Liang, L.-L., Xiao, P., Sun, L.-P., Huang, Y.-Y., Ran, Y., Jin, L., Guan, B.-O., 2018. A label-free cardiac biomarker immunosensor based on phase-shiftedmicrofiber Bragg grating. Biosens. Bioelectron. 100, 155–160. https://doi.org/10.1016/j.bios.2017.08.061.

Loyez, M., Hassan, E.M., Lobry, M., Liu, F., Caucheteur, C., Wattiez, R., Derosa, M.C., Willmore, W.G., Albert, J., 2020. Rapid detection of circulating breast cancer cells using a multiresonant optical fiber aptasensor with plasmonic amplification. ACS Sens. 5, 454–463. https://doi.org/10.1021/acssensors.9b02155.

Mahmoudpour, M., Ezzati Nazhad Dolatabadi, J., Torbati, M., Pirpour Tazehkand, A., Homayouni-Rad, A., de la Guardia, M., 2019. Nanomaterials and new biorecognition molecules based surface plasmon resonance biosensors for mycotoxin detection. Biosens. Bioelectron. 143, 111603. https://doi.org/10.1016/j.bios.2019.111603.

Makhneva, E., Farka, Z., Pastucha, M., Obrusník, A., Hor´aˇckov´a, V., Skl´adal, P., Zajíˇckov´a, L., 2019. Maleic anhydride and acetylene plasma copolymer surfaces for SPR immunosensing. Anal. Bioanal. Chem. 411, 7689–7697. https://doi.org/10.1007/s00216-019-01979-9.

Malachovsk´a, V., Ribaut, C., Voisin, V., Surin, M., Lecl`ere, P., Wattiez, R., Caucheteur, C., 2015. Fiber-Optic SPR immunosensors tailored to target epithelial cells through membrane receptors. Anal. Chem. 87, 5957–5965. https://doi.org/10.1021/acs. analchem.5b00159.

Mittal, S., Wong, I.Y., Yanik, A.A., Deen, W.M., Toner, M., 2013. Discontinuous nanoporous membranes reduce non-specific fouling for immunoaffinity cell

capture. Small 9, 4207–4214. https://doi.org/10.1002/smll.201300977.

Nootchanat, S., Jaikeandee, W., Yaiwong, P., Lertvachirapaiboon, C., Shinbo, K., Kato, K., Ekgasit, S., Baba, A., 2019. Fabrication of miniature surface plasmon resonance sensor chips by using confined sessile drop technique. ACS Appl. Mater. Interfaces 11, 11954–11960. https://doi.org/10.1021/acsami.9b01617.

Prasad, A., Choi, J., Jia, Z., Park, S., Gartia, M.R., 2019. Nanohole array plasmonic biosensors: emerging point-of-care applications. Biosens. Bioelectron. 130, 185–203. https://doi.org/10.1016/j.bios.2019.01.037.

Rumpf, R.C., Garcia, C.R., Berry, E.A., Barton, J.H., 2014. Finite-difference frequency-domain algorithm for modeling electromagnetic scattering from general anisotropic objects. Prog. Electromagn. Res. 61, 55–67. https://doi.org/10.2528/PIERB14071606.

Sancho-Fornes, G., Avella-Oliver, M., Carrascosa, J., Fernandez, E., Brun, E.M., Maquieira, A., 2019. Disk-based one-dimensional photonic crystal slabs for label-free immunosensing. Biosens. Bioelectron. 126, 315–323. https://doi.org/10.1016/j. bios.2018.11.005.

Schneider, A.K., Niemeyer, C.M., 2018. DNA surface technology: from gene sensors to integrated systems for life and materials sciences. Angew. Chem. Int. Ed. 57, 16959–16967. https://doi.org/10.1002/anie.201811713.

Sridevi, S., Vasu, K.S., Asokan, S., Sood, A.K., 2015. Sensitive detection of C-reactive protein using opticalfiber Bragggratings. Biosens. Bioelectron. 65, 251–256. https:// doi.org/10.1016/j.bios.2014.10.033.

Sypabekova, M., Korganbayev, S., Gonz´alez-Vila, ´A., Caucheteur, C., Shaimerdenova, M., Ayupova, T., Bekmurzayeva, A., Vangelista, L., Tosi, D., 2019. Functionalized etched tilted fiber Bragg grating aptasensor for label-free protein detection. Biosens. Bioelectron. 146, 1–9. https://doi.org/10.1016/j.bios.2019.111765.

Wang, J., Sanchez, M.M., Yin, Y., Herzer, R., Ma, L., Schmidt, O.G., 2020a. Silicon-based integrated label-free optofluidic biosensors: latest advances and roadmap. Adv. Mater. Technol. 5 https://doi.org/10.1002/admt.201901138.

Wang, X., Sperling, M., Reifarth, M., B¨oker, A., 2020b. Shaping metallic nanolattices: design by microcontact printing from wrinkled stamps. Small 16, 1–8. https://doi.org/10.1002/smll.201906721.

Wang, X.D., Wolfbeis, O.S., 2020. Fiber-Optic chemical sensors and biosensors (2015-2019). Anal. Chem. 92, 397–430. https://doi.org/10.1021/acs.analchem.9b04708.

Wong, X.Y., Sena-Torralba, A., ´Alvarez-Diduk, R., Muthoosamy, K., Merkoçi, A., 2020. Nanomaterials for nanotheranostics: tuning their properties according to disease needs. ACS Nano 14, 2585–2627. https://doi.org/10.1021/acsnano.9b08133.

Xu, L., Shoaie, N., Jahanpeyma, F., Zhao, J., Azimzadeh, M., Al Jamal, K.T., 2020. Optical, electrochemical and electrical (nano)biosensors for detection of exosomes: a comprehensive overview. Biosens. Bioelectron. 161 https://doi.org/10.1016/j.bios.2020.112222.

Yariv, A., Yeh, P., 2007. Photonics: Optical Electronics in Modern Communications, 6. Oxford university press, New York.

Zhang, L., Ying, Y., Li, Y., Fu, Y., 2020. Integration and synergy in protein-nanomaterial hybrids for biosensing: strategies and in-field detection applications. Biosens. Bioelectron. 154, 112036. https://doi.org/10.1016/j.bios.2020.112036.

Zhao, Y., Hu, X., Hu, S., Peng, Y., 2020. Applications of fiber-optic biochemical sensor in microfluidic chips: A review. Biosens. Biosens. Bioelectron 166, 112447. https://doi. org/10.1016/j.bios.2020.112447.

Zhao, Y., Tong, R. jie, Xia, F., Peng, Y., 2019. Current status of optical fiber biosensor based on surface plasmon resonance. Biosens. Bioelectron. 142, 111505. https://doi. org/10.1016/j.bios.2019.111505.

Zhu, Z., Brown, T.G., 2002. Full-vectorial finite-difference analysis of microstructured optical fibers. Optic Express 10, 853–864. https://doi.org/10.1364/OE.10.000853.

Supplementary information

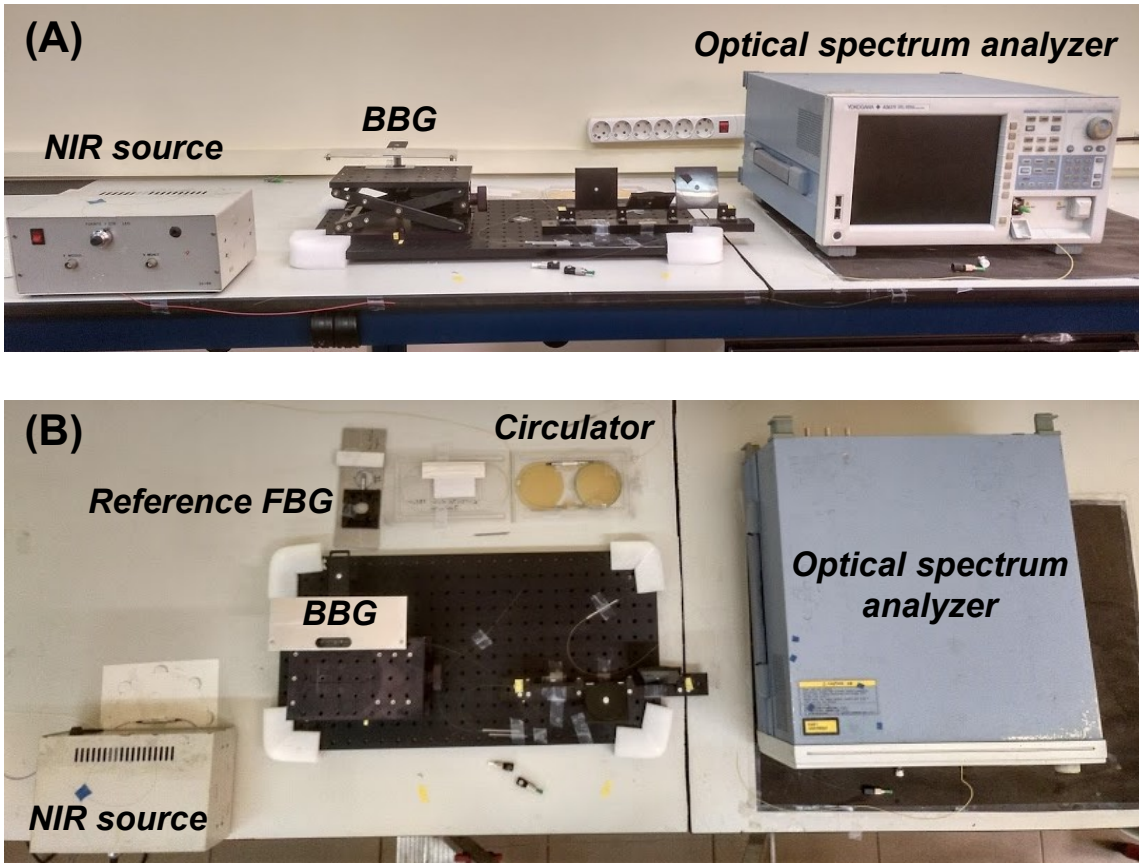

Figure S1. Front **(A)** and top **(B)** view of the optical setup used for the measurement and characterization of the BBGs.

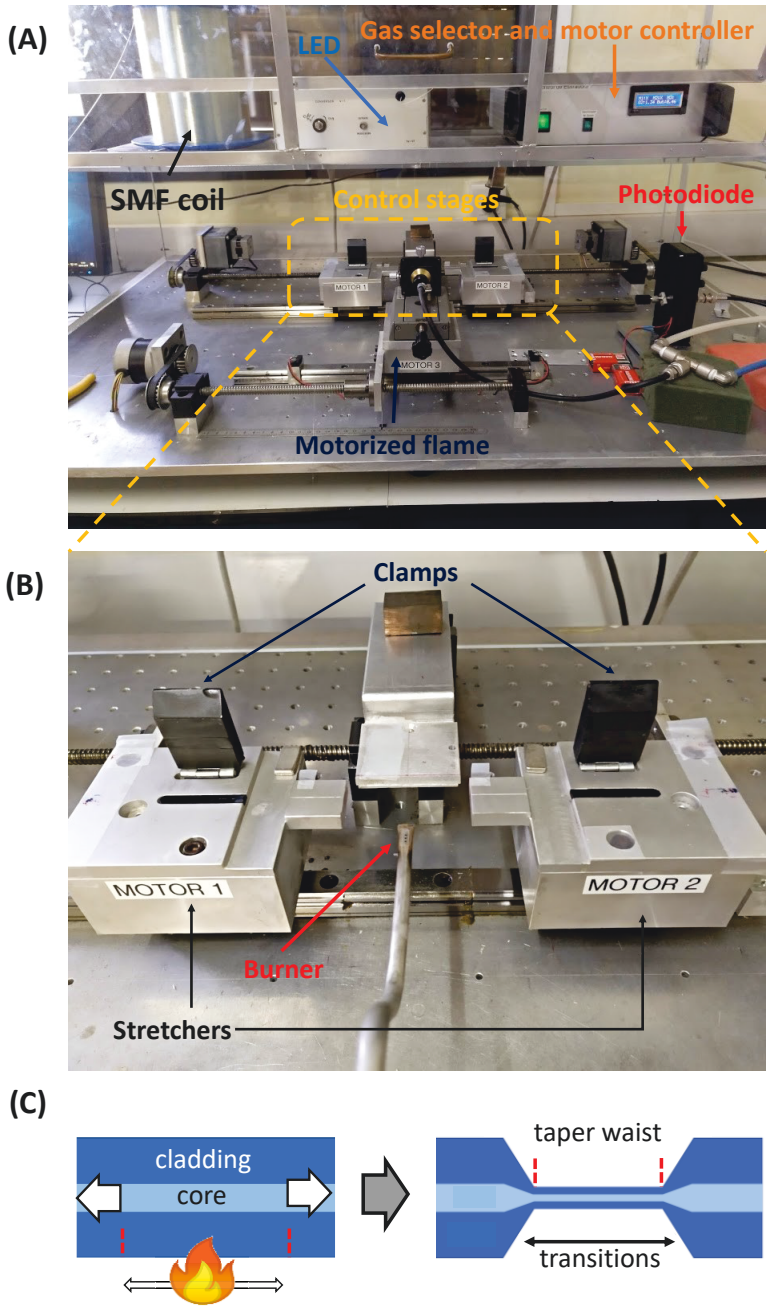

Figure S2. (A) Custom tapering rig station used for the fabrication of tapered optical fibers. The system is fully automatized and it is composed by two gas flow controllers (oxygen and butane) and three motor controllers, one manages the speed of the sweeping flame and the two others control motor the pulling speed of the fiber. An IR LED and an InGaAs photodiode were used for monitoring the losses during taper fabrication. **(B)** Zoomed picture of the stretchers (where the fiber is clamped) and the burner. **(C)** Scheme of the taper fabrication. A single-mode fiber is peeled off, cleaned with acetone, and clamped onto the motorized stretchers. Next, the fiber is stretched while the flame sweeps along the fiber. As a result, the fiber reaches the plastic

deformation temperature of the silica, and the stretching narrows the diameter of the fiber, while maintaining the scale of its internal structure and shape. After fabrication, three regions can be identified: the taper waist (with a uniform, reduced diameter along several centimeters), the non-modified region with the original diameter, and the taper transitions (which are the transition regions from original to final diameters, typically several centimeters long). The shape and length of these transitions can be designed on demand, within certain limits.

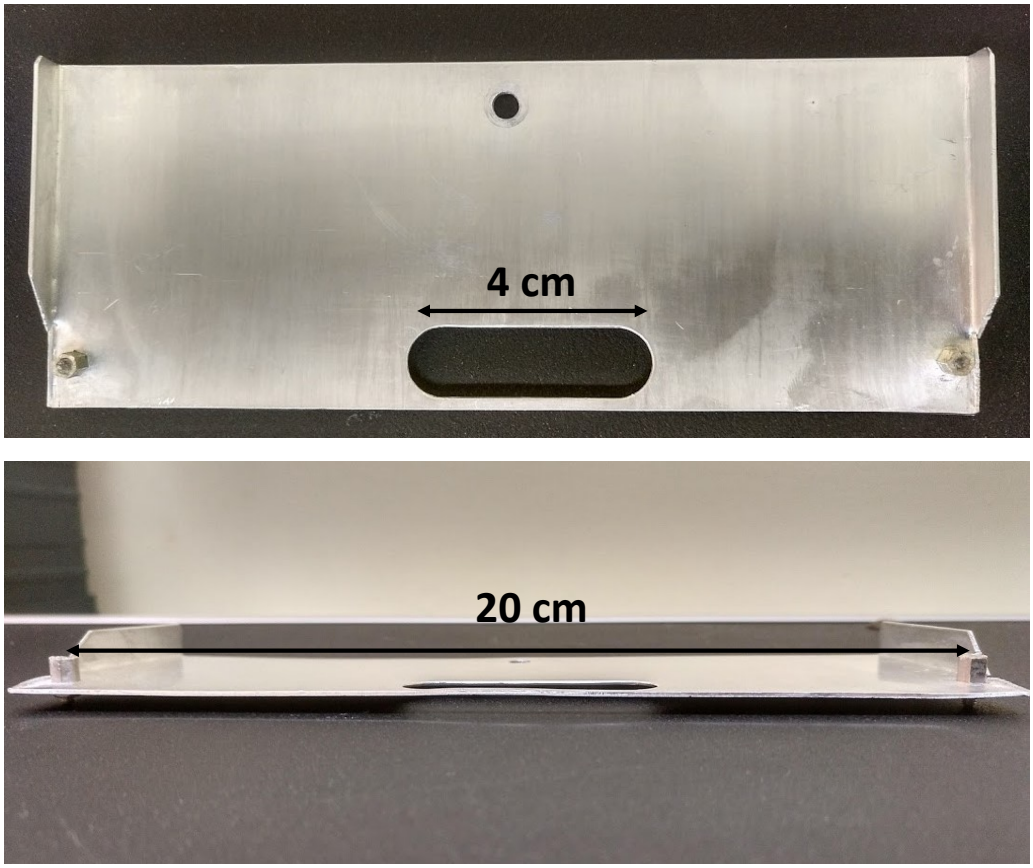

Figure S3. Pictures taken from two different perspectives (top and side) of the custom holder fabricated to keep and manipulate the microfiber. The holder is made of aluminum and has two small cylindrical platforms placed at both ends for fixing the fiber. A 4-centimeter length hole was generated in the middle distance between both platforms to facilitate the contact between the stamp and the hanged fiber. For our experiments, the total length of the tapers including the taper transitions was 20 cm (length of the waist: 2 cm).

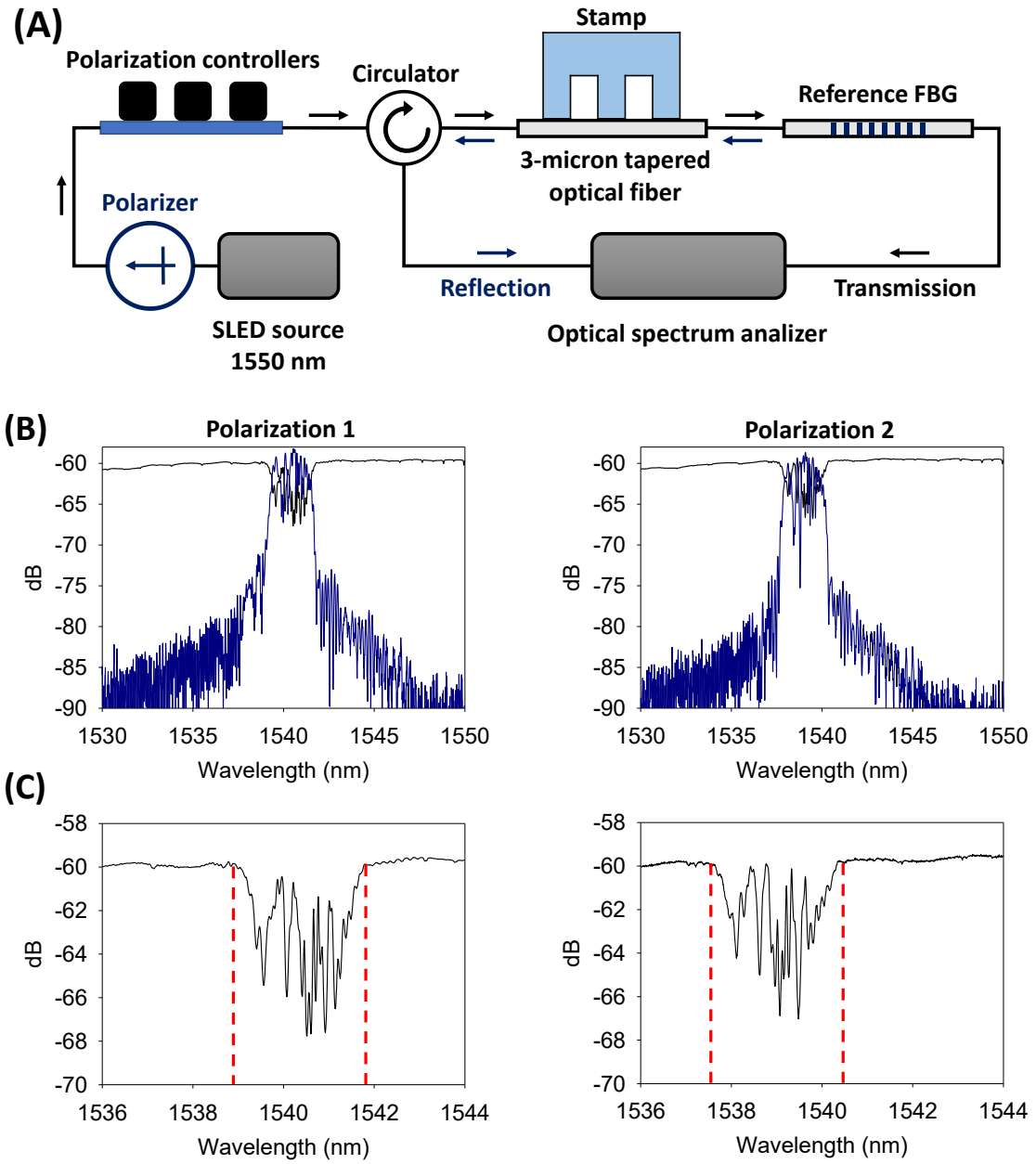

Figure S4. Experimental results on the polarization dependence. **(A)** Scheme of the optical setup used for studying the polarization effect in the system. An in-fiber linear polarizer (Thorlabs, operation wavelength 1550 nm, bandwidth 50 nm) and polarization controllers (Thorlabs, operation wavelength 1550 nm, 56 mm loop) were included after the output of the source to control its linear polarization. **(B)** Reflection (bottom blue line) and transmission (top black line) spectra experimentally obtained at two different linear polarizations for a 3 µm fiber in contact with a grooved PDMS stamp. **(C)** Zoomed view of the transmission notches in the corresponding figures above.

Note that Bragg wavelength of the peak corresponding to the grooved PDMS stamp clearly changes together with the polarization (longer for polarization 1, and shorter for

2). This fact indicates a birefringence caused by the different refractive index of the polarization modes of the microfiber and the asymmetry introduced by the lateral contact of the PDMS stamp on the microfiber.

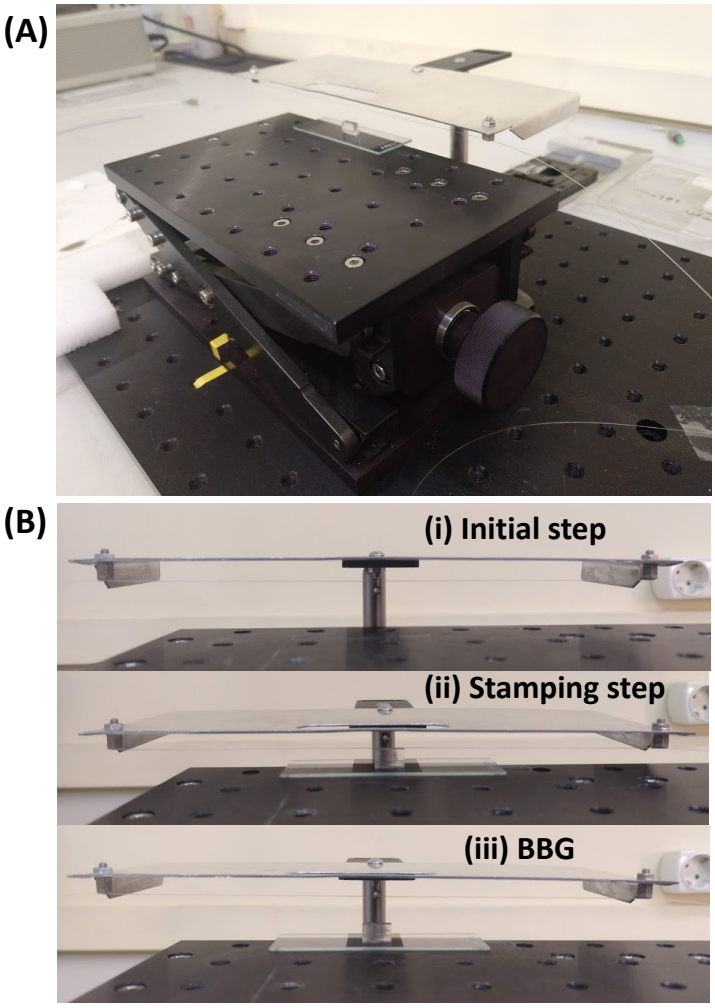

Figure S5. (A) Mechanical elevator used to uplift the inked stamps in the stamping stage of the BBGs fabrication by microcontact printing. **(B)** Real images of the stamping system at the different steps of the BBG fabrication. At initial step (i), the microfiber is fixed in the holder and held just above the elevator. Next, the stamp is placed and oriented right below the microfiber, and the stamp is uplifted until its grooved side becomes in contact with the microfiber (ii). Finally, the stamp and the microfiber are separated and a BBG becomes patterned (iii).

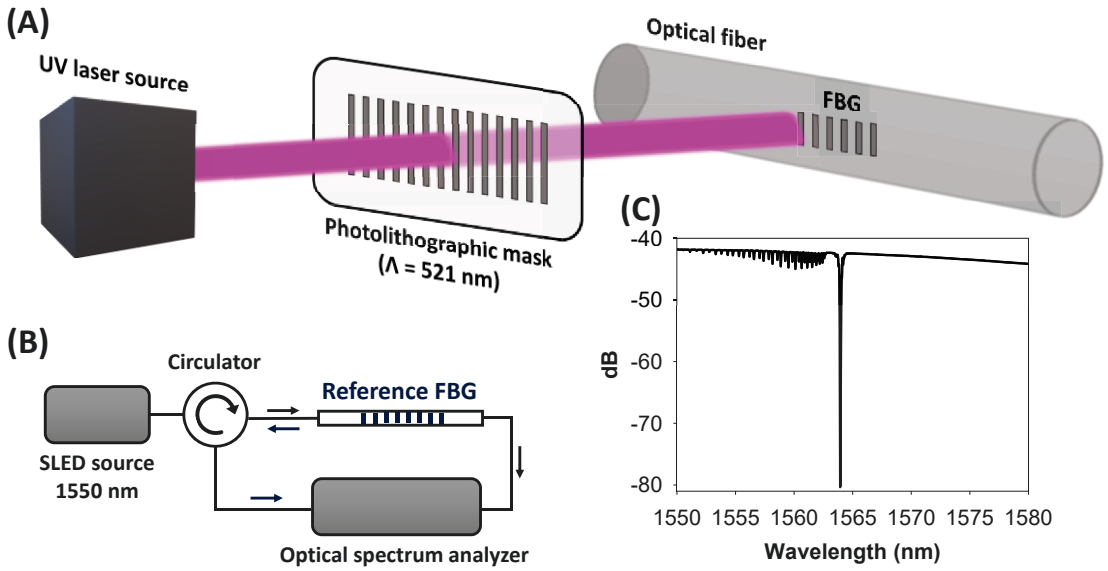

Figure S6. (A) Schematic illustration of the fabrication process of a Fiber Bragg Grating (FBG) used for the reference signals. A CW frequency double Ar laser (λ = 244 nm) irradiates a photolithographic phase mask generating an interferometric UV pattern with the desired pitch for the FBG. A section of a bare boron codoped photosensitive fiber (Fibercore PS1550) is located within the focal length of the interferometric UV pattern, which generates a permanent modulation in the refractive index of the fiber core material. The laser beam sweeps along the length of the fiber, thus the length of the FBG can be of several cm long (in our case, 10 mm). Our FBG was located at 1564.09 nm, with bandwidth < 1 nm and a minimum transmittance of -36 dB, see Figure S6c. **(B)** All-fiber optical circuit used to characterize the FBG. A custom superLED source centered at 1550 nm (1,3 mW, bandwidth > 100 nm) provided the light launched to the FBG. A circulator (Thorlabs, central wavelength: 1550 nm, bandwidth: 90 nm) was placed before the FBG to allow the measurement of the reflection spectrum. **(C)** Transmission spectrum of the reference FBG measured with an AQ6370D optical spectrum analyser from Yokogawa (Tokyo, Japan). As it is shown, the Bragg's wavelength of the FBG is observed at 1564 nm, the notches located at the blue side of the transmission spectrum correspond to the light coupled to different cladding modes of the fiber.

Supplementary information 7

The equivalence between logarithmic and linear scale of the transmission and reflection spectrum levels was calculated as follows:

$$dB = 10 \cdot \log_{10}\left(\frac{P_1}{P_0}\right)$$

where dB stands for the logarithmic scale, P_1 stands for the intensity level in linear scale, and P_0 is the instrumentation reference power level.

The logarithmic and linear reflection spectra are shown in Figure S11. The area of the reflection peaks associated to the bioreceptor BBGs and the reference FBG were obtained by numerical integration of the linear traces, and this area corresponds to the total optical power reflected by each grating. The reflectivity of the BBG was referenced to that of the FBG to separate the reflectivity increase due to the biorecognition event, from any broadband optical loss induced along the fabrication and immunosensing with the BBGs. To do so, we employed the following equation:

$$R = \frac{A_{BG}}{A_{REF}} \cdot 100$$

where A_{BG} and A_{REF} are the areas of the reflection peaks attributed to the BBG and the reference FBG, respectively.

Finally, the change of reflectivity due to the biorecognition assay (net reflectivities) were estimated by subtracting the reflectivity of the BBG generated by the probes (R_{probes}), to the reflectivity achieved by the BBG after target incubation ($R_{targets}$):

$$R_{neat} = R_{targets} - R_{probes}$$

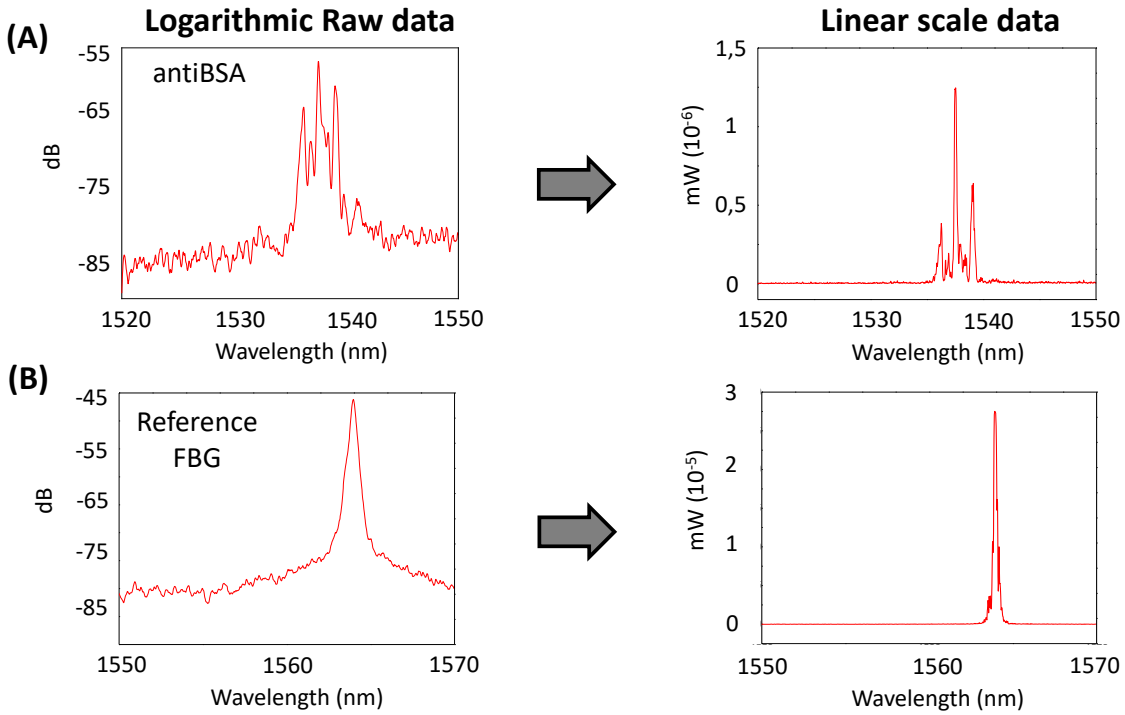

Figure S8. (A) Reflection spectrum with logarithmic scale (left) measured after the target IgG incubation (10 µg·mL^{-1}) and the corresponding spectrum transformed into linear scale (right). **(B)** Reflection spectrum of the reference FBG (left) and the corresponding spectrum in linear scale (right).

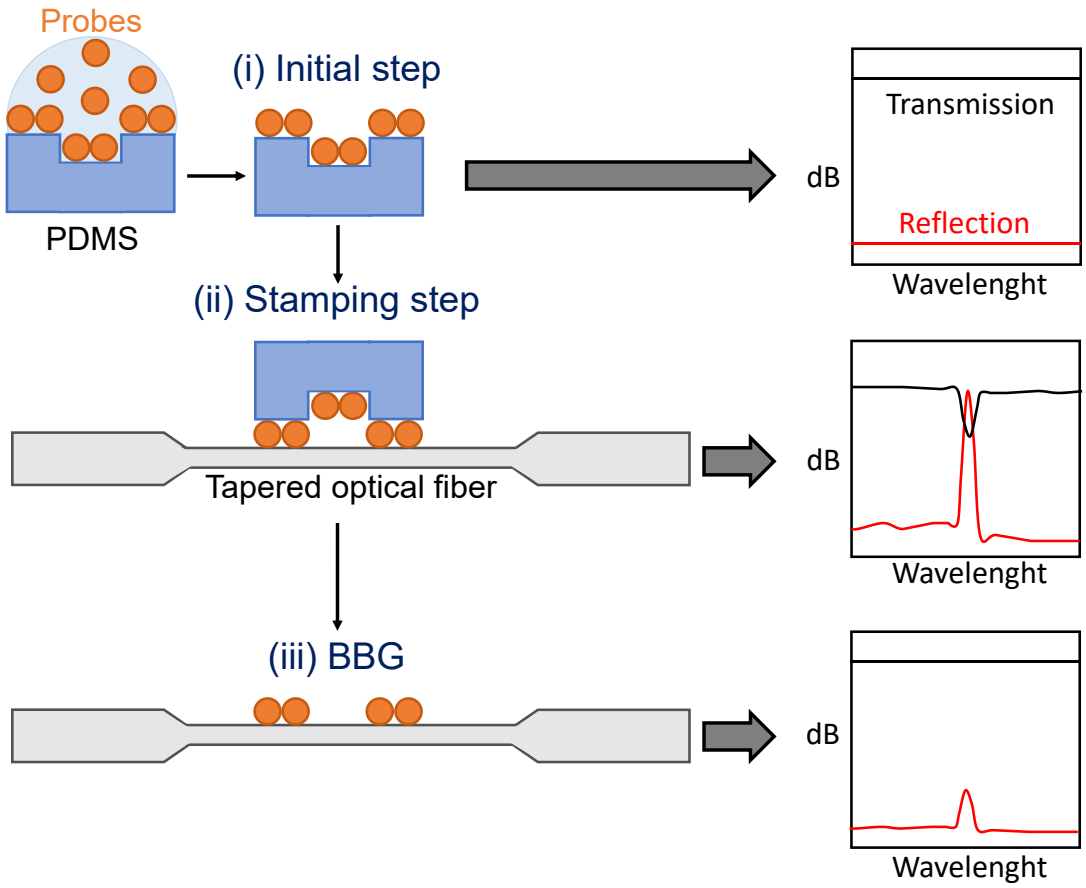

Figure S9. Schematic illustration of the bioreceptor BBGs patterning process on the microfibers by microcontact printing. The transmission and reflection spectra were acquired as a feedback system to monitor and check the success of the patterning process at each step. At the initial stage (i) grooved PDMS stamps are inked with the probe solution, and before their stamping on the microfiber, the transmission and reflection spectra are flat and their levels are defined by the taper losses (< 1dB). Next, the inked PDMS structure is stamped on the microfiber (ii). The contact between the microfiber and the stamp introduces some temporary loss (thus, the transmission level decreases), and more importantly it leads to an intense reflection peak whose wavelength (1537 nm) meets the Bragg condition:

$$\lambda'_B = 2n_{eff} \cdot \Lambda_{BBG}$$

where λ'_B is the Bragg's wavelength, n_{eff} is the refractive index of the fundamental mode at λ'_B, and Λ_{BBG} is the period of the grating (555 nm). This intense reflection peak appears together with its corresponding notch in the transmission spectrum at the same wavelength. Finally, after separating the stamp from the microfiber (iii), a weaker

reflection peak (and a negligible transmission notch) at the same wavelength remains on the spectra, which confirms the transfer of the bioreceptor probes from the stamp to the microfiber surface and their proper periodic structuration.

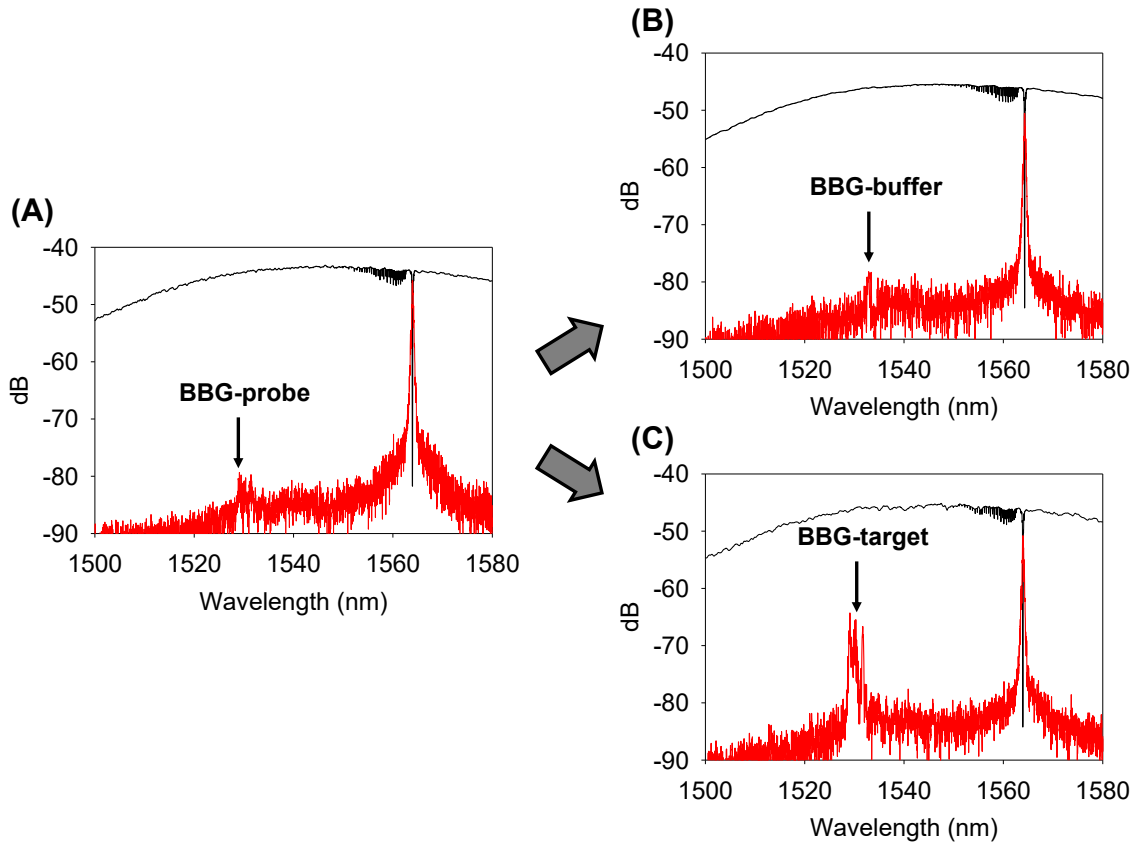

Figure S10. Reflection spectra obtained **(A)** after patterning BSA protein, **(B)** after incubating PBS-T buffer on them, and **(C)** after incubating a solution of 1 µg·mL^{-1} antiBSA in PBS-T**.** The reflectivity increase after incubating PBS-T is negligible, whereas a 20 dB increase (x100) is reached after incubating the antiBSA solution. Consequently, these results demonstrate that the increase of the reflection peak is due to biorecognition events. The transmission spectra indicate that some broadband loss (< 1 dB) is induced during the biorecognition process, which must come from some optical scattering due to the immersion of the microfibers in the solutions. To separate this effect from the biorecognition events, the reflectivity of the BBG was referenced to that of the FBG.

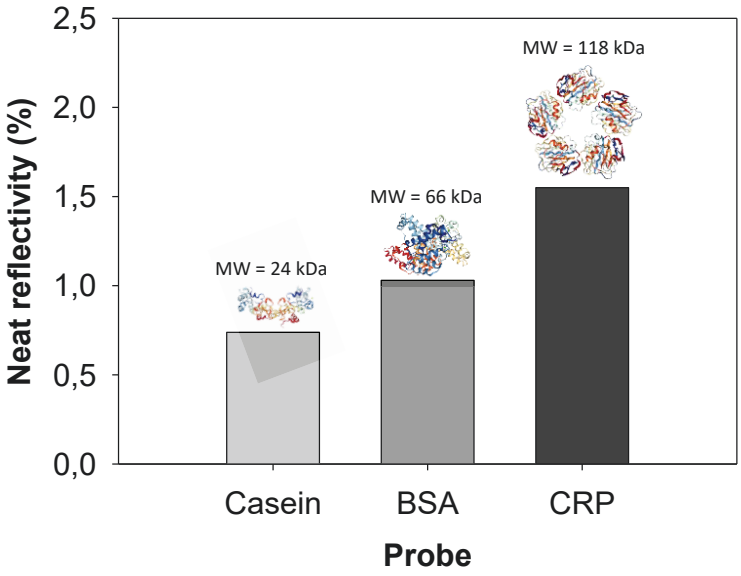

Figure S11. Peak reflectivities registered for BBGs of casein, BSA and CRP patterned on different microfibers.

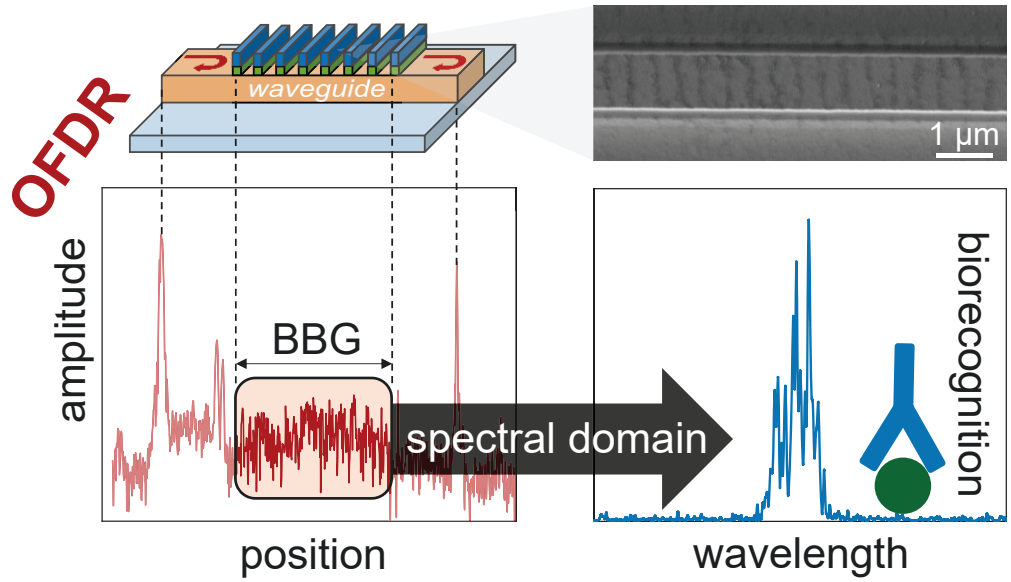

Chapter 3.2: Transducing Biorecognition Events Using Surface Bragg Gratings of Proteins Patterned on Integrated Waveguides

Sensors and Actuators B: Chemical (submitted)

SENSORS and ACTUATORS B Chemical

ELSEVIER

TRANSDUCING BIORECOGNITION EVENTS USING SURFACE BRAGG GRATINGS OF PROTEINS PATTERNED ON INTEGRATED WAVEGUIDES

Augusto Juste-Dolz,[a] Estrella Fernández,[a] Gloria Micó,[b] Luis A. Bru,[b] Rosa Puchades,[a,c] Pascual Muñoz,[b] Miquel Avella-Oliver,[a,c]* Daniel Pastor,[b,]* Ángel Maquieira.[a,c]*

[a]*Instituto Interuniversitario de Investigación de Reconocimiento Molecular y Desarrollo Tecnológico (IDM), Universitat Politècnica de València, Universitat de València, 46022 Valencia, Spain.*

[b]*Photonics Research Labs, ITEAM, Universitat Politècnica de València, 46022, Valencia, Spain.*

[c]*Departamento de Química, Universitat Politècnica de València, 46022 Valencia, Spain.*

**Corresponding author: miavol@upv.es (M. Avella-Oliver), dpastor@dcom.upv.es (D. Pastor), amaquieira@qim.upv.es (Á. Maquieira)*

Abstract

The incorporation of biomacromolecules onto photonic integrated platforms constitutes a growing trend that pushes towards compact and miniaturized biosensing systems. Herein we present the integration of one-dimensional periodic networks of proteins on the surface of silicon waveguides for transducing biorecognition events. This study demonstrates by theoretical calculations that rib waveguides (1-1.6 µm width) are compatible with this transduction principle and predicts the periods of the protein gratings (495-515 nm) that display suitable spectral responses. Then, protein gratings of bovine serum albumin are fabricated on the surface of the waveguides, characterized by electron microscopy, and their optical response measured by optical frequency domain reflectometry along the fabrication and the subsequent biorecognition stages. Detection and quantification limits of 0.3 and 3.7 µg·mL^{-1} of specific IgGs are inferred from experimental dose-response curves in this first demonstration. Among other

interesting features, this biosensing approach points towards miniaturized and integrated biosensors for label-free analysis.

Keywords: diffraction ● biosensor ● photonic ● label-free● immunoassay

The study of recognition events between biomacromolecules is an important part of the current impact of nanoscience and nanotechnology,[1–4] and a crucial topic in a great number of disciplines.[5–7] Among many other aspects, focusing nanoscience on sensing purposes points towards the development of miniaturized and integrated nanobiosensors to provide unique bioanalytical solutions.[8–12] A paradigmatic approach in this direction relies on incorporating biomacromolecules onto silicon-based waveguides.[13,14] These materials are designed to guide electromagnetic waves through its core, whereas part of the light participates in biorecognition assays arranged on the surface of the guides. This strategy involves a major scientific activity in the recent years, with some flagship examples such as ring resonators or Mach-Zehnder and Young interferometers among others.[15–17]

A fundamental issue in the innovation of this field relies on discovering and implementing new photonic phenomena for transducing biorecognition events. The impact of these advances is nowadays greatly supported by active and passive waveguiding technologies and their integration, pointing towards prospective biosensors that combine all the sensing elements (light sources, waveguides, detectors, etc.) in a monolithic chip.[18,19]

Herein we focus on the incorporation of one-dimensional periodic assemblies of proteins on the surface of micrometric silicon waveguides for transducing immunoassays. The principle behind this approach relies on protein nanostructures patterned as Bragg gratings tailored to undergo a diffractive interaction with the evanescent field on the surface of the waveguide. As schematized in Figure 1, this light-matter interaction reflects part of the guided light, which appears as a peak in the reflection spectrum. When the patterned protein probes bind their target molecules, the periodic refractive index modulation that conforms the grating increases, and the reflected light becomes enhanced. As a result, the concentration of target molecules in

solution can be quantified by means of the intensity of the reflected peak. After preliminary insights into tapered optical fibers,[20] herein we introduce these biomolecular Bragg gratings (BBGs) on photonic circuits.

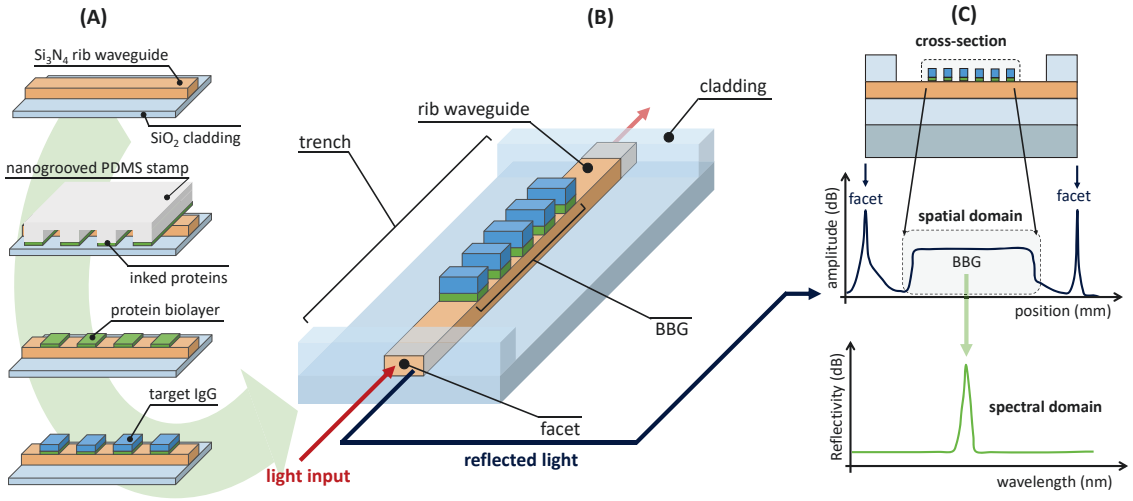

Figure 1. Schemes of **(A)** the fabrication of protein gratings by microcontact printing on the waveguides, **(B)** the photonic sensing device, and **(C)** the resulting optical signals.

This diffractive phenomenon requires for a suitable contribution of light propagating through the top surface of the guide, on which the BBGs are patterned. Photonic circuits constituted by rib waveguides of silicon nitride with a fixed thickness of 300 nm and widths from 1.0 to 1.6 µm are herein assessed, and our theoretical calculations (Figure 2A, Supplementary Information 1) indicate that an important part of the fundamental mode propagates through the top surface of these planar waveguides. As observed in Figure 2B, the magnitude of this evanescent field decreases with the width and slightly increases with the wavelength, reaching about a 13.5% of the total field intensity of the guided mode for 1 µm waveguides at λ = 1550 nm, which supports the potential of these waveguides to sense interactions within the evanescent field.

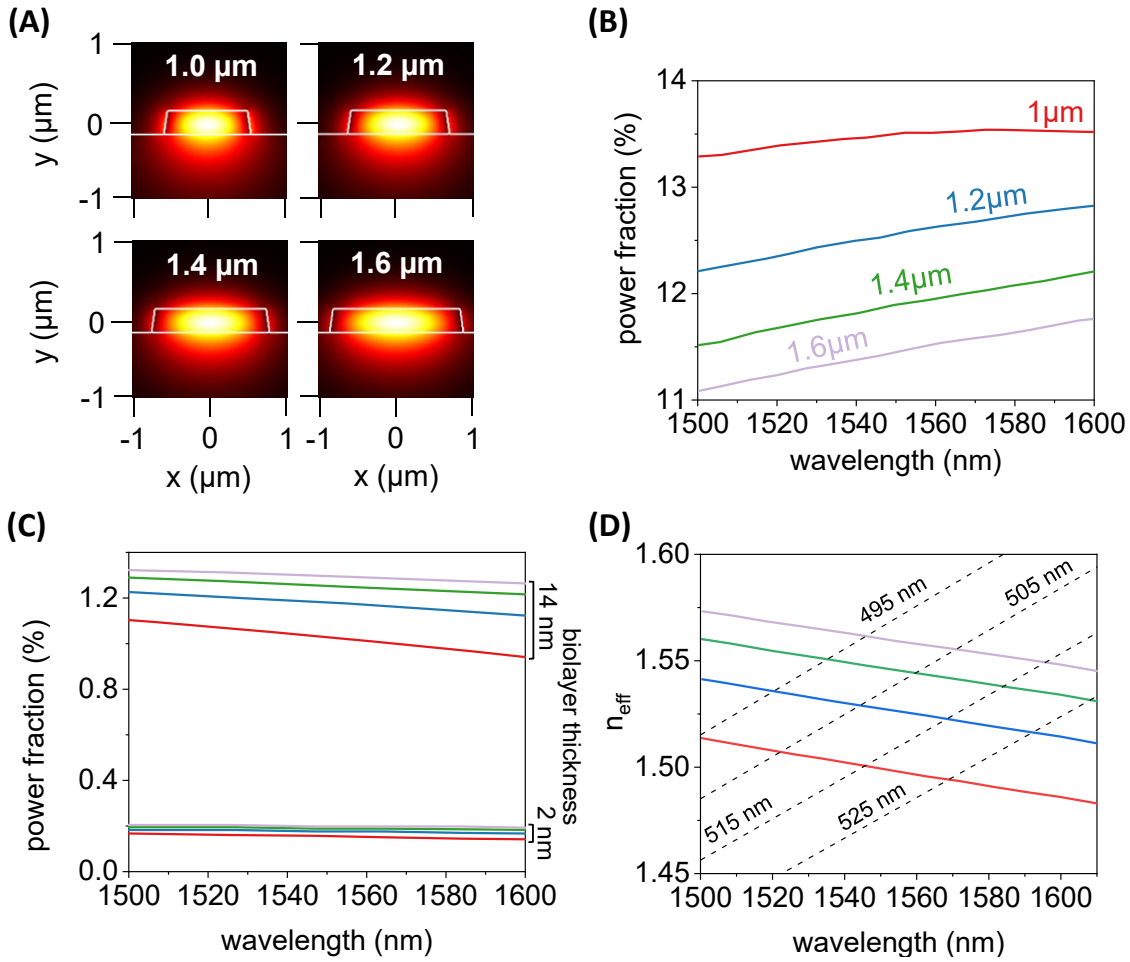

Figure 2. Results of the theoretical calculations. **(A)** Spatial distribution of the field intensity (fundamental mode, λ = 1550 nm) for different waveguide widths. **(B)** Fraction of light power of the evanescent field in the external medium (air), for different waveguide widths and input wavelengths. **(C)** Fraction of light power in the evanescent field within two different thicknesses of protein layers on the top surface of the guide, for different waveguide widths (color code in Figure 2B) and wavelengths. **(D)** Effective refractive indexes for a range of guided wavelengths and waveguide widths (solid lines, color code in Figure 2B), together with the BBG periods that meet the Bragg equation at each condition (dashed lines).

The power fraction of the guided mode for protein biolayers was also calculated for different waveguide widths. As shown in Figure 2C, the intensity of the evanescent field contained within different biolayer thicknesses on the top of the waveguide increases together with this thickness. This calculation includes a common value for a protein

monolayer (2 nm) and a typical thickness after a subsequent binding of specific antibodies (14 nm), and the result suggest a suitable distribution of energy to sense changes on the biolayer thicknesses induced by biorecognition events. It can also be observed that the power fraction slightly increases together with the waveguide width. The guided mode is less confined and expands vertically (Figure 2B) when this width decreases, which distributes the transverse profile of the guided mode in a broader area, and the amount of available energy in a thin layer becomes reduced.

The width of the waveguides also determines the grating periods that meet the Bragg condition and the spectral response of the patterned biolayers. Figure 2D shows the simulated values of the effective refractive index as a function of the guided wavelength and the waveguide width (solid lines). The Bragg condition is satisfied by $\lambda_B = 2n_{eff} \cdot \Lambda$, where n_{eff} is the effective refractive index and Λ is the Bragg period. Note that n_{eff} also depends on the wavelength and the Bragg condition is expressed as $\lambda_B/2\Lambda = n_{eff,\lambda_B}$. In the figure, the left side of the equation is represented for different Bragg periods (dashed lines), and the crossing points between the two sets of curves indicate the corresponding λ_B values. As shown in Figure 2D, within the expected range of effective refractive index for these structures surrounded by air,[21] grating periods from 495 to 525 nm display an appropriate response for the spectral window of the standard near infrared analyzers typically employed for these waveguides.

The optical waveguides for this investigation were fabricated by standard photolithographic procedures (Supplementary Information 2). A silica cladding is included at the edges of the chip to meet the light coupling conditions, and the top surface of the guides is uncovered for patterning the BBGs on them and for the subsequent incubation of samples. For that, rectangular (0.8 x 1.8 μm) trenches in the cladding layer were created in the center part of the silicon chips, which contain guides of different widths. (Supplementary information 2).

In this study, the BBGs were patterned on the guides by microcontact printing. This is a versatile technique based on creating stamps of polydimethylsiloxane by replica molding from a master structure, inking biomacromolecules on the stamps, and then transferring them onto solid surfaces by stamping (Figure 1A).[22–24] One-dimensional grooved stamps,

with a period of 416 nm, a duty cycle of 50%, and a groove depth of 100 nm, were used for patterning BBGs of bovine serum albumin (BSA) (Supplementary Information 3). As shown in Figure 3A, this approach provides periodic protein nanostructures onto the top surface of the waveguides, defined by a period of 415.6 ± 2.4 nm and a duty cycle of 48 ± 5 % (Supplementary information 4). Furthermore, this characterization performed by field emission scanning electron microscopy (FESEM) also suggests an accumulation of biological matter onto the strips of the protein nanostructures after incubating specific IgG targets (Figure 3A iii), which indicates that the patterning process keeps the functionality of the binding sites of the patterned proteins. It is also worth mentioning that the flexibility of the polydimethylsiloxane allows to overcome the height of the cladding trench and to reach the top surface of the waveguide for a suitable protein transfer (Figure S5), which means an interesting new insight into the versatility of microcontact printing to pattern biomolecules.

As commented above (Figure 2C), the spectral response of the assay depends on the period of the BBG, and we adjusted this parameter by controlling the angle between the grooved relief of the stamp and the longitudinal direction of the guide in the stamping stage (Supplementary information 5). Patterning different periods by microcontact printing enables tuning the wavelength of the reflection peak without requiring additional master structures. As observed in Figure 3B, the resulting period scales exponentially with the stamping angle, and a good agreement is obtained between the simulated and the experimental periods, especially for angles up to 45°. These results show that stamping angles between 32° and 38.6° yield protein grating periods whose reflection peak falls within the expected spectral window selected from the theoretical calculations (490-530 nm, Figure 2C) for these waveguides.

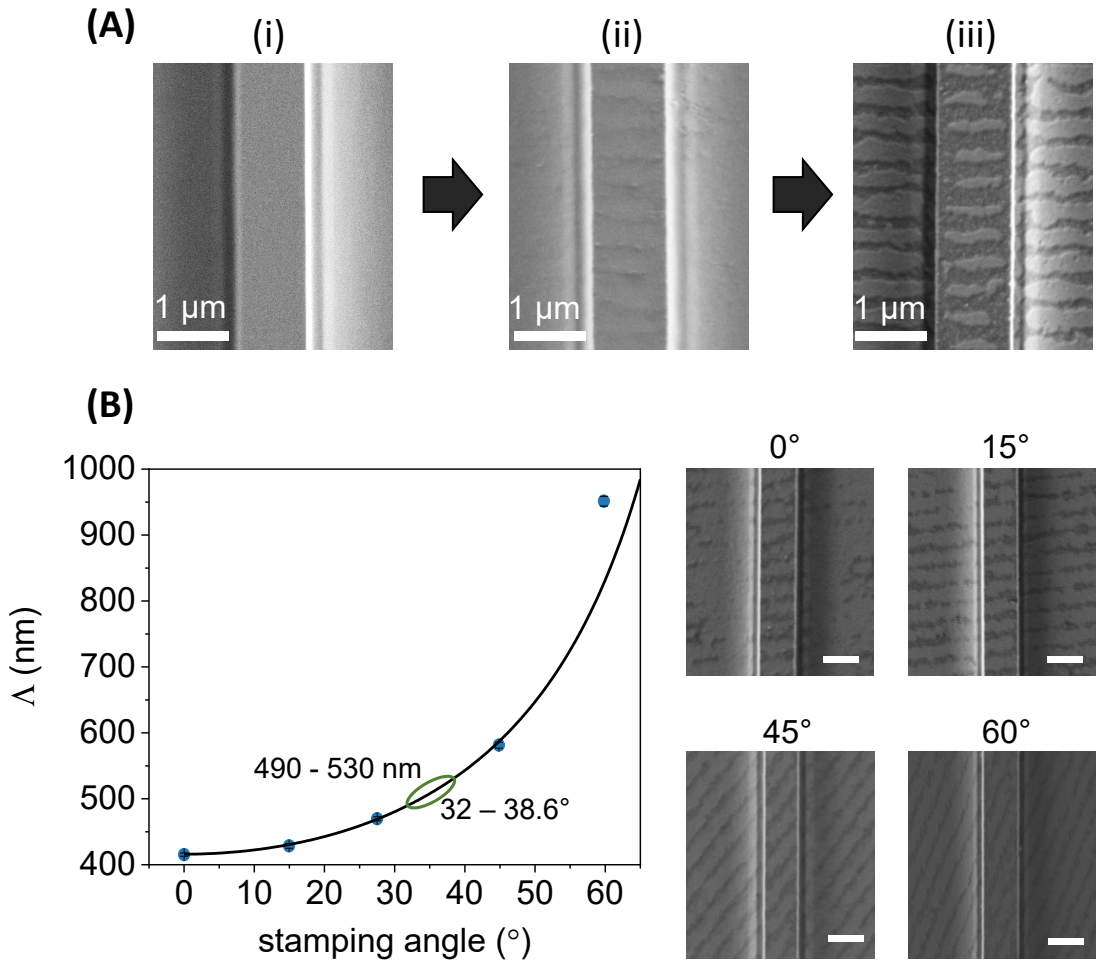

Figure 3. (A) FESEM images of a 1 µm waveguide (i) before and (ii) after patterning a BSA BBG by microcontact printing, and (iii) after the incubation of specific antiBSA IgGs (10 $\mu g \cdot mL^{-1}$). **(B)** Experimental (blue dots) and simulated (black line) periods of the protein nanostructures for different patterning angles, and the corresponding FESEM images of the BBGs (scale bars: 1 µm). See Supplementary information 5 for FESEM images at further magnifications.

To experimentally measure the optical response of these biomolecular gratings, light from a tunable infrared laser (1500-1600 nm) was coupled in the guides through the facets using lensed optical fiber pigtails, and the reflected light was acquired with an optical spectrum analyzer. The reflection generated by the in and out facets of the guides is much more intense than that expected for the BBG, and to discriminate the diffracted peak of the BBGs from this background signal coming from the facets, the system was interrogated by optical frequency domain reflectometry (OFDR)

(Supplementary Information 6). On the one hand, this method allows to determine the longitudinal position at which each reflective event takes place within the waveguide, thus enabling to separate the background reflection of the facets from the signal of the biomolecular gratings. On the other hand, this analysis also provides the spectral response of the reflective events along the guide. As a result, the biomolecular assays can be examined both in the spatial and spectral domains (Figure 1C).

To prove the concept, we measured the optical response of the protein nanostructures at each step of the BBG fabrication and after incubating a selective antibody, using a representative model immunoassay based on BSA probes and antiBSA IgGs as targets (Figure 4A). The higher reflection peaks observed at 0 and 5 mm correspond to the facets and the less intense peaks at 1 and 4 mm correspond to the cladding transitions of the trench. As expected for the raw guides, no signals are observed between the two peaks of the cladding transitions (BBG region) neither in the spatial domain nor in the spectral domain data. After stamping the BBGs, the amplitude signal increases in the central part of the spatial domain data (BBG region, see also Figure S12) and a reflection peak appears in the spectral domain at 1578 nm. This reflection peak meets the Bragg condition for a BBG period of 525 nm and corroborates the structured transfer of proteins to the waveguide surface. Finally, the incubation of specific IgG (100 $\mu g \cdot mL^{-1}$) displays an important enhancement of the reflectivity that becomes about one order of magnitude greater in the reflection peak of the spectral domain, which is not observed after incubating only buffer solution (Figure S13). These results also confirm that the binding event between the patterned proteins and the targets IgGs produce an accumulation of biological matter on the strips of the nanostructure, which complements the FESEM characterization and demonstrates our initial hypothesis of this photonic transduction system for biosensing.

We explored and compared the experimental response of the BBGs on waveguides of different widths. As observed in Figure 4B, the position of this reflection peak shifts to higher wavelengths with increasing waveguide widths, and this trend follows the cosine trend predicted by the simulations. The experimental BBG peaks for 1.4 and 1.6 µm waveguides fall outside the measuring window of the employed OFDR analyser (1525 – 1610 nm), and the reflection peak for 1 and 1.2 µm waveguide widths appear within this

range. In particular, the BBG peak in 1 μm waveguides is centred in the measuring window (1568 nm), and these waveguides were selected for the subsequent experimental assessment of the label-free biosensing capabilities of this approach. For that, BBGs of BSA probes were patterned on a set of chips and incubated with increasing concentrations of specific antiBSA IgG targets in buffer to perform an experimental dose-response curve. The difference of the reflection peak area before and after incubating specific targets was employed as analytical signal, since it represents the overall change of the reflected power (Supplementary information 6). As shown in Figure 4C, the enhancement of the peak reflectivity is proportional to the concentration of targets and correlates well with a 4-parameter logistic curve (R^2 = 0.997). From this fitting, an experimental detection limit of 0.3 $\mu g \cdot mL^{-1}$ and quantification limit of 3.7 $\mu g \cdot mL^{-1}$ of specific IgG were inferred from the dose-response curve by interpolating the mean of ten blank measurements (0 $\mu g \cdot mL^{-1}$ of IgG) plus three and ten times its standard deviation, respectively. Those are promising values especially considering that it is a label-free system and that this is the first demonstration of the BBG transduction mechanism in integrated waveguides. Another interesting aspect to highlight of this approach is the possibility to regenerate the waveguides for performing further experiments on them (Supplementary information 8). This regeneration is a valuable advantage to simplify, and to minimize the costs and ecological fingerprint, of prospective research and development activities for BBG-based systems as well as for other photonic biosensors.

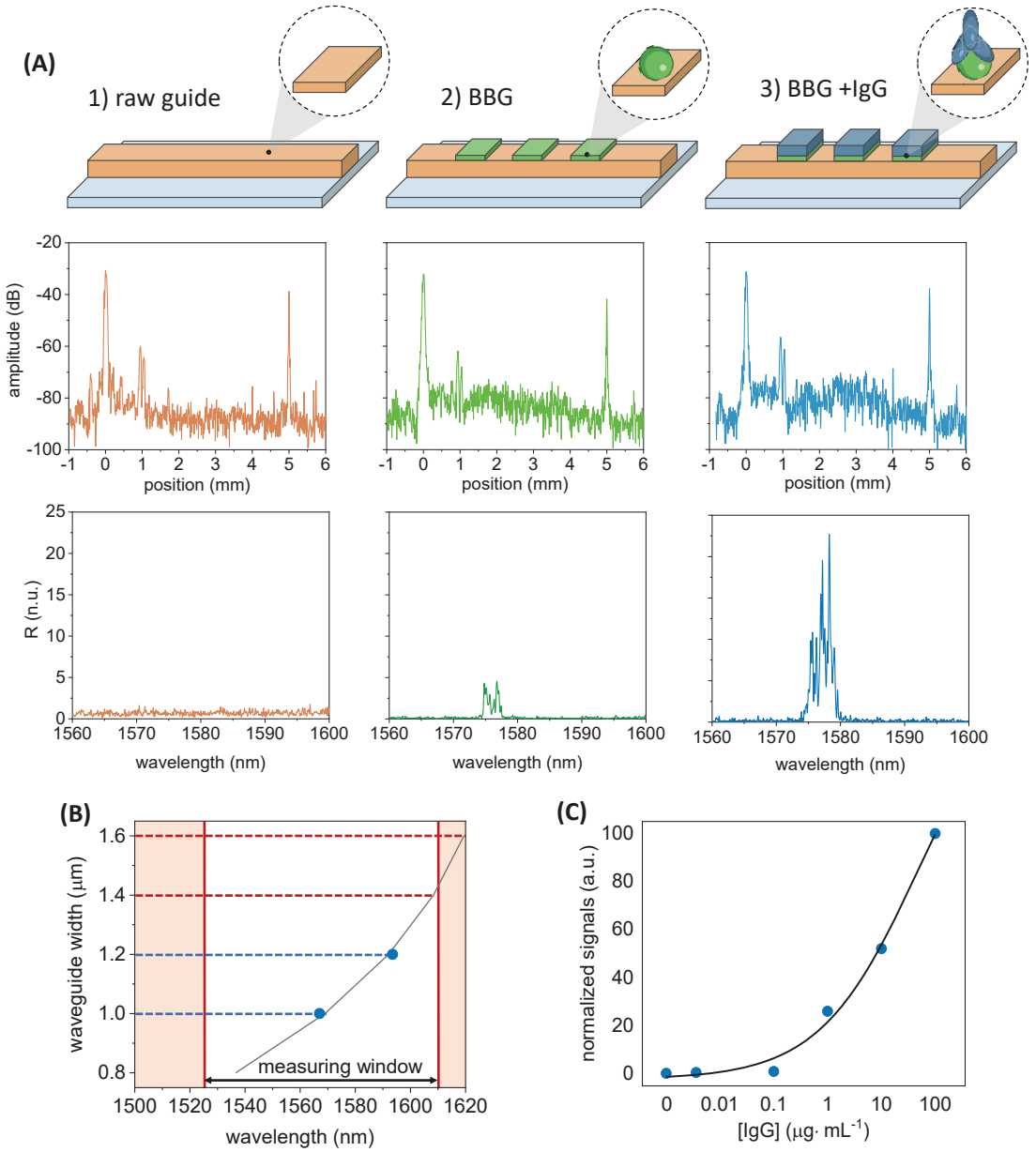

Figure 4. (A) Reflection spectra processed by OFDR in the (i) spatial and (ii) spectral domains. The optical measurements were performed before and after patterning BBGs of BSA proteins onto a 1 µm waveguide and after incubating a solution of specific antiBSA IgG targets (100 µg·mL^{-1}). See Figure S12 for a zoomed view of the spatial domain response of the BBG region in linear scale. **(B)** Position of the reflected peak for each waveguide width. The black line represents the simulated trend, and the blue points show the experimental results obtained with protein BBGs (period of 525 nm) patterned on waveguides of different widths. **(C)** Experimental dose-response immunoassay curve fitted to a sigmoidal (logistic 4-parameter) regression.

In summary, this work demonstrates for the first time the BBG concept in photonic integrated waveguiding platforms. The theoretical calculations provide evidence that support the hypothesis of this biosensing transduction strategy and allow to define the design for its subsequent experimental materialization. This study also confirms the capability of microcontact printing to create patterns of biomacromolecules onto rib waveguides, preserving their binding functionality, overcoming the height step introduced by the cladding trench, and tunning the BBGs peak by just controlling the stamping angle. The experimental results with a model immunoassay display the expected reflection peak from protein BBGs and its intensity enhancement after interacting with specific IgGs. The potential of this approach to quantify biorecognition events is demonstrated and characterized by means of a dose-response curve.

The outcome of this investigation suggests future innovations for the monolithic integration of active components (light sources, detectors, etc.) in silicon-based waveguides with BBGs, to conceive fully integrated photonic devices for point-of-care biosensing.[25] Along these lines, other advances for patterning biolayers on surfaces may be compatible with this BBG concept and support its scope.[26,27]Also, the easy tunability of the BBG peak as well as the OFDR interrogation introduces great possibilities to perform and quantify multiple assays in a single analysis.[20] Besides, transducing biorecognition events by means of diffractive biological gratings entails a unique potential to avoid signal contributions from non-specific bindings.[27,28] In general, all these advantages together point towards label-free biosensors, capable of performing and measuring many assays in a single integrated and miniaturized chip, and solving non-specific binding issues in the direct analysis of untreated biological samples.

Acknowledgements

This work was financially supported by the Ministerio de Ciencia e Innovación/Agencia Estatal de Investigación (MCIN/AEI/10.13039/501100011033) co-funded by the European Union “ERDF A way of making Europe” (PID2019-110713RB-I00, TED2021-132584B-C21, PID2019-110877GB-I00), Ministerio de Economía y Competitividad (TEC2016-80385-P), Generalitat Valenciana (PROMETEO/2020/094,

PROMETEO/2021/015, IDIFEDER/2021/046). A.J.D. ackowledges the FPI-UPV 2017 grant program. The authors acknowledge Instituto de Microelectrónica de Barcelona CNM-CSIC for the support in the fabrication of the measured chip samples on the Multiproject CNM-VLC silicon nitride technology platform.

References

(1) Li, Y.; Wang, X.; Zhang, Y.; Nie, G. Recent Advances in Nanomaterials with Inherent Optical and Magnetic Properties for Bioimaging and Imaging-Guided Nucleic Acid Therapy. *Bioconjug. Chem.* **2020**, *31* (5), 1234–1246. https://doi.org/10.1021/acs.bioconjchem.0c00126.

(2) Escorihuela, J.; González-Martínez, M. Á.; López-Paz, J. L.; Puchades, R.; Maquieira, Á.; Gimenez-Romero, D. Dual-Polarization Interferometry: A Novel Technique to Light up the Nanomolecular World. *Chemical Reviews*. 2015, pp 265–294. https://doi.org/10.1021/cr5002063.

(3) Wang, J.; Zhou, Y.; Jiang, L. Bio-Inspired Track-Etched Polymeric Nanochannels: Steady-State Biosensors for Detection of Analytes. *ACS Nano* **2021**, *15* (12), 18974–19013. https://doi.org/10.1021/acsnano.1c08582.

(4) Musetti, S.; Huang, L. Nanoparticle-Mediated Remodeling of the Tumor Microenvironment to Enhance Immunotherapy. *ACS Nano* **2018**, *12* (12), 11740–11755. https://doi.org/10.1021/acsnano.8b05893.

(5) Goscianska, J.; Freund, R.; Wuttke, S. Nanoscience versus Viruses: The SARS-CoV-2 Case. *Adv. Funct. Mater.* **2022**, *32* (14), 2107826. https://doi.org/10.1002/adfm.202107826.

(6) Wong, X. Y.; Sena-Torralba, A.; Álvarez-Diduk, R.; Muthoosamy, K.; Merkoçi, A. Nanomaterials for Nanotheranostics: Tuning Their Properties According to Disease Needs. *ACS Nano* **2020**, *14* (3), 2585–2627. https://doi.org/10.1021/acsnano.9b08133.

(7) Ai, Y.; Hu, Z.; Liang, X.; Sun, H.; Xin, H.; Liang, Q. Recent Advances in Nanozymes:

From Matters to Bioapplications. *Adv. Funct. Mater.* **2022**, *32* (14), 2110432. https://doi.org/10.1002/adfm.202110432.

(8) Lopez, G. A.; Estevez, M.-C.; Soler, M.; Lechuga, L. M. Recent Advances in Nanoplasmonic Biosensors: Applications and Lab-on-a-Chip Integration. *Nanophotonics* **2017**, *6* (1), 123–136. https://doi.org/10.1515/nanoph-2016-0101.

(9) Alba-Patiño, A.; Vaquer, A.; Barón, E.; Russell, S. M.; Borges, M.; de la Rica, R. Micro- and Nanosensors for Detecting Blood Pathogens and Biomarkers at Different Points of Sepsis Care. *Microchim. Acta* **2022**, *189* (2), 74. https://doi.org/10.1007/s00604-022-05171-2.

(10) Krämer, J.; Kang, R.; Grimm, L. M.; De Cola, L.; Picchetti, P.; Biedermann, F. Molecular Probes, Chemosensors, and Nanosensors for Optical Detection of Biorelevant Molecules and Ions in Aqueous Media and Biofluids. *Chem. Rev.* **2022**, *122* (3), 3459–3636. https://doi.org/10.1021/acs.chemrev.1c00746.

(11) Vikesland, P. J. Nanosensors for Water Quality Monitoring. *Nat. Nanotechnol.* **2018**, *13* (8), 651–660. https://doi.org/10.1038/s41565-018-0209-9.

(12) Yang, T.; Duncan, T. V. Challenges and Potential Solutions for Nanosensors Intended for Use with Foods. *Nat. Nanotechnol.* **2021**, *16* (3), 251–265. https://doi.org/10.1038/s41565-021-00867-7.

(13) Luan, E.; Shoman, H.; Ratner, D.; Cheung, K.; Chrostowski, L. Silicon Photonic Biosensors Using Label-Free Detection. *Sensors* **2018**, *18* (10), 3519. https://doi.org/10.3390/s18103519.

(14) Ettabib, M. A.; Marti, A.; Liu, Z.; Bowden, B. M.; Zervas, M. N.; Bartlett, P. N.; Wilkinson, J. S. Waveguide Enhanced Raman Spectroscopy for Biosensing: A Review. *ACS Sensors* **2021**, *6* (6), 2025–2045. https://doi.org/10.1021/acssensors.1c00366.

(15) Luchansky, M. S.; Bailey, R. C. High- Q Optical Sensors for Chemical and Biological Analysis. *Anal. Chem.* **2012**, *84* (2), 793–821. https://doi.org/10.1021/ac2029024.

(16) Steglich, P.; Hülsemann, M.; Dietzel, B.; Mai, A. Optical Biosensors Based on Silicon-On-Insulator Ring Resonators: A Review. *Molecules* **2019**, *24* (3), 519. https://doi.org/10.3390/molecules24030519.

(17) Soler, M.; Estevez, M. C.; Cardenosa-Rubio, M.; Astua, A.; Lechuga, L. M. How Nanophotonic Label-Free Biosensors Can Contribute to Rapid and Massive Diagnostics of Respiratory Virus Infections: COVID-19 Case. *ACS Sensors* **2020**, *5* (9), 2663–2678. https://doi.org/10.1021/acssensors.0c01180.

(18) Artundo, I. Photonic Integration: New Applications Are Visible. *Opt. Photonik* **2017**, *12* (3), 22–25. https://doi.org/10.1002/opph.201700015.

(19) Chandrasekar, R.; Lapin, Z. J.; Nichols, A. S.; Braun, R. M.; Fountain, A. W. Photonic Integrated Circuits for Department of Defense-Relevant Chemical and Biological Sensing Applications: State-of-the-Art and Future Outlooks. *Opt. Eng.* **2019**, *58* (02), 1. https://doi.org/10.1117/1.OE.58.2.020901.

(20) Juste-Dolz, A.; Delgado-Pinar, M.; Avella-Oliver, M.; Fernández, E.; Pastor, D.; Andrés, M. V.; Maquieira, Á. BIO Bragg Gratings on Microfibers for Label-Free Biosensing. *Biosens. Bioelectron.* **2021**, *176* (December 2020). https://doi.org/10.1016/j.bios.2020.112916.

(21) Vörös, J. The Density and Refractive Index of Adsorbing Protein Layers. *Biophys. J.* **2004**, *87* (1), 553–561. https://doi.org/10.1529/biophysj.103.030072.

(22) Bernard, A.; Renault, J. P.; Michel, B.; Bosshard, H. R.; Delamarche, E. Microcontact Printing of Proteins. *Adv. Mater.* **2000**, *12* (14), 1067–1070. https://doi.org/10.1002/1521-4095(200007)12:14<1067::AID-ADMA1067>3.0.CO;2-M.

(23) Avella-Oliver, M.; Ferrando, V.; Monsoriu, J. A.; Puchades, R.; Maquieira, A. A Label-Free Diffraction-Based Sensing Displacement Immunosensor to Quantify Low Molecular Weight Organic Compounds. *Anal. Chim. Acta* **2018**, *1033*, 173–179. https://doi.org/10.1016/j.aca.2018.05.060.

(24) Juste-Dolz, A.; Avella-Oliver, M.; Puchades, R.; Maquieira, A. Indirect Microcontact Printing to Create Functional Patterns of Physisorbed Antibodies.

Sensors (Switzerland) **2018**, *18* (9). https://doi.org/10.3390/s18093163.

(25) Wang, J.; Sanchez, M. M.; Yin, Y.; Herzer, R.; Ma, L.; Schmidt, O. G. Silicon-Based Integrated Label-Free Optofluidic Biosensors: Latest Advances and Roadmap. *Adv. Mater. Technol.* **2020**, *5* (6), 1901138. https://doi.org/10.1002/admt.201901138.

(26) Delamarche, E.; Pereiro, I.; Kashyap, A.; Kaigala, G. V. Biopatterning: The Art of Patterning Biomolecules on Surfaces. *Langmuir* **2021**, *37* (32), 9637–9651. https://doi.org/10.1021/acs.langmuir.1c00867.

(27) Juste-Dolz, A.; Delgado-Pinar, M.; Avella-Oliver, M.; Fernández, E.; Cruz, J. L.; Andrés, M. V.; Maquieira, Á. Denaturing for Nanoarchitectonics: Local and Periodic UV-Laser Photodeactivation of Protein Biolayers to Create Functional Patterns for Biosensing. *ACS Appl. Mater. Interfaces* **2022**, *14* (36), 41640–41648. https://doi.org/10.1021/acsami.2c12808.

(28) Gatterdam, V.; Frutiger, A.; Stengele, K. P.; Heindl, D.; Lübbers, T.; Vörös, J.; Fattinger, C. Focal Molography Is a New Method for the in Situ Analysis of Molecular Interactions in Biological Samples. *Nat. Nanotechnol.* **2017**, *12* (11), 1089–1095. https://doi.org/10.1038/nnano.2017.168.

Supplementary information

- **Supplementary Information 1: Electromagnetic simulations**

Electromagnetic simulations to calculate the optical response of the system were carried out by means of finite difference method in the Quasi TE & TM approach, implemented on Matlab™.[1,2] The electromagnetic field distribution results were validated with commercial software MODE Lumerical (Finite Difference Eigenmode). The overlapping integrals (i.e. proportion of the total field interacting with the Bragg perturbation) were calculated from the obtained field distribution over the complete waveguide and compared with the field localized onto the BBG area. The conditions and the parameters of the waveguides that were employed for the simulations are represented in Figure S1. A refractive index of 1.43 was considered for the protein biolayers.[3]

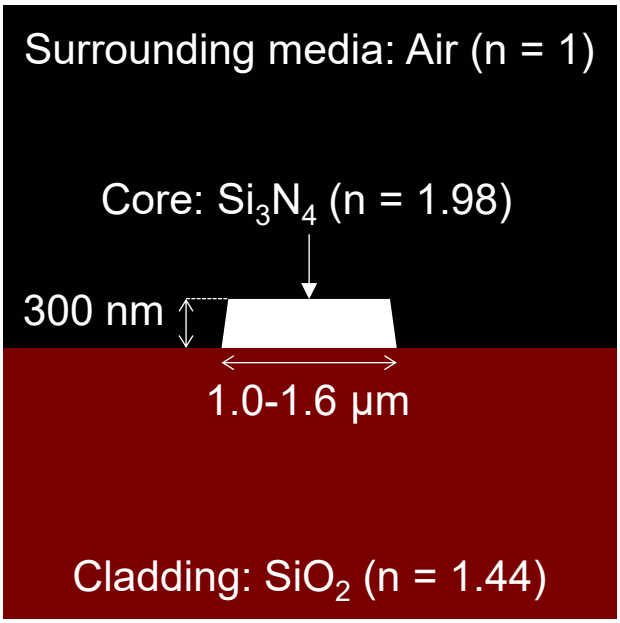

Figure S1. Scheme of the waveguide structure, materials and refractive indexes employed to perform the theoretical calculations.

- **<u>Supplementary information 2:</u> waveguide fabrication**

The fabrication process starts by growing a 2.5 µm thick SiO_2 buffer by thermal oxidation of a Si wafer of 100 mm (4 inch). Following, a 300 nm layer of Si_3N_4 is deposited by low-pressure chemical vapour deposition. In the next step, the waveguide cross-sections are patterned by photo-lithography employing an in-line stepper, whose minimum feature size is 500 nm. Afterwards, the definition of the core cross-section is accomplished by reactive ion etching of the silicon nitride film. Lastly, a SiO_2 cladding of 2 µm thickness is deposited by means of plasma enhanced chemical vapour deposition, whereby the guides are fully defined. After the waveguide fabrication steps, air wells (trenches) are created by selectively etching away the cladding oxide, where the waveguide core becomes in direct contact with the surrounding media (Figure S2).[4] The chips were fabricated on CNM-VLC silicon nitride platform and other actors providing silicon nitride foundry services on open-access scheme have reported their technologies on a review paper.[5]

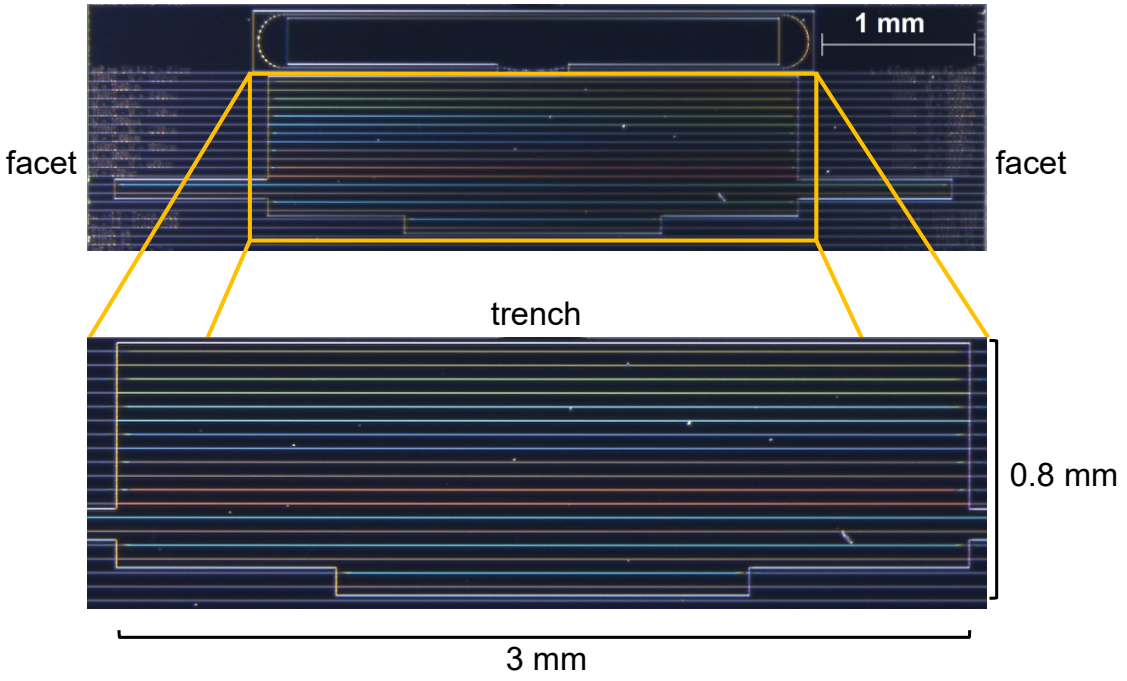

Figure S2. Optical microscopy image of the cladding trench zone of the silicon chip, containing the rib waveguides used in this study.

- **<u>Supplementary information 3</u>: fabrication of the BBGs**

Nanogrooved microcontact printing stamps were created by dispensing a mixture of polydimethylsiloxane (PDMS) monomer and curing agent (10:1 w/w) onto the structured side of a silicon master (period 416 nm, 100 nm groove depth and duty cycle 50%). Next, the mixture was degassed in a vacuum chamber for 30 minutes, and cured overnight at 60°C. Thereafter, the polymerized PDMS was peeled off from the master and chopped into squared pieces (2 x 2 mm). The resulting stamps were sonicated three times for 5 minutes in ethanol (30 % in MilliQ water) and air dried before use. See Figure S3 for a FESEM characterization of the stamp surface.

Then, a solution of 250 µg·mL^{-1} of bovine serum albumin (BSA) in sodium phosphate buffer (8 mM Na_2HPO_4, 2 mM KH_2PO_4, 137 mM NaCl, 2.7 mM KCl, milliQ water, pH 7.4) was incubated onto the structured side of the stamps for 160 minutes at room temperature. Next, the stamps were cleaned with milliQ water and air dried. Then, the structured side of the stamp was placed in contact with the silicon photonic platform for 20 minutes to transfer the BSA proteins to the top surface of the waveguides. This

stamping step was performed using a custom mechanical setup to apply a controlled and reproducible stamping pressure (Figure S4) to overcome the trench and reach the waveguide surface (Figure S5). Finally, the stamps were removed and the waveguides with the patterned BBGs were rinsed with PBST (sodium phosphate buffer with polysorbate 20 at 0.05% v/v) and water, and air dried.

To perform the biorecognition assays, solutions of antiBSA specific IgG (0-100 $\mu g \cdot mL^{-1}$) in PBST were incubated onto the BBGs. After 20 minutes of incubation, the photonic platforms were rinsed with PBST and milliQ water and air dried. A scheme of the overall process is illustrated in Figure 1A.

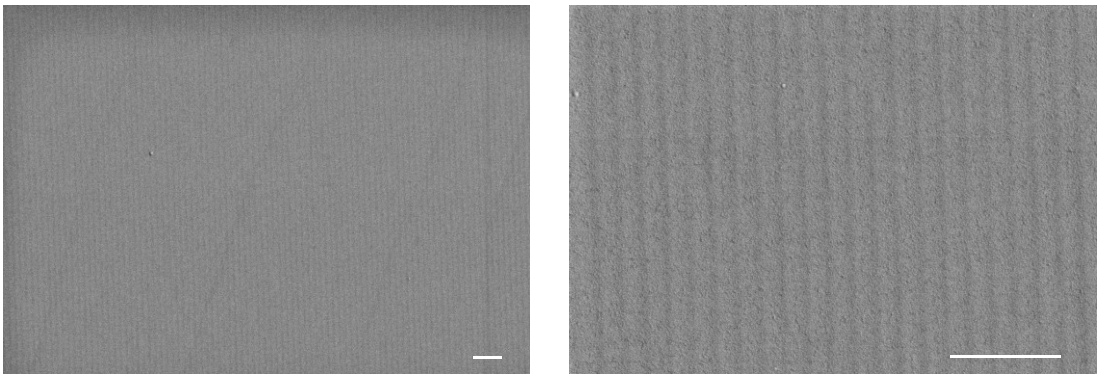

Figure S3. FESEM images of the PDMS stamps employed to fabricate the BBGs. Scale bars: 2 µm.

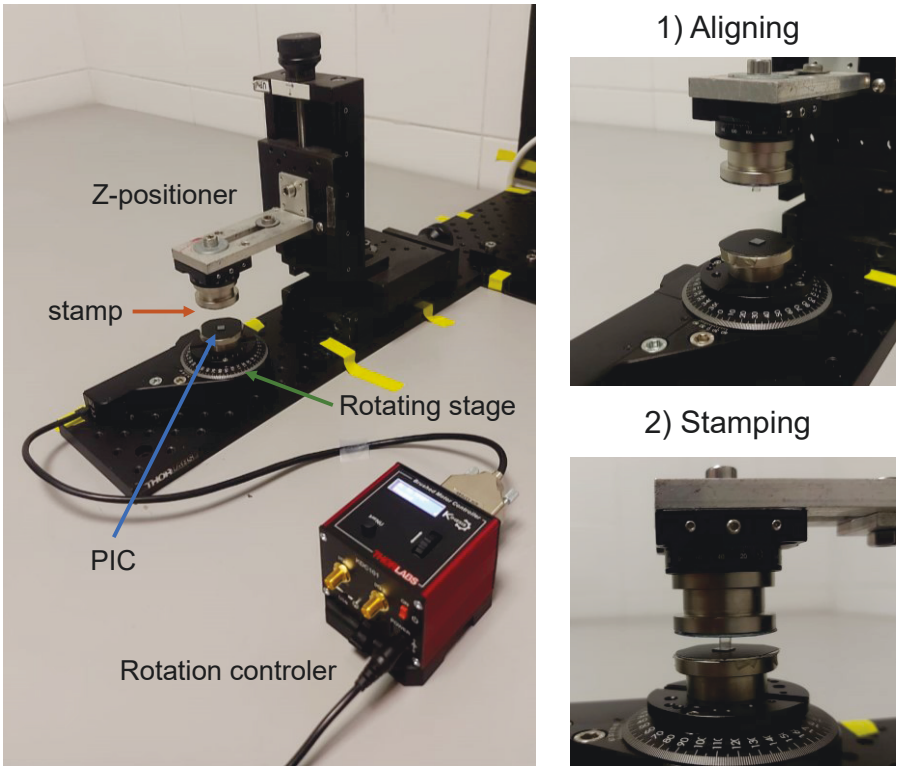

Figure S4. Photography of the mechanical setup used for stamping on the top surface of the waveguides.

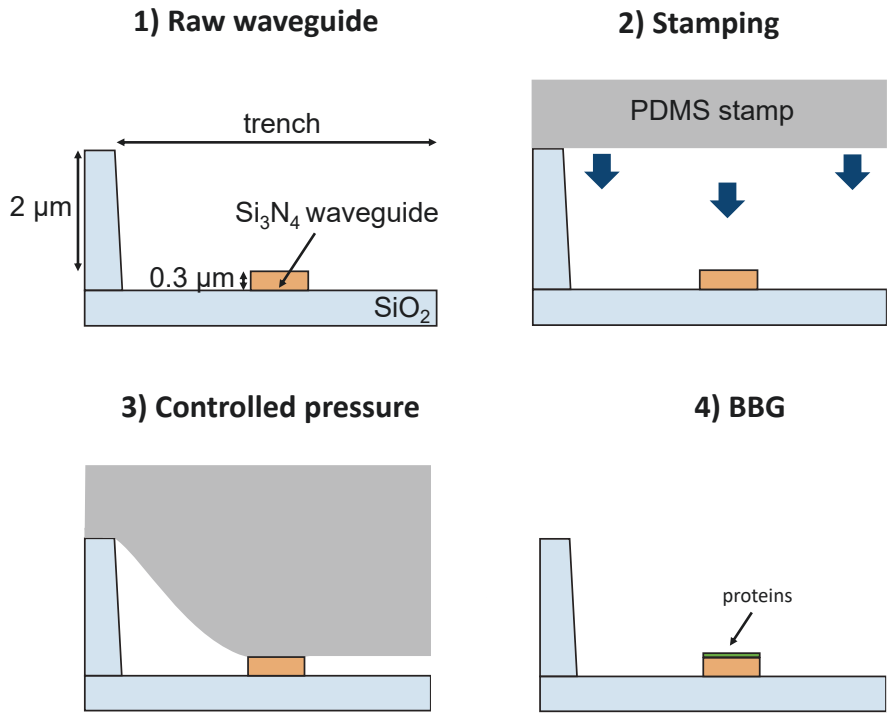

Figure S5. Scheme of a zoomed view of the stamping stage on the top surface of the waveguides within the trench area.

- **<u>Supplementary information 4</u>: structural characterization of the BBGs**

The structural characterization of the BBGs was performed by Field Emission Scanning Electron Microscopy (FESEM, ZEISS ULTRA-55 microscope, ZEISS, Oxford Instruments). The period of the structures was calculated as the sum of the average width of the protein strips and the average width of the gaps between them, measured form the FESEM images. The duty cycle was calculated as the average width of the protein strips divided by the period and multiplied by 100.

- **<u>Supplementary information 5</u>: tuning the BBG period**

The custom mechanical setup employed for the patterning (Figure S4) was also arranged to control the angle between the grooved relief of the stamp and the longitudinal direction of the guide (stamping angle). This strategy enables to obtain different BBGs periods on the waveguides (Figure S6 and Figure S7-S10).

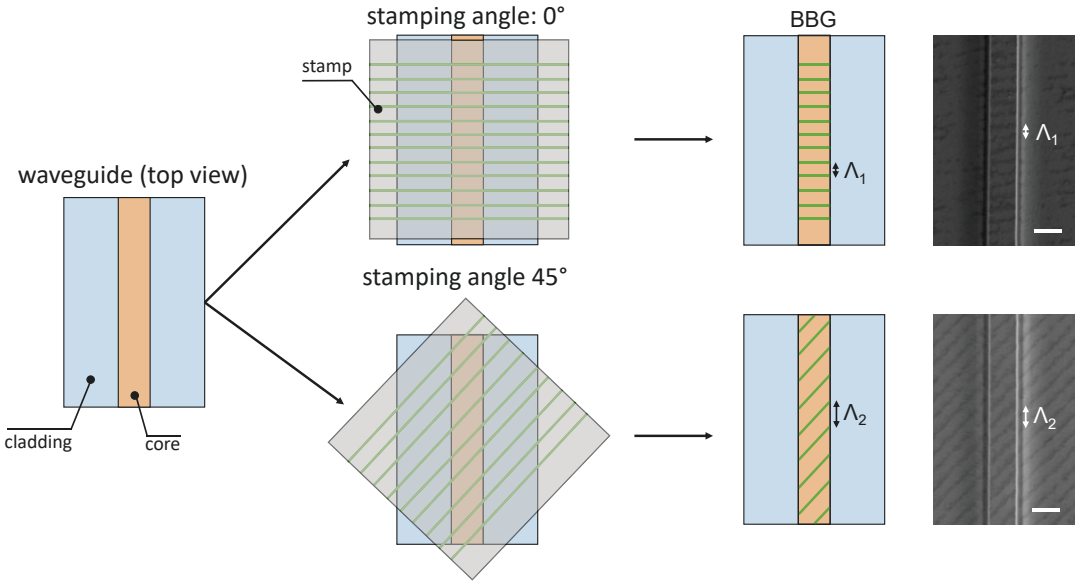

Figure S6. Scheme of the BBG period tuning by modifying the stamping angle.

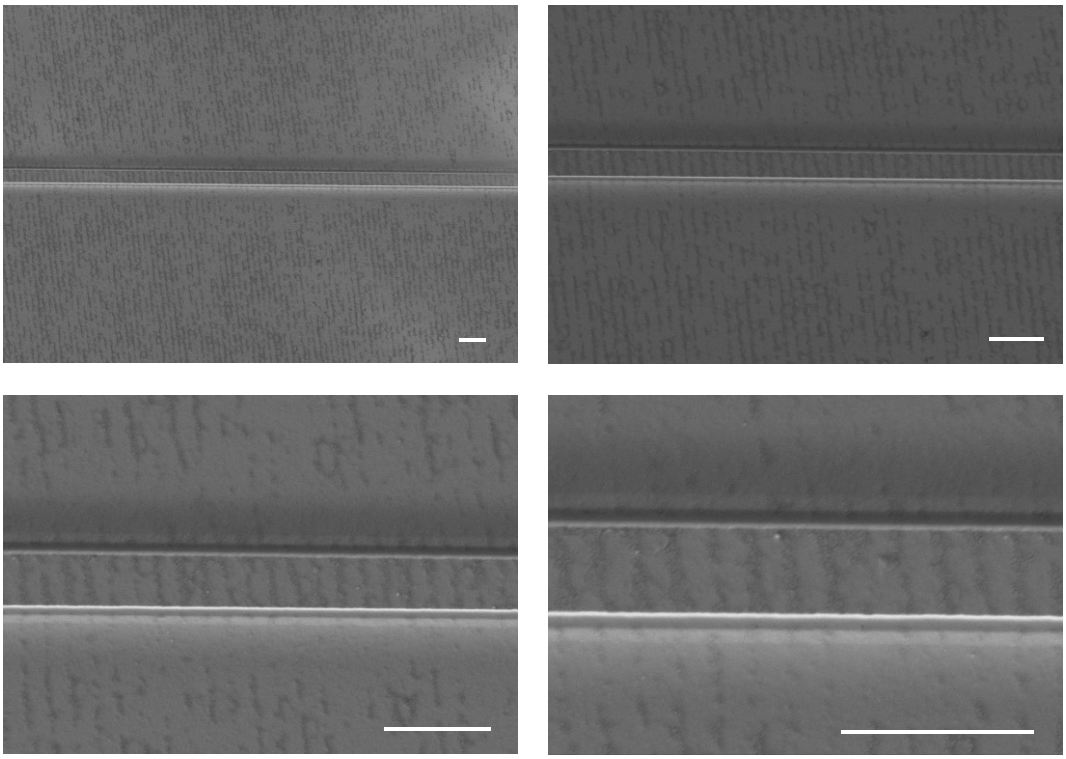

Figure S7. FESEM images of protein BBGs fabricated on 1 µm waveguides and a stamping angle of 0 degrees. Scale bars: 2 µm.

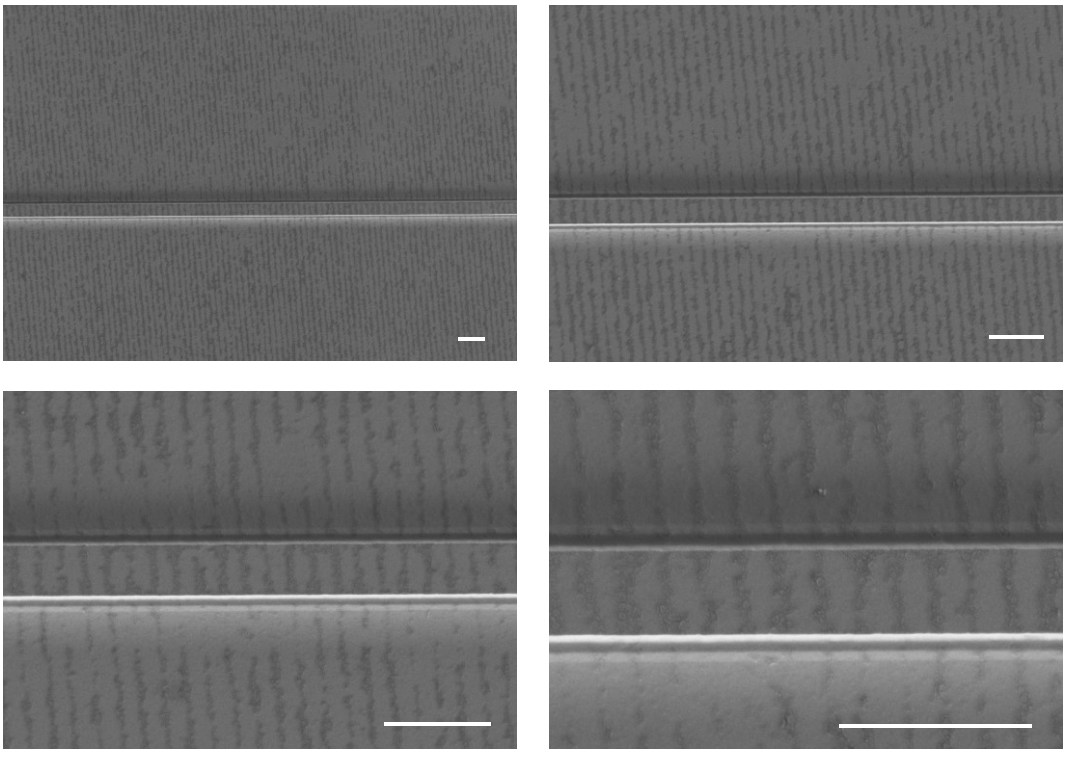

Figure S8. FESEM images of protein BBGs fabricated on 1 µm waveguides and a stamping angle of 15 degrees. Scale bars: 2 µm.

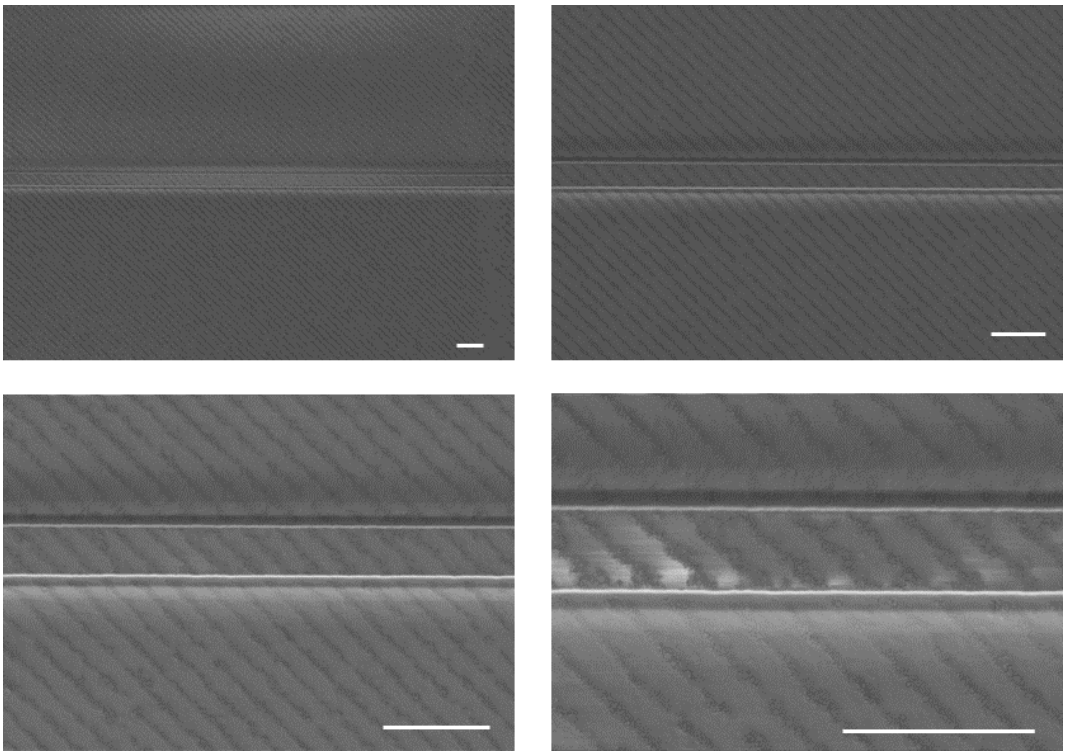

Figure S9. FESEM images of protein BBGs fabricated on 1 µm waveguides and a stamping angle of 45 degrees. Scale bars: 2 µm.

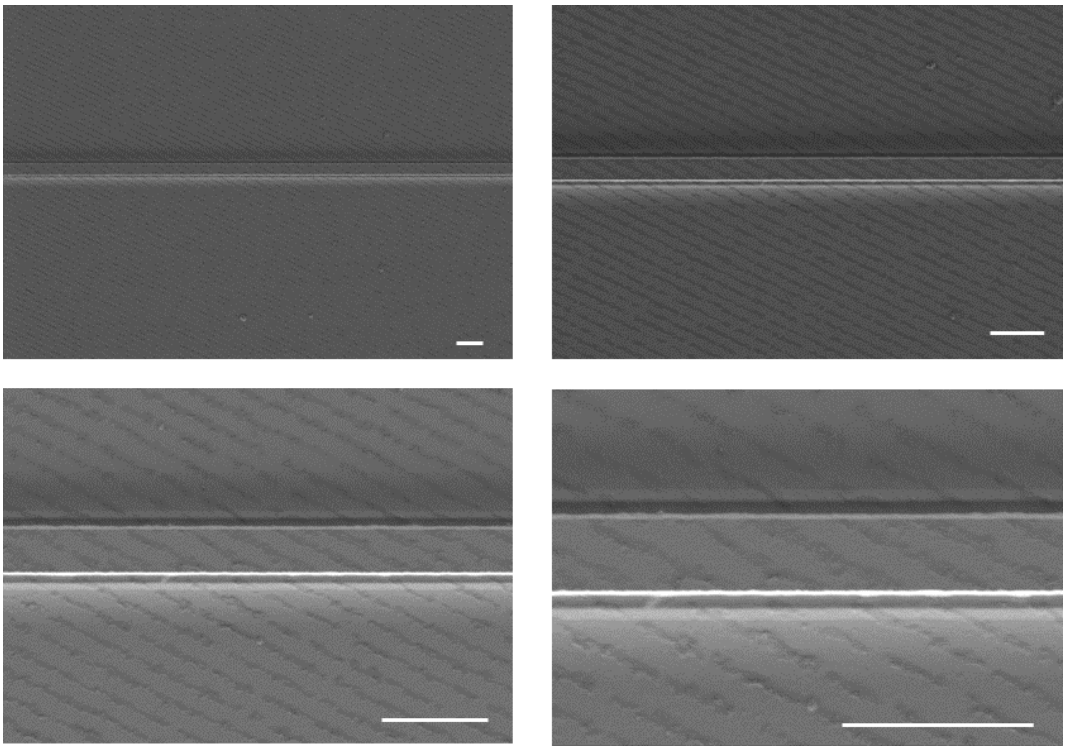

Figure S10. FESEM images of protein BBGs fabricated on 1 µm waveguides and a stamping angle of 60 degrees. Scale bars: 2 µm.

- **<u>Supplementary information 6</u>: optical measurements**

In order to assess the optical response in space-spectral domain we employ Optical Frequency Domain Reflectometry (OFDR).[6,7] As illustrated in Figure S11, the setup for these measurements is composed of two imbalanced Mach-Zehnder interferometers (MZI) in standard single-mode fibre, connected in parallel and fed by a scanning tunable laser (TL) (10 mW along 1490-1650 nm, Yenista TUNICs T100R). The device under test (DUT), in our case the Si_3N_4 chip, is placed in the upper MZI (DUT-MZI). In/out coupling can be done either through lensed fibres or microscope objectives. A polarization beam splitter (PBS) is connected to the output fibre and before the photodetectors to acquire both interferograms. Finally, the signals are collected by a digital acquisition card (DAQ) (National Instruments USB-6259). The lower MZI is employed as triggering (TRIG-MZI), since the DUT-MZI response is resampled (offline) by points provided by TRIG-MZI interferogram. This ensures that the DUT-MZI response is self-referenced against possible nonlinearities of the continuous TL scan. The time/distance events of the DUT (amplitude and phase) can be isolated by applying the inverse fast Fourier transform (IFFT) to the DUT-MZI interferogram. Time/distance event information is a key OFDR feature since it allows to eliminate the spurious reflections in the facets and unwanted transitions along the photonic path, thus focusing onto the BBG interaction range as indicated in Figure 1.

The BBG regions of the OFDR spectra were isolated and converted to the spectral domain in the logarithmic scale. The equivalence between logarithmic and linear scale was $dB = 10 \cdot log_{10}\left(\frac{P_1}{P_0}\right)$, where dB is the value of the power in logarithmic scale, P_1 is the intensity level in linear scale, and P_0 is the reference power level of the employed optical instrumentation. Then, the reflection peaks in the linear scale were integrated to provide the overall reflectivity of the BBG.

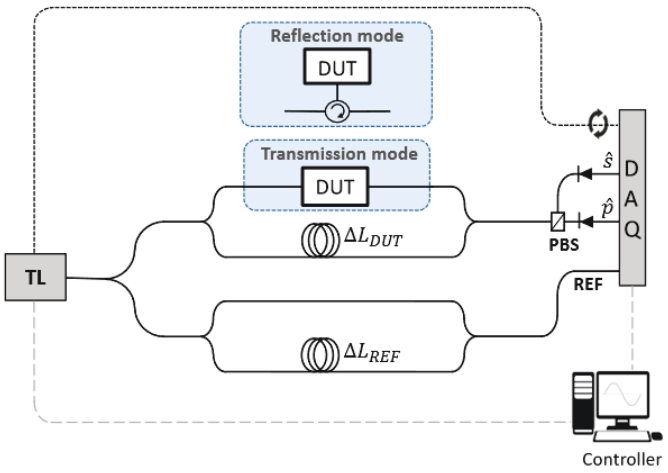

Figure S11. Scheme of the optical setup employed to perform the OFDR measurements.

- **<u>Supplementary information 7</u>: immunosensing**

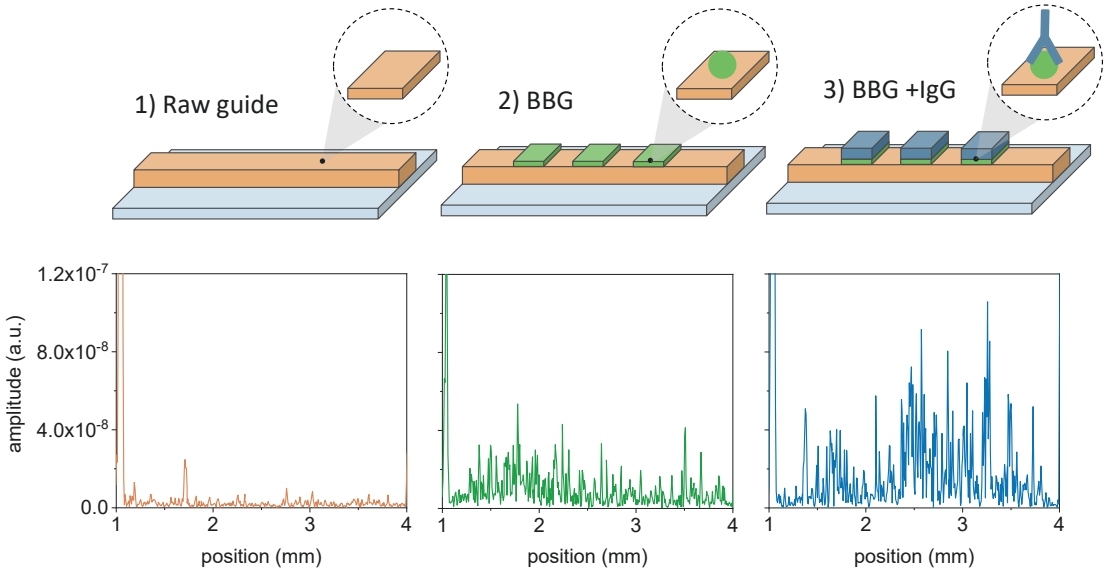

Figure S12. Zoomed view of the spatial domain spectra represented in linear scale, for better visualization of the increasing trend of the reflected signal along the successive fabrication and assay stages. See Figure 4A in the main manuscript for the equivalent graph in dB scale.

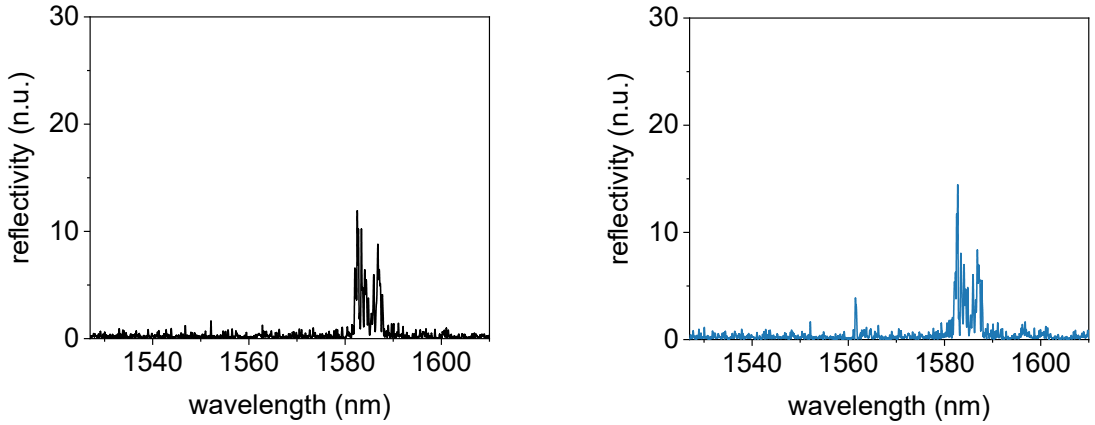

Figure S13. Reflection spectra before (left graph) and after (right graph) incubating PBST onto a BBG of BSA. It can be observed that the magnitude of the peak remains constant after this buffer incubation, unlike its counterpart experiment with the incubation of selective antiBSA IgGs (Figure 4A).

- **<u>Supplementary information 8</u>: regeneration**

To regenerate the waveguides after performing immunoassays on patterned BBGs of proteins, the silicon chips were sonicated for 10 minutes in a mixture of H_2O_2 (30%)/NH_4OH (32%)/H_2O (1:1:2). The process was repeated three times, and then the chips were rinsed with milliQ water. Finally, substrates were sonicated for five minutes in milliQ water, and dried under a stream of air. A FESEM image of a waveguide with a patterned BBG and its reflection spectra before and after performing the regeneration are shown in Figure S14.

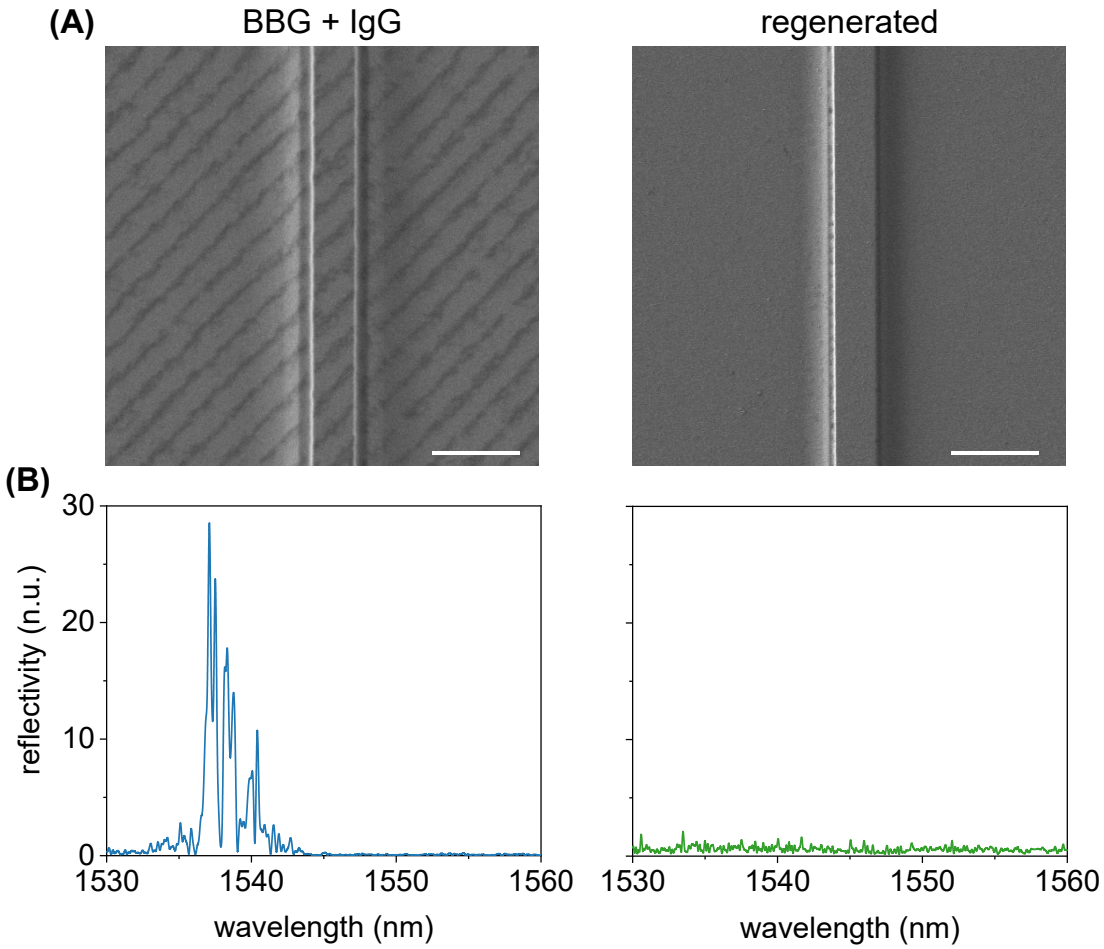

Figure S14. (A) FESEM images and **(B)** spectral-domain reflection response of a 1 µm waveguide with a BSA grating after incubating antiBSA (100 µg·mL^{-1}), before (left) and after (right) performing the regeneration process. Scale bars: 2 µm.

References

(1) Rumpf, R. C.; Garcia, C. R.; Berry, E. A.; Barton, J. H. Finite-difference frequency-domain algorithm for modeling electromagnetic scattering from general anisotropic objects. *Prog. Electromagn. Res. B* **2014**, *61*, 55–67. https://doi.org/10.2528/PIERB14071606.

(2) Zhu, Z.; Brown, T. Full-Vectorial Finite-Difference Analysis of Microstructured Optical Fibers. *Opt. Express* **2002**, *10* (17), 853. https://doi.org/10.1364/OE.10.000853.

(3) Freeman, N. J.; Peel, L. L.; Swann, M. J.; Cross, G. H.; Reeves, A.; Brand, S.; Lu, J. R. Real Time, High Resolution Studies of Protein Adsorption and Structure at the Solid-Liquid Interface Using Dual Polarization Interferometry. *J. Phys. Condens. Matter* **2004**, *16* (26), 0–4. https://doi.org/10.1088/0953-8984/16/26/023.

(4) Micó, G.; Gargallo, B.; Pastor, D.; Muñoz, P. Integrated Optic Sensing Spectrometer: Concept and Design. *Sensors* **2019**, *19* (5), 1018. https://doi.org/10.3390/s19051018.

(5) Munoz, P.; van Dijk, P. W. L.; Geuzebroek, D.; Geiselmann, M.; Dominguez, C.; Stassen, A.; Domenech, J. D.; Zervas, M.; Leinse, A.; Roeloffzen, C. G. H.; Gargallo, B.; Banos, R.; Fernandez, J.; Cabanes, G. M.; Bru, L. A.; Pastor, D. Foundry Developments Toward Silicon Nitride Photonics From Visible to the Mid-Infrared. *IEEE J. Sel. Top. Quantum Electron.* **2019**, *25* (5), 1–13. https://doi.org/10.1109/JSTQE.2019.2902903.

(6) Bru, L. A.; Pastor, D.; Muñoz, P. Integrated Optical Frequency Domain Reflectometry Device for Characterization of Complex Integrated Devices. *Opt. Express* **2018**, *26* (23), 30000. https://doi.org/10.1364/OE.26.030000.

(7) Bru, L. A.; Pastor, D.; Muñoz, P. Advanced and Versatile Interferometric Technique for the Characterization of Photonic Integrated Devices. *Opt. Express* **2021**, *29* (22), 36503. https://doi.org/10.1364/OE.435683.

GENERAL DISCUSSION

Exploiting diffraction to transduce biorecognition events is an appealing and powerful way to conceive innovative, compact, and miniaturized biosensing systems. In this way, grating structures composed of biological probes have demonstrated interesting biosensing capabilities, including a unique potential to avoid undesired signals from non-specific binders.

The first study of this thesis identifies and solves an important limitation of standard μCP, related to the loss of protein activity when patterning biogratings (Chapter 1.1). The results of this investigation, performed with biogratings of antibodies, reveal that the conformational changes undergone by the biomacromolecules during the patterning are critical when they contain the paratopes. This problem is hard to predict and constitutes an important limitation to develop biosensing approaches. We propose an alternative method called indirect μCP to assess this issue. It relies on patterning backfilling agents by standard μCP and then immobilizing the bioreceptors of interest in the nanostructured gaps by physisorption. BSA proteins presented great capabilities to be patterned as backfilling agents for indirect μCP in multiple materials with different compositions and hydrophilicity. Besides, other proteins could also be employed as backfilling agents as long as they generate structured gaps after their patterning. Moreover, the denaturation of the backfilling agents does not affect the performance of indirect μCP, which expands the number of species that can be used to this end.

Immunochemical approaches based on IgGs and IgEs as probes and analytes were employed to demonstrate the performance of indirect μCP, reaching limits of detection of 0.4 $\mu g \cdot mL^{-1}$ and 0.2 $\mu g \cdot mL^{-1}$, respectively. These results prove that the indirect patterning strategy keeps the advantages of μCP and allows the easy fabrication of functional patterns of antibodies that can detect their complementary counterparts by diffractive measurements. However, the low SNR values achieved suggest that these biogratings would be more suitable for qualitative analysis. Along these lines, there are experimental aspects as other backfilling agents, incubation of the probes, etc. to be explored in future works that may improve the bioanalytical performance of indirect μCP. From a general viewpoint, this investigation introduces an alternative patterning strategy for those cases in which standard μCP leads to biogratings of non-functional biological species.

In addition to solve problems associated with the activity of the patterned proteins, μCP can be also tailored to implement chemical reactions to achieve more stable immobilizations. This thesis reports a comprehensive comparison of the fabrication of biogratings by μCP combined with physisorption, imine reactions, and thiol-ene coupling. The study first demonstrates that the UV-ozone treatment of the PDMS stamps, typically employed to improve the transfer of inked molecules to the substrates, deteriorates the structuration of the gratings when patterning at submicron scale. In other experiments not included in this thesis involving micrometric structures and higher irradiation doses, this UV-ozone treatment allowed a more controlled modulation of the stamp hydrophilicity without damaging its surface.

Biogratings fabricated through the chemical routes were similar to those fabricated by physisorption in terms of homogeneity, strip thickness, and surface coverage, but displayed lower bioanalytical performances when assessing their functionality with a model immunoassay. Moreover, the thiol-ene route requires an adjustment of the UV dose to avoid the denaturation of the patterned proteins. It is important to highlight that this study employed albumins as bioreceptors and these proteins are especially suitable to be patterned by physisorption. Therefore, covalent μCP may be a useful alternative for patterning biomacromolecules that are prone to become physisorbed, as well as in assays that involve long sample incubations that may favor the desorption of physisorbed biogratings.

The diffraction efficiencies of the patterned biogratings increased in all the cases after incubating specific antibodies, and their ability to quantify biorecognition events was then demonstrated in three different immunoassays to detect allergies to antigens present in cow milk. Biogratings of BSA, casein and β-lactoglobulin were fabricated by physisorption and were implemented as diffractive transducers to sense specific IgGs, reaching limits of detection of 30, 35, and 44 $ng \cdot mL^{-1}$, respectively. Furthermore, the study provides insights into the selectivity and the potential to avoid NSB issues in the analysis of target biomolecules in serum samples. From a broader perspective, this work establishes the basis to fabricate diffractive structures by different μCP combinations and emphasize their potential to be applied in the quantification of immunoglobulins and biomolecules involved in other biological systems.

In view of all these findings, μCP has demonstrated to be a powerful and stimulating alternative to the standard nanofabrication techniques. Its simplicity, inexpensiveness, and versatility constitute an important advantage when addressing the fabrication of biogratings in a wide range of configurations and substrates. However, μCP still presents some inherent limitations such as low reproducibility of the resulting patterns, high concentrations of inking molecules, and long inking times that mostly restricts its applicability to lab environments. Along these lines, alternatives to μCP and the standard nanostructuration methods are nowadays a scientific challenge that is contributing to most areas of research.

The third investigation of this thesis reports a new photopatterning method to fabricate biogratings based on the local and periodic mild denaturation of protein biolayers by UV-laser irradiation. The characterization results demonstrate that these photopatterned biolayers are only composed of a periodic modulation of the protein functionality so they are free of topographic contributions. These biogratings proved to be excellent diffractive transducers of biorecognition events, allowing to reach sensitivities of tens of $ng \cdot mL^{-1}$ when sensing specific antibodies. Moreover, this investigation also suggests that keeping the chemical composition in both parts of the patterned biolayer contributes positively to minimize the signal contribution of non-specific bindings.

Compared to μCP, this photopatterning method presents an important improvement in terms of homogeneity, reproducibility, and fabrication time (Table 3). Large areas (15 x 1.2 mm) of homogeneous biogratings can be patterned in less than 2 minutes, while longer times (160 minutes for the inking and 20 minutes for the stamping) are needed in μCP. Moreover, the concentration of probes for this photopatterning (50 $\mu g \cdot mL^{-1}$) is lower than for the inking of the stamps (250 $\mu g \cdot mL^{-1}$), although it requires an overnight incubation. On the other hand, μCP does not need expensive facilities such as lasers and phase masks and can be carried out in traditional laboratories. Regarding the sensitivity, multiplexing, and capability to minimize the signal contribution of NSB, both methodologies present similar performances.

In addition to all the above-mentioned advantages, the photopatterning method opens up new venues to perform further investigations that expand its scope and exploit its

potential for biosensing. For example, it can be adapted to other bioreceptors and immunoassays (other proteins, IgG, DNA, etc.), and other irradiation systems (laser interference, direct laser writing, etc.). Moreover, it shows a great potential to be easily tailored to photochemical reactions to immobilize biomolecules.

Table 3. Qualitative comparison of the techniques studied to fabricate biogratings.

Features	µCP	Photopatterning
Homogeneity	-	+ +
Reproducibility	-	+ +
Fabrication speed	-	+ +
Fabrication facilities	- -	+
NSB	+	+
Multiplexing	+	+
Sensitivity ($\mu g \cdot mL^{-1}$)*	0.035	0.053

-- very low, - low, + high and ++ very high.

**LOD for the BSA-antiBSA system in phosphate saline buffer.*

In addition to finding scalable and homogeneous alternatives to fabricate nanostructures of biomolecules, a key aspect to expand the scope of diffractive biosensing relies on integrating biogratings in waveguiding substrates. The use of waveguides in biosensing points towards the development of miniaturized and compact devices that can be introduced for the development of point-of-need biosensors. Among other interesting features, most configurations based on waveguides allow the monolithic integration of active components such as laser sources and detectors, making it possible to converge all the optical functionalities in one single device.

Along these lines, the last chapter of this thesis focuses on bio Bragg gratings (BBGs), fabricated onto waveguiding structures that are able to diffract the guided light. The fourth study reports a theoretical and experimental research that demonstrates the transduction mechanism with BBGs on micrometric optical fibers. Optical fibers are very inexpensive materials that can be tapered to the desired diameters without inducing

optical losses during their fabrication. Despite their fragility and non-flat surface, BBGs can be patterned by microcontact printing with good homogeneity. However, with this technique only a portion of the fiber surface is patterned. A possible solution to increase the area covered by the BBG could be to implement the photopatterning method reported in the second chapter in this kind of devices. Regarding the bioanalytical performance of the BBGs, well-correlated dose-responses were obtained using a model immunoassay based on patterned proteins and antibody targets, reaching a limit of detection of 100 $ng \cdot mL^{-1}$. This is a promising sensitivity compared to the recent label-free diffractive biosensing approaches in the state-of-the-art. A relevant aspect that distinguishes this approach from the standard FBG is the inherent capability of biogratings to minimize the signal contribution of non-specific bindings, which is essential to analyze biorecognition events in complex samples. Besides, the easy tunability of the optical response by changing the fiber diameter or the period of the BBG provides appealing prospects to perform multiplexed assays on one single fiber. In addition to demonstrating for the first time this novel transduction mechanism, this investigation also states the basis to transfer BBGs to other waveguides and configurations.

Within this context, the last investigation of this thesis reports the integration of BBGs on waveguides embedded in silicon platforms to conceive more robust and integrable devices. In this approach, BBGs were also fabricated by μCP, which provides more evidences about the versatility of this patterning method. The theoretical calculations and experimental results revealed that different rib waveguides (0.8-1.2 μm width) are compatible with the transduction principle behind BBGs. The use of OFDR in this approach allows to isolate the BBG signals from other unwanted optical contributions such as the reflections of the facets. The use of OFDR could also be useful to perform multiplexed analysis in one single waveguide without changing the period of the BBGs, but require expensive equipment and more complex detection systems. Finally, this investigation provides a starting point to develop more sophisticated PICs tailored to the specific needs of the BBGs.

One of the main advantages of the silicon platforms compared to optical fibers rely on their higher capability to integrate a huge number of waveguides with different

configurations in a very small size (from µm to mm), improving significantly the multiplexing capabilities. Moreover, silicon platforms also allow the integration of active components such as laser sources and detectors, which constitutes nowadays an increasing trend in the photonic field to fabricate fully functional devices without needing peripheral accessories. However, their design and fabrication require sophisticated that are still expensive nowadays.

Optical fibers are very cheap and can be modified with simple techniques in standard laboratories. This fact makes them ideal to address a first approximation to a new biosensing approach, as done in this research with the BBGs. However, their fragility when reduced at micrometric (1-10 µm) scale and their lower capacity to integrate active components restrict their applicability when conceptualizing point-of-care biosensing approaches. Compared to diffractive biosensing in free space, optical fibers still represent an important improvement in terms of miniaturization, integration, and remote monitoring. A comparison of the main features of the different strategies studied in this thesis to exploit biogratings is shown in Table 4.

Table 4. Qualitative comparison of general features of the biogratings in the platforms studied in this thesis.

Feature	Free-space	Microfibers	PICs
Size	cm-mm	cm-mm	mm-µm
Cost[A]	--	--	++
Fabrication facilities[A]	--	-	++
Integration[A]	-	+	++
Fragility[A]	-	++	+
Active components	Peripheral	Peripheral	Peripheral-integrated
LOD (µg·mL^{-1})[B]	0.03-0.05	0.1	0.3
LOQ (µg·mL^{-1})[B]	0.07-0.2	0.4	3.7

[A] -- very low, - low, + high and ++ very high.

[B] experimental LOD and LOQ obtained with BSA biogratings and anti-BSA IgG targets in PBS-T.

In summary, the results of this thesis provide an in-depth study of the fabrication of biogratings by μCP, investigate alternative manufacturing strategies to those existing in the state of the art, and extend the scope of these systems by reporting for the first time their integration in photonic devices. Beyond the results herein introduced, this thesis also establishes new perspectives to improve the performance of biogratings in waveguiding structures. For example, their homogeneity and reproducibility may be improved and standardized by implementing the photopatterning method presented in this research. Also, these results point towards new BBG PICs with light sources and detectors integrated monolithically to offer new solutions for point-of-care analysis.

GENERAL CONCLUSIONS

The investigations englobed in this thesis provide scientific innovations that extend the scope of diffractive biosensing. In particular, this thesis explores new tools and methodologies to fabricate biogratings, exploits their biosensing capabilities, shows their integration in waveguiding structures, and provides appealing insights toward the integration of all the optical functionalities in one single photonic platform. From a general perspective, this research is focused on model biological systems to prove the concepts and aims to provide insights into the applicability of the resulting advances to other biorecognition systems.

The main conclusions of this thesis and the prospects are listed below:

- Indirect microcontact printing is a new strategy to fabricate functional biogratings for biosensing. It offers a simple alternative to standard μCP, especially useful for patterning biomolecules that are susceptible to suffering conformational changes that lead to a loss of their biological activity. Moreover, our results also established the basis to implement indirect microcontact printing to a broad range of substrates and other biomolecules of interest.

- The incorporation of chemical reactions into μCP opens a new range of opportunities to fabricate functional biogratings at the submicron scale to act as diffractive transducers for the label-free quantification of biorecognition events. In this sense, biogratings fabricated using chemical reactions display homogeneities and surface coatings similar to those fabricated by physisorption, and the versatility of μCP to incorporate different biosensing systems was demonstrated. The results obtained in this investigation also provide important insights into the combination of other chemical reactions with μCP and its application in real immunosensing scenarios.

- The new photopatterning method developed permits the fabrication of large areas of biogratings. This strategy, based on the local and periodic mild denaturation of protein layers, also represents an important advantage compared to μCP in terms of homogeneity, reproducibility, fabrication time, and scalability. Moreover, the improved ability of the photopatterned biogratings to

minimize the signal contribution of non-specific bindings provides a unique advantage in the analysis of raw biological samples. These results also indicate the high potential of the photopatterning method to be carried out by other laser configurations in order to extend the scope of this tool to further biogratings designs and applications.

- BBGs exploit the benefits of waveguides and biogratings to develop compact and miniaturized biosensing devices. This first approach based on optical fibers highlights the easy tunability of the optical response and provides promising multiplexing prospects. Moreover, the results reported in this investigation state the background to implement BBGs into other waveguiding configurations with improved integration capabilities.

- The use of waveguides integrated into silicon platforms significantly extends the applicability of BBGs in the biosensing scenario. The wide range of waveguiding configurations and designs that can be conceptualized provides great versatility in the customization of the BBG performance. Furthermore, the potential to incorporate active components allows to implement all-optical functionalities in one fully functional device, constituting an interesting and ambitious solution for the real application of BBGs to different scenarios and analytical needs.